A STUDY ON THE FUNDAMENTAL BEHAVIOUR OF SOIL-STRUCTURE INTERACTION AND MITIGATING EFFECTS OF EPS GEOFOAM INCLUSIONS IN INTEGRAL ABUTMENT BRIDGES

Ahmed Al-qarawi

MSc. Engineering

This thesis is submitted as a fulfilment for the degree of

Doctor of Philosophy

School of Engineering

Western Sydney University

March 2021

This thesis is dedicated to,

My wife, Nesmah Abdullah, My kids, Leen and Ali

and

My beloved Mother

Declaration

Date: 29 March 2021

Author: Ahmed Swadi Mohammed Al-qarawi

Title: A STUDY ON THE FUNDAMENTAL BEHAVIOUR OF SOIL-STRUCTURE INTERACTION AND MITIGATING EFFECTS OF EPS GEOFOAM INCLUSIONS IN INTEGRAL ABUTMENT BRIDGES

Degree: Doctor of Philosophy

I certify that the work presented in this thesis is, to the best of my knowledge and belief, original, except as acknowledged in the text, and the material has not been submitted, either in full or in part, for a degree at this or any other institution.

I certify that I have complied with the rules, requirements, procedures and policy relating to my higher degree research award of Western Sydney University.

I declare that this study is funded by the Australian Government through the Research Training Program.

[redacted]

Author’s signature

Acknowledgments

First, I would like to extend my sincere gratitude and appreciation to my principal supervisor, Professor Chin Leo, for his invaluable and great support throughout the research period. His constant attention and guidance have been vital in publishing the outcomes of this research in addition to the successful completion of the thesis. Professor Leo provided me with a great knowledge, not only about the topic of this research, but also about different research skills including how to initiate concepts, develop and publish research articles. I am deeply grateful to him for every effort and advice he provided toward the completion of my degree. Apart from the research work, Professor Leo is a great person with all his empathy and care. He has been a great supervisor, a teacher and a friend.

I also extend my gratitude to my co-supervisor, Associate Professor Samanthika Liyanapathirana, for her assistance and attention throughout every stage in my research period. Her valuable feedback and guidance have been of great help in completing this thesis.

I would like to acknowledge Western Sydney University, the School of Engineering for providing the necessary laboratory facilities and the wok environment. I would like to thank Mr. Van Doan and Mr Lila Sigdel for their assistance and help in my research work.

I would also like to gratefully thank my lovely wife for her great support, efforts and interest she has provided throughout my study.

Publications

The outcomes of this study have been summarized and submitted for publication as described below:

- Alqarawi, A. S., Leo, C. J., Liyanapathirana, D. S., Sigdel, L., Lu, M., & Hu, P. (2021). A spreadsheet-based technique to calculate the passive soil pressure based on the log-spiral method. *Computers and Geotechnics*, *130*, 103926.
- Al-Qarawi, A., Leo, C., & Liyanapathirana, D. S. (2020). Effects of wall movements on performance of integral abutment bridges. *International Journal of Geomechanics*, *20*(2), 04019157.
- Al-Qarawi, A., Leo, C. J., & Liyanapathirana, S. (2017). A study on the effects of mode of abutment wall movements in integral abutment bridges. In *Proceedings of the 1st International Conference on Geomechanics and Geoenvironmental Engineering (ICGMGE2017), 20-22 November 2017, Sydney, Australia* (pp. 180-185).
- Sigdel, L.D., Leo, C., Liyanapathirana, S., Hu, P. Alqarawi, A., Doan, V., 2021. Response of approach to Integral Abutment Bridge under cyclic thermal movement. *Sustainable Infrastructure*s, *6th Geo-China International Conference, China 2021*. (Manuscript accepted)
- Alqarawi, A. S., Leo, C. J., Liyanapathirana, D. S., Sigdel, L., Doan, V., & Hu, P. (2021). Experimental study on the soil-structure interaction in response to cyclic loading. (Manuscript under preparation)
- Sigdel, L.D., Leo, C., Liyanapathirana, S., Hu, P. Alqarawi, A., Doan, V., 2021. Geotechnical Design Guidelines and Recommended Practices for Integral Abutment Bridge Systems: A Review. (Manuscript under preparation)

Previous Publications

- Alqarawi, A., Leo, C. J., Liyanapathirana, D. S. and Ekanayake, S. D. (2015). Parametric study on the approach problem of an integral abutment bridge subjected to cyclic loading due to temperature changes. *Journal of Applied Mechanics and Materials*
- Alqarawi, A., Leo, C. J., Liyanapathirana, D. S. and Ekanayake, S. D. (2016). A study on the effects of abutment cyclic movements on the approach of integral abutment bridges. *Australian Geomechanics Journal.*
- Alqarawi, A., Leo, C. J., Liyanapathirana, D. S. and Ekanayake, S. D. (2016). The approach problem of an integral abutment bridge subjected to cyclic loading due to temperature changes. *19th Southeast Asian Geotechnical Conference and 2nd Association of Geotechnical Societies in Southeast Asia, Malaysia 2016*.

Abstract

The traditional construction procedure of bridges involves the use of expansion joints to allow for unrestricted superstructure movements against the temperature induced deformations. However, expansion joints have been demonstrated to be vulnerable to deterioration thus requiring frequent and costly maintenance. In that regard, the Integral Abutment Bridge (IAB) system presents an attractive alternative to overcome such problems. In addition to the advantages achieved by eliminating the expansion joints, the IABs have desirable structural performance and offer simple and rapid construction procedures. In the last few decades, IABs have been increasingly utilised in many countries around the world. Nowadays, the integral and semi-integral abutment bridges are becoming the first choice in the construction of bridges.

Nevertheless, the IABs yet have their unique problems that ensue from the regular expansions and contractions (including shrinkage) in the superstructure. The structural system of IABs relies on the abutments movements to accommodate such changes in the dimensions of the bridge. The repetitive abutment movements, against and away from the retained soil, result in long term build-up of the lateral earth pressure and development of settlement bump at the approach. In consequence to these effects, the abutments will experience an escalated soil pressure that may exceed the design values and potentially damages the abutment. Moreover, the developed settlement bump at the abutment approach could lead to riding quality, if not safety, issues for the bridge users. These problems have negated some of the advantages of IABs and restricted their use.

The complex soil-structure interaction mechanism in IABs has made it difficult for engineers to find the appropriate solution to address the approach issues in this type of bridges. Adopted remedy measures include the use of run-on concrete approach slabs, heavily compacted approach fill, compressible inclusion between the soil and the abutment, and self-stable MSE approach fill with gap separation between the abutment and the MSE fill. However, no single solution can adequately address the broad array of IAB cases, each under a different setting, across the world.

The present thesis extends current insights on the soil-structure interaction of IABs, with particular emphasis on the effects on the soil settlement and the lateral pressure at the integral abutment approach. The aim is to provide a sound basis to develop potential or improve current mitigating solutions. The thesis then investigates using EPS geofoam as a mitigating solution through a study of soil-EPS and EPS–abutment interactions. A combination of physical modelling and numerical analyses has been utilized to perform these investigations.

In the thesis, a comprehensive review of the existing practices in dealing with the soil-structure interaction effects in IABs has been undertaken. A novel analytical solution is developed to estimate the passive earth pressure based on an earlier hypothesis of Terzaghi. This solution provides an efficient tool to calculate the passive earth pressure which represents a fundamental input in the estimation of earth pressure in IABs.

The study also involves an experimental program conducted on small-scale and large-scale physical models to study soil-wall interaction, with emphasis on the effects of the movement mode (rotation and translation) and the presence of an EPS inclusion. The data from the experimental tests was then used to validate a 2D Mohr-Coulomb finite element model developed in ABAQUS/standard (2017) software. After the validation, the finite element model was geometrically extended to simulate a prototype full-scale integral abutment supported on steel piles and subjected to lateral displacement. The numerical study provided insights and evidence to support the use of EPS inclusions as a mitigating solution in full scale prototype scenario.

The large-scale physical model with similar stress and strain fields to the full-scale prototype was used to study the soil-structure interactions of the integral abutment. It sheds new light on the ratcheted lateral pressure distribution of translational cyclic abutment movements, which was found to exceed those recommended in PD-6694-1 (a set of recommendations for design of structures subject to traffic loading to BS EN 1997-1:2004+A1:2013), including a lower location of the maxima. These would result in greater bending moment in the abutment. The study also found clear evidence of cyclical soil slumping that leads to increased settlement trough. The soil-EPS and EPS-abutment study provides further evidence of the efficacy of EPS geofoam inclusion in mitigating lateral pressure and settlement trough.

A 3D finite element model, simulating the large scale test chamber, was also developed based on the GSK constitutive model for the soil. Unlike Mohr-Coulomb model, the GSK model takes into account the nonlinear stress dependency of the soil friction angle. The thesis extended the original GSK model (referred herein as the EGSK model) to include stress dependency of the soil stiffness. The 3D EGSK FEM was validated using results from the large-scale physical model tests. This model was then used to numerically investigate a full-scale prototype concrete abutment attached to inclined wing walls and supported by steel H piles. The modelling results of the full-scale abutment, suing the EGSK model, showed a notable nonlinear behaviour in both the settlement as well as the lateral earth pressure compared to those computed using Mohr Coulomb model. The study and the large-scale physical modelling suggest that some work is still needed to design a self-stable system to reduce soil slumping.

Finally, the research conclusions and recommendations for future studies in regard to the soil-structure interaction behaviour in IABs and the further studies of mitigating solutions using the EPS geofoam are presented.

Table of Contents

List of Figures

List of Tables

List of Symbols

Roman

C	Celsius temperature
c	Cohesion of soil
d	Horizontal wall displacement
d_d	Deck displacement
E	Elasticity modulus
E_{50}	Large-strain modulus
$E_{\circ}$	Small-strain modulus
E_p	Operational stiffness of soil
F	Fahrenheit temperature
g	Gravity
H	Height of the retained soil
K^*	The critical coefficient of lateral earth pressure according to the UK BA42/96 and PD 6694/1 specifications
K_a	Active coefficient of lateral earth pressure
K_o	At-rest coefficient of lateral earth pressure
K_p	Passive coefficient of lateral earth pressure
N	Number of wall movement cycles
n	Scale factor between centrifuge and prototype dimensions
P_p	Passive soil pressure
z	Depth from soil surface

Greek

β	Backfill slope angle
γ	Unit weight of the retained soil
δ	Angle of friction between the soil and the wall
Δ_a	Axial deformation
Δ_r	Radial deformation
Δ_x	Deformation in *x* direction
Δ_z	Deformation in *z* direction
ε	Total strain
ε_o	Immediate strain
ε_t	Time dependant strain in EPS
ε_v	Volumetric strain
θ	The inclination angle of the interface planar between the EPS and the soil
ν	Poisson ration
ξ	The radial distance related to the Pole location
σ_h	Horizontal stress
σ_v	Vertical stress
ϕ	Friction angle of the soil
ψ	Dilation angle of soil
ω	Wall inclination angle

Abbreviations

AASHTO	American Association of State Highway and Transportation Officials
C3D10	Ten-node quadratic tetrahedron element with reduced integration
CPE8R	Eight-node quadratic element with reduced integration
DOT	Department of Transportation
EGSK	Extended GSK finite element model
EPS	Expanded Polystyrene
FE	Finite Element
FHWA	American Federal Highway Association
FIABs	Full Integral Abutment Bridges
IABs	Integral Abutment Bridges
LVDT	Linear variable differential transformer
MC	Mohr Coulomb
SIABs	Semi-Integral Abutment Bridges

Chapter One

Introduction

1.1 Background

Bridges are conventionally designed and constructed with expansion joints to allow for unrestricted movements in the longitudinal direction of the bridge. These movements are caused by various factors such as the expansion and contraction associated with the ambient temperature fluctuations, post-construction shrinkage, creep and long term settlements in the bridge support system. Expansion joints are constantly exposed to severe loading conditions due to the deck movements as well as the continuous traffic loading. As a result, they are vulnerable to deterioration quicker than other components of the bridge. Hence, the expansion joints require regular maintenance throughout the lifetime of the bridge to maintain them in a permissible operational standard which is costly and inconvenient for the bridge users. A study conducted in the United Kingdom on 200 bridges revealed that the expansion joints are the dominant source of costly and traffic-retarding bridge maintenance works (Lock, 2000). A study on 71 bridges in Portugal reported that the maintenance cost of bridge joints represents approximately 25% of the global maintenance cost of the bridges (Lima and Brito, 2009). That is in addition to the road closures and traffic interventions required during the maintenance works causing significant inconvenience for road users. Moreover, defective expansion joints can sometimes produce serious hazards to drivers due to broken or loosen parts. Therefore, expansion joints have always been a source of construction and maintenance inconvenience to bridge engineers. Consequently, the concept of jointless or integral abutment bridges (IABs) has been receiving increasing interest in the past few decades.

The first use of integral abutment bridges was recorded in 1938 in the United States and have been widely utilised around the world ever since. Currently, IABs represent the standard choice of bridge construction in many countries such as the USA and the United Kingdom. The IAB system provides an excellent alternative to overcome the expansion joint issues in addition to achieving substantial savings in the construction and maintenance costs.

1.2 Integral Abutment Bridges (IABs)

The principle structural merits of IABs ensue from the elimination of the expansion joints. A deck girder in an IAB acts as a continuous beam with fixed ends rather than a simply supported beam. This feature helps to minimise the bending moment developed at the girder’s mid-span and consequently reduces the design requirements for the bending moment. It also improves the overall structural performance against seismic loads.

Although IABs often have similar superstructure systems, they may have different substructures. The substructure of an IAB consists of the bridge abutments and the supporting foundation. The abutments are responsible for transferring the vertical and/or horizontal loads and bending moments to the underlying foundation. The abutments also represent those elements where the bridge interacts with the approach backfill soil. Therefore, the type of the abutment plays an important role in the structural behaviour of the substructure and consequently the design approach of the substructure system of IABs.

Integral abutment bridges are broadly classified into, full integral abutment bridges (FIAB) and semi integral abutment bridges (SIAB). The primary variation between these two types is the connection between the abutment and the supporting foundation. In full integral abutment bridges, the abutment, which often termed as Full Integral Abutment (FIA), is rigidly connected to the foundation in the bottom end. Therefore, any potential movement in the deck will be reflected on the abutment as well as the foundation of the bride. On the other hand, the abutment in Semi integral abutment bridges (SIABs) is physically and structurally not connected with the foundation of the bridge and can move independent to the latter. Figure 1.1 shows typical sections of abutments in FIAB and SIAB

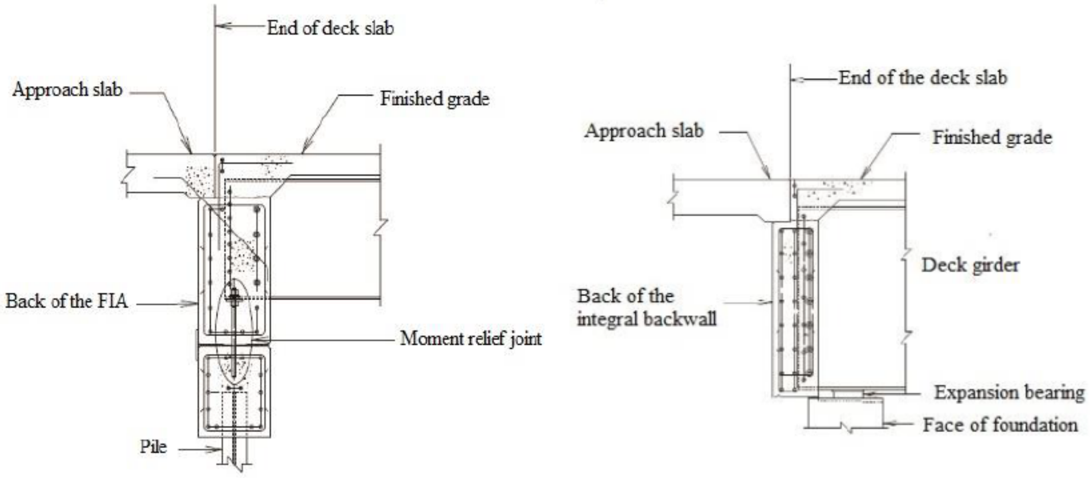

(a) (b)

Figure 1.1 Typical section in (a) full integral abutment and (b) semi integral abutment (Hoppe et al., 2016)

1.3 Attributes of IAB Systems

Integral bridges are generally performing efficiently and last longer than traditional bridges with less maintenance works (Burke, 2009). The attributes of IABs are principally attained by the elimination of the expansion joints, and bearings in some cases, from the bridge deck. The main advantages of IABs are,

- Lower construction cost and shorter project time.
- Significant savings in the potential maintenance costs throughout the lifetime of the bridge.
- Ease of design and construction
- The structural continuity improves the bridge structural performance in terms of resisting seismic loads

- Elimination of the possible safety issues due to defective joints and alleviate riding quality issues.

1.4 Limitations of IABs

In spite of the various merits of the IAB system, it is not without some inherent problems of its own, which largely limit its use. The problems in the IABs are due to the complex soil-structure interaction unique to this type of bridges. The expansion and contraction of the bridge deck particularly in response to the variations in the ambient temperatures will be reflected on the abutments in cycles of passive/active movements due to the absence of expansion joints (Figure 1.2a). Although the amplitude of such movements is very small and only ranges within few tens of millimetres, it could result in significant structural and geotechnical problems in the long term.

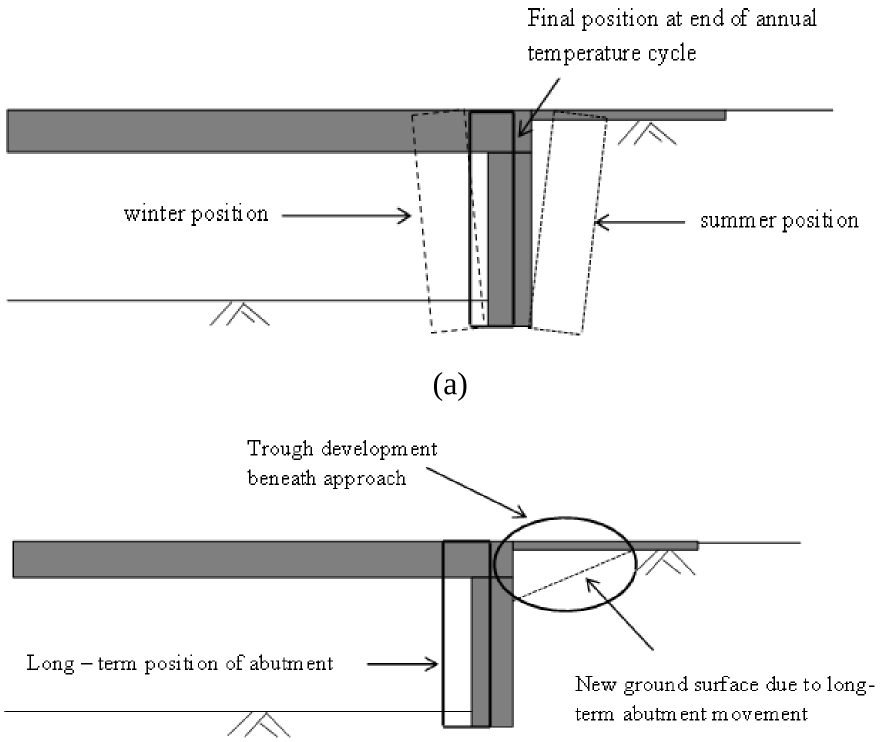

(a)

(b)

Figure 1.2 Abutment thermally induced movements and the subsequent effects on bridge approaches (Horvath, 2000)

There are two primary detrimental effects, from geotechnical viewpoint, resulting from the abutment movements as discussed below:

1.4.1 Long Term Build–up of Lateral Earth Pressures:

The continuous active and passive displacements of the abutment results in cycles of loading/unloading to the backfill soil adjacent to the abutment. As the number of movement cycles increases, the retained backfill becomes increasingly densified causing an escalation in the lateral earth pressure exerted on the abutment or the so called *stress ratcheting* (England et al., 2000; Horvath, 2000). The build-up of lateral earth pressure under this phenomenon may take many years to occur, but it can produce a serious structural problem that may result in a structural distress for the abutment.

The high passive resistance from the approach backfill can affect the superstructure as well. In the hot seasons, bridge deck tends to expand. The rigidly confined deck will, therefore, experience high axial (in non-skewed bridges) or eccentric (in heavily skewed bridges) forces that combine with the existing live and dead loads. The interaction of such loads is very complex and hard to predict or be addressed during the design of the abutment. These loads may result in significant stability issues especially in skewed semi integral abutment bridges.

1.4.2 Deformation of the Approach Soil

The cyclic movements of the abutment towards and away from the retained soil and the associated increase in lateral pressure will result in soil densification and volume contraction (Ng et al., 1998). Soil slumping will also occur during the active movement of the abutment. The aforementioned impacts will collectively contribute to develop the classical soil trough and/or bump at the bridge approach. Figure 1.3 shows a typical soil trough developed at an IAB approach. The size, pattern and depth of the soil trough depend on different factors such as the frequency and amplitude of the cyclic movement, depth and type of the abutment, mode of abutment movement and the properties of the backfill (Cosgrove and Lehane, 2003).

The aforementioned temperature-induced effects in IABs represent primary impediments that largely restrict the use of IABs to a limited range of bridge lengths. Therefore, introducing a practical engineering solution to rectify or at least alleviate the effects of the approach issues in IABs has been a principle concern of the geotechnical and structural engineers dealing with this type of bridges. Such a solution will broaden the use of IABs and maximize their engineering and economical advantages.

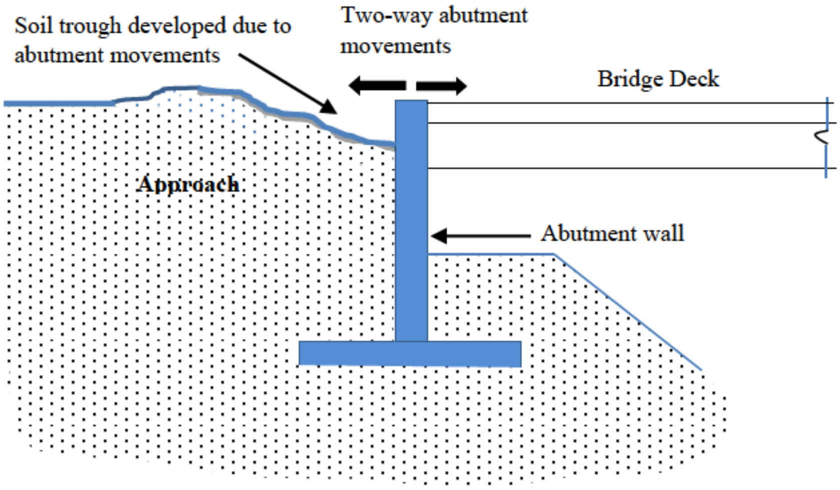

Figure 1.3 Typical approach settlement in integral bridge due to abutment cyclic movements

1.5 Measures to Mitigate the Approach Problems in IABs

The traditional practices utilized to overcome the approach problems in IABs involve the use of concrete run-on slab at the bridge approach to span the possible settlement trough. However, the use of run-on slab is not always tenable and engineers in some countries such as the UK do not recommend it as it complicates the approach maintenance work. In such cases, the engineers rely on regular approach patching and pavement overlying to rectify the settlement problem. Other available measure is using a well compacted backfill at the bridge approaches, which may minimise the soil settlement. However, it has been found that heavily compacted backfill result in significant escalation in the lateral earth pressure acting on the abutment wall due to the cyclic movements. There are a few trials that have been initiated recently utilising either a partial or full separation between the abutment and the approach soil. In the partial separation scenario, some sort of compressible material/inclusion is provided at the interface between the abutment and the approach soil to alleviate the adverse effects of the wall movements. In the full separation, the soil is built as a self-stable mass, such as that in an MSE wall, and a gap is left between the backfill and abutment. None of these attempts is yet recognised as a practical method general enough to overcome the approach problems in the broad spectrum of IABs. Hence, current remedial measures have only a limited success in alleviating the problems produced by the abutment movements.

A logical approach in developing any potential solution for these problems requires an in-depth knowledge of the fundamental interaction mechanism that leads to these adverse effects. This may involve, qualitative and quantitative evaluations of the lateral earth pressure development/escalation in response to the abutment movement. It also involves the investigation of the deformations, densification/loosening and the active/passive failures occurring in the approach soil as a result of abutment cyclic movements. Moreover, the effects of the mode of wall movement (translation or rotation) must also be studied rigorously. Such research-based knowledge is currently unavailable in sufficient depth and hence complicates the efforts to develop a practical and efficient remedial measure for the approach problems in IABs.

This study aims to develop an understanding of the soil-abutment interaction behaviour in the IABs and provide insights into the important factors affecting such behaviour. This research will thus include a study of the fundamental interaction behaviour between the abutment and the soil and develop conclusions to improve the existing design approaches. The study also aims to investigate the potential application of a non-collapsible compressible material acting as a partial separation between the abutment wall and the retained soil. The inclusion will then absorb the abutment movements with a minimal disturbance to the adjacent soil. It is hypothesized that such a remedial measure will greatly attenuate the settlements and lateral earth pressure issues in IABs. Among many of the fill materials, the expanded polystyrene geofoam (EPS) provides an excellent choice for such a purpose. The EPS is highly compressible and possesses high compressive strength to weight ratio. It has an excellent record of success in a wide range of geotechnical applications such as a fill material for light weight embankments, compressible inclusion behind retaining structures and stabilisation of soil slopes, etc. Nevertheless, the potential use of EPS geofoam in rectifying the intractable approach problems in IABs has not been thoroughly investigated.

1.6 Research Motivation and Objectives

A considerable amount of research has been expended in the past to investigate the temperature effects on IABs. The majority of studies were focussed on the structural impact on the bridge superstructure. Soil-structure interactions and the impact on the bridge approach were studied to a much lesser extent. Even so, the majority of soil-structure interaction studies were focused on predicting the ratcheting lateral pressures on the bridge abutment, much less on the settlement of bridge approaches and even less on developing a practical and effective remedial measure for these problems. Therefore, the existing design practices do not include explicit guidelines about the possible remedial measures for approach problems in IABs except in recommending soil-structural interaction studies be conducted in certain cases of IABs. Accordingly, the primary aim of this thesis is to investigate the soil-structure interaction in IABs to better understand the fundamental causes of the approach problems and develop the existing knowledge for the possible application of the EPS geofoam to mitigate these approach problems. The specific objectives of this study include:

- Perform a comprehensive review of the provisions found in the major international design standards regarding the evaluation of the lateral earth pressure acting on the abutment, the approach soil settlement, the limitations on the construction of IABs and the potential measures considered to alleviate the approach problems in IABs. The review will also include the primary characteristics of the EPS geofoam and its current applications in IABs.
- Develop a comprehensive and easy to apply solution to estimate the limiting passive earth pressure on rigid retaining walls. This is necessary because the latter plays an important role in the estimation of the lateral earth pressure developed due to the cyclic movements of the abutment.
- Conduct small-scale physical model experiments of soil-wall interaction to study the fundamental soil responses in the approach fill. This will also involve the investigation of the potential influence of an EPS inclusion on the approach settlement and lateral pressure escalation on the abutment.
- Develop a two-dimensional finite element model to study the soil-wall interaction and potential use of EPS inclusions as outlined in the above, to collaborate and provide further insights on the experimental investigation.
- Perform dimensional analysis and leverage on the experience from small-scale physical model experiments to develop a large-scale physical model replicating an abutment of an IAB in the field scale.
- Conduct large-scale physical model experiments to investigate the soil-wall interaction under similar conditions to real world prototype and quantify the soil settlements and the lateral earth pressures.

- Develop a new material model that takes into account the nonlinear soil behaviour, and the changes in the strength and stiffness of soil during cyclical soil-wall interactions. A three-dimensional finite element model will be created using the new material model and validate it using the data from the large-scale physical model.
- Draw conclusions and highlight the important factors that govern the soil-wall interaction and the potential use of EPS geofoam in attenuating the approach settlement and lateral pressure ratcheting in IABs.

1.7 Structure of the Thesis

- Chapter two

  Chapter two presents a comprehensive review of the present guidelines available in the major international design standards in regards to the soil-structure interaction in IABs in addition to the literature dealing with the approach problems in IABs. Particular focus is given to the effects of the temperature-induced abutment movements and the subsequent lateral pressure escalation and soil settlement. Then the existing measures utilized to alleviate the approach problems are discussed. The general characteristics and applications of the EPS geofoam in the geotechnical engineering are also reviewed. Finally, the gaps in the current knowledge of the soil-structure interaction in IABs are identified.
- Chapter Three

  This chapter consists of the development and validation of a generalised analytical solution to estimate the limiting passive earth pressure using a composite (log spiral arc and a straight line) failure surface. The solution is formulated to address the effects of a range of parameters including the internal soil friction angle, the inclination of the backfill, the soil-wall interface friction as well as the inclination of the face of the wall. The solution is validated against experimental and numerical studies found in the literature, then used to produce a table of passive earth pressure coefficient K_p. For ease of reference, this solution is referred to as the “log-spiral solution”.

- Chapter Four

  In this chapter, a laboratory experimental program is carried out on a physical model of a small wall retaining loose sand and subjected to passive/active movement cycles. The experiments aim to provide further validation data for the log-spiral solution and to investigate the principles of the soil-wall interaction with and without the presence of an EPS inclusion. During these tests, the settlement at the soil surface and lateral soil pressures acting on the wall are measured.

  This chapter also involves the development of a plane-strain numerical model of a full-size concrete abutment supported by steel H piles using the ABAQUS Standard (2017) finite element software. This numerical model is used to investigate the influence of the EPS inclusion on the soil-structure interaction behaviour.

- Chapter Five

  This chapter discusses the development of a large-scale physical model to study the soil-structure interactions in IABs under conditions similar to those in the field. The development of this model involves a number of stages including, dimensional analysis, determination of the dimensions of the physical model and identifying and acquiring the materials used in the tests.

- Chapter Six

  Results of four experimental tests conducted using the large-scale physical model are presented in this chapter. The tests include, monotonic passive movement, rotational and translational cyclic movements and one test with the presence of an EPS inclusion. The results from these tests provide valuable data to further validate the log-spiral solution (developed in Chapter 3) and to visually observe the passive failure surface. The data from these tests also help to investigate the soil-wall interaction behaviour under different modes of wall movements and observe the efficacy of utilising an EPS inclusion to mitigate the adverse effects emerged from the wall cyclic movements. The results are also used to develop a pressure profile that realistically addresses the lateral earth pressure acting on the abutment to modify the existing British Standard PD6694-1 (2011).

- Chapter Seven

  In this chapter, three-dimensional models were developed, using the ABAQUS Standard (2017), and validated using data from the large-scale test results. In these models, the soil is simulated using the Extended GSK model proposed in this thesis extending the principles of the GSK model proposed by Krabbenhoft et al. (2012). The aforementioned material model addresses the changes in the stiffness and the strength parameters of the soil due to the changes in the minor principle stress σ_3. After the validation, the proposed soil model was used in simulating the interaction behaviour in a 5 m deep full integral concrete abutment, with inclined wing walls, and supported by steel H piles.

- Chapter 8

  In this chapter, the final conclusions derived from the work conducted in this study and the recommendations for future studies in regard to the soil-structure interaction in IABs and the use of EPS geofoam to overcome the approach problems in the IABs are presented.

Chapter Two

Literature Review

2.1 Introduction

Integral abutment bridges (IABs) have been used since 1938 in Ohio, United States (Burke, 2009). During the construction boom of the National Interstate Highway System, in the late 1950's and mid of 1960's, several US states began to use the IABs as a construction choice for bridges. In 1980, the American Federal Highway Association (FHWA) recommended bridges with overall lengths up to 90 m for steel bridges, 150 m for cast-in-place concrete bridges and 183 m for post-tensioned bridges be constructed as IABs (Hassiotis and Roman, 2005). In 1996, the British Highway Agency recommended adopting the integral bridge system for any bridge up to 60 m length (Lock, 2002). IABs in other regions and countries, like Europe, Japan, China and Oceania, also witnessed a rapid development in the last few decades. In Japan, the construction of the first IAB was completed in 1996 while South Korea constructed its first integral bridge in 2002 (Burke, 2009). In Australia, IABs are receiving growing interest and considered as a viable option in recent projects. In the Peninsula Link Highway project in Victoria, eleven out of thirty bridges were constructed as IABs (Gibbens and McManus, 2011).

Currently, IABs are the standard design choice in many USA states (Tabatabai et al., 2017). Although IABs are still outnumbered by conventional or jointed bridges, the overall trend of bridge construction seems to be moving towards IABs.

2.2 Types of Integral Abutment Bridges

The term "Integral Abutment Bridges" (IABs), or joint-less bridges, refers to single or multi-spans bridges constructed without any joints between the spans or between the span and the abutment. Accordingly, the bridge deck is continuous and rigidly connected with the abutments forming one integral unit. IABs are generally classified as Full Integral or Semi Integral in accordance with the supporting substructure.

2.2.1 Full Integral Abutment Bridges (FIABs)

In this type of bridges, the abutment is supported by a single row of piles distributed along the transverse length of the abutment. The piles used in this type are often steel H piles oriented in the weak axis bending with the pile head encased in the concrete abutment. This type of substructure is conventionally termed as 'flexible foundation', because piles sway into and away from the approach backfill in response to the elongation and shortening of the superstructure. For this reason, using two or more rows of piles is always avoided as a foundation for FIABs. In FIABs, the expansion and/or contraction of the deck results in mobilising an interaction along the interface between the abutment-pile system and the adjoining soil. Therefore, piles that support the abutment in FIABs are often inserted in pre-driven shaft filled with loose sand to ease the pile movement and to minimise the stresses developed at the pile cap or the pile-abutment joint due to the abutment displacements. (White et al., 2010). In a number of the US states as well as European countries the construction of FIABs requires providing a moment-relief joint to alleviate the effects of abutment movements on the substructure. The joint is achieved by providing a single row of large diameter and closely-spaced reinforcing bars with a high durometer value neoprene gasket. According to Hoppe et. al. (2016), this technique has been effective in reducing the bending moment transferred into the pile.

2.2.2 Semi Integral Abutment Bridges (SIABs)

In this type of bridges, the abutment is generally shorter than that in FIABs and is supported by the substructure using bearings. Therefore, the abutments in SIABs may move laterally independent to the substructure which results in less interaction with the approach soil (compare to that in FIABs). Unlike the FIABs, which are supported on yielding foundations, the semi integral abutments are commonly constructed on rigid foundations such as a footing on the bedrock, two rows of end-bearing piles (vertical and battered), pedestals that extend to the bedrock, etc. (Burke, 2009). The joint between the abutment and the foundation, in this type of bridges, is provided with seating elastomeric pads or metal bearings. However, any type of seating used at this joint does not restrain the horizontal movement of the abutment.

Being able to move longitudinally independent of the substructure foundation has helped the use of SIABs in a wider design context. However, semi integral bridges involve unusual characteristics that need to be understood and provided for in the design. For instance, the longitudinal stability can be an issue in this type of bridges unless properly addressed. The semi integral bridges rely on the friction between the approach slab, if it exists, and the subbase layer, the shearing resistance of the elastomeric bearing and, most importantly, the lateral pressure of the approach backfill to achieve longitudinal stability (Burke, 2009). However, during cold seasons, the backfill support is limited to the active earth pressure. In this case, bridge stability against the external longitudinal forces may not be satisfactorily achieved. As a possible remedy to this problem, Burke (2009) emphasized to place and compact the granular backfill at the abutments during the cold season or at least at night during hot weather.

Furthermore, heavily skewed semi integral bridges may suffer rotational instability unless a proper bearing type is utilized. According to Burke (2009), semi integral abutment bridges with skew angle exceeding 15º need to be provided with guide bearings to avoid the development of rotational movements in the bridge superstructure.

In view of the above, the fundamental difference between FIABs and SIABs is the way in which the abutment interacts with the substructure as well as the adjoining soil. In accordance with this variation, abutments in SIABs lateral movements are dominantly translation while that of FIABs is dominantly rotation.

The terminologies used by different design organizations are broadly different. In USA, terms like integral and semi integral abutment bridges are widely used and they refer to FIABs and SIABs respectively. However, terms such as diaphragm walls and backwalls are also found in the USA practice and they refer to full integral and semi integral abutments respectively

In the UK practice the full integral abutments are often termed as frame walls or fully embedded walls, while semi integral abutments are described as shallow abutments such as bank pads or end screen abutments. Figure 2.1 shows schematic diagrams of different types of abutments.

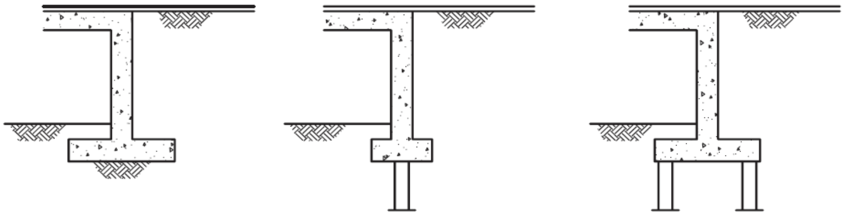

(a) Frame abutments

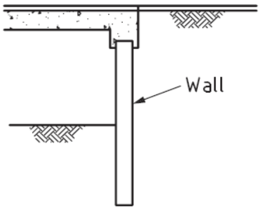

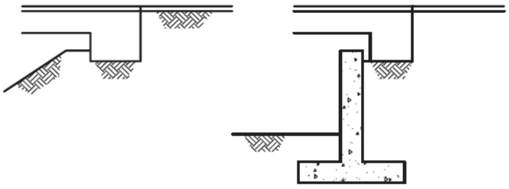

(b) Embedded wall abutment (c) Bank pad abutments

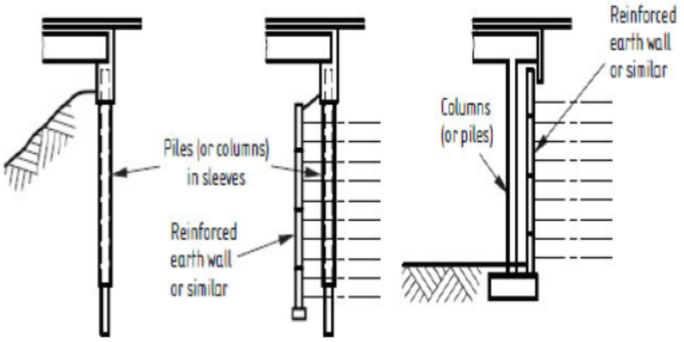

(d) Flexible support abutments

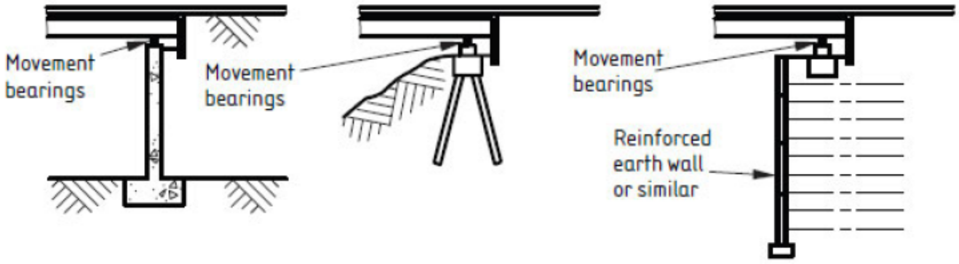

(e) Semi integral end screen

Figure 2.1 Schematic diagrams of different types of abutments in IABs

2.3 An Overview of the Existing Theories

Much research has been conducted on various structural and geotechnical aspects of the IABs. Studies investigating the temperature induced soil-structure interaction issues involved experimental studies on prototype or scaled models at normal gravity (England et al., 2000; Cosgrove and Lehane, 2003; Tatsuoka et al., 2009; Frosch and Lovel, 2011; Thomson and Lutenegger, 2013; Khasawneh, 2014, Huang et al., 2020) as well as centrifuge tests at high gravity (Springman et al., 1996; Ng et al., 1998; Springman et al., 2001; Lehane, 2011). Other studies utilized field observation data to analyse the behaviour of IABs (Broms and Ingelson, 1971; Alampalli and Yannotti, 1998; Hoppe and Gomez, 1996; Lawver et al., 2000; Laman and Kim, 2009; Frosch and Lovell, 2011; Putorsson et al., 2011; Huntly and Valsangkar, 2013; Tatsuoka et al., 2014; Hoppe et al., 2016; Huntly and Valsangkar, 2016; Lafave et al., 2017). In addition, numerical modelling has also been employed by researchers to study IABs

(Greimann et al., 1986; Ng et al., 1998; Arzoy et al., 1999; Dicleli, 2000; Horvath, 2000; Kim and Laman, 2010; Bloodworth et al., 2011). These studies have generally concluded that IABs are susceptible to unique geotechnical problems as a result of the seasonal and diurnal abutment movements. The effects of thermally-induced abutment movements are detrimental to the lateral soil pressure as well as deformations of the soil in the vicinity of the abutment wall.

2.3.1 Lateral Earth Pressures

Lateral earth pressures behind bridge abutments are generally estimated using classical theories such as Coulomb (1776), Rankine (1857) and Terzaghi (1943). Coulomb and Rankine theories of active and passive earth pressures assume the presence of a planar failure surface. Rankine theory assumes a linear variation of stress at the soil interface with a frictionless wall and gives the active and passive pressures for a cohesionless soil as,

$$\sigma_a = \gamma z K_a \tag{2.1}$$

$$\sigma_p = \gamma z K_p \tag{2.2}$$

where γ is the unit weight of the soil, z is the depth from the soil surface, K_a and K_p are the active and passive coefficients of lateral earth pressures respectively and are defined as,

$$K_a = \frac{1-\sin\phi'}{1+\sin\phi'} \tag{2.3}$$

$$K_p = \frac{1+\sin\phi'}{1-\sin\phi'} \tag{2.4}$$

Coulomb's theory uses the wedge analysis to compute the earth pressures coefficients behind a vertical wall retaining a backfill as given in equations 2.5 and 2.6,

$$K_a = \frac{\cos^2\phi'}{\cos\delta\left\{1+\left[\sin(\phi'+\delta)\sin\phi'/\cos\delta\right]^{1/2}\right\}^2} \quad (2.5)$$

$$K_a = \frac{\cos^2\phi'}{\cos\delta\left\{1-\left[\sin(\phi'+\delta)\sin\phi'/\cos\delta\right]^{1/2}\right\}^2} \quad (2.6)$$

where ϕ' refers to the effective internal friction angle of the soil and δ is the angle of friction between the soil and the wall.

Under the *in situ* or the at-rest conditions, the coefficient of lateral earth pressure K_o, of normally consolidated soils, is commonly estimated using equation 2.7 (Jaky, 1948). For overconsolidated soils, the equation proposed by Mayne and Kulhawy (1982), equation 2.8, is often used to calculate K_o.

$$K_o = 1-\sin\phi' \quad (2.7)$$

$$K_o = (1-\sin\phi')OCR^{\sin\phi'} \quad (2.8)$$

where, OCR is the over consolidation ratio

Terzaghi (1943), Caquot and Keriesel (1948) and Kerisel and Abbsi (1990) proposed a different failure mechanism in which the rupture surface is a log-spiral curve or a composite surface of log-spiral and a tangent line. However, Coloumb and Rankine theories are yet more popular and often used by geotechnical engineers due to their simplicity.

Despite the presence of various earth pressure theories, there is no single theory that appropriately applies to evaluate the lateral earth pressure in IABs. As a result, there is no standard or unified design approach to estimate the magnitude and distribution of lateral earth pressure acting on the abutment (Huntly and Valsangkar, 2013, Tabatabai et al., 2017). The current design guidelines are based on empirical approaches or the experience from previously constructed structures, which do not yet sufficiently address the knowledge gaps of the soil-structure interaction issues unique to these structures.

2.3.2 The Practice in USA

The United States is among the first countries that utilised integral bridges on a large scale. According to Paraschos and Amde (2011), there are 41 American states using IABs with some of them having built thousands of integral bridges such as Missouri has more than 4000 IABs and Tennessee over 2000 IABs. However, the US practice, yet, involves significant variations in the design guidelines and limitations of the integral bridges among different states. In this section, the USA practice will be reviewed with emphasis on:

- The lateral earth pressure considered in the design of IABs
- The limitations considered by different states when constructing IABs

2.3.2.1 Assessment of Design Lateral Earth Pressure

The consideration of the design loads emerged from the lateral earth pressure acting on the abutment of IABs vary among the USA states. In fact, there is no single approach in the USA practice to address this particular point. The states' transportation departments (DOTs) rely largely on previous experiences and, in a few cases, on data from in-service bridges to develop their design methodologies. The following are recommendations from selected states' DOTs in regard to the design lateral earth pressure.

Alaska

In the state of Alaska, only semi-integral bridges are used. The bridge design manual of the state of Alaska stipulates that the design of semi-integral abutments must account for the lateral earth pressure (Alaska Bridge design manual, 2017). However, the magnitude and distribution of earth pressure are not explicitly discussed.

Colorado

The bridge design manual of Colorado (2020) does not provide explicit guidelines about the earth pressure to be considered in the design of IABs. However, it stipulates "Appropriate earth pressures and predicted settlement should be provided in a geotechnical investigation". It also recommends using a combination of MSE wall with a non-collapsible gap (between the MSE wall and the abutment) filled with low density polystyrene when reduced earth pressure effects are required.

Idaho

The department of transportation of Idaho considers a lateral earth pressure profile that varies linearly from zero to the full passive pressure over the top third of the abutment height then to reduce it linearly to the at-rest pressure at the bottom of the abutment (see Figure 2.2) (Tabtabai et al., 2017). This distribution is described for concrete bridges up to 97.5 m in length and steel bridges up to 36.5 m in length. The design manual of Idaho states that, a more in-depth analysis of soil pressure distribution should be made for longer bridges.

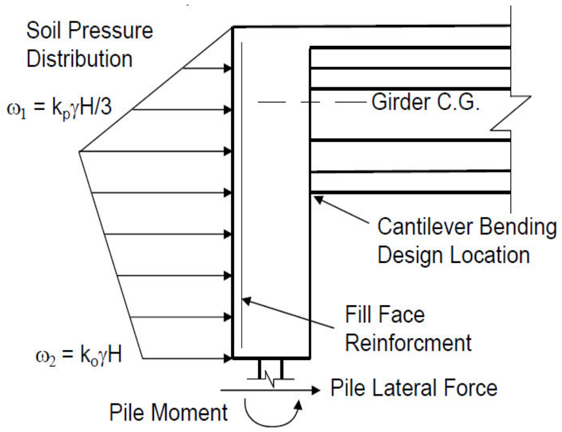

Figure 2.2 Earth pressure on integral abutment during bridge expansion – Idaho DOT (Tabatabai et al., 2017)

Illinios

Illinois bridge design manual (2019) does not provide an explicit description about the design earth pressures for IABs. However, it states that retaining walls must be designed considering Coulomb passive pressure.

Maine

According to Maine bridge design manual (2018), Coulomb triangular passive pressure is recommended in the design of abutments for IABs

Massachusetts

In the state of Massachusetts, a displacement-dependent formula is used to calculate the magnitude of lateral earth pressure coefficient *K* as shown in equation 2.9 (Tabatabai et al., 2017).

$$K_h = 0.43 + 5.7\left(1 - e^{-190\left(\frac{\Delta}{H}\right)}\right) \tag{2.9}$$

where K_h is the coefficient of lateral earth pressure, Δ is the horizontal displacement of the abutment and H is the height of the abutment.

Minnesota

The bridge design manual of Minnesota (2016) uses a lateral earth pressure profile that varies linearly from zero to a Rankine passive pressure over the upper part of the abutment (above the moment relief joint) and remain constant over the lower part of the abutment as shown in Figure 2.3.

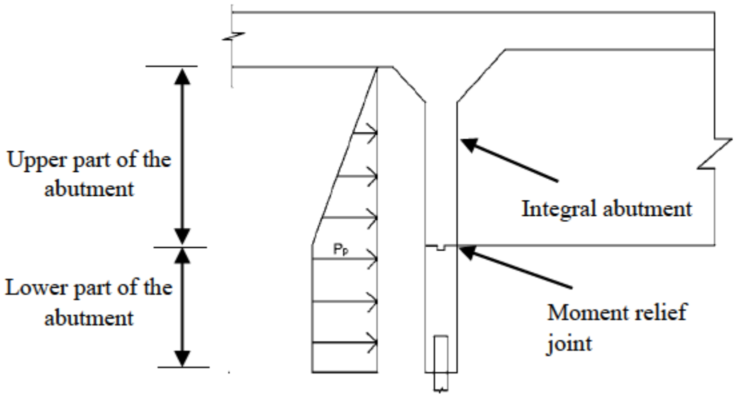

Figure 2.3 Earth pressure on integral abutment - Minnesota DOT (Minnesota bridge design manual 2016)

Nevada

In the state of Nevada, the AASHTO LFRD 3.11 guidelines are followed to estimate the lateral earth pressure acting on abutments in IABs (Nevada bridge design manual, 2009)

New Hampshire

According to New Hampshire bridge design manual (2016), the design earth pressure varies linearly from zero to the full passive pressure at the bottom of the diaphragm and remains constant over the stem of the abutment as shown in Figure 2.4. The abutment is then designed as a continuous beam with girders as supports.

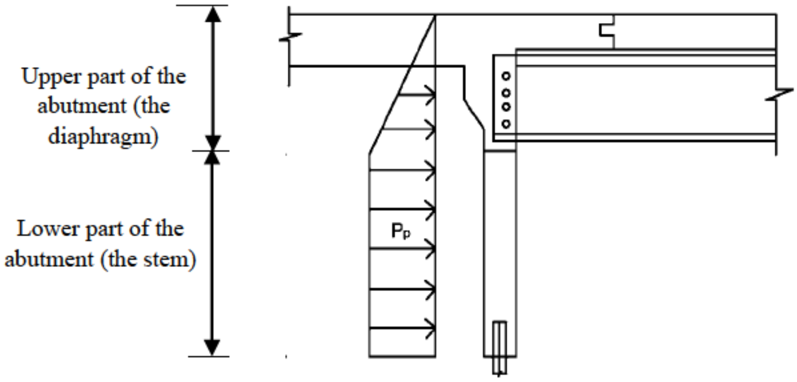

Figure 2.4 Design earth pressure in IABs (NH bridge design manual, 2016)

New Jersey

The bridge design manual of New Jersey (2016) states that integral abutments need to be designed considering full passive earth pressure. However, the method of calculation and the distribution of the pressure are not explicitly discussed.

New York

The NY bridge design manual (2019) states that integral abutments need to be designed for full passive earth pressure. However, the calculation and distribution of the passive pressure have not been clarified.

North Dakota

North Dakota bridge design manual (2013) states that a uniform pressure of 47.8 kPa (1000 psf) needs to be considered in the design of integral abutments and 31.1 kPa (650 psf) in the design of the wing walls.

Ohio

In the state of Ohio, the abutments of IABs are designed according to an earth pressure ranging between the at-rest and the full passive pressure depending on the temperature induced movements of the abutment (Ohio bridge design manual, 2020). Following the guidelines of AASHTO LRFD, C3.11 (2020) the displacement required to mobilise the full passive earth pressure is identified. Interpolation is used, to estimate the earth pressure, when the movement of the abutment is less than that corresponding to the full passive pressure.

Oregon

The bridge design manual of Oregon (2019) does not involve an explicit description about the lateral earth pressure behind the integral abutments. However, the manual states that the non-yielding walls such as integral abutments must be designed using the at-rest earth pressure.

Pennsylvania

The design manual of Pennsylvania (2014) does not provide any provisions to consider the lateral backfill pressure on integral abutments. The manual recommends using a 50 mm thick polystyrene inclusion between the abutment and the backfill to attenuate the earth pressure. (polystyrene is the American trade name of the expanded polystyrene geofoam, EPS)

South Dakota

The design manual of South Dakota (2020) provides the following statement in describing the soil load considered on integral abutments, “A value of 40 lb/ft^3 (2 kPa) equivalent fluid pressure is used for lateral earth pressure.”

Virginia

Triangular passive earth pressure is used behind the abutment. Virginia bridge design manual (2020) provides the following guidelines to determine the coefficient of earth pressure K as shown below:

K = 4 when an EPS inclusion is used

K = 12 when a structural backfill is used behind the abutment without an EPS inclusion

Utah

In the state of Utah, a uniform earth pressure over the height of the abutment is considered as a result of bridge expansion (Utah bridge design manual, 2017). The pressure is calculated using the formula below (equation 2.10):

$$P_u = \gamma(\Delta/0.03H_d)(2H_d/3) \tag{2.10}$$

where P_u is the earth pressure in Ksf

γ a load factor, in this case it is equal to 2

Δ is the effective abutment displacement, and is defined as:

The total abutment displacement - gap (if any gap is provided behind the abutment).

H_d is the height from the finished grade to the bottom of the abutment.

2.3.2.2 Allowable Limits in the Construction of IABs

The allowable limits of some design parameters, as reported in the design manuals of different states, are summarised in Table 2.1

Table 2.1 Allowable limits of IABs in the USA (Design manuals of different DOTs; Tabatabai et al., 2017)

Length (m)					Skew angle (deg)	Height (m)	
State or Province	Thermal movement (cm)	Steel girder	Pre-cast concrete girder	Cast-in-place concrete girder		Abutment	Stem
AK	7.6	-	61.0	-	30	-	-
CO	10.2	140.2	140.2	140.2	30	4.9	
DE	-	122	122	122	30	No limit	No limit
IA	Limited by length	122	175	175	30	0.9 -1.5	Length dependent
ID	-	107	198	198	-	-	-
IL	No limit	94	125	125	45	No limit	No limit
KS	5.1	91.5	152.5	152.5	45	By design	By design
MA	Not defined	107	183	183	30	Minimize	Minimize
ME	-	61	101	101	25	3.6	-

MN	No limit	91 for skew less than 20° 30 for skew less than 45°	91 for skew less than 20° 30 for skew less than 45°	91 for skew less than 20° 30 for skew less than 45	45	1.0	1.0
ND	Limited by length	122	122	122	0	3.7	1.5-1.8
		$122\ \cos\theta$	$122\ \cos\theta$	$122\ \cos\theta^*$	45		
NH	3.8	91.5	183	183	20	-	-
NJ	-	137	137	137	30	-	-
NV	2.5	76.3	76.3 – 122 FIAB - SIAB	76.3 – 122 FIAB - SIAB	20-30	Design	Design
NY	Limited by length	122	122	122	45	-	0.3-0.6
OH	-	122	152	152	30	-	-
PA	5.1	119	180	180	20-45	-	-
SD	Limited by length	106.8	213.5	213.5	35	No limit	-
TN	5.1	152	244	244	-	-	No limit
VA	5.7	45.7-137.2	76.2-229	-	30 - 0	No limit	No limit
VT	Limited by length	120	212	212	30	No limit	No limit

* θ is the skew angle

2.3.2.3 AASHTO LRFD Design Specifications 2020

The AASHTO LRFD Bridge Design Specification (2020) provides guidelines about the design of bridges and, in particular, calculations of earth pressures behind bridge abutments. Article 11.6.1.3 of LRFD Design Specification (2020) states that the design of the integral abutments should account for the shrinkage, creep and thermal deformations of the superstructure. The estimation of the earth pressure, emerging from the temperature changes, behind the integral abutments is established through the following steps,

- Estimation of the thermal displacement

  The total displacement as a result of the expansion and/or contraction of the superstructure is determined, using equation 2.11,

  $$\Delta = \alpha L \Delta t \tag{2.11}$$

  where Δ is the total thermal displacement of the superstructure

L is the expansion length and measured from the centreline of one abutment to the centreline of the other abutment

Δt is the temperature range and,

α is the coefficient of thermal expansion

The temperature range specified in AASHTO LRFD Bridge Design Manual (2020) is shown in Table 2.2

Table 2.2 Temperature ranges (AASHTO LRFD, 2020)

Climate	Bridge material		
	Steel or Aluminium	Concrete	Wood
Moderate	0° to 120° F (-17.8° to 49°C)	10° to 80°F (-12.2° to 26.7°C)	10° to 75°F (-12.2° to 23.9°C)
Cold	-30° to 120°F (-34.4° to 49°C)	0° to 80°F (-17.8° to 26.7°C)	0° to 75°F (-17.8° to 23.9°C)

Climate is deemed moderate when the number of the freezing days during the year is less than 14 days. A freezing day is the day when the average temperature is less than 32°F (0°c).

- Calculation of Earth Pressure

Methodologies used to calculate the lateral earth pressure coefficients, K_o, K_a and K_p are discussed in the AASHTO LRFD Specification (2020).

The coefficient of at-rest pressure coefficient K_o is calculated using the same equations discussed earlier, equation 2.7 (for normally consolidated soils) and equation 2.8 (for over consolidated soils).

The coefficient of active earth pressure K_a is calculated using Coulomb's earth pressure theory (equation 2.5). The AASHTO LRFD Specifications (2020) refers to the graphs developed by the U.S. Department of Navy (1982) to determine the coefficient of passive earth pressure coefficient, K_p. However, for conditions that deviate from those described by the U.S. Department of Navy (1982), the AASHTO LRFD Specification recommends to use the wedge theory (Terzaghi, 1996) to determine the magnitude of K_p.

- Calculation of Mobilised Earth Pressure

The mobilised earth pressure is calculated depending on the thermal expansion/contraction calculated earlier. The AASHTO LRFD Specification (2020) provides guidelines about the minimum displacements required to mobilise the full active and full passive earth pressure as shown in Table 2.3.

Table 2.3 Approximate values of normalised movements (Δ/H) required to reach active or passive earth pressure (Tabatabai et al., 2017)

I. ype of Backfill	II. alues of (Δ/H)	
	Active	Passive
Dense sand	0.001	0.01
Medium dense sand	0.002	0.02
Loose sand	0.004	0.04
Compacted silt	0.002	0.02
Compacted lean clay	0.01	0.05
Compacted fat clay	0.01	0.05

However, the AASHTO LRFD Specification (2020) do not provide explicit guidelines regarding;

- Calculations of K_p when the normalised movement is more than zero but less than that corresponding to the full passive pressure. Hence, some USA states use linear interpolation to estimate the mobilised earth pressure in similar cases.
- The abutment movement, Δ, is taken as the linear displacement at the top of the abutment regardless of the mode of the movement, rotation or translation. In this case the effects of the mode of wall movement is not taken into account.

- The guidelines given in AASHTO LRFD (2020) (Table 2.3) are based on a study conducted by Clough and Duncan (1991) in which the limiting normalized displacements (Δ/H), under monotonic loading, were estimated. However, the soil-abutment interaction in IABs involves cyclic loading which certainly differs from the monotonic conditions.

2.3.3 UK Practice

The UK Design Manual for Roads and Bridges, BA42/96 (2003) provides some guidelines to estimate the value and distribution of the lateral earth pressure acting on abutments of integral bridges. These guidelines are largely based on the experimental and analytical data reported by Springman et al. (1996). BA42/96 (2003) emphasise that the lateral earth pressure developed behind the abutment is a function of the shear strain γ in the soil. The latter is described by the ratio d/H, where d is the horizontal displacement at one end of the bridge deck and H is the height of the abutment. It is worthwhile mentioning that the ratio d/H refers to the normalised abutment movement in which the displacement d sometimes termed as d_d (deck movement), however they shall have the same meaning.

BA42/96 (2003) proposed the following equations to calculate the design lateral earth pressure coefficient, K^*, of IABs:

For shallow abutment walls $H \leq 3$ m (bank pad and end screen abutment)

$$K^* = K_o + \left(\frac{d}{0.025H}\right)^{0\ 4} K_p \tag{2.12}$$

For Full height abutments $H > 3$ m (hinged at its bottom end)

$$K^{*} = K_o + \left(\frac{d}{0.03H}\right)^{0.6} K_p \tag{2.13}$$

For Full height abutment with rigid support or full height embedded wall abutments

$$K^{*} = \left(\frac{d}{0.05H}\right)^{0.4} K_p \tag{2.14}$$

where K_o represents the theoretical at-rest lateral earth pressure coefficient $(1 - \sin\phi)$ and K_p is the coefficient of passive earth pressure according to the Eurocode 7 and calculated when the soil-abutment friction angle δ equals to $\phi/2$.

Figure 2.5 shows the distribution of the lateral earth pressure behind (a) frame abutment and (b) full height embedded wall as suggested by the UK BA42/96 (2003). It is seen that the coefficient of lateral pressure is assumed to be a constant equal to K^{*} at the upper part of the abutment and decreases linearly towards K_o at the bottom of the wall.

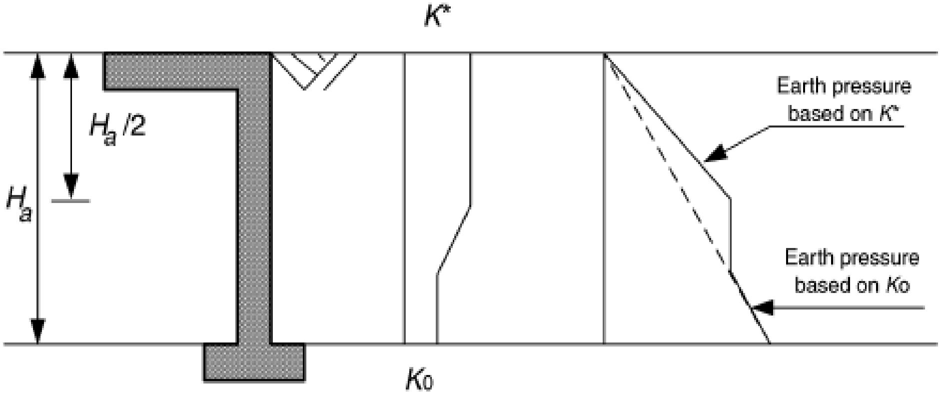

Figure 2.5 a. Lateral earth pressure distribution behind frame abutment (BA42/96, 2003)

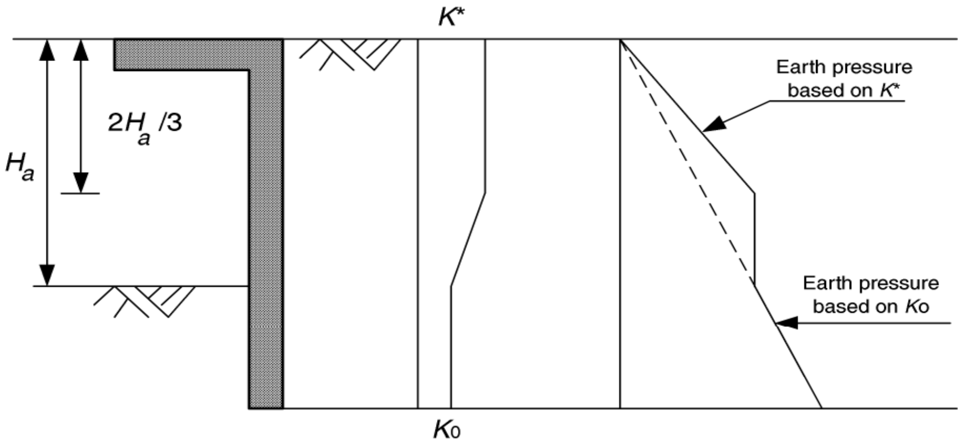

Figure 2.5 b. Lateral pressure distribution behind full height embedded wall (BA42/96, 2003)

Later, the BA42/96 (2003) was modified by the recommendations stipulated in BS PD 6694-1 (2011). The latter was developed based on experimental and analytical data obtained from several studies. According to PD 6694-1 (2011), equation 2.14 does not realistically reflect the behaviour of integral abutments and therefore is no longer considered. The PD 6694-1 (2011) provided single equation (equation 2.15) for all abutments that accommodate thermal movements by rotation and/or flexure. In accordance with equation 2.15, the shear strain in the soil must be specified in terms of the ratio d'_d/H, (instead of d/H), where d'_d is the displacement at $H/2$ when the movement of the deck is d_d as shown in Figure 2.6. Accordingly, equation 2.13 has been modified as illustrated in equation 2.15

$$K_d^* = K_o + \left(\frac{Cd'_d}{H}\right)^{0\ 6} K_{p,t} \tag{2.15}$$

where C is a parameter depending on the restraints of the abutment. For an abutment wall with a rigid boundary, C equals to 66 and for abutments without a rigid boundary, the magnitude of C is reduced to 20 (PD 6694-1, 2011). $K_{p,t}$ represents the passive coefficient calculated based on the triaxial friction angle. However, the recommendations in PD 6694-1 (2011) do not include any changes to the calculation of earth pressure behind short abutment because the amount of rotation is deemed insignificant and d'_d is, hence, approximately equal to d_d. Accordingly, equation 2.12 and the definition of the shear strain d_d/H remains as defined earlier by BA42/96 (2003).

The BS PD 6694-1 (2011) also proposed a modification to the vertical distribution of the lateral earth pressure stipulated in the BA42/96 (2003). In accordance with BS PD 6694-1 (2011), the

pressure increases linearly from zero, at the soil surface, to $\gamma K^* H/2$ at the mid height of the abutment and thereafter reduces linearly to $\gamma K H$ at the toe of the abutment

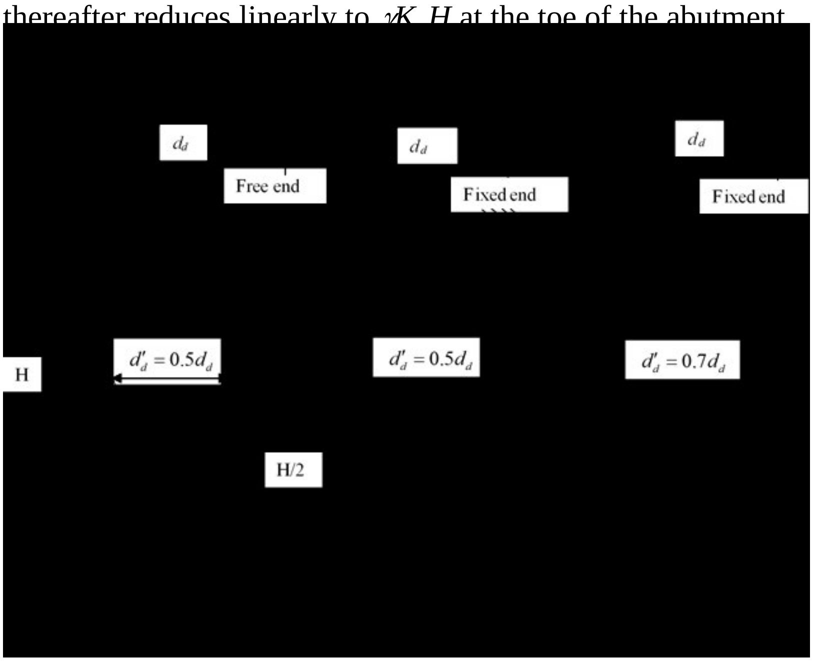

Figure 2.6 Different abutment movements, PD 6694-1 (2011)

2.3.4 The Practice in Australia

In Australia, the design of IABs is primarily based on the UK Design Manual for Roads and Bridges, BA42/96(2003) and the recommendation given in PD 6694-1 (2011) (VicRoads, 2018; Queensland Bridge Design Manual, 2020).

2.4 Review of Studies of Lateral Earth Pressure in IABs

As mentioned earlier, there have been many research studies conducted about the development of earth pressure behind the abutments of IABs.

Lehane (2011) conducted centrifuge tests at the University of Western Australia on a deep wall integral abutment hinged at its bottom and subjected to rotational movements. The tests involved the application of rotational amplitudes ranging between 0.05% and 0.63%. It is worthwhile mentioning that these amplitudes represent the normalised displacement (Δ/H) but in terms of a percentage. Lehane (2011) reported that the stresses behind the abutment wall were insensitive to the wall movements at a smaller amplitude (0.05%). However, at greater amplitudes (0.1% to 0.63%) the stress increases linearly with the logarithm of the number of cycles, *N*, then asymptotes and levels off after a certain number of cycles. It is noted that the lateral stress levels off earlier for tests with smaller amplitudes compared to tests conducted with greater amplitudes. At amplitude equals to 0.1%, the lateral stress, at $z/H = 0.5$ (*z* is the depth from the soil surface and *H* is the height of the wall), asymptotes after approximately 20 cycles while the stress at the same location levels off after 50 - 100 cycles when the displacement amplitude is 0.2%.

The results also show that the location of the maximum lateral pressure is observed at the upper half of the wall height. This can be attributed to the mode of wall movement which involves pure rotation. In such movement mode, larger soil deformations are closer to the soil surface or generally in the upper half of the retained soil height.

According to Lehane (2011), the escalation in the lateral stresses is associated with an increase in the stiffness of the soil adjacent to the wall. He emphasised that the estimation of lateral stresses has to account for the actual or, as described by Lehane (2011), the “operational stiffness” of the soil, E_p. Based on a backward analysis from test results, he found that, at a relatively small wall displacements, the operational stiffness (E_p) of the soil relates primarily to the small-strain modulus, E_o, and is independent of the initial soil density. Lehane (2011) suggested that the E_p can be assumed as 40% of the small-strain stiffness of the compacted backfill, E_{oc}.

Lehane (2011) compared the lateral stresses computed using a simple elastic finite element model that utilises the operational stiffness of the soil, E_p, with the recommendations given in the UK Highway Agency publication BA42/96(2003), i.e. equations 2.12 and 2.13 (which are used for shallow and full height abutments with hinge at the bottom). He found that the UK BA42/96(2002) recommendations underestimate the lateral earth pressure at the upper third of the abutment, as shown in Figure 2.7.

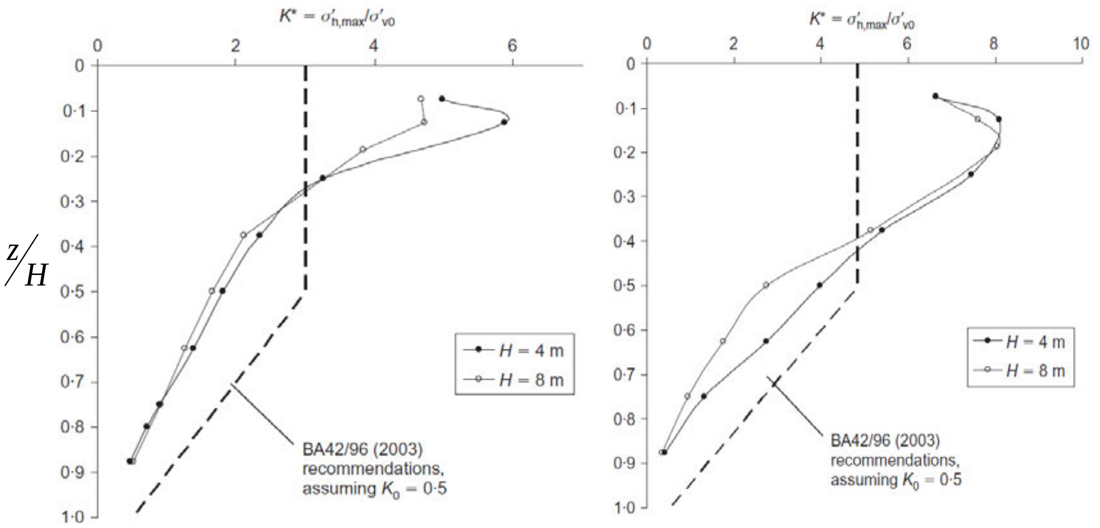

(a) (b)

Figure 2.7 Comparison of the value of K^* as predicted by Lehane (2011) with those recommended in the UKBA42/96 (2003) at displacement amplitude equal to (a) $\Delta/H = \pm 0.2\%$ and (b) $\Delta/H = \pm 0.5\%$

Broms and Ingelson (1971) measured the lateral earth pressures acting on abutments in 150 m and 110 m length integral bridges in Sweden. Based on the observed data, they proposed that the lateral earth pressure behind an abutment experiencing cyclic movements varies linearly from zero at the top (at the soil surface) to Rankine passive pressure at $H/3$. Then decreases linearly to Rankine active pressure at the bottom of the wall (H refers to the retained height of the soil). This proposed envelope for lateral pressure accounts for the stresses developed due to the compaction of the backfill in addition to the rotational movements of the abutments. Sandford and Elgaaly (1974) modified this pressure envelope, as shown in Figure 2.8, considering the pressure acting at the toe of the abutment equals to the at-rest pressure instead of the Rankine active pressure.

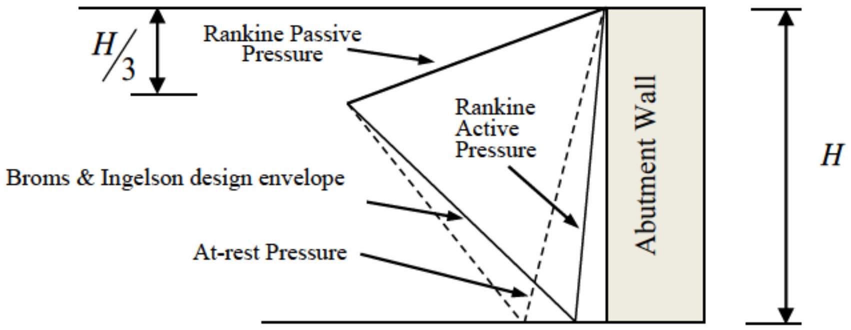

Figure 2.8 Earth pressure distribution behind Abutment (Bayoglu, 2004)

Springman et al. (1996) conducted centrifuge tests on two prototype systems represented by spread-base abutment wall and embedded abutment wall, both of which were founded in a fine dry sand. The tests involved the application of rotational movements of ± 6 mm (0.2% = θ = 0.12°), ± 12 mm (0.4% = θ = 0.23°), ± 30 mm (1% = θ = 0.57°) and ± 60 mm (2% = θ = 1.15°), where θ is the angle of rotation. The study focused on investigating the response of the soil to the abutment movements. Springman et al. (1996) reported that the lateral pressure increased in almost logarithmic fashion within the first twenty cycles of wall movement followed by a gradual increase in the following cycles. They reported that the pressure tends to asymptote after 100 cycles of movements. The pressure distribution showed that the maximum pressure readings were observed at the upper third of the retained height.

Ng et al. (1998) conducted centrifuge tests on loose and dense sand backfills subjected to a range of cyclic perturbations. According to Ng et al. (1998) the temperature effects in IABs result in rotational and translational movements in bridge abutments. It was found that the active movements of the wall lead to slippage of soil particles into the gap between the wall and soil, which resulted in an increase in lateral earth pressure. They stated that the development of high lateral pressures is dependent on the magnitude of perturbation, number of cycles and the density of the soil. However, at a given magnitude of perturbation, the lateral earth pressure coefficient K increases with the number of cycles at a decreasing rate.

The test results showed that, 50% to 70% of the total increase in the value of K after 100 cycles is actually occurring within the first 20 cycles.

Throughout the test, the value of K has always been exceeding the at-rest pressure coefficient K_o. After applying the annual perturbations of ± 30 mm the maximum measured value of K exceeded the theoretical value of Rankine passive earth pressure coefficient K_p. The critical values of lateral pressures observed in the test were all located closer to the surface of the soil than to the base of the wall.

England et al. (2000) conducted an experimental program on a small wall retaining a sandy soil. Rotational amplitudes (d/H) ranging from 0.125% to 0.9% were applied. The test results reported by England et al. (2000) showed a rapid escalation in the lateral stresses from the initial K_o value during the first ten cycles. However, stresses thereafter showed an increase at a slower rate. The maximum value of the lateral pressure coefficients K measured at passive state, after 300 cycles of ± 0.125% amplitude, was 2.6 and was recorded at the upper third of the wall height. On the other hand, the active pressure coefficient was found to be insensitive to the increase in the number of cycles and varied within a small range between 0.2 and 0.25 as shown in Figure 2.9.

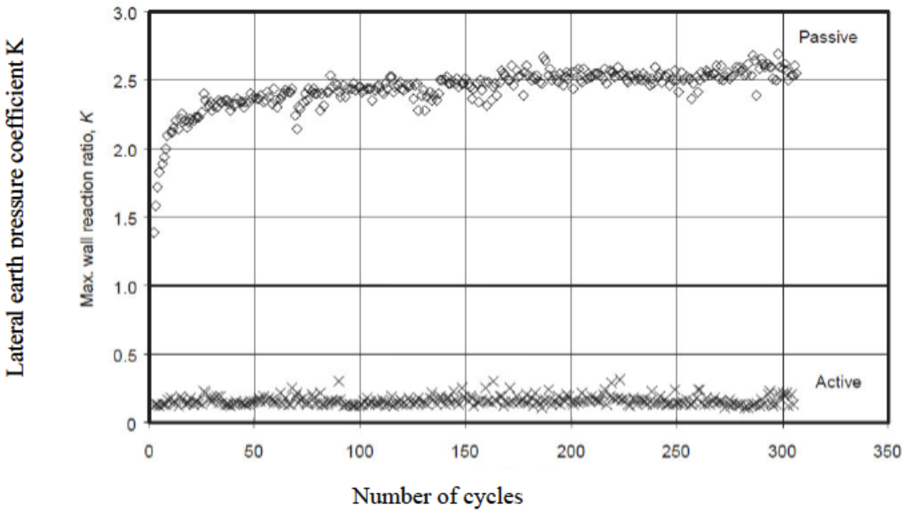

Figure 2.9 Variation of the pressure coefficient K with the number of cycles (England et al., 2000).

Tatsuoka et al. (2009) conducted a series of plane-strain tests on a 505 mm high small wall retaining loose sand. Tests were performed using a wall with a hinged connection at its bottom end, which allowed only rotational wall movements. Also, they used an embedded wall in which translational movements are allowed. Horizontal amplitudes ($^{d}\!/_{H}$) ranging between 0.1% and 0.6% were applied at the top of the wall. Two styles of horizontal displacements involving "active-only" and "active/passive" were applied (active-only refers to the wall movement within a range between initial and active positions while active/passive refers to the wall movement within the range of passive-active positions).

After several loading cycles, escalations in the lateral stresses were apparent in both active and active/passive tests. Figure 2.10 shows that the magnitude of K recorded when the wall at the neutral position becomes five times higher than K_o after 200 cycles of 0.2% active-only displacement.

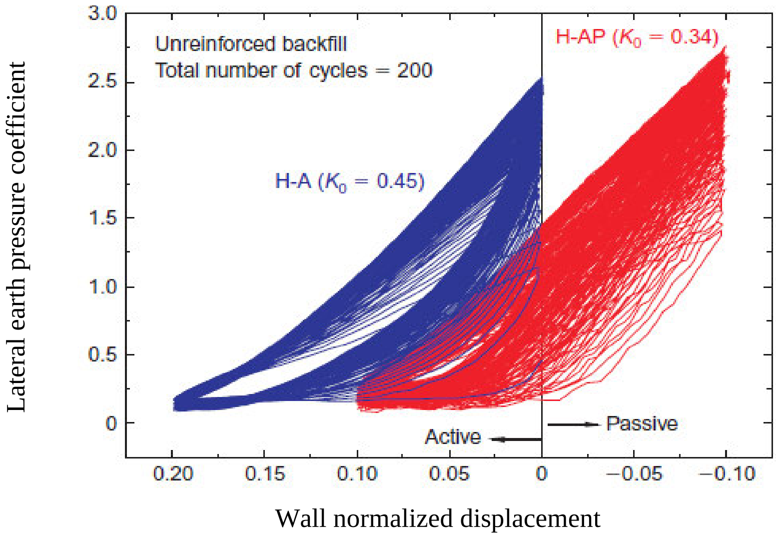

Figure 2.10 Relationship between the lateral pressure coefficient, *K* and the horizontal wall displacement, in active and active/passive conditions (Tastsouka et al., 2009)

Huntley and Valsangkar (2013) reported field data collected, over three years, from a 76 m length two-span integral bridge in Brunswick, Canada. Bridge abutments are identical, and both are 4 m high and 1.5 m thick supported by single row of, 15 HP 310 x 132, steel piles oriented in the week axis bending. The bridge abutments were instrumented during the construction with six load cells (three at each abutment) mounted at 0.25*H*, 0.5*H* and 0.75*H* (*H* refers to the abutment height). The abutments were also provided with deformation and tilt meters to detect any translation or rotation in the abutment. The results showed that the movements of the abutments, translation and rotation, are generally conforming to the temperature fluctuations. However, the abutments did not exhibit equal movements where the eastern abutment movement was almost pure translation while the western abutment movement involved combination of rotation and translation. According to Huntly and Valsangkar (2013) this variation may ensue from different exposure to the sun light or from some differences in degree of compaction of the approach backfill.

Maximum lateral earth pressures were recorded during summer in each of the three years. The stresses at the western abutment recorded high values at the upper sensor compared to the mid and lower sensors, while in the eastern abutment, stresses were almost constant throughout the height of the abutment. This highlights the influence of the movement mode on stress distribution, where the motion in the eastern abutment was predominantly translation with a very small amount of rotation.

Huntly and Valsnagkar (2013) compared the measured data with those calculated using different theoretical models. The comparison illustrated in Figure. 2.10 shows that none of the existing models suitably captures the behaviour of lateral earth pressure acting on the abutment. It is apparent that all the models are largely conservative in the lower part of the abutment while in the upper part, passive pressure was fully mobilised and exceeded most of the theoretical values.

Huntly and Valsangkar (2013) also stated that stress ratcheting trend has not been observed in the field data. However, it is evident that the period of observation reported by them is considerably short (three years), which consists of only three seasonal cycles (N=3). Moreover, the movement envelopes of the abutments are relatively small (approximately ±7 mm = ${}^{d}\!/_{H}$ = 0.175% for the eastern abutment and ± 9 mm = ${}^{d}\!/_{H}$ = 0.225% for the western abutment), which reflects a small displacement amplitude. Therefore, stress ratcheting effects are unlikely to occur under these conditions.

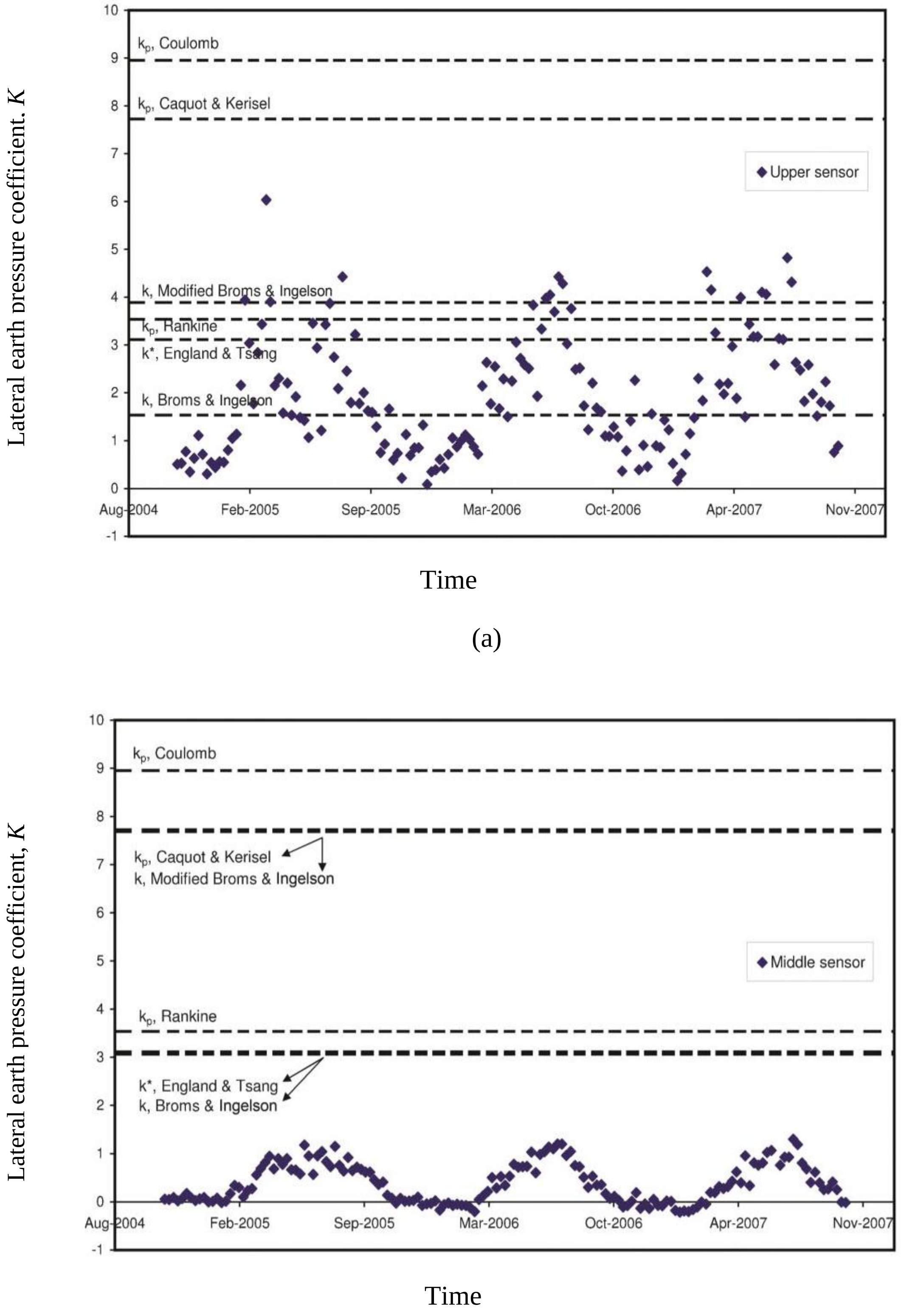

(a)

(b)

Figure 2.11 Measured earth pressures at (a) the upper and (b) middle sensors of the western abutment (Huntly and Valsangkar, 2013)

Hoppe and Gomez (1996) reported field data collected from a 98 m two-span semi integral abutment bridge, with 2.7 m height concrete abutment, in Virginia, USA. The bridge was instrumented during the construction stage and data were recorded for two and a half years. The collected data showed a daily variation in the lateral pressures acting on the abutment wall in conformance with the temperature changes. Full passive earth pressure was mobilised at the back of the abutment and recorded at the upper pressure cell (at 1.3 m from the top). The maximum weekly pressures acting on the abutment for the period between January 1994 and January 1996 are presented in Figure 2.12. It is apparent that a slight escalation in the average values of maximum stresses occurred during this period. Abutments A and B showed similar behaviour in terms of lateral pressure development but with differences in the magnitudes. Maximum lateral stresses recorded in Abutments A and B were 175 kPa and 200 kPa, respectively. According to Hoppe and Gomez (1996) such variations might be due to different degree of compaction of soil in both approaches.

Based on a backward analysis from the field data, they observed that the computed internal friction angle and unit weight of the soil (35°, 18 kN/m^3) are higher than the initial values used in the design. This indicates densification effects occurred in the approach backfill.

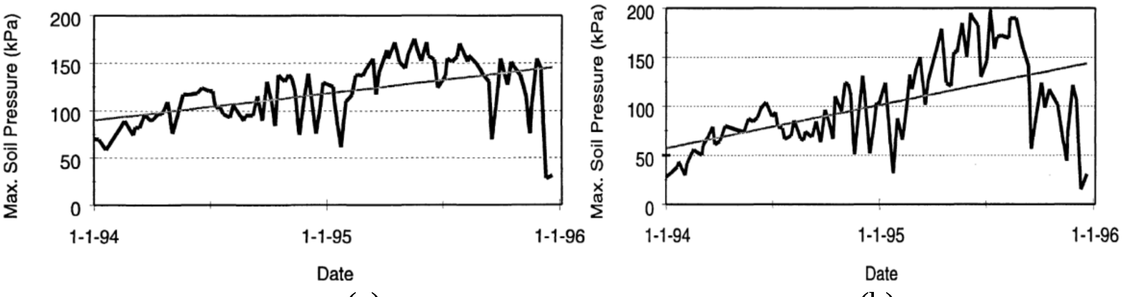

(a) (b)

Figure. 2.12 Maximum weekly soil pressures acting on (a) back-wall A and (b) back-wall B (Hoppe and Gomez, 1996)

Huang et al (2020) studied the soil-abutment-pile interaction behaviours, in IABs, in response to cyclic perturbations applied on the abutment. They conducted a study on a large-scale experimental model that involved 1 m high concrete abutment rigidly connected to a 2.9 m high H-section steel pile. Variable displacement perturbations were applied using a hydraulic actuator. The loading regime begun with ± 2 mm (d/H = 0.2%) and increased by 2 mm every three cycles until a maximum displacement of ± 16 mm (d/H = 1.6%) is reached. During the test, a considerable ratcheting in the lateral soil pressure is observed, particularly at $2H/3$ from the soil surface (*H* represents the retained height of the soil). According to Huang et al. (2020), the coefficient of earth pressure *K*, at $2H/3$, increases rapidly during the wall passive movements reaching to a value of 13 after 24 cycles. This value exceeds Coulomb passive pressure coefficient by 30%. Huang et al. (2020) also found that the ratcheting effects in the retained soil decreases progressively away from the wall until they become insignificant at 1.5*H* from the wall.

It can be observed from the above review, that predicting the maximum lateral pressures in IABs using various models depends primarily on the theoretical value of passive earth pressure coefficient K_p. However, due to the lack of a unified approach, designers are usually free to choose the method to determine the value of K_p, which consequently reflect a difference in the design outcomes. Tan et al. (2015) compared the UK BA42/96 (2003) lateral earth pressure coefficient K^* computed based on Rankine and Coulomb theories (using $\phi = 30$, $\delta = \phi/2$), as shown in Figure. 2.13. It was found that at a displacement , d/H , equal to 1%, the values of K^* calculated using Coulomb method were approximately 30% and 20% higher than those calculated using Rankine method in equation 2.13 and equation 2.12 respectively.

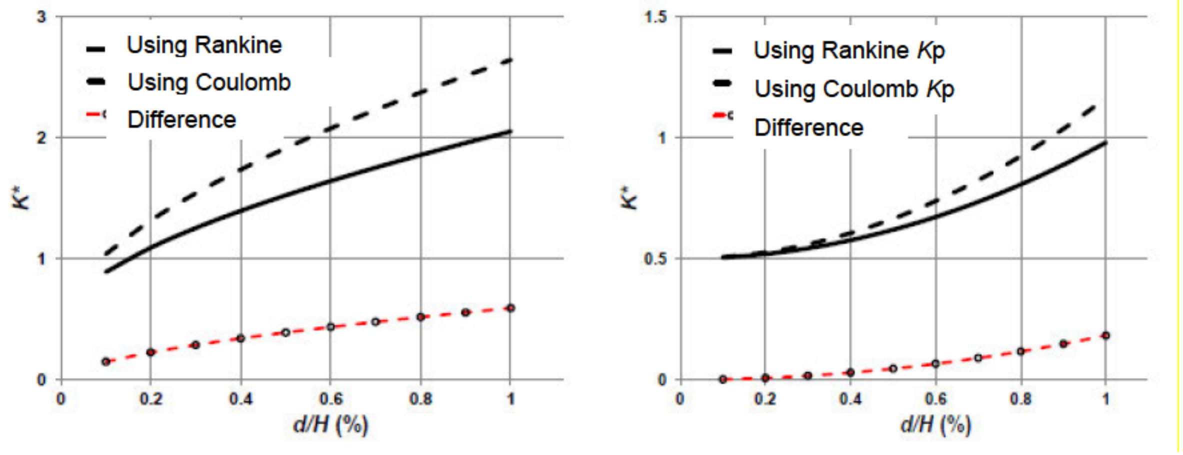

(a) (b)

Figure. 2.13 Variation in the Value of K^*computed based on (a) equation 2.13 & (b) equation 2.12 (After Tan et al., 2015)

2.5 Settlement of the Approach Soil

The settlement at bridge approaches has been a long-standing issue encountered by bridge engineers for decades. The approach settlement emerges from several causes including the loss of backfill soil by erosion, poor soil compaction, high traffic loads, improper design practices resulting in large differential settlements, etc. However, according to the literature of IABs, the primary cause of approach settlement is the lateral abutment movements (White et al., 2005). Both, experimental tests as well as field observations show that the retained backfill experiences a significant settlement as a result of the lateral movement of abutments (Ng et al., 1998; England at al., 2000; Cosgrove and Lehane, 2003; White et al., 2005; Tatsuka et al., 2009; Alqarawi et al., 2016; Huang et al., 2020).

The centrifuge test results by Ng et al. (1998) showed significant soil settlements in the proximity of the wall after 100 cycles of (± 60 mm) perturbations. According to Ng et al. (1998), the combination of the rotational and translational movements of the wall resulted in densification and volume contraction in the adjacent soil. Initially dense and initially loose soils exhibited different settlement profiles, as illustrated in Figure. 2.14. A sink-like trough was observed in the dense backfill with a maximum settlement of 660 mm. On the other hand, the loose soil produced a steady settlement increasing towards the abutment wall with maximum settlement reaching 700 mm. The influence zone of settlement in loose soil was approximately two times greater than that in the dense soil.

Ng et al. (1998) stated that the settlement depends primarily on the displacement amplitude and the number of perturbation cycles. They also used the spot-chasing technique to produce a contour map for the shear strain developed within the soil mass near the wall. It was observed that the magnitude of the maximum shear strain developed at the end of 100 cycles of given amplitude is 3 - 20 times higher than the value under monotonic loading conditions with the same displacement amplitude.

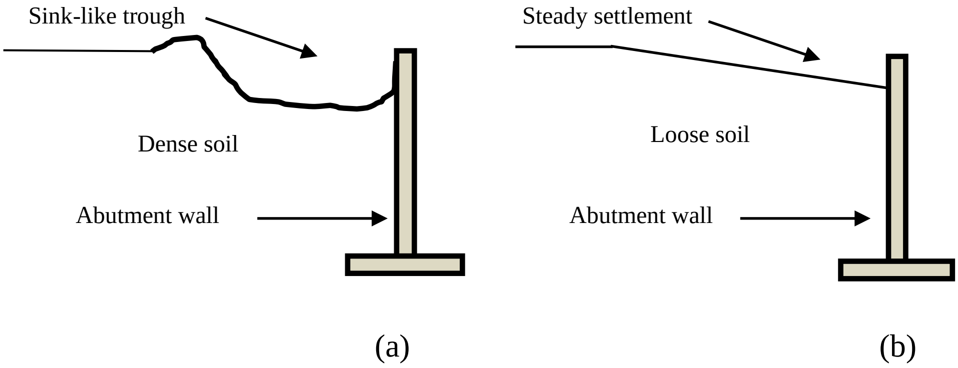

Figure. 2.14 Typical Soil Settlement Profiles in (a) dense soil and (b) loose soil

The settlement results observed by England et al. (2000) showed a progressive increase in the maximum settlement of soil surface with the number of cycles but at a slightly reducing rate. Their results indicated that the settlement is sensitive to the amplitude of wall movement and, unlike the lateral stresses, did not approach a limiting value after 300 cycles, as illustrated in Figure 2.15. According to England et al. (2000), the settlement occurred due to densification effects in the backfill due to the wall movements against and away from the soil. Such effects are identified by the heave in the free surface of the soil at 350 mm distance from the wall. The results reported by England et al. (2000) showed an active slip wedge of soil developed adjacent to the wall. It is apparent, from Figure 2.16, that the slip wedge was progressing with the number of cycles to reach an absolute settlement of approximately 40 mm after 60 cycles of combined daily (${}^{d}\!/_{H} = 0.042\%$) and annual (${}^{d}\!/_{H} = 0.25\%$) perturbations.

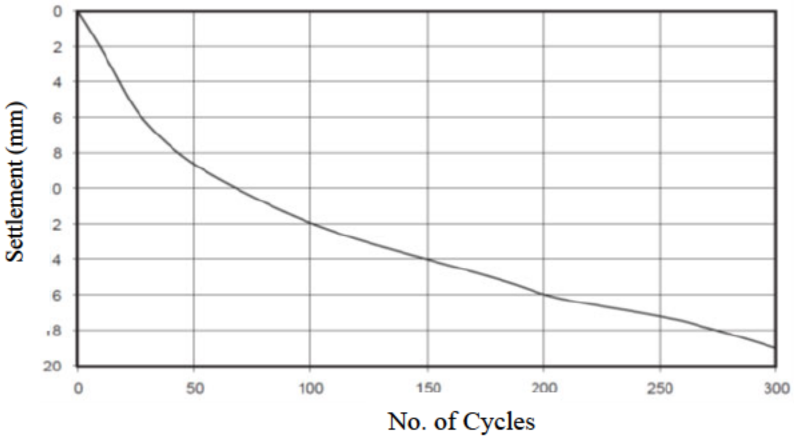

Figure. 2.15 Relationship between maximum settlement and the number of cycles (England et al., 2000)

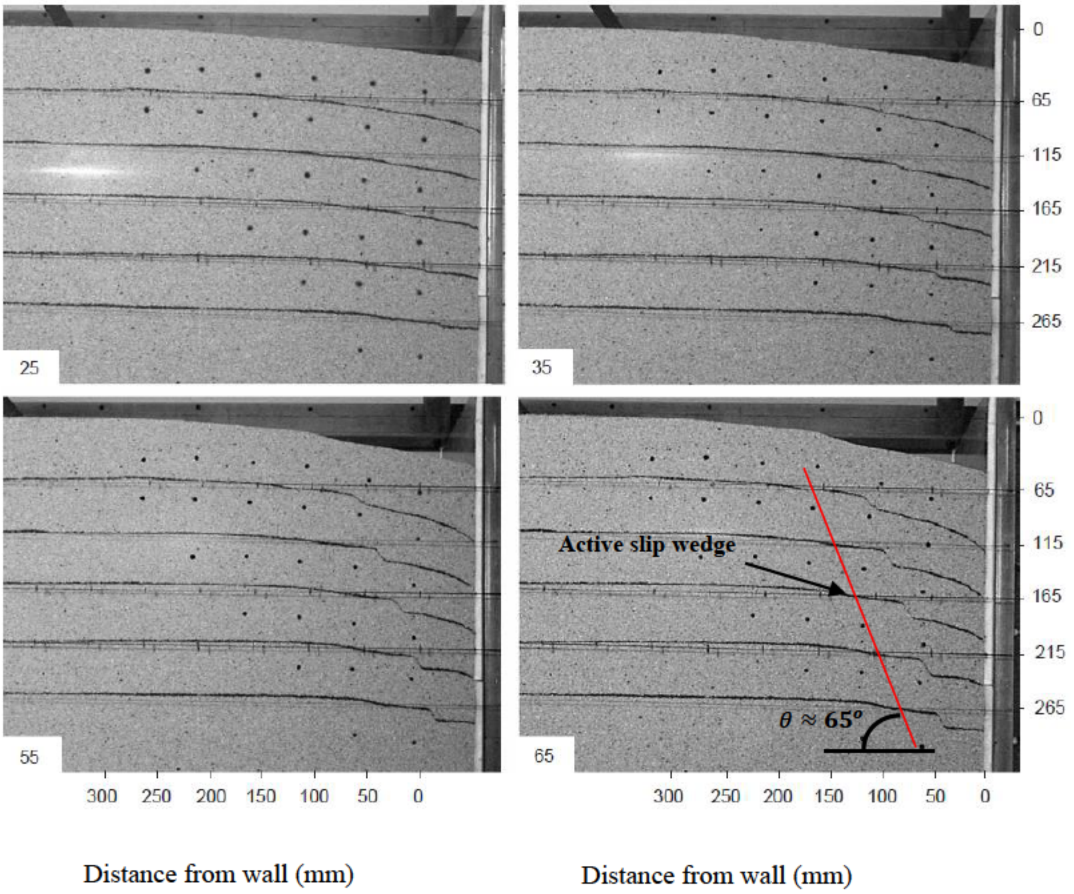

Figure. 2.16 Settlement of loose sand after 25, 35, 55 and 65 of combined daily and annual cycles (England et al., 2000)

Tatsuoka et al. (2009) reported similar conclusions after testing loose sand retained by a 505 mm high wall and subjected to cyclic displacements. The settlement of the soil, in response to the wall movement, gradually increased with the number of cycles. Maximum settlement observed at 5 cm from the wall after 50 cycles of $d/H = 0.2\%$ perturbations was almost 7% of the wall height H. Tatsuoka et al. (2009) justified the settlement in the soil surface by the dual ratcheting mechanism. A small active sliding occurs in the loosened soil adjacent to the wall, due to active wall movement, forming an active soil wedge. During the passive phase of wall movement, the active wedge is going to be compressed as part of a larger passive soil wedge. According to Tatsuoka et al. (2009), the deformation in the small active wedge will not be substantially recovered during the passive movement and will therefore be accumulated with further deformations in the subsequent active movements. On the other hand, the passive wedge, which is not completely affected by the active movement, experiences a repetitive compression that leads to densification and volumetric contraction. Therefore, the settlement is eventually a result of accumulated dual volumetric deformations in the active and passive wedges of the backfill soil. The mechanism proposed by Tatsuoka et al. (2009) is illustrated in Figure. 2.17.

Cosgrove and Lehane (2003) conducted experiments on a 1 m high loose backfill retained by a steel wall hinged at its bottom and subjected to rotational perturbations. The tests were intended to represent an abutment wall subjected to temperature induced cyclic loading. Two tests were conducted in which different numbers of cycles and loading amplitudes were applied as shown in Table 2.4. They used an optical measurement system, in which several visual targets had been embedded in the soil, to capture the extent and direction of soil movements in response to the cyclic displacements of the wall.

Table 2.4 Tests details as described by Cosgrove and Lehane (2003)

Test	Displacement (*d/H*) %	Number of Cycles (*N*)
1	0.63	120
2	0.23	500

According to Cosgrove and Lehane (2003), both tests showed significant settlements in the soil surface after 100 cycles of wall movement. They stated that the settlement in the soil surface varies nonlinearly with the number of cycles. The absolute measured settlements, after 100 cycles, were equal to 20% and 10% of the total wall height in test 1 and test 2, respectively.

Based on the movement vectors illustrated in Figures 2.18 (a) and 2.18 (b), a triangular small wedge of soil moves in the downward direction during active wall displacement, while a reversal movement direction is observed during the passive wall displacement. As observed in Figure 2.18 (b) (during the passive phase of the cycle), the direction of movement is predominantly horizontal with a very small vertical component. That means the precedent inclined active motion was not equally reversed during the passive phase of the movement. This behaviour indicates the occurrence of unrecoverable vertical deformation in the active wedge. The subsequent cycles are also expected to behave similarly, perhaps with different deformation behaviour in the active soil wedge. The accumulation of such deformations is the likely primary reason contributing to settlements observed at the approach of IABs.

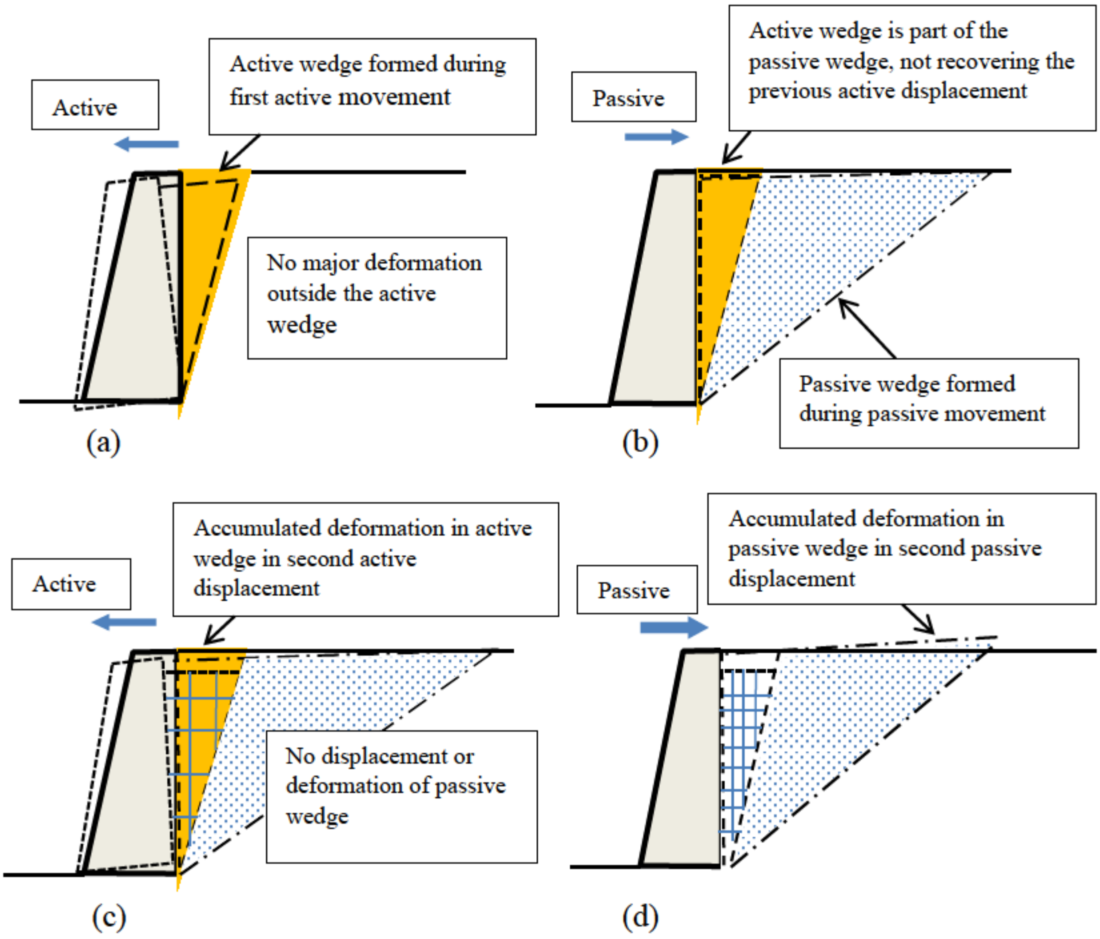

Figure 2.17 Dual ratchet mechanism due to wall rotational movement (After Tatsuoka et al., 2009)

It is apparent from Figures 2.18 (a) and 2.18 (b) that the movement effects during the first cycle ($N = 1$) are very small or negligible at or beyond 500 mm from the wall. That defines the boundaries of the *influence zone* in response to wall rotation. In contrast to the movement styles at $N = 50$, less extents of active and passive displacements are observed. That may justify the reduction in the incremental rate of settlement after many cycles of wall movements. However, the *influence zone,* after 50 cycles, extend to more than 600 mm from the wall, which indicates more volume of soil is being affected by the wall movements.

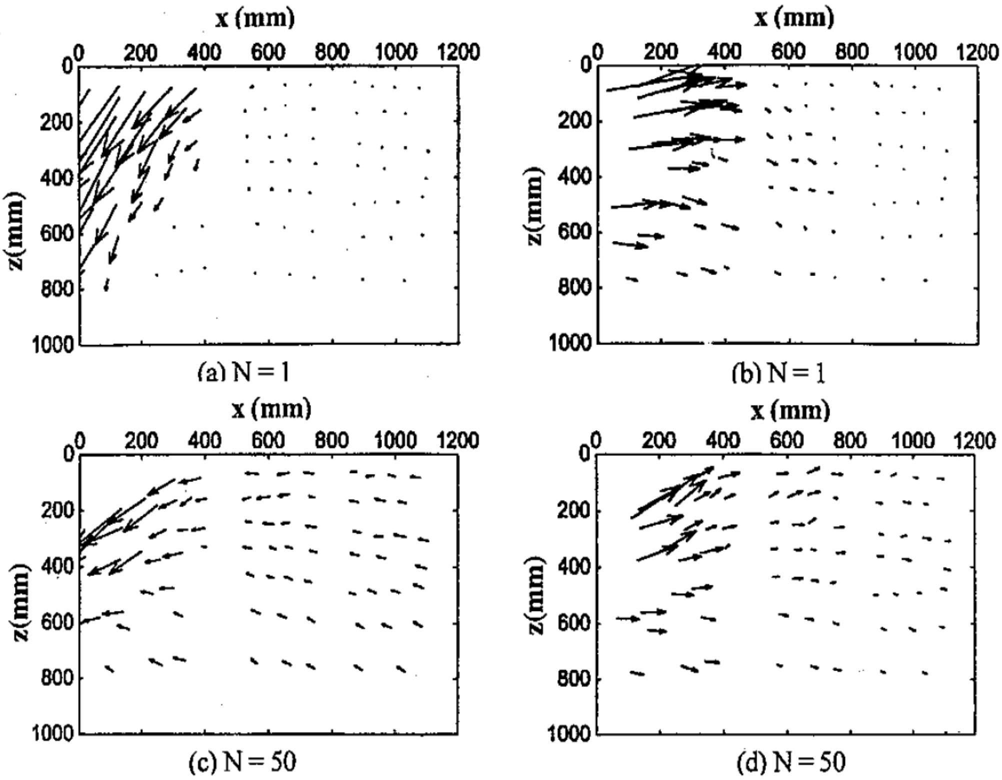

Figure 2.18 Active and passive movement vectors (Cosgrove and Lehane, 2003)

The experimental study conducted by Huang et al. (2020) showed a similar behaviour in the soil surface settlements. They observed a large trough developed at the soil adjacent to the wall in response to 24 cycles of rotational wall displacements. An extent of soil deformation was also observed at the wall-pile joint resulting in a small void beneath the abutments as shown in Figure 2.19.

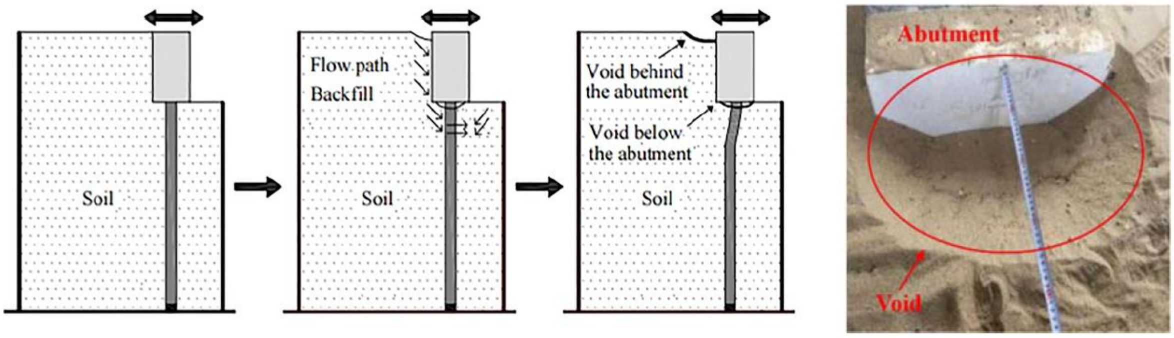

Figure 2.19 Voids formation adjacent to the wall and at the wall-pile joint
(after Hunag et al., 2020)

2.6 Solutions to the Approach Problems in IABs

The design guidelines of IABs vary widely from one country to another and therefore standard measures utilised to alleviate the approach problems in IABs are not clearly established. The use of run-on slab and well compacted soil in the vicinity of the abutment are the common suggestions to alleviate the approach settlements (Horvath, 2000; Lock, 2002). Although the use of the run-on slab is generally adopted in the US practice, it does not seem to be free of problems. Settlements of the approach backfill sometimes results in large troughs that a run-on slab is incapable to span. This will lead to the damage of the latter under the traffic loading as illustrated in Figure 2.20 (White et al., 2005).

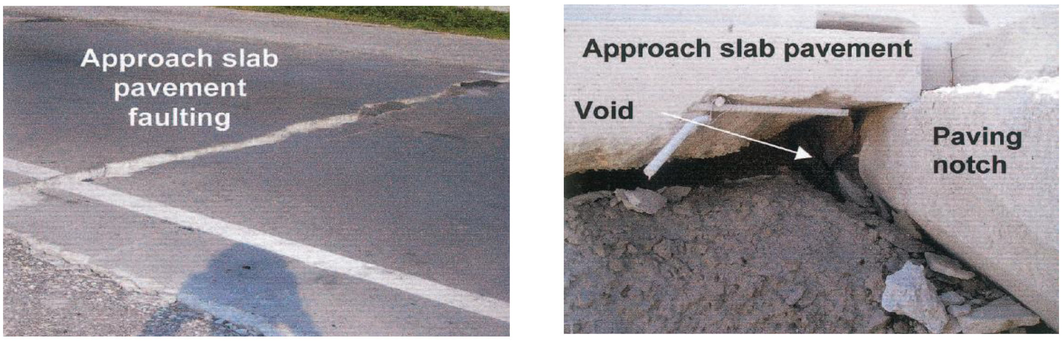

Figure 2.20 Failure at the run-on slab due to backfill settlement (White et al., 2010)

In some of the European countries, including UK, Ireland and Sweden, the use of the run-on slab is not recommended as the settlement will occur even when a run-on slab is provided (White et al., 2010). Varmazyar et al. (2017) stated that the use of a run-on slab does not help to mitigate the approach problems in IABs because it will eventually suffer a flexure failure due to the development of a settlement trough underneath. A broken run-on slab will complicate and increase the cost of the maintenance works for settled backfill as compared to soil overlay and pavement patching (Hoppe and Gomez, 1996). Therefore, the presence of the run-on slab does not offer a practical and effective remedial measure for the settlement of the approach backfill in IABs.

On the other hand, the use of heavily compacted backfill does not help to reduce the approach settlement, in IABs, but was proven to increase the stiffness of the retained soil and consequently results in high lateral pressures on the bridge abutments (Oesterle and Tabatabai, 2014).

Nam and Park (2013) reported some construction details and field observations from the first IAB constructed in South Korea. In an attempt to minimize the lateral earth pressures on the abutment, 1.0 m wide and 3.3 m high *pressure relief zones* were provided at bridge approaches adjacent to the abutments. The zone was filled with coarse sub-base cohesionless material type A-1-a (according to AASHTO classification system). The concept of using this material was to minimize the interlocking effects of the backfill material due to the horizontal movements of the abutments and consequently alleviate the passive earth pressures. However, the reported data represents only the first two years after the opening of the bridge (two annual cycles) during which the maximum recorded displacement amplitudes were + 8.8 mm (passive) and - 3.3 mm (active). Both are relatively small amplitudes. Nevertheless, passive pressure was mobilised behind the wall and maximum recorded value of K reached approximately 4.4 (50% of Rankine passive pressure) during the summer of the second year. Such results show no evidence of avoiding higher lateral pressures after many cycles of abutment movements.

The traditional methodologies implementing well compacted backfill and/or concrete approach slab to mitigate the lateral earth pressure escalation and approach settlements in IABs have shown to be unsuccessful. Therefore, design agencies around the world have been experimenting different methods to solve these problems.

2.6.1 Compressible Inclusions

Research studies showed that using a compressible inclusion, or a pressure relief layer, at the interface between the abutment and the approach backfill, can alleviate the effects of abutment movements on the adjoining soil (Hoppe, 2005; Alqarawi, 2016, Hoppe et al., 2016). The inclusion materials, used in previous studies, involve rubber, expanded polystyrene geofoam, and tyre shreds.

Evidence of using the compressible inclusions in the construction of IABs is common in the USA practice. The department of transportation in South Dakota investigated the use of a rubber tyre chips behind the abutment in an integral bridge (Reid et al., 1999). A 24 in (610 mm) thick layer of tyre chips was placed behind the abutment with a cardboard separation layer between the backfill and tyre chips. The cardboard was provided to prevent the backfill from entering the voids between the tyre chips. The results showed that the tyre chips helped to reduce the lateral backfill pressure significantly. However, the cyclic abutment movements resulted in continuous rearrangement of the rubber chips, leading to the development of a void below the approach slab but at a smaller extent than that developed in a normal backfill without compressible layer (Reid et al., 1999).

In North Dakota, the design guidelines require a pressure-relief layer placed behind the abutment. Such layer includes a several inches thick elastic material, behind it is a corrugated metal sheet (Hassiotis and Roman, 2005). In Delaware and Pennsylvania, 1 to 2 inches (25 – 50 mm) thick polystyrene inclusion must be provided behind the abutment. In the state of Virginia, the use of an elastic inclusion has recently become a design requirement after conducting successful field trials using EPS inclusions (Hoppe et al., 2016; VDOT Design Manual, 2020). The bridge design manual of Virginia provides the equation below (equation 2.16) to estimate the design thickness of the EPS inclusion.

$$EPS_t = 10[0.01H + 0.67(\Delta L)] \geq 10 \text{ in} \tag{2.16}$$

where EPS_t is thickness of the EPS inclusion in inches

H is height of abutment in inches

ΔL is the total movement (expansion and contraction) in inches

Unlike USA, the European practice does not integrate experiences in using compressible inclusions in IABs. According to Barr et al. (2013), none of the European countries require the use of any type of inclusion behind the abutments of IABs. However, a recent study in Poland, investigated the use of rubber tyre bales as a backfill material in IAB approaches. Duda and Siwowski (2020) used large tyre bales, sand filling and tyre shreds to fill 5 m x 5 m x 5.3 m test chamber. The study aimed to investigate the lateral pressure exerted on the retaining wall due to different modes of displacements. The study showed that the proposed backfill reduced the active and passive pressure by, approximately, ten times compared to the case where a granular backfill is used

2.6.2 Mechanically Stabilised Earth (MSE)

In this technique, the approach soil is designed to become self-stable without relying on the abutment as a retaining element. The approach is constructed using mechanically stabilised earth or reinforced soil with a gap between the facing of the MSE and the abutment. The gap may or may not be filled with a compressible material. This technique has been utilised in the USA practice. In the state of South Dakota, a trial using MSE for IAB approaches was applied in three bridges (Reid et al., 1999). The approaches were constructed using geosynthetic-reinforced backfill with a 16 inch (406 mm) gap between the reinforced soil wall and the abutment (following the design practice used by the state of Wyoming). The results collected from these bridges showed that the lateral pressure and the approach settlements issues were eliminated. However, problems of different nature were arisen in these bridges, including the interaction between the soil and the wing walls, erosion of soil from the sides of the approach into the gap behind the abutment and the movements of the reinforced-soil wall subsequently reducing the gap size.

The European practice, again, does not incorporate the technique of MSE walls at the approaches of IABs. However, after conducting a numerical study, Fartaria (2012) proposed the use of an elasticized EPS inclusion behind the abutment together with a curtain of soil-cement columns to restrain the backfill soil during the active phase of the abutment movement. The numerical results showed that the proposed approach system is efficient in reducing the lateral soil pressure especially during large abutment displacements.

2.7 Expanded Polystyrene (EPS) Geofoam

In this section, the engineering behaviour of expanded polystyrene (EPS) geofoam is discussed because in this thesis, mitigating measures are explored using EPS geofoam, which is a polymeric material belonging to the family of the geosynthetics. The EPS possesses unique favourable characteristics and one of them is the extremely low density. The EPS used in civil engineering applications has density as low as 12 kg/m^3, which is equivalent to hundredth of typical soil fill density (Horvath, 1994). Also it has favourable mechanical and thermal properties such as its compressive strength and thermal insulation characteristics (BASF, 2006). In addition to that, the EPS is an environmentally friendly material and provides a cost-effective choice for construction. These features have collectively put the EPS geofoam as one of the best light-weight materials available. Therefore, it has several geotechnical applications such as a light weight fill for embankments, a compressible inclusion for retaining structures, and a stabilization material for slopes, in addition to its potential use in integral abutment bridge systems.

2.7.1 Physical Properties

The EPS is a cellular rigid material formed of polyhedron expanded polystyrene particles. The expanded polystyrene particles are fused together during the manufacturing process forming an integrated cellular structure with air voids in between particles. The polystyrene particles themselves are formed of vast number of air-filled closed cells. Figure 2.21 shows the internal micro structure of an EPS specimen.

The density of EPS is an important factor that affects many of its physical and mechanical properties. During the manufacturing process, it is possible, to a certain extent, to control the density of EPS by controlling the quantity of moulded polystyrene beads. Therefore, EPS can be produced in variety of densities between 10 kg/m^3 and 50 kg/m^3. However, in most of the geotechnical applications, the density of EPS used is 20 kg/m^3 (Horvath, 1994).

In addition to its ultra-light weight, EPS is inherently a non-biodegradable material and chemically inactive with soil or water (Horvath, 1994). It also does not offer a nutritive medium for undersoil organisms. These features made the EPS a durable geotechnical material.

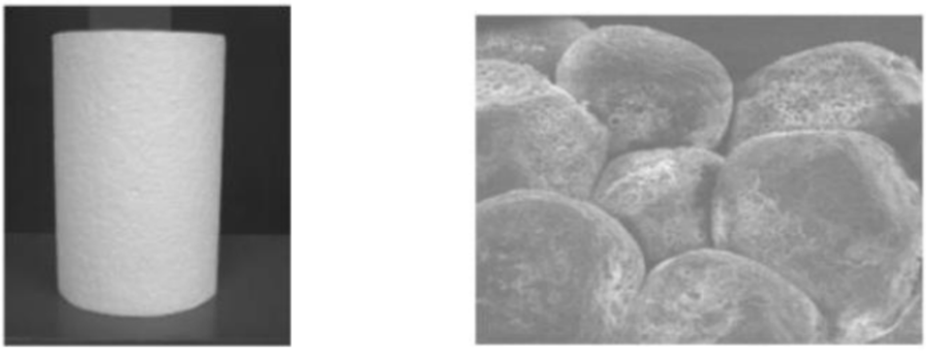

(a) EPS specimen (b) EPS Particles

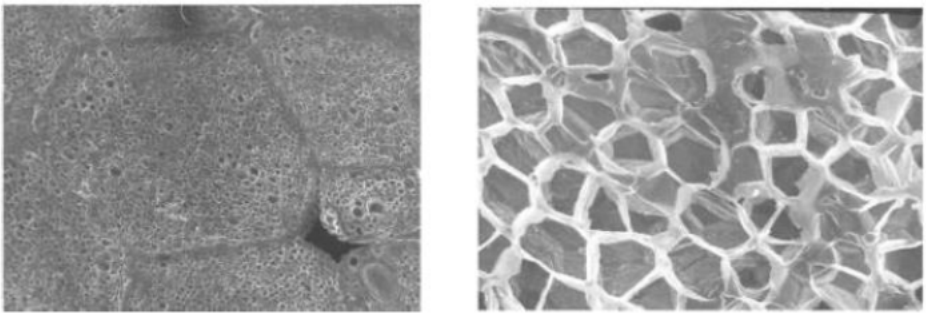

(c) EPS particles and cells (d) Air filled closed cells

Figure 2.21 Internal structure of EPS (Ossa and Romo, 2009)

2.7.2 Mechanical Properties of EPS

2.7.2.1 Stress-Strain Relationship

The stress-strain relationship of EPS in compression, like other mechanical and physical properties, correlates to its density. The higher the density of EPS, the higher will be its compressive strength. Table 2.5 shows selected values of EPS densities with the corresponding compressive strength. Nevertheless, the stress-strain relationship of EPS is qualitatively similar irrespective of its density (Horvath, 1994). Figure 2.22 shows a typical stress-strain curve of an EPS specimen in a rapid unconfined compression test (Arellano and Stark, 2009).

Table 2.5 10% strain - compressive strength of EPS with different densities (Elraji 2000)

Density (Kg/m^3)	12	15	18	22	29
Compressive Strength at 10% strain (kPa)	35	69	90	104	173

In rapid compression tests, EPS is known to exhibit a linear elastic behaviour immediately after loading. That behaviour is represented by the initial straight part of the stress-strain diagram. Slope of that linear part is defined as the elastic modulus or Young's modulus of EPS. The value of the elastic modulus of EPS, as mentioned before, is affected by its density. Within this zone (the elastic zone) the micro cell walls tend to bend and buckle in an attempt to absorb the energy induced by the applied load. As a result, the elastic stiffness of the material will be decreased and its behaviour transforms into a plastic stiffness (E_p) (Ossa and Romo, 2009). It was found that the linear relationship between the applied stress and strain continues until the value of strain reaches to approximately between 1% - 1.5% (Horvath, 1994). For well conservative design considerations, it is recommended to identify the elastic limit as the point where the developed strain is equal to 1% (Arellano and Stark, 2009). Therefore, the stress measured at 1% strain is often referred as the elastic limit of the EPS.

Beyond the point of elastic limit, the material starts to yield. During this phase, large amount of energy is dissipated by the continuous deformation of cell walls and hinges and through expelling cells encapsulated air (Ossa and Romo, 2009). The yield of EPS is found to occur over a range rather than a certain point at the stress-strain diagram. That zone of the stress-strain relationship ends up at approximately 10% strain. The stress measured at this point (strain equal to 10%) is generally referred as the compressive strength of EPS (Horvath, 1994).

Following the yield range, EPS exhibits a pure plastic strain-hardening behaviour. During this phase, the internal structure and particle geometry are continuously modified. The internal voids between particles are mostly vanished while the closed cell walls are completely collapsed. The change in the internal structure of the material continues until the polystyrene particles are totally damaged and reversed to their original state as polystyrene beads. However, no clear mode of failure appears in the stress-strain relationship of EPS.

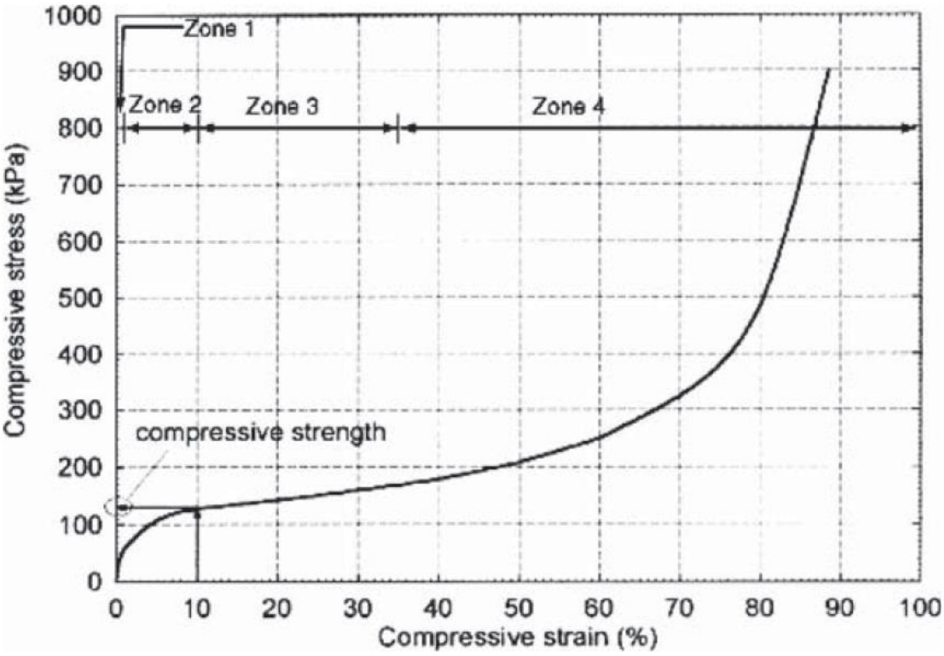

Figure 2.22 EPS Stress-Strain relationship in rapid unconfined compression test (Arellano and Stark, 2009)

2.7.2.2 Time Dependent Behaviour

EPS is found to exhibit time dependent behaviour represented by the creep and stress relaxation when it is subjected to sustained loading conditions. Creep refers to the plastic deformation developed over a period under sustained load, while the stress relaxation is expressed as the reduction in stress with time under a constant strain. Creep and relaxation are in fact reciprocal phenomena appearing in EPS behaviour due to the visco-plasticity characteristics.

In a typical axial compression test, an EPS specimen will deform elastically upon application of load. Shortly after and when specimen exceeds its elastic limit, it will enter the plastic zone and some part of the developed strain becomes irreversible. The total strain at this stage is the combination of elastic strain plus the creep or time dependent strains. Therefore, total strain can be decomposed into immediate and time-dependent components as follows:

$$\varepsilon = \varepsilon_o + \varepsilon_t \tag{2.17}$$

where ε is the total strain developed after a certain time (t), ε_o is the immediate strain due the load application, which also represents the elastic component of the strain and ε_t is the creep or the time-dependant strain developed during the time (t)

The amount of creep in EPS is susceptible to the initial applied load and EPS density (Chun et al., 2004). According to Horvath (1994), a small or negligible amount of creep is observed in specimens subjected to an initial strain below 1%, but significant increase in the developed creep occurred when the specimen was initially strained by more than 1%. Accordingly, a design criterion was suggested to limit the applied load on EPS blocks below the elastic limit to avoid excessive time dependent deformation (Arellano and Stark, 2009).

Elraji (2000) reported the results of creep tests for different EPS specimens with different initial loading levels. The results, shown in Figure 2.23, indicate a dramatic increase in creep when the initial loading was 70% of compressive strength, while the creep effects were limited when the initial stress levels were 30% and 50 % of its compressive strength

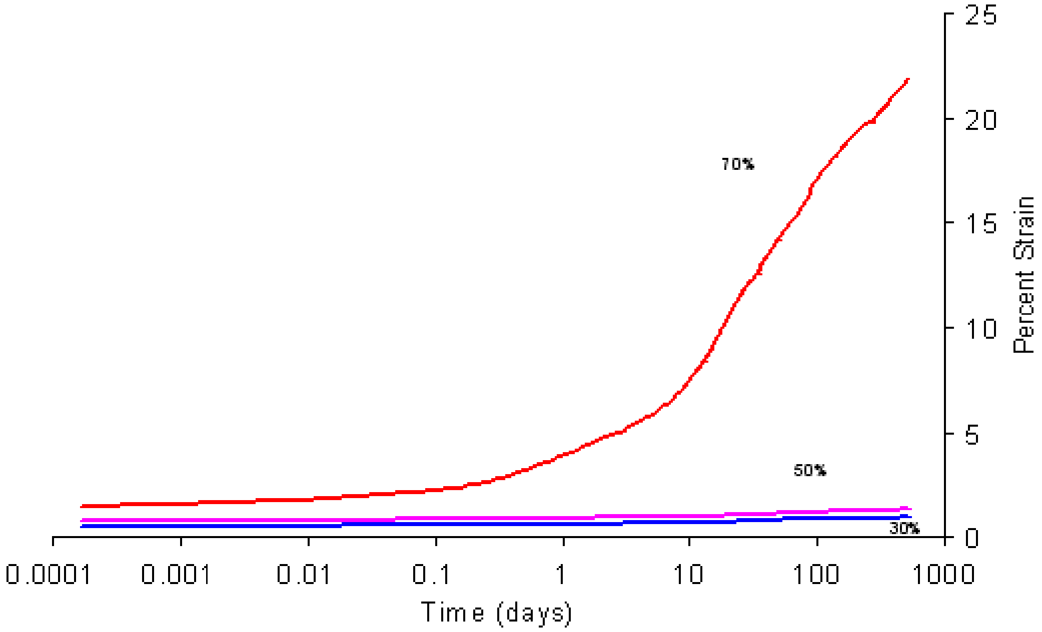

Figure 2.23 Time dependant behaviour of EPS at different stress levels (Elraji, 2000)

2.7.3 Applications of EPS in Mitigating Approach Problems in IABs

The inherent properties of EPS make it a perfect remedy for the persistent lateral pressures and soil settlements in IABs. The EPS is highly compressible with relatively low Young's modulus. These merits enable the EPS inclusion to absorb most of the abutment movement with minimal disturbance to the adjacent soil. In other words, the actual displacement transferred to the soil will be significantly reduced by the EPS inclusion. This characteristic, which is known as the *transfer function* of the EPS, is illustrated in Figure 2.24.

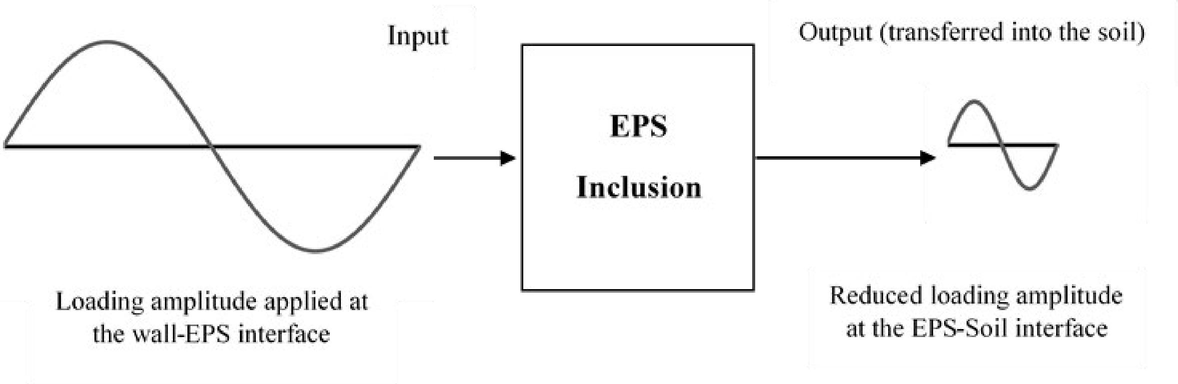

Figure 2.24 The transfer function of EPS Geofoam inclusion

Despite of having unique characteristics that made it suitable for various geotechnical applications, the use of EPS geofoam in mitigating the approach problems in IABs is very limited (Hoppe, 2005; Hoppe et al., 2016). This highlights the lack of research and reliable evidence-based data about the possible application of EPS inclusions in AIB approaches.

The EPS geofoam has a great potential, as a highly compressible material, to serve as an inclusion to alleviate the challenging earth pressure ratcheting and soil settlements problems in IAB. Therefore, investigating the potential use of EPS geofoam in this application forms one of the main objectives of this thesis.

Hoppe (2005) reported field data collected, over five years, from an integral abutment bridge on Jackson River in state of Virginia in the United States. The bridge was the first IAB in the US to include a compressible inclusion with the aim to mitigate the settlements and lateral pressure problems. The inclusion was a 250 mm thick board of elasticised polystyrene (EPS) and it was placed between the retained backfill and the concrete abutment along the width of the bridge (see Figure 2.25). The height of the EPS board was terminated at 0.76 m from the top of the wall to allow for placing a pressure cell that measures the lateral pressures acting on the abutment wall (without inclusion).

The 100 m long and 16.6 m wide three span integral bridge was instrumented during the construction stage and was opened for traffic in 1999. Three pressure cells were provided at each abutment mounted at 0.63 m, 1.12 m and 1.6 m from the top of the wall. The reported data include lateral soil pressure acting on the abutment walls and the settlement in the approach soil recorded during the period from 1999 until 2005.

Figure 2.25 EPS inclusion in Jackson River Bridge, Virginia, US (Hoppe, 2005)

According to Hoppe (2005) lateral earth pressures were reduced significantly behind the EPS inclusion compared to the upper part of the abutment (where there is no EPS inclusion). Maximum stress in the middle sensor was approximately 7% to 10% of the upper sensor. However, lateral pressure in the upper part of the abutment is certainly higher than that in the middle or the lower parts. Therefore, for a fair comparison, pressures need to be measured at similar locations.

The settlement at the approach soil for the period between November 1999 and December 2004 was monitored. Limited surface settlement, approximately 20 mm, was observed at the end of that period. The bridge approaches were maintained only once with pavement patching since the opening of the bridge. Hoppe (2005) compared maintenance works carried out for another IAB in Rockingham County with approximately the same length but without any EPS inclusion. The latter suffered excessive settlement at the vicinity of abutment and approach pavement was repeatedly patched.

Hoppe et al. (2016) reported the use of 380 mm thick elasticised EPS inclusion in a highly skewed semi integral abutment bridge on Route 18 in the state of Virginia, USA. The abutments were instrumented with 8 pressure cells on each abutment. All of them, except two, were covered by the EPS inclusion. The data collected during the period between January 2007 and August 2011 involved the average temperature, the strain in the EPS inclusion and the pressure readings from the pressure cells. A summary of results is shown in Table 2.6. It is apparent that the EPS inclusion proved to significantly reduce the earth pressure.

Table 2.6 Some of the field data reported by Hoppe et. al, (2016)

Results	Minimum	Maximum	Envelope
Temperature (c°)	-9.8	28.9	38.7
Pressure in the middle of the abutment (kPa) (without EPS)	-	91	-
Pressure in middle of the abutment (kPa) (with the EPS)	-	4.56	-
Strain in the EPS inclusion (%)	0.65	2.38	1.7

Hoppe et al. (2016) stipulated that the current practice in Virginia Department of Transportation requires to adopt an EPS inclusion when constructing IABs.

In addition to its advantages in mitigating the approach problems in IABs, the EPS geofoam has a potential in attenuating dynamic loads. Several experimental and numerical studies have shown that EPS blocks can successfully be used as a seismic buffer between the rigid walls and soil backfill to attenuate the seismic loads transferred to the wall (Zarnani and Bathurst, 2009; Bathurst and Zarnani, 2013; Bartlett and Neupane, 2017). However, the suitability of the EPS geofoam to counter seismic loading is outside the scope of this thesis and therefore, it will not be discussed.

2.8 Gaps in knowledge

The literature review has identified the following gaps in knowledge related to IABs which this thesis has attempted to address:

(a) The physics of the approach soil-abutment interaction has not been comprehensively and rigorously dissected and analysed. Earlier research has identified the importance of soil slumping, densification and confining stress due to the abutment moving away and pushing against the retained soil in response to cyclical temperature changes. However, soil slumping, densification and confining stress will be influenced by several factors, mostly unique to IABs. For instance, one key factor noteworthy of consideration is the nature of the cyclic displacements of the abutment, that is, whether it is primarily of rotational or translational mode or a combination of both. The importance of this factor is so far understated and has not been critically analysed.

(b) Although some remedial solutions have been proposed, an effective solution is yet to be found to deal with the development of settlement trough in a broad spectrum of IABs. Lack of effective solution would eventually lead to the settlement bump in the abutment approach.

(c) Almost all of the studies in literature using physical models did not attempt to achieve similarity in the stress conditions between the model and full-scale prototype. Since the soil is stress dependent, the critical effects of the soil-structure interaction in the IAB may not have been observed in such models.

(d) A fundamental understanding of the physics of the interactions of a three-layered system, soil-inclusion-abutment in IABs is lacking, indeed not yet formulated. Managing the transfer of effects between soil and abutment, and vice-versa, through the inclusion will be a significant factor in managing the alleviation of approach settlement and lateral stress ratcheting on the abutment. Without new fundamental knowledge of the transfer function of the inclusion, any proposed remedial measure can only be based on limited empirical understanding established mainly on experimental data, and its application beyond the parameters and assumptions tied to the experiments would be questionable.

(e) The current practices utilised to estimate the lateral earth pressure on the abutments of IABs are largely dependent on the limiting earth pressure coefficients, particularly the passive pressure coefficient K_p. This review showed that design agencies are using different theoretical methodologies in calculating K_p which certainly results in considerably different outcomes. Moreover, design engineers are often attracted to use Rankine or Coulomb methodologies in estimating K_p, due to their simplicity, although their assumption of a planar failure surface is in question. Therefore, a comprehensive, yet simple, solution that addresses the true failure mechanism of soil in the passive state needs to be developed.

(f) There have been several research studies investigating structural and geotechnical aspects of IABs bridges. However, a comprehensive study that addresses the fundamental soil-structure interaction in IABs, through a combination of analytical, experimental and numerical analyses, is lacking. Such integrated study would provide evidence-based knowledge about the interaction mechanism in IABs approaches and sheds lights into the possible mitigation measures.

2.9 Research Questions

In view of the knowledge reviewed in this chapter and the gaps identified in section 2.8, the following questions have been identified and will be addressed as the focus of this thesis:

(a) The temperature-induced abutment movement in IABs leads to two major issues, namely, escalation in the lateral earth pressure (stress ratchetting) as well as settlement bump in the approach soil. What is the fundamental soil-structure interaction mechanism that leads to the development of the stress ratchetting and the approach settlements in IABs as a result of the abutment movements?

(b) The international design standards involve considerable disparity in terms of the estimation of the magnitude and the distribution of the lateral earth pressure behind the abutments in IABs. In this regard, which of these design guidelines is more relevant and appropriately applies in estimating the lateral earth pressure in IABs than the others?

(c) The estimation of the lateral earth pressure in IABs depends heavily on the static coefficient of passive earth pressure K_p. There are currently different methodologies used to calculate K_p (such as Rankine, Coulomb, Caquote and Kerisel, etc.) that vary in their simplicity and their accuracy. What is the best approach to calculate the value of the passive earth pressure coefficient K_p that realistically captures the static passive earth pressure?

(d) The use of a compressible inclusion (the EPS in particular) has been reported as a potential remedy for the approach problems in IABs. What are the fundamental characteristics of the "two-way" soil-EPS-wall interactions and how the presence of an EPS inclusion can help to alleviate the approach problems in IAB?

(e) What is the significance of the type or the mode of the abutment movement (translation or rotation) on the consequent stress ratchetting and settlement bump in the IAB approaches?

(f) How to design a large-scale physical model of an integral abutment to achieve similarity in key areas between the model and full-scale prototype in order to study the soil-structure interactions?

(g) The numerical modelling of the approach soil in IABs requires the consideration of a number of effects that ensue from the interaction with the abutment. These include the change in the strength and stiffness of the soil, the non-linearity of the soil response as well as the confinement effects. Can the traditional Mohr-Coulomb model be extended to capture some of these effects?

Chapter 3

Estimation of Passive Earth Pressure on Retaining Systems

3.1 Introduction

The lateral earth pressure is one of the primary parameters influencing the interaction between the soil and adjacent structural members. Therefore, estimation of earth pressure is vital when the design of such structural members is sought. While many retaining structures are designed considering an active or at-rest state for the backfill, in practice there are certain cases, where the interaction mobilizes a passive earth pressure. Particularly, in integral abutment bridges, the research studies show that a full passive earth pressure is likely to develop behind the abutments due to the movements of the bridge deck (Hassiotis and Xiong, 2007). Therefore, the passive earth pressure forms a fundamental input in estimating the lateral earth pressure during the design of integral bridge abutments. An efficient and reliable method to estimate the passive earth pressure is necessary for the design of integral bridge abutments.

3.2 Overview of Passive Earth Pressure Theories

Various theories have been developed to estimate the passive earth pressures exerted on retaining walls over the past several decades. They used different methodologies in calculating the passive earth pressure which sometimes resulted in largely different outcomes. In this Chapter, a number of theories that are currently utilised in estimating passive earth pressure are briefly reviewed.

3.2.1 Earth Pressure due to Planar Failure Surfaces

Classical theories that assume planar failure surface, such as Coulomb (1973) and Rankine (1857) are widely used as the fundamental methodologies to estimate the lateral passive pressure of the backfill on retaining walls. The review conducted earlier, in Chapter 2, showed that Rankine and Coulomb methodologies are largely used in USA and European practices in the estimation of passive earth pressure behind the abutments of Integral abutment bridges. These theories use the limit equilibrium approach to calculate the passive earth pressure and the coefficient of passive pressure, K_p. Although the cited theories involve a number of differences, they both assumed the passive failure surface to be planar surface. Coulomb (1973), assumed that the failure occurs along a plane surface that passes through the toe of the wall at an angle θ with the horizontal such that the passive pressure acting on the retained structure is a minimum. Rankine (1857), on the other hand stipulated that the passive failure surface is a plane, inclined at $(45-\phi/2)$ to the principle horizontal axis (where ϕ represents the internal friction angle of the soil).

3.2.2 Earth Pressure due to Non-Planar Failure Surfaces

The assumption of a planar failure surface has shown to be problematic when the interface between the wall and the soil is not smooth (Terzaghi, 1943). Accordingly, new methodologies estimating the passive earth pressure using a non-planar failure surface were developed. Caquot and Kerisel (1948) proposed a new method to calculate the passive earth pressure of a cohesionless deposit using a failure surface following a spiral arc. This method assumes the soil immediately behind the wall complies with Coulomb criterion of limit equilibrium inside an angle beyond which the soil is in a Rankine equilibrium state (Kerisel and Absi, 1990). The calculations in this method are too complicated, therefore, the authors provided ready-made tables to estimate the coefficient of passive earth pressure K_p (Kerisel and Absi, 1990).

Another methodology of a non-planar failure surface was developed by Terzaghi (1943). The latter suggested that the failure surface is not a plane when the angle of the interface friction δ between the wall and the retained backfill is more than zero. Terzaghi (1943) stated that sufficiently accurate results can be obtained when a logarithmic spiral arc is used to represent the bottom part of the rupture surface (curve *bg* in Figure 3.1) while the rest of the surface is a tangential line to the log-spiral curve rising up at an angle equals to ($45-\phi/2$) with the horizontal.

3.3 Proposed Methodology

In a real practical case, the interface friction between the wall and the soil is far from being ideally smooth, hence appropriate estimation of the passive earth pressure must account for the curvature in the failure surface. In this chapter, a new analytical solution is developed using the hypotheses of Terzaghi (1943).

The log-spiral method proposed by Terzaghi (1943) was used by a number of experimental studies and showed to be in closer agreement, with the measured data, than Rankine or Coulomb methods. Duncan and Mokwa (2001) studied the passive earth pressure mobilized due to the translation of 1 m high concrete bulkhead embedded in the soil. They concluded that the log-spiral method is the most accurate theory for estimating the passive earth pressure over a wide range of interface friction angles. Fang et al. (2002) reported experimental results from a number of tests using dry sand under monotonic rigid wall movements. They stated that the log-spiral method proposed by Terzaghi can successfully replicate the passive earth pressure by using the critical state concept. Wilson and Elgamal (2010) conducted large scale model tests using granular soil to measure the passive earth pressure. They reported that the log-spiral prediction provided very good estimation by comparing with the measured data. Rollins et al. (2017) reported that the lateral passive pressure calculated using the log-spiral method replicates the measured force within an error of less than 10% compared to 47% and 60% respectively, using Coulomb and Rankine methods.

Although the log-spiral theory can provide an accurate means to estimate the passive earth pressure, design engineers often prefer Rankine and Coulomb methods, due to their simplicity, despite of the potential misrepresentation of the actual conditions. The primary reason behind that is the lack of a rigorous solution to evaluate the passive earth pressure using the log-spiral theory. Even though, the latter was developed a few decades ago, (Terzaghi 1943), limited research studies utilized the log-spiral composite failure to estimate the static passive earth pressure (Terzaghi, 1943; Terzaghi et al., 1996; Patki et al., 2015; Liu et al., 2018), and none have developed comprehensive and easy-to-implement solutions. Terzaghi's (1943, 1996) solution is proposed only for the cases when the pole of the log-spiral is located inside the slip mass; Liu et al. (2018) proposed a complicated solution based on the pole outside the slip mass. The solution developed by Patki et al. (2015) does not apply for sloping backfills.

This chapter aims to develop a comprehensive and rigorous numerical solution, based on the log-spiral theory, such that it can be easily formulated on a spreadsheet to estimate the passive pressure of the soil acting on a rigid retaining wall. The proposed solution is versatile and can examine different internal friction angles, soil-wall interface friction angles, wall inclinations, backfill slopes and external surcharge, and covering the possibility of the pole located either inside or outside the slip mass. In this chapter, the proposed solution will be referred to as the "log-spiral solution".

3.3.1 Properties of the Failure Surface

Figure 3.1 shows a hypothetical case, where a rigid wall retains a homogenous deposit of dry cohesionless soil with a unit weight of γ and friction angle of ϕ. The backfill is inclined at an angle β with the horizontal, while the wall face is inclined at an angle ω to the vertical. Imagine the wall translates monotonically against the backfill until a localized plastic equilibrium is reached in the soil close to the wall. This state is expressed by the mobilization of a passive failure in the retained soil. The failure occurs when the passive wedge *abge* is at the verge of sliding along *bge*. Therefore, the latter is often termed as the sliding or the failure surface.

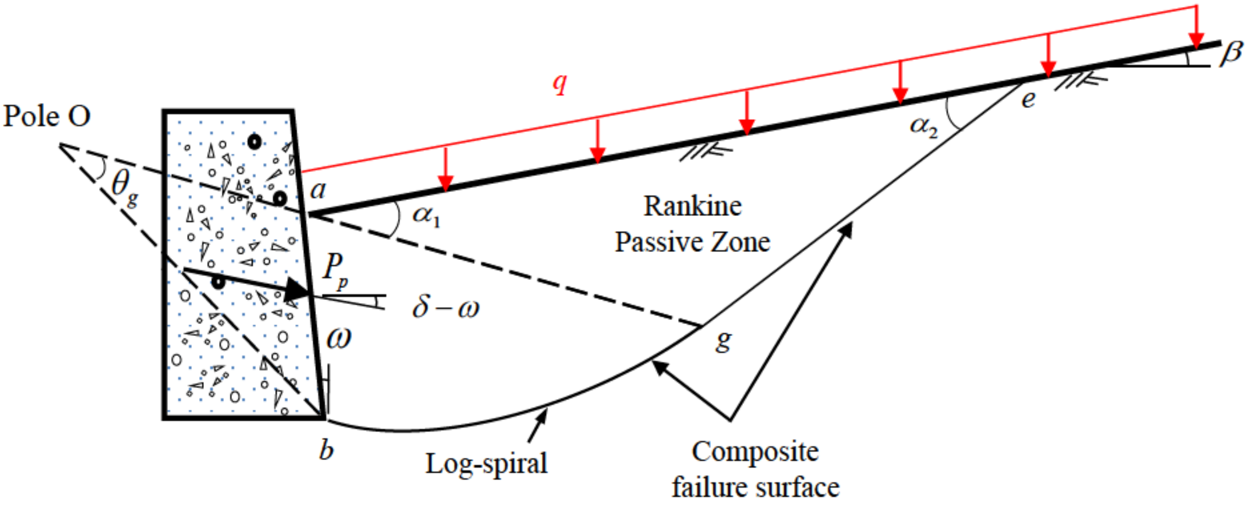

Figure 3.1 The composite log-spiral failure surface

The composite failure surface *bge*, in the case prescribed in Figure 3.1, is based on the hypotheses of Terzaghi (1943). Hence, it comprises a logarithmic spiral arc, *bg*, and a straight line *ge*, which is a tangent to the spiral at point *g*. The passive wedge consists of the area *abg* (outlined by the log-spiral arc) and the Rankine passive zone outlined by the isosceles triangle *age* (Terzaghi et al. 1996). Liu et al. (2018) stated that the angles α_1 and α_2 for a cohesionless sloped backfill can be calculated using the following relationships,

$$\alpha_1 = \frac{\pi}{4} - \frac{\phi}{2} + \frac{1}{2}\arcsin\left(\frac{\sin\beta}{\sin\phi}\right) - \frac{\beta}{2} \tag{3.1}$$

$$\alpha_2 = \frac{\pi}{4} - \frac{\phi}{2} - \frac{1}{2}\arcsin\left(\frac{\sin\beta}{\sin\phi}\right) + \frac{\beta}{2} \tag{3.2}$$

Therefore, when the backfill is horizontal $(\beta = 0)$, $\alpha_1 = \alpha_2 = \frac{\pi}{4} - \frac{\phi}{2}$.

The force P_p that mobilises the passive failure acts on the wall at an angle ($\delta - \omega$) with the horizontal, whereas δ represents the interface friction angle.

The log-spiral arc, *bg*, is given by the formula,

$$r_i = r_o e^{\theta_i \tan\phi} \tag{3.3}$$

where r_o is the initial radius of the spiral arc at point *b*, r_i represents the radius of the spiral at any random point *i* on the spiral arc , θ_i is the angle of rotation subtended by r_o and r_i , and ϕ represents the internal friction angle of the soil. Hence, at point *g*, the equation (3.3) can be written as,

$$r_g = r_o e^{\theta_g \tan\phi} \tag{3.4}$$

It is apparent that the size of the spiral arc is characterized by $r_o, r_{g,} \theta_g$ and ϕ . While ϕ is taken as a constant for a given type of soil, the remaining parameters are functions of the virtual location of the Pole O of the log-spiral. The location of the Pole O, therefore, is essential in developing a generalised solution for the problem illustrated in Figure 3.1.

Logically, the Pole O can be located either outside the soil mass (Figure 3.2-a) or inside the soil mass (Figure 3.2-b). While the Pole can also fall at point *a*, this can be treated as a unique limiting case of either (a) or (b) above (the Pole lies outside and inside the soil mass, respectively) but not as an independent case. Terzaghi et al. (1996) suggested that the Pole lies on the line O*g* inside the soil mass (i.e., case b above). However, they did not discuss the possibility of the Pole to be located outside the soil mass. Until recently, Liu et al. (2018) developed a mathematical formulation to estimate the passive earth pressure coefficient, K_p, assuming that the Pole of the spiral falls outside the soil mass. However, developing a solution based on the assumption of the Pole either inside or outside the soil mass only may not cover all potential solutions. Moreover, the solutions developed by Liu et al. (2018) are based on minimising the passive force objective function expressed in terms of the "design variable" which is the y-coordinate of an intersection point vertically above point *g* and horizontally aligned with point *a*, in Figure 3.2. As will be shown later, this chapter proposes an alternative, simpler "design variable" ξ which is based on the distance O*a*. Patki et al. (2015) proposed a numerical solution to determine the lateral earth pressure using the log-spiral method assuming an arbitrary location of the Pole O along the spiral radius. However, their solution is limited to horizontal backfill $(\beta = 0)$and does not apply for sloping backfill. Therefore, the present chapter aims to develop a generalised solution that examines both cases of Pole O location (inside and outside the soil mass) and applies to horizontal and sloping backfill, vertical and inclined wall and to a wide range of interface friction angles.

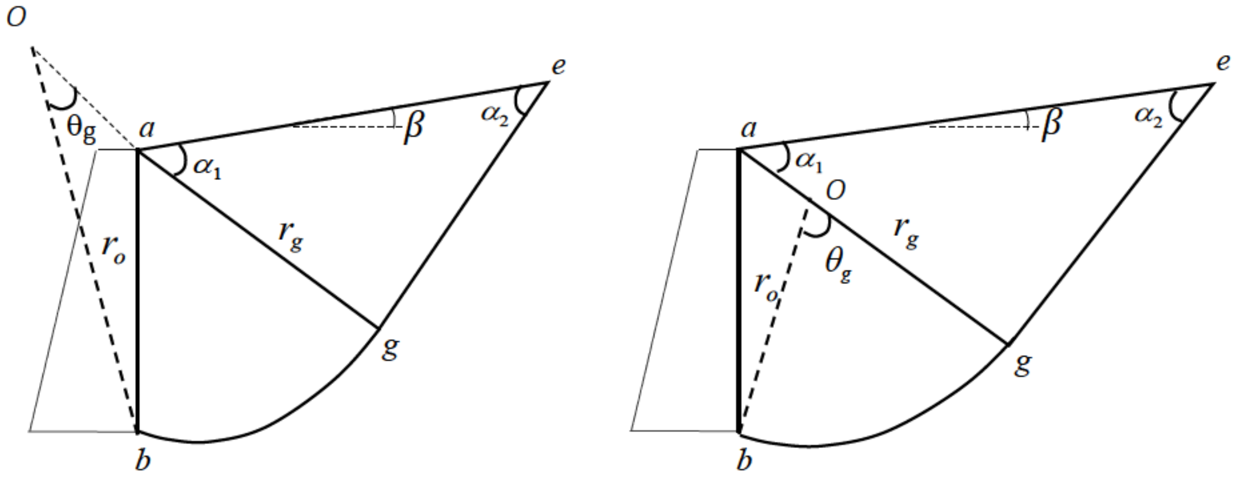

(a) (b)

Figure 3.2 The failure surface when the spiral pole is (a) outside the soil mass and (b) inside the soil mass

From the simplified description above, it is understood that the magnitude of the force due to passive soil pressure, P_p, in Figure 3.1, can be calculated using the principle of the limit equilibrium. This requires accounting for the forces acting on the passive wedge, the wall and the failure surface. These forces include the self-weight of the passive soil wedge, the soil reaction forces acting along the slip surface in addition to the force P_p. In order to achieve a determinate solution for the problem, the area *fge* of the passive wedge is replaced by a Rankine passive pressure triangle as shown in Figure 3.3 (Terzaghi et al. 1996).

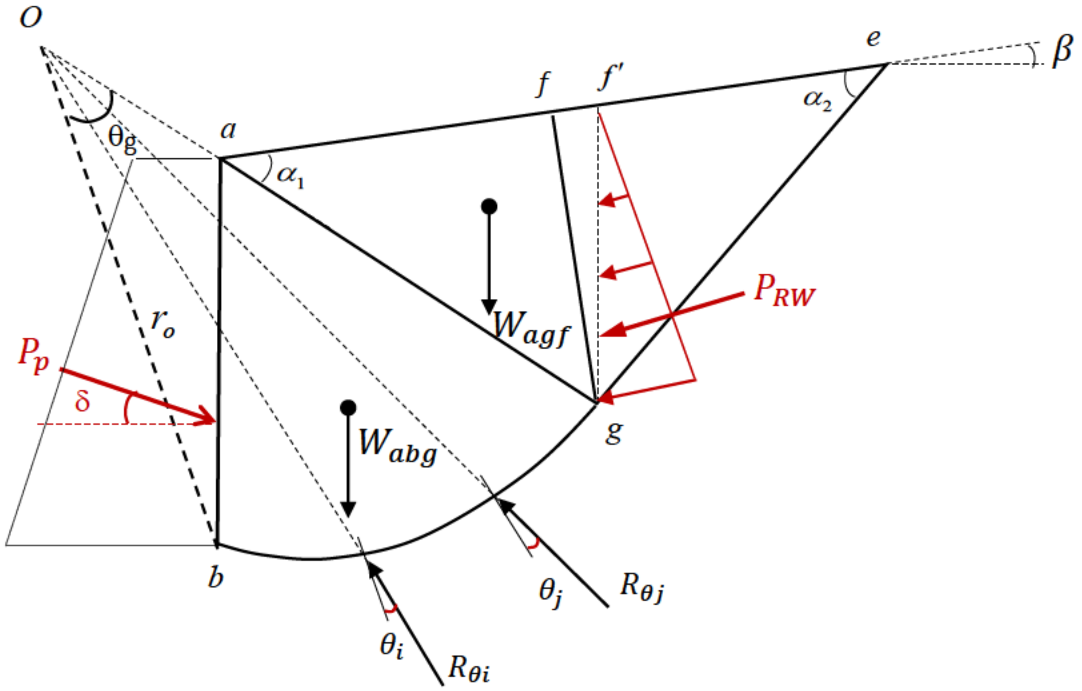

Figure 3.3 Free body diagram of the failure wedge

However, the system given in Figure 3.3 is just an illustration of the free body diagram of the failure wedge with an arbitrary location of the Pole O outside the soil mass (Case-a). As the location of the Pole is normally unknown, it is impossible to figure out the characteristics of the failure surface and accordingly the passive earth pressure. A meaningful approach to deal with such a problem is to find the unique solution given as the minimum magnitude of the passive earth pressure corresponding to the failure surfaces defined by the parameter ξ.

3.3.2 Formulation of the Limiting Equilibrium State

As described earlier, the proposed log-spiral solution is formulated based on the principles of the limit equilibrium. Hence, the moment equilibrium about the Pole O is applied. This however, depends heavily on the location of the Pole inside or outside the soil mass.

Therefore, the solution will be presented firstly for Case-a (Pole outside the soil mass) and then for Case-b (Pole inside the soil mass) separately.

Case-a: The Pole Lies Outside Slip Mass

Let us assume that the Pole O lies on the line O*a* outside the slip mass *abge* (see Figure 3.4) at an arbitrary distance ξ ("design parameter") from point *a*. Pole O slides along the direction of O*a* to generate a range of log-spiral curves *bg*.

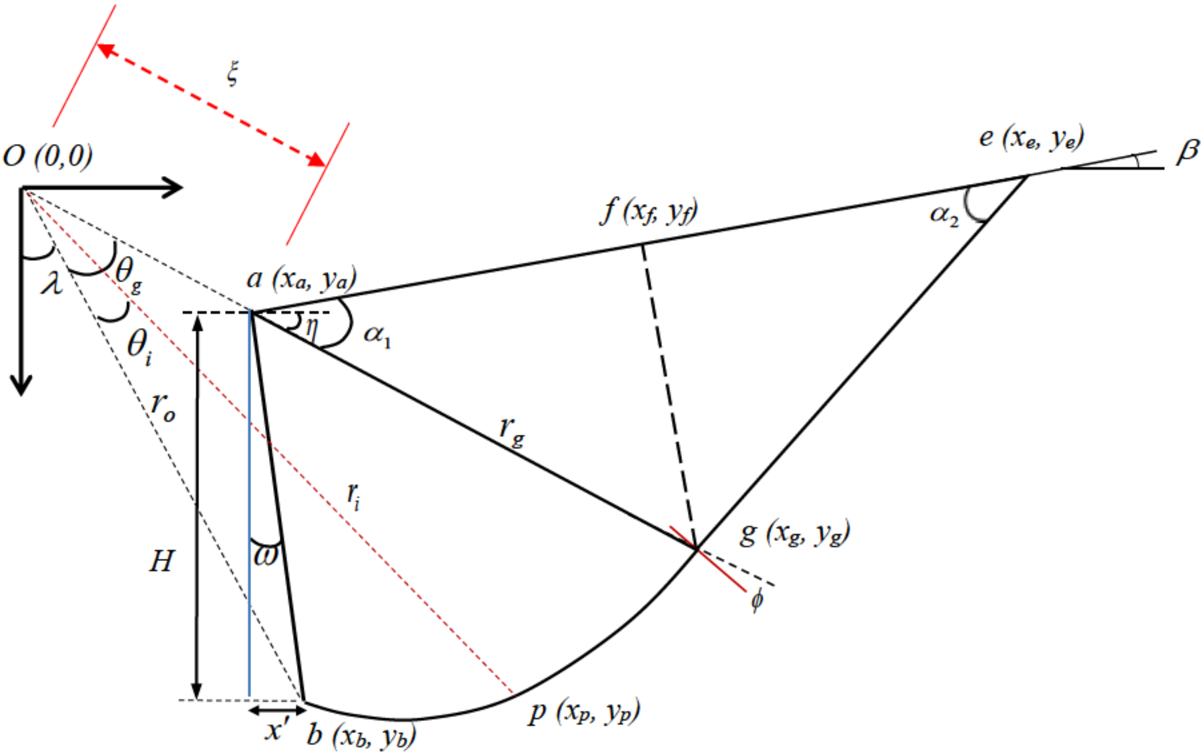

Figure 3.4 Slip mass when the Pole of the spiral is outside the slip mass

According to the given assumptions, the following relationships can be established,

$$H\text{ (the vertical projection of the retained length ab)} = |ab|\cos\omega \tag{3.5}$$

$$x'\text{ (the horizontal offset between points a and b)} = |ab|\sin\omega \tag{3.6}$$

$$\eta = \alpha_1 - \beta \tag{3.7}$$

Distance O*a* = $|\xi|$ (3.8)

In a given trial, let ξ be specified (note: ξ is taken as negative when the Pole lies outside the soil mass as in Case-a), and based on that, the following parameters can be computed:

Coordinates of point *a* (x_a, y_a):

$$x_a = |\xi| \cos\eta \tag{3.9}$$

$$y_a = |\xi| \sin\eta \tag{3.10}$$

$$r_o = \sqrt{(H + y_a)^2 + (x_a + x')^2} \tag{3.11}$$

Coordinates of point *b* (x_b, y_b):

$$x_b = x_a + |x'| \tag{3.12}$$

$$y_b = y_a + H \tag{3.13}$$

$$\theta_g = \sin^{-1} \frac{y_b}{r_o} - \eta \tag{3.14}$$

Coordinates of point *g* (x_g, y_g):

$$x_g = r_g \cos\eta \tag{3.15}$$

$$y_g = r_g \sin\eta \tag{3.16}$$

$$|ag| = r_g - |\xi| \tag{3.17}$$

$$|fg| = |ag| \sin\alpha_1 \tag{3.18}$$

Coordinates of point *f* (x_f, y_f):

$$x_f = x_g - |fg| \sin\beta \tag{3.19}$$

$$y_f = y_g - |fg| \cos\beta \tag{3.20}$$

The slip mass *abge* is also defined, including the log-spiral *bg*, the coordinates of which can be established using the log-spiral relationship (equation 3.3), where θ is the angle subtended between the log-spiral radius *r* and r_o (see Figure 3.4). The coordinates of point *p* on the log-spiral curve are then given by:

$$x_p = r\sin(\theta+\lambda) \tag{3.21}$$

$$y_p = r\cos(\theta+\lambda) \tag{3.22}$$

where λ is an angle subtended by r_o and the vertical axis.

The area moment of *abg* about the Pole O is given by,

$$M^a_{abg} = M^a_{obg} - M^a_{oba} \tag{3.23}$$

where M^a_{obg} is the area moment of the log-spiral sector *obg* and M^a_{oba} is the area moment of the triangle *oba* (see Figure 3.4). Now an infinitesimal sector with subtended angle $d\theta$ of the log-spiral is considered in Figure 3.5. The centroid of that sector is located at $\frac{2}{3}r$ from the Pole O.

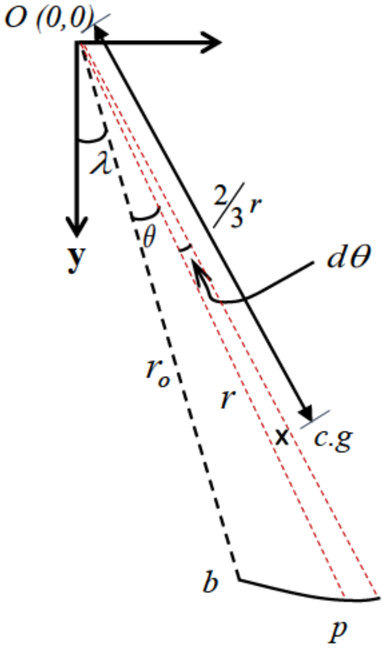

Figure 3.5 Infinitesimal sector of log-spiral in Case-a

Then the anticlockwise incremental area moment dM^a about O is given by:

$$dM^a = \frac{1}{2} d\theta r^2 . \frac{2}{3} r \sin(\theta + \lambda) \tag{3.24}$$

Expanding and considering that $r = r_o e^{\theta \tan\phi}$ gives:

$$dM^a = \frac{1}{3} r_o^3 e^{3\theta \tan\phi} (\sin\theta \cos\lambda + \cos\theta \sin\lambda) d\theta \tag{3.25}$$

which leads to,

$$M^a_{obg} = \frac{1}{3} r_o^3 \int_0^{\theta_g} e^{3\theta \tan\phi} (\sin\theta \cos\lambda + \cos\theta \sin\lambda) d\theta \tag{3.26}$$

Integrating by parts, equation (3.27) is obtained:

$$\begin{aligned} M^a_{obg} = {} & \frac{r_o^3 \cos\lambda}{3\left(1 + 9\tan^2\phi\right)} \left[1 + e^{3\theta_g \tan\phi} \left(3\tan\phi \sin\theta_g - \cos\theta_g \right) \right] + \\ & \frac{r_o^3 \sin\lambda}{3\left(1 + 9\tan^2\phi\right)} \left[e^{3\theta_g \tan\phi} \left(\sin\theta_g + 3\tan\phi \cos\theta_g \right) - 3\tan\phi \right] \end{aligned} \tag{3.27}$$

Similarly, the anticlockwise moment arm of triangle *oba* is,

$$\bar{x}_{oba} = \frac{1}{3}(x_a + x_b) \tag{3.28}$$

so that,

$$M^a_{oba} = \frac{1}{6}(x_a y_b - x_b y_a)(x_a + x_b) \tag{3.29}$$

The anticlockwise moment due to self-weight of slip mass abg about O is:

$$M_{abg} = \left(M^a_{obg} - M^a_{oba} \right) \gamma \tag{3.30}$$

Considering Figure 3.6, the following relationships can be derived,

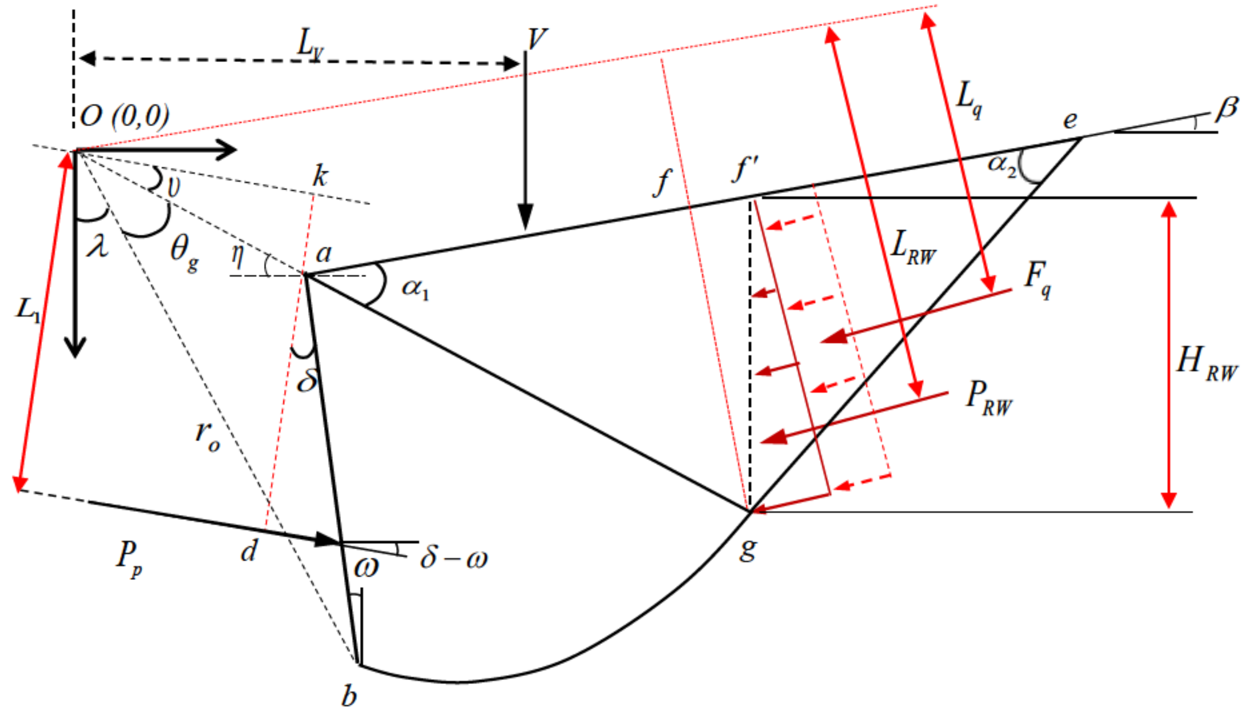

Figure 3.6: Forces and moment arms about the Pole O in Case-a

$$\upsilon = \eta - \delta + \omega \tag{3.31}$$

$$|ka| = |\xi| \sin \upsilon \tag{3.32}$$

$$|da| = \left(\frac{2}{3}|ab|\right)\cos\delta \tag{3.33}$$

$$L_1 = |ka| + |da| \tag{3.34}$$

$$L_{RW} = r_g \sin \alpha_1 - \left(\frac{1}{3}|fg|\right) \tag{3.35}$$

Surcharge load, $V = q|af'|$ (3.36)

where $af' = |af| + |fg| \tan\beta$

$$af = \frac{|x_f - x_a|}{\cos\beta} \tag{3.37}$$

M_q is the moment produced by the surcharge *q* about the Pole O

$$M_q = V\left|x_a + \left(\frac{x_{f'} - x_a}{2}\right)\right|, \text{ where } x_{f'} = x_g \tag{3.38}$$

$$P_{RW} = \frac{1}{2}K_p \gamma H_{RW}^2 \cos\beta \tag{3.39}$$

where H_{RW} is calculated as,

$$H_{RW} = \frac{|fg|}{\cos\beta} \tag{3.40}$$

K_p is Rankine’s passive pressure coefficient for sloped backfill and calculated as,

$$K_p = \frac{\cos\beta + \sqrt{\cos^2\beta - \cos^2\phi}}{\cos\beta - \sqrt{\cos^2\beta - \cos^2\phi}} \tag{3.41}$$

$$M_{agf'} = \frac{1}{6}|af'||fg|\gamma\left(x_a + x_g + x_{f'}\right) \tag{3.42}$$

$$F_q = q\cos\beta K_p H_{RW} \tag{3.43}$$

$$L_q = r_g \sin\alpha_1 - \left(\frac{|fg|}{2}\right) \tag{3.44}$$

$$M_{qh} = F_q L_q \tag{3.45}$$

By taking moment equilibrium about O:

$$P_p = \frac{1}{L_1}\left(P_{RW}L_{RW} + M_{qh} + M_{abg} + M_q + M_{agf'}\right) \tag{3.46}$$

Finally, passive force = min P_p

For a given wall geometry (wall height and slope angles) and set of geotechnical properties (internal friction angle, unit weight of soil and soil-wall interface friction), the passive force P_p is a function of ξ through the parameters L_1, P_{RW}, L_{RW} etc. in equation (3.46). Thus, a spreadsheet can be easily set up to compute P_p and determine its minimum value as a function of ξ.

Case-b: The Pole Lies Inside Slip Mass

In Case-b, the Pole is assumed to be located inside the slip mass as shown in Figure 3.7. Under this assumption, the area moments are different compared to those discussed for Case-a.

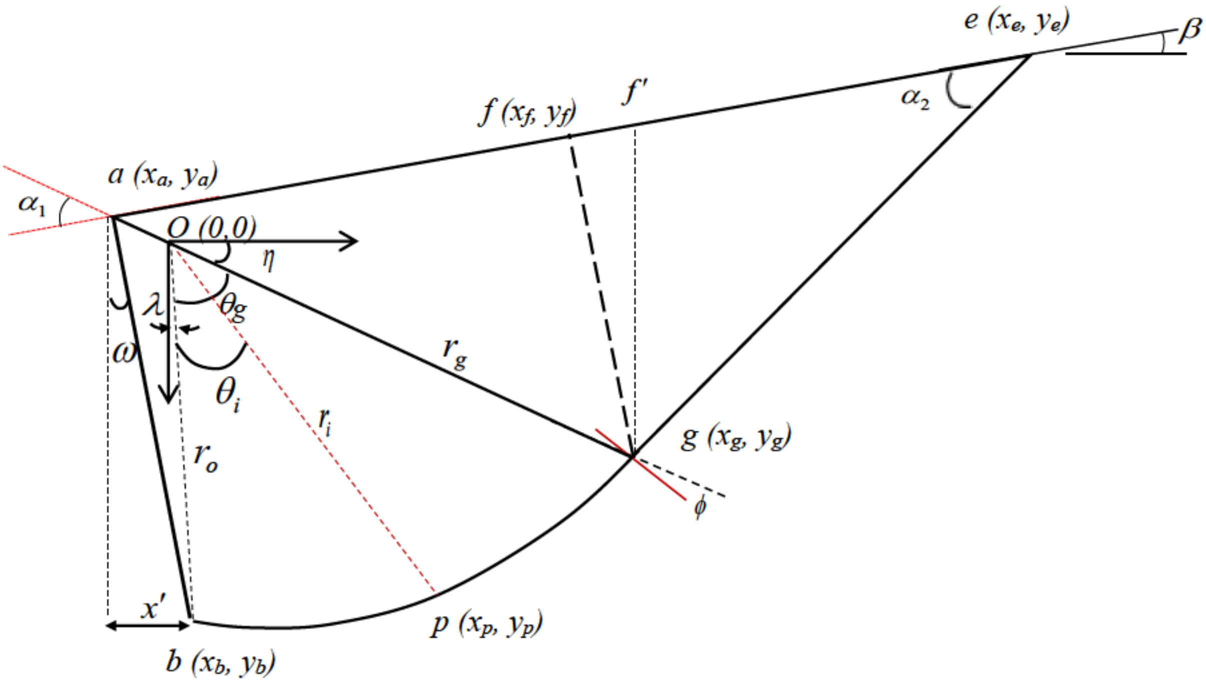

Figure 3.7 Slip mass when the Pole of the log-spiral is inside the slip mass

Similar to Case-a, at a given ξ (note: ξ is taken as positive when the Pole lies inside the soil mass) the following relationships can be established,

Coordinates of point a,

$$x_a = -(\xi \cos\eta), \tag{3.47}$$

$$y_a = -(\xi \sin\eta) \tag{3.48}$$

Coordinates of point *b*,

$$x_b = x' + x_a, \tag{3.49}$$

$$y_b = H + y_a \tag{3.50}$$

$$r_0 = \sqrt{x_b^2 + y_b^2} \tag{3.51}$$

$$\lambda = \sin^{-1}\frac{x_b}{r_o} \tag{3.52}$$

$$\theta_g = 90^\circ - \lambda - \eta \tag{3.53}$$

$$r_g = Og = r_o e^{\theta_g \tan\phi} \tag{3.54}$$

Coordinates of point *g*,

$$x_g = r_g \cos\eta \tag{3.55}$$

$$y_g = r_g \sin\eta \tag{3.56}$$

$$ag = |\xi| + r_g \tag{3.57}$$

$$fg = |ag| \sin\alpha_1 \tag{3.58}$$

Coordinates of point *f*,

$$x_f = x_g - (fg \sin\beta), \tag{3.59}$$

$$y_f = y_g - fg\cos\beta \tag{3.60}$$

$$x_p = r\sin(\theta + \lambda) \tag{3.61}$$

$$y_p = r\cos(\theta + \lambda) \tag{3.62}$$

Calculation of the area moments of *oba*, agf' (see Figure 3.8)

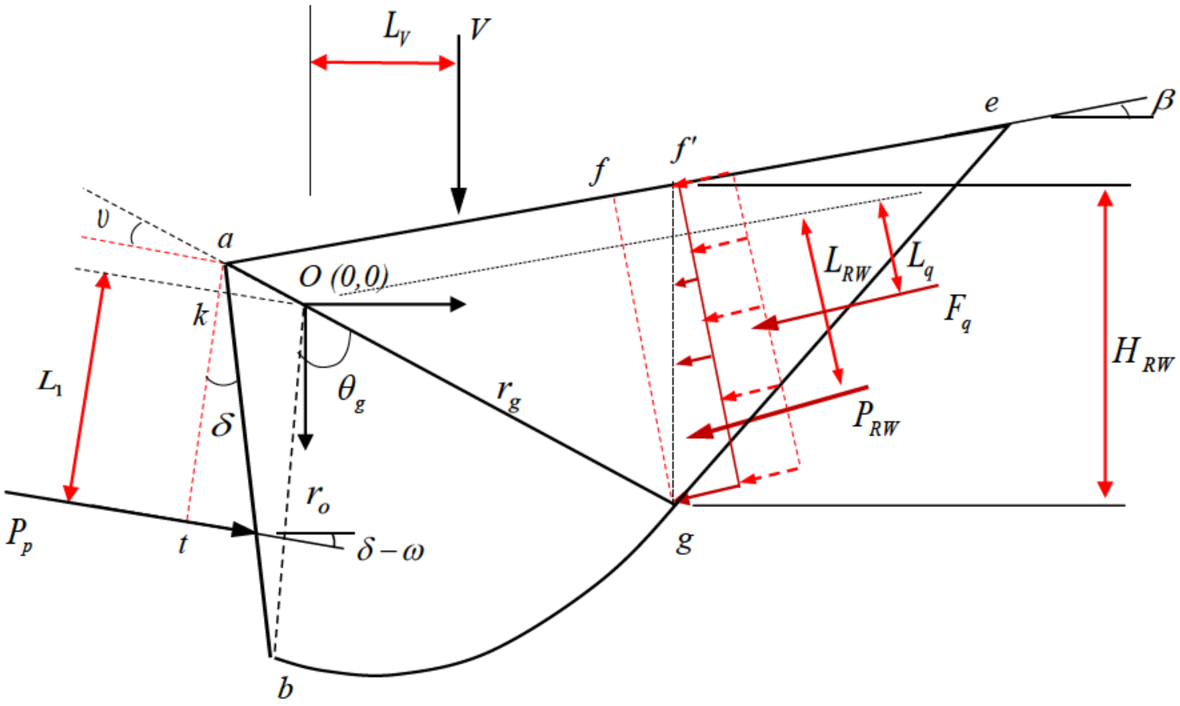

Figure 3.8 Forces and moment arms about Pole O in Case-b

$$M^{a}_{oba}=\frac{1}{6}(x_a+x_b)(x_a y_b-x_b y_a) \tag{3.63}$$

$$M^{a}_{agf'}=\frac{1}{6}|af'||fg|\gamma\left(x_a+x_g+x_{f'}\right),\ \text{where}\ x_{f'}=x_g \tag{3.64}$$

The area moment of *obg* is calculated in the same way for Case-a, equation (3.27). Accordingly, the moment of the wedge $abgf'$ is given by,

$$M_{abgf'}=\left(M^{a}_{obg}+M^{a}_{oba}+M^{a}_{agf'}\right)\gamma \tag{3.65}$$

Now, by taking moment equilibrium about the Pole O for the forces shown in Figure 3.8,

$$L_1=|at|-|ak| \tag{3.66}$$

$$|at|=\frac{2}{3}|ab|\cos\delta \tag{3.67}$$

$$|ak|=|\xi|\sin\upsilon \tag{3.68}$$

where $\upsilon=\eta-\delta+\omega$

Calculation of the passive zone forces P_{RW} and F_q are shown below,

$$H_{RW} = \frac{|fg|}{\cos\beta} \tag{3.69}$$

$$P_{RW} = \frac{1}{2}\gamma H_{RW}^2 K_p \cos\beta \tag{3.70}$$

$$F_q = q\cos\beta K_p H_{RW} \tag{3.71}$$

$$L_{RW} = \frac{2}{3}|fg| - |\xi|\sin\alpha_1 \tag{3.72}$$

$$af = |ag|\cos\alpha_1 \tag{3.73}$$

$V = q|af'|$, where $af' = af + fg\tan\beta$ (3.74)

$$L_V = \left| \left(\frac{\left(|x_a| + |x_{f'}|\right)}{2} \right) - |x_a| \right| \tag{3.75}$$

$$M_{qh} = F_q L_q \tag{3.76}$$

$$L_q = \frac{1}{2}|fg| - |\xi|\sin\alpha_1 \tag{3.77}$$

Finally,

$$P_p = \frac{1}{L_1}\left(P_{RW}L_{RW} + VL_V + M_{qh} + M_{abgf'}\right) \tag{3.78}$$

Passive force = min P_p

3.4 Validation of the Solution

The validation of the above solution was conducted over two stages. The first stage involves validation against experimental and numerical data from the literature (as discussed in section 3.4.1). The second stage involves the verification of the log-spiral solution against results obtained from laboratory tests conducted on a laboratory scaled physical model. The latter will be discussed in detail in Chapter 4.

3.4.1 Validation Using Data from the Literature

Experimental Data

In order to validate the log-spiral solution proposed in this chapter against real data measured at a larger scale, reference was made to experimental results reported by Fang et al. (2002). They conducted a series of tests on dry Ottawa sand to measure the passive pressure acting on a rigid steel wall under a monotonic translational movement. The properties of the backfill used by Fang et al. (2002) are summarized in Table 3.1.

Table 3.1 Properties of sand used by Fang et al. (2002)

Soil Sample	Unit weight kN/m^3	Soil friction angle °		Interface friction δ°
		Peak	Critical	
Loose	15.7	33	31.5	9.8
Medium dense	16.3	38	31.5	12.6
Dense	16.8	42	31.5	14

The proposed log-spiral solution was used to calculate the passive earth pressure based on the critical state properties. The results show that the proposed method successfully replicated the measured data within an error of less than 10% as shown in Table 3.2.

Table 3.2 Comparison between the calculated results and the data reported by Fang et al. (2002)

Soil Sample	Measured force (N)	Calculated force (N) (log-spiral, this chapter)	Error %
Loose	6300	6826	± 8.3
Medium dense	10125	11044	± 9.07
Dense	15600	15011	± 3.7

Numerical Data

The log-spiral solution has also been used to produce results for the coefficient of passive earth pressure K_p and compared with those reported by Shiau et al. (2008) and other researchers. They reported results of K_p calculated using different methods. The comparison is shown in Table 3.3. It is apparent that the results of the present log-spiral solution fits well in the admissible solution field of Shiau et al. (2008). They also closely agree with the data reported by Caquot and Kerisel (1948).

Table 3.3 Comparison between the values of K_p calculated using the log-spiral solution and those calculated using different methods (Shiau et al., 2008)

$\phi = 40^\circ, \beta = 0, \omega = 0$							
δ/ϕ	Coulomb theory	Caquot and Kerisel (1984)	Log spiral method (Ducan et al., 2001)	Sokolovski (1960)	Upper bound Chen, (1975)	Lower bound - Upper bound Shiau et al. (2008)	**Log-spiral solution (this chapter)**
0	4.60	4.59	4.60	4.60	4.60	4.60-4.61	**4.61**
$\frac{1}{3}$	8.15	8.13	8.17	_	7.73	6.87-7.79	**7.58**
$\frac{1}{2}$	11.77	10.36	10.50	9.69	10.08	8.79-10.03	**9.74**
$\frac{2}{3}$	18.72	13.10	13.08	_	13.09	11.30-12.87	**12.24**
1	92.72	17.50	17.50	18.20	20.91	18.64-20.10	**18.86**

It is worth noting that the log-spiral solution will be used to replicate the experimental results discussed later in Chapter 6. The solution will be used to obtain the distribution of lateral earth pressure on abutment wall under a monotonic passive movement.

3.5 Parametric Study Using the Log-Spiral Solution

This section discusses the use of the log-spiral solution, developed in this chapter, to investigate the individual effects of various parameters on the passive earth pressure. These parameters involve the soil-wall interface friction, the backfill slope (β) and the angle of wall inclination (ω).

3.5.1 Effects of the Soil-Wall Interface Friction

According to Terzaghi et al. (1996), the angle of friction between the backfill and the retaining structure influences the curvature of the log-spiral arc and consequently the passive soil pressure acting on the wall. Hence, it is worthwhile to investigate the interaction behaviour at different interface friction angles. The log-spiral solution developed in this chapter is used to calculate the earth pressure at different interface friction angles (δ). At this stage, the magnitudes of angles β,ω and the surcharge q are equated to zero.

Figure 3.9 shows the relationship between the passive earth pressure and the retained height of the soil at different values of the interface friction angle δ as well as soil friction angle ϕ. It is apparent that the passive force acting on the wall relates proportionally to the soil-wall interface friction angle at a given soil friction angle ϕ.

According to Figure 3.9 ($\phi = 25^{\circ}$), when $\delta = \phi$ the passive soil force is 77% higher than that obtained with $\delta = 0$ for a 4 m retained soil height. This justifies the low passive forces calculated using Rankine method, which assumes a smooth interface between the backfill and the wall. However, the influence of the interface friction becomes more significant at a higher friction angle ϕ. According to Figure 3.9 ($\phi = 30^{\circ}$) and ($\phi = 35^{\circ}$), the passive earth pressure at $\delta = \phi$ are 119% and 185% greater than those calculated at $\delta = 0$, respectively.

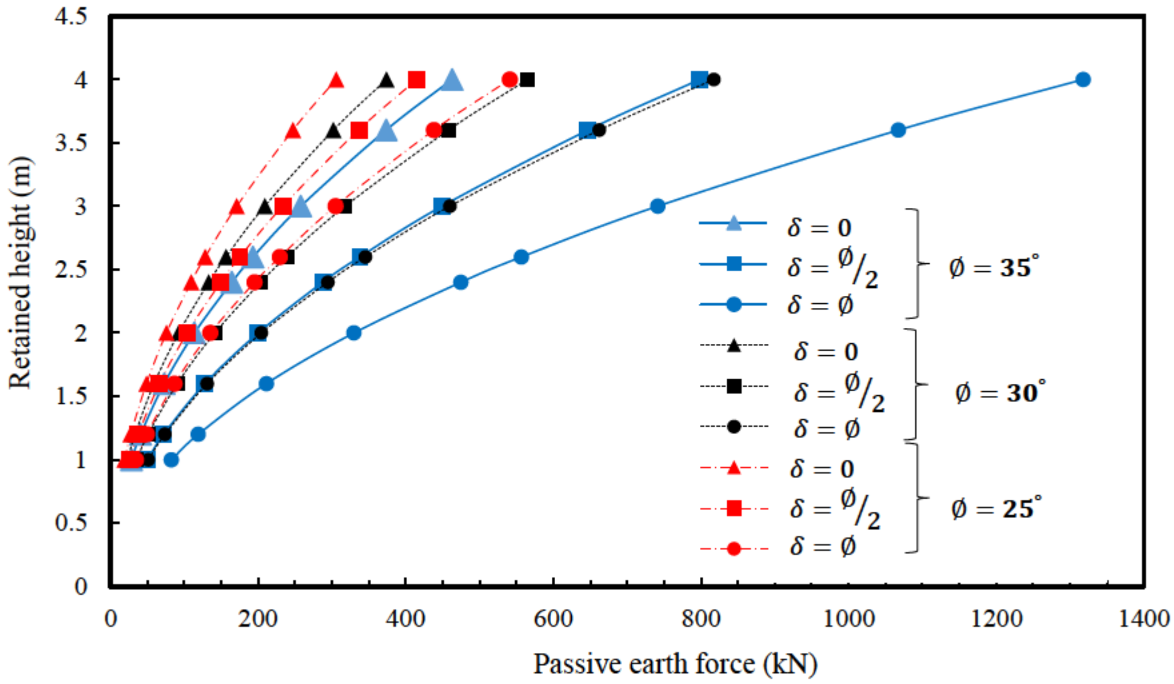

Figure 3.9 The effect of the interface friction on the passive earth pressure

Figure 3.10 illustrates how the log-spiral solution addresses the effect of the ratio δ/ϕ on the passive earth force P_p. At a given magnitude of soil friction angle ϕ, the curvature of the log-spiral arc is governed by the interface friction angle δ. While the angles α_1 and α_2 are independent of δ, the passive Rankine zone enlarges when the ratio δ/ϕ increases. This, in turn, results in a larger passive soil wedge, $abg'e'$, and consequently a greater passive earth force. The increase in the size of the spiral arc emerges from a reduction in the radial distance ξ. Hence the Pole moves closer to the soil mass so that r_o decreases while the area *abg* increases.

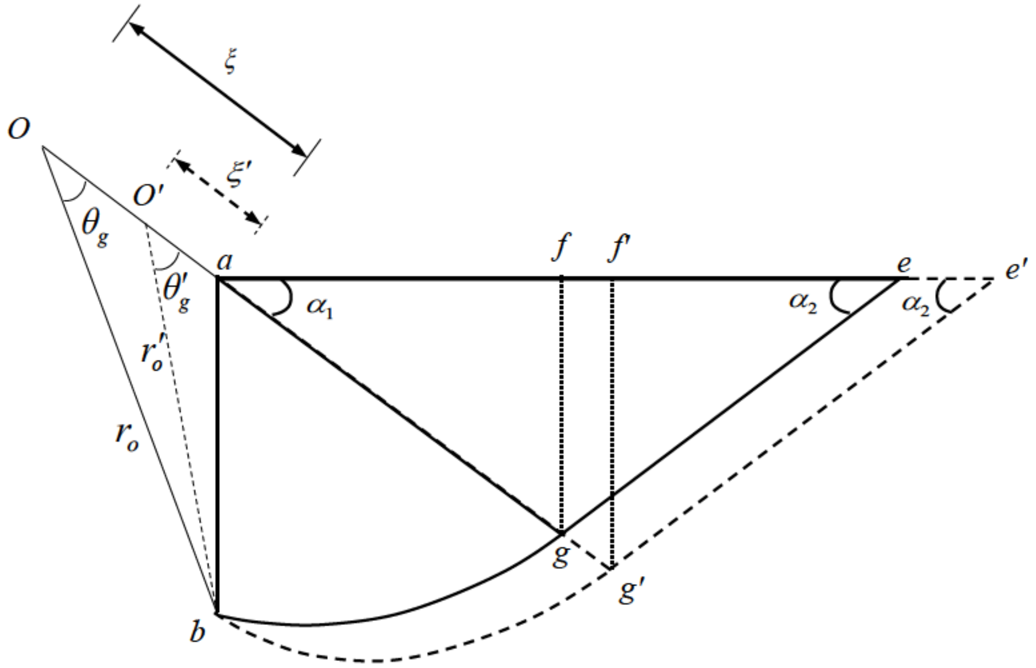

Figure 3.10 The effect of the interface friction on the size of the passive wedge

This fact leads to another conclusion about the interrelation between the ratio δ/ϕ and the radial distance ξ. This relation was examined by plotting the $P_p - \xi$ diagram over a range of δ/ϕ ratios. According to Figure 3.11, in regular conditions (when the ratio δ/ϕ is between zero and 1), the Pole is generally located outside the soil mass. However, the location of the Pole moves toward the soil mass as the ratio δ/ϕ increases. At some extreme cases where $\delta/\phi = 2$, the Pole becomes clearly inside the soil mass. This phenomenon is associated with a dramatic increase in the magnitude of the passive soil force P_p.

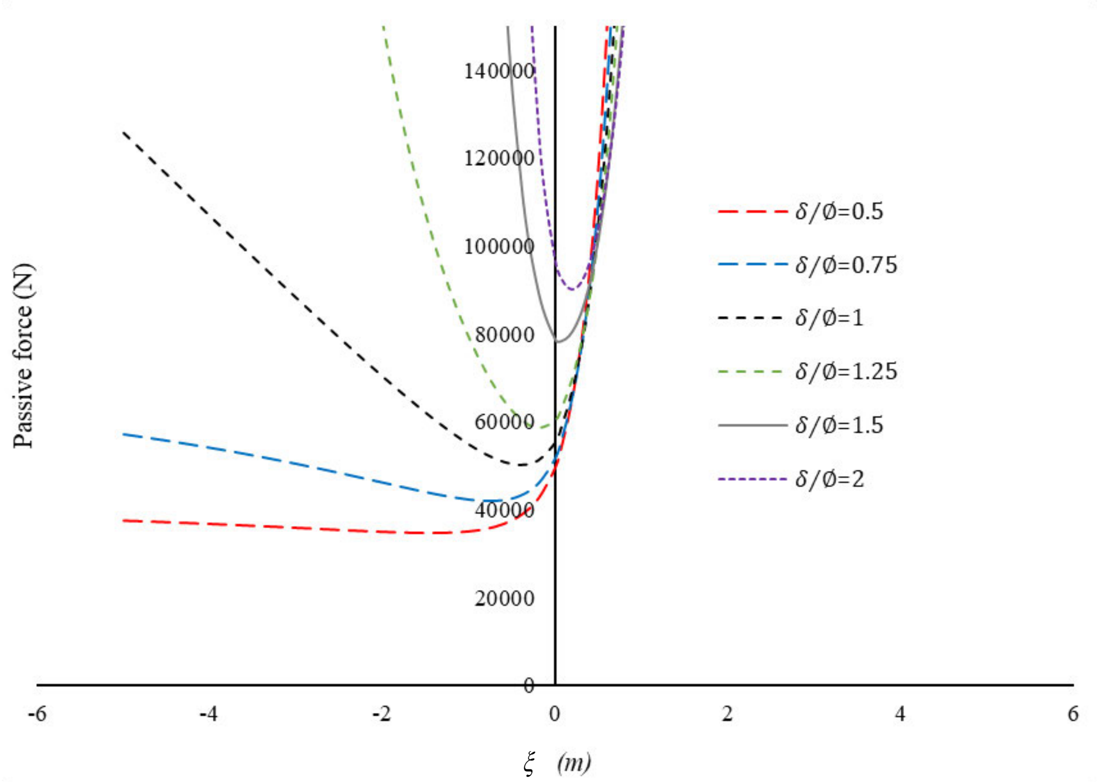

Figure 3.11 The relationship between the interface friction and the location of Spiral Pole

3.5.2 Effects of Backfill Slope Angle

The influence of the backfill slope β on the response of the retained soil to a passive wall movement has been reported by a number of studies. Shiau et al. (2008) investigated the effects of the backfill slope on the passive earth pressure coefficient using a finite element analysis. Fang et al. (1997) conducted experiments on a sloped backfill to study the effect of the backfill slope on the coefficients of lateral earth pressure K_p and K_a. Those researchers concluded that, both the magnitude of the horizontal passive earth pressure coefficient, K_p, and the wall movement needed for the backfill to reach a passive state increase when the backfill inclination angle β increases.

The data reported by Fang et al. (1997), for a normalised horizontal wall displacement (*S/H*) equals to 0.3, and Shiau et al. (2008) were used to quantitatively validate the log-spiral solution at different backfill slope angles. Figure 3.12 shows that the results of the log-spiral solution fits perfectly between the upper and lower bound results reported by Shiau et al. (2008) but underestimate the experimental data of Fang et al. (1997). It is worth noting that the values computed using the log-spiral solution are based on a plane strain case. On the other hand, physical models, especially those with relatively small dimensions, would involve frictional forces, between the sides of the chamber and the soil, as well as boundary reactions effects which may collectively result in a slight overestimation of the measured data. This could justify the fact that the values computed using the log-spiral solution slightly underestimate the measured data reported by Fang et al. (1997).

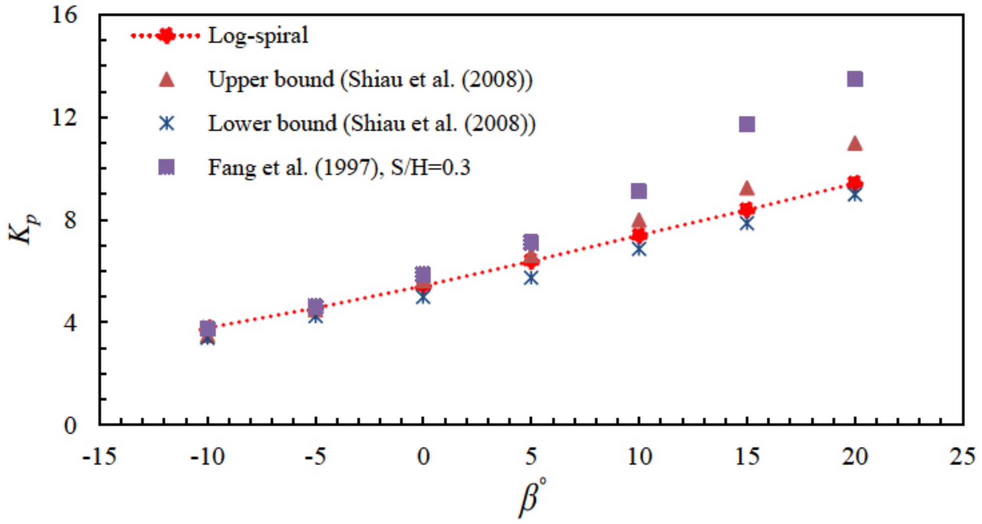

Figure 3.12 Comparison with experimental results (after Fang et al. (1997) and Shiau et al. (2008))

The results obtained from the log-spiral solution have also shown qualitative agreement with the findings of Fang et al. (1997) and Shiau et al. (2008) in relation to the effects of the backfill slope angle β. Figure 3.13 shows that the magnitude of the passive earth force P_p increases with the backfill slope angle β at a given δ/ϕ ratio. The effect of β is greater for higher internal friction angle.

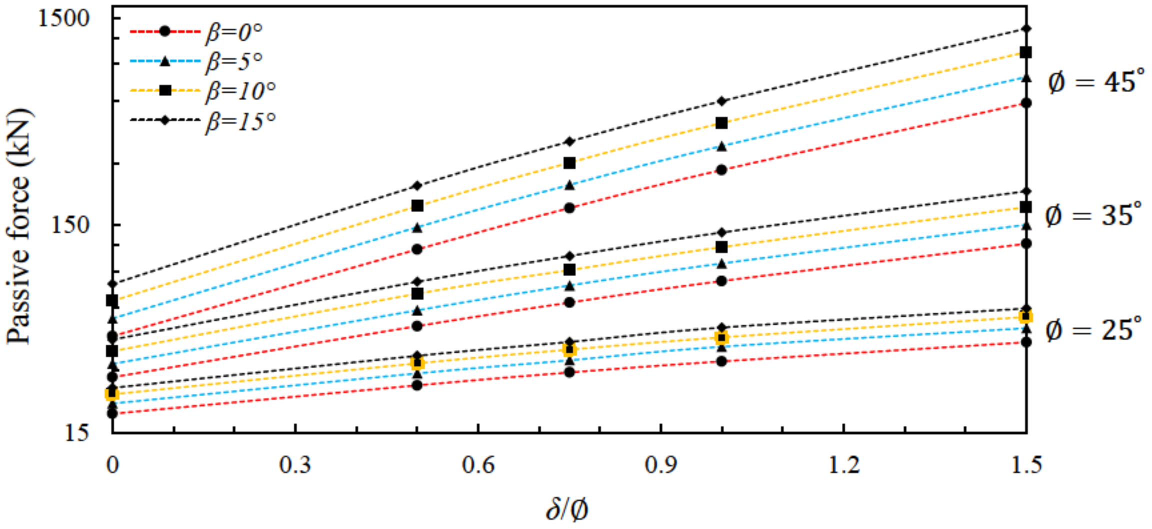

Figure 3.13 The effect of the backfill slope on the passive earth pressure

3.5.3 Effects of Wall Inclination

Shiau et al. (2008) reported a relationship between the internal friction angle and the passive earth pressure coefficient, K_p, at a different wall angles, ω. The log-spiral solution was compared with the corresponding results reported by Shiau et al. (2008). Figure 3.14 shows that the results of the proposed log-spiral solution agree well with those reported by Shiau et al. (2008) with an error margin not exceeding 10%.

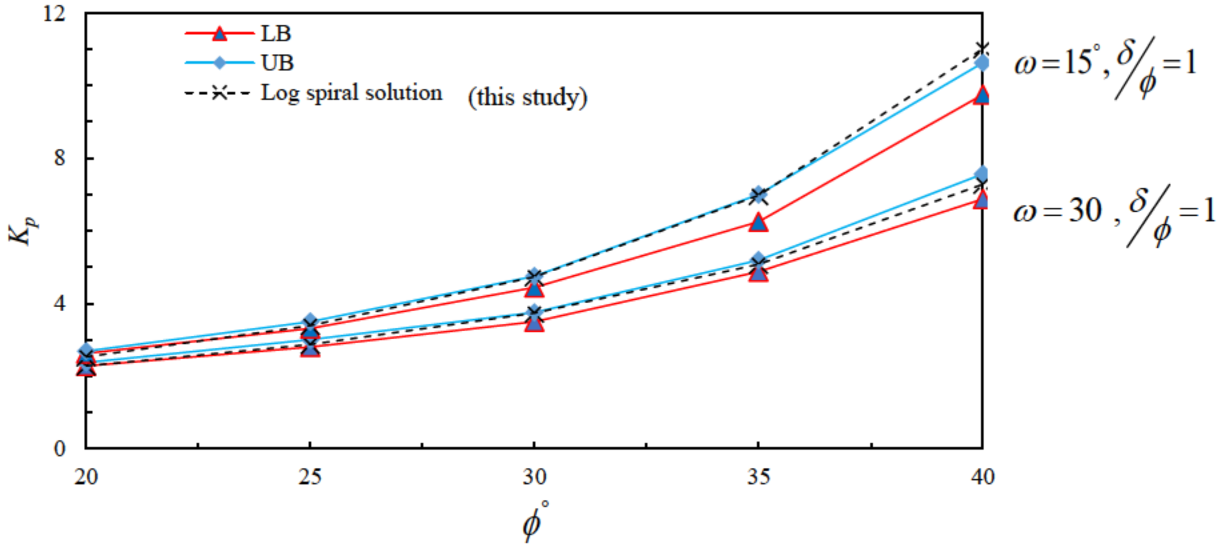

Figure 3.14 Validation of the log-spiral solution against results from Shiau et al. (2008)

The effects of wall inclination then were investigated at different interface friction angles (δ) as well as backfill slopes. It has been concluded that the inclination angle, ω, contributes to reduce the passive earth force P_p as well as the passive earth pressure coefficient, K_p. Such influence, however, is insignificant when the wall is frictionless ($\delta = 0$). The effects of the angle ω becomes prominent when the ratio δ/ϕ increases. Figure 3.15 shows that when $\delta/\phi = 1$, the passive earth force decreases by approximately 35% as the angle ω increases from zero to 20°. This behaviour was observed to be independent of the backfill slope angle β.

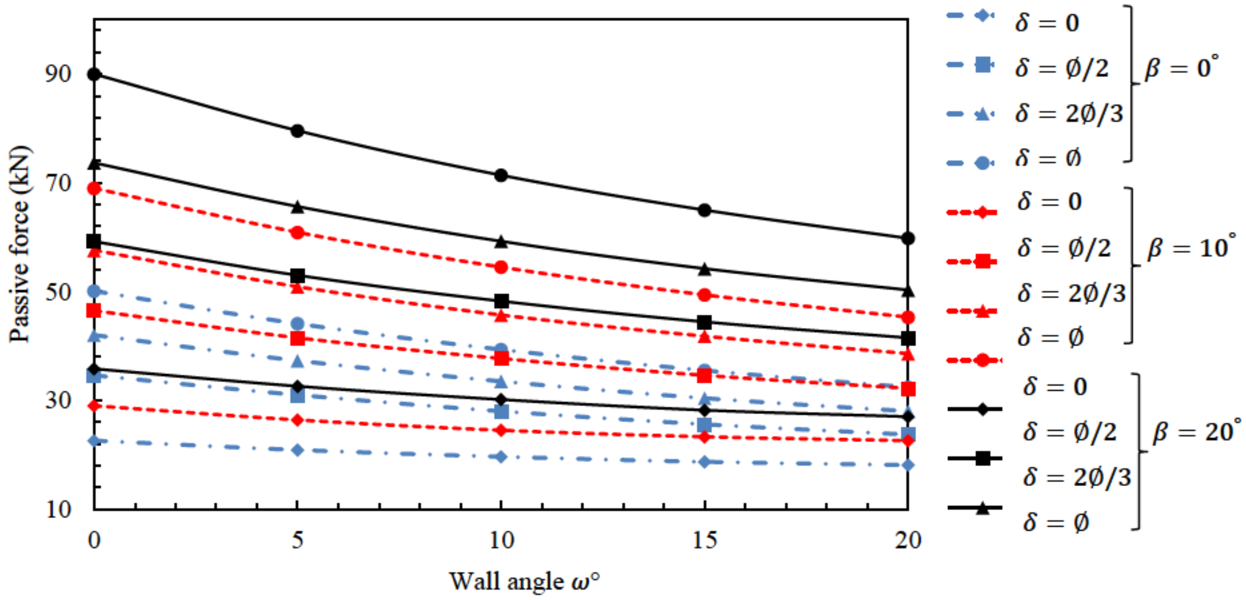

Figure 3.15 The effect of the wall inclination angle on the passive earth pressure

3.6 Calculation of Passive Pressure Coefficient K_p

The solution developed in this chapter is applied to calculate the coefficient of passive earth pressure K_p. Tables 3.4 – 3.7 provide ready-made data sheets to identify the magnitude of K_p with respect to different wall, slope and soil conditions. It is worthwhile noting that the magnitudes of K_p in these tables apply to a rigid wall retaining dry cohesionless soil. Effects of factors such as the moisture conditions are not considered.

Table 3.4 Coefficient of passive pressure K_p ($\phi = 40^\circ$)

$\frac{\delta}{\phi}$	$\phi = 40^\circ$															
	$\omega = 0^\circ$				$\omega = 5^\circ$				$\omega = 10^\circ$				$\omega = 15^\circ$			
	$\beta = 0^\circ$	$\beta = 5^\circ$	$\beta = 10^\circ$	$\beta = 15^\circ$	$\beta = 0^\circ$	$\beta = 5^\circ$	$\beta = 10^\circ$	$\beta = 15^\circ$	$\beta = 0^\circ$	$\beta = 5^\circ$	$\beta = 10^\circ$	$\beta = 15^\circ$	$\beta = 0^\circ$	$\beta = 5^\circ$	$\beta = 10^\circ$	$\beta = 15^\circ$
0	4.61	5.47	6.45	7.55	4.1	4.8	5.61	6.54	3.7	4.32	5	5.78	3.46	4.03	4.65	5.31
$\frac{1}{3}$	7.58	9.27	11.2	13.5	6.44	7.84	9.5	11.5	5.56	6.76	8.17	9.72	4.86	5.92	7.13	8.5
$\frac{1}{2}$	9.74	12.2	14.6	17.4	8.14	10.0	12.3	14.7	6.97	8.56	10.5	12.5	6.03	7.42	9.05	10.9
$\frac{2}{3}$	12.2	15.2	18.6	22.6	10.3	12.7	15.5	18.8	8.67	10.8	13.2	16	7.46	9.3	11.5	13.8
1	18.8	23.7	29.7	35.9	15.6	19.5	24.2	29.6	13	16.3	20.3	25.8	11	13.9	17.2	21

Table 3.5 Coefficient of passive pressure K_p ($\phi = 35^\circ$)

$\frac{\delta}{\phi}$	$\phi = 35^\circ$															
	$\omega = 0^\circ$				$\omega = 5^\circ$				$\omega = 10^\circ$				$\omega = 15^\circ$			
	$\beta = 0^\circ$	$\beta = 5^\circ$	$\beta = 10^\circ$	$\beta = 15^\circ$	$\beta = 0^\circ$	$\beta = 5^\circ$	$\beta = 10^\circ$	$\beta = 15^\circ$	$\beta = 0^\circ$	$\beta = 5^\circ$	$\beta = 10^\circ$	$\beta = 15^\circ$	$\beta = 0^\circ$	$\beta = 5^\circ$	$\beta = 10^\circ$	$\beta = 15^\circ$
0	3.7	4.29	4.95	5.63	3.34	3.86	4.42	5.02	3.1	3.56	4.06	4.58	2.9	3.36	3.83	4.3
$\frac{1}{3}$	5.42	6.44	7.54	8.7	4.75	5.64	6.6	7.64	4.21	5	5.86	6.78	3.79	4.5	5.29	6.12
$\frac{1}{2}$	6.54	7.85	9.36	10.9	5.67	6.78	8.01	9.37	5	6	7.06	8.2	4.46	5.34	6.31	7.36
$\frac{2}{3}$	7.8	9.36	11.1	13	6.76	8.12	9.62	11.2	5.92	7.16	8.48	9.9	5.22	6.3	7.52	8.85
1	10.8	13.1	15.7	18.5	9.2	11.2	13.4	15.8	8.26	9.69	11.6	13.7	7.13	8.75	10.6	12.1

Table 3.6 Coefficient of passive pressure K_p ($\phi = 30^\circ$)

$\frac{\delta}{\phi}$	$\phi = 30^\circ$															
	$\omega = 0^\circ$				$\omega = 5^\circ$				$\omega = 10^\circ$				$\omega = 15^\circ$			
	$\beta = 0^\circ$	$\beta = 5^\circ$	$\beta = 10^\circ$	$\beta = 15^\circ$	$\beta = 0^\circ$	$\beta = 5^\circ$	$\beta = 10^\circ$	$\beta = 15^\circ$	$\beta = 0^\circ$	$\beta = 5^\circ$	$\beta = 10^\circ$	$\beta = 15^\circ$	$\beta = 0^\circ$	$\beta = 5^\circ$	$\beta = 10^\circ$	$\beta = 15^\circ$
0	3	3.43	3.86	4.29	2.76	3.15	3.54	3.92	2.59	2.96	3.33	3.68	2.47	2.83	3.19	3.53
$1/3$	4.02	4.66	5.33	5.97	3.61	4.2	4.79	5.37	3.28	3.81	4.37	4.9	3.02	3.52	4.04	4.54
$1/2$	4.62	5.4	6.2	7	4.13	4.81	5.53	6.23	3.73	4.36	5.02	5.66	3.41	4	4.61	5.21
$2/3$	5.27	6.17	7.11	8.03	4.71	5.52	6.36	7.18	4.22	4.69	5.75	6.52	3.83	4.51	5.23	5.93
1	6.68	7.9	9.2	10.4	5.88	6.97	8.1	9.22	5.34	6.35	7.41	8.47	4.78	5.7	6.65	7.6

Table 3.7 Coefficient of passive pressure K_p ($\phi = 25^\circ$)

$\frac{\delta}{\phi}$	$\phi = 25^\circ$															
	$\omega = 0^\circ$				$\omega = 5^\circ$				$\omega = 10^\circ$				$\omega = 15^\circ$			
	$\beta = 0^\circ$	$\beta = 5^\circ$	$\beta = 10^\circ$	$\beta = 15^\circ$	$\beta = 0^\circ$	$\beta = 5^\circ$	$\beta = 10^\circ$	$\beta = 15^\circ$	$\beta = 0^\circ$	$\beta = 5^\circ$	$\beta = 10^\circ$	$\beta = 15^\circ$	$\beta = 0^\circ$	$\beta = 5^\circ$	$\beta = 10^\circ$	$\beta = 15^\circ$
0	2.47	2.77	3.06	3.3	2.31	2.6	2.87	3.11	2.19	2.48	2.75	3	2.12	2.41	2.68	2.91
$1/3$	3.06	3.48	3.88	4.2	2.81	3.2	3.57	3.88	2.61	3	3.34	3.63	2.46	2.81	3.15	3.44
$1/2$	3.4	3.86	4.32	4.7	3.1	3.55	3.97	4.33	2.87	3.29	3.7	4.02	2.68	3.08	3.47	3.8
$2/3$	3.73	4.28	4.81	5.24	3.41	3.91	4.4	4.8	3.13	3.6	4.05	4.43	2.92	3.37	3.8	4.16
1	4.52	5.21	5.88	6.43	4.05	4.68	5.29	5.79	3.7	4.27	4.83	5.3	3.4	3.95	4.48	4.91

3.7 Conclusions

This chapter presented a comprehensive and rigorous generalised solution formulated based on the Terzaghi method to estimate the lateral passive pressure of the soil exerted on a retaining structure. Unlike Terzaghi method, which assumes the Pole of the log spiral falls inside the soil mass, the developed method provides solutions for any potential location of the pole, inside or outside the soil mass. The developed method can be used to calculate the passive force, and hence the passive pressure coefficient K_p , under different values of soil friction angle, soil-wall interface friction, backfill slope and wall inclination angles. The developed equations were validated against measured and numerical data reported in the literature. Based on the results, following conclusions can be reached,

- The log-spiral solution developed herein is an accurate method to calculate the lateral earth pressure. The results calculated using the proposed method agree with the measured data better than those calculated using Rankine or Coulomb methods.
- The passive earth pressure depends heavily on the internal friction angle of the soil and the interface friction between the backfill and the retaining wall.
- The location of the Pole of the log-spiral arc is often located outside the soil mass. However, in cases where the interface friction is too high, the Pole may be located inside the soil mass.
- The log-spiral solution can be easily programmed using MATLAB or even using an EXCEL spreadsheet, which provides an efficient and easy tool for engineers to estimate the passive earth pressure accurately.

Chapter 4

Soil-Structure Interaction in Integral Bridges

4.1 Introduction

This chapter discusses the results of series of experimental tests conducted using a laboratory physical model. The primary objectives of these laboratory tests are, first, to validate of the log-spiral solution developed in Chapter 3 and, second, to investigate the interaction behaviour between a granular fill and a small wall replicating an abutment in an integral abutment bridge. The tests also provide an insight into the effects of utilising an EPS geofoam inclusion on the soil-wall interaction behaviour.

The laboratory test chamber (see Figure 4.1) includes a 700 mm x 250 mm x 300 mm tank to accommodate the soil and a 250 mm x 300 mm x 13 mm steel wall to retain the soil. The front side of the tank is made of a 50 mm thick clear acrylic panel to allow for visual observation. The steel wall is supported by two metal bars, to maintain pure translational movement, and being moved using a threaded movement bar. A load cell is placed between the movement bar and the wall to measure the total applied force. The movement is monitored during the tests using a linear variable differential transducer (LVDT). The lateral soil pressure was measured using a pressure cell, located at 80 mm from the bottom of the wall, and readings were digitally recorded to a PC using a data logging software. The chamber on one side of the wall was backfilled with dry siliceous sand sourced from a local vendor in Sydney, Australia. Sieve analysis showed that the sand is quite uniform with a particle size ranging between 150-300 μm. The unit weight of the sand used in each test was calculated by measuring the weight of the sand and the volume occupied.

Direct shear tests were conducted to determine the internal friction angle of the sand as well as the sand-wall and sand-acrylic interface friction angles. Table 4.1 summarises the properties of the sand used in the tests.

Table 4.1. Properties of the soil used in the tests

Unit weight (loose) (kN/m^3)	15.3
Internal friction angle	35.5°
Sand-wall friction angle	18°
Sand-acrylic friction angle	15°

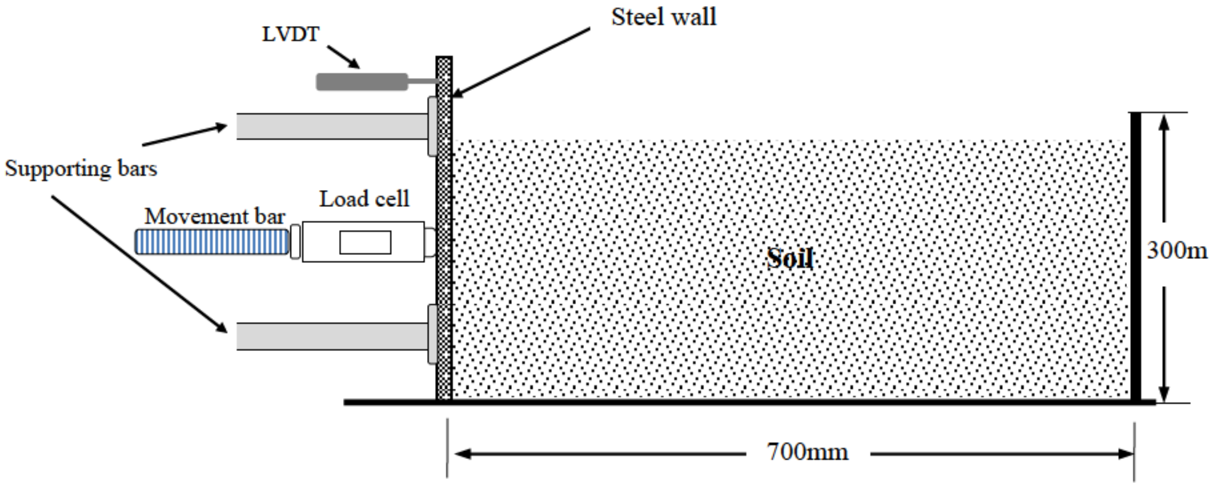

Figure 4.1 The test chamber of the laboratory physical model

4.2 Validation of the Log-Spiral Solution

This part of the experimental laboratory program aims to obtain real data about the passive earth pressure to validate the log-spiral solution. Therefore, attention was given to estimate the frictional forces between the wall and the sides/base of the tank as well as between the sand and the sides of the tank. Subsequently these forces were subtracted from the total measured force. Three tests were conducted with soil heights 200 mm, 240 mm and 280 mm. Displacement-controlled passive wall movement was applied by spinning the movement bar clockwise, which pushes the wall against the soil. The fine threads in the movement bar helped to achieve a slow and uniform displacement throughout the test. Figure 4.2 shows the passive force-displacement curves for three different experiments.

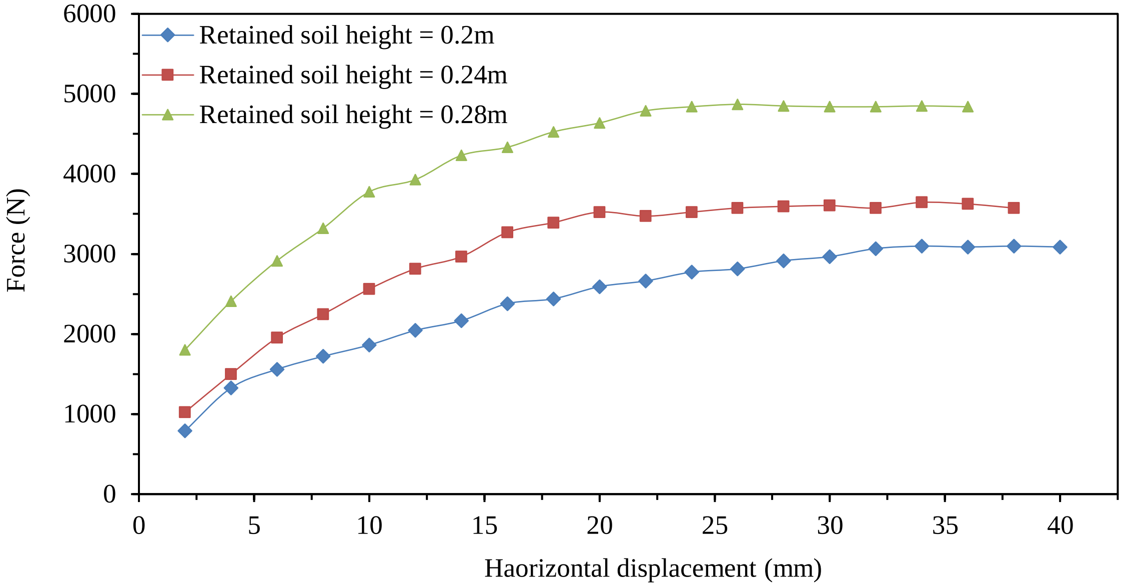

Figure 4.2 Passive force vs Horizontal displacement

The log-spiral solution, developed in Chapter 3, was formulated in a spreadsheet, and then used to calculate the passive earth pressures for the same conditions prescribed in the experiments. The passive force of each test is determined as the minimum force in the $P_p - \xi$ diagram. Figure 4.3 shows the $P_p - \xi$ plots for the three tests.

The positive values of the distance ξ in Figure 4.3 refer to the Pole of the log-spiral located inside the soil mass, while the negative values refer to the Pole located outside the soil mass. It is evident that the Pole in all three tests was located outside the soil mass but at different radial distances.

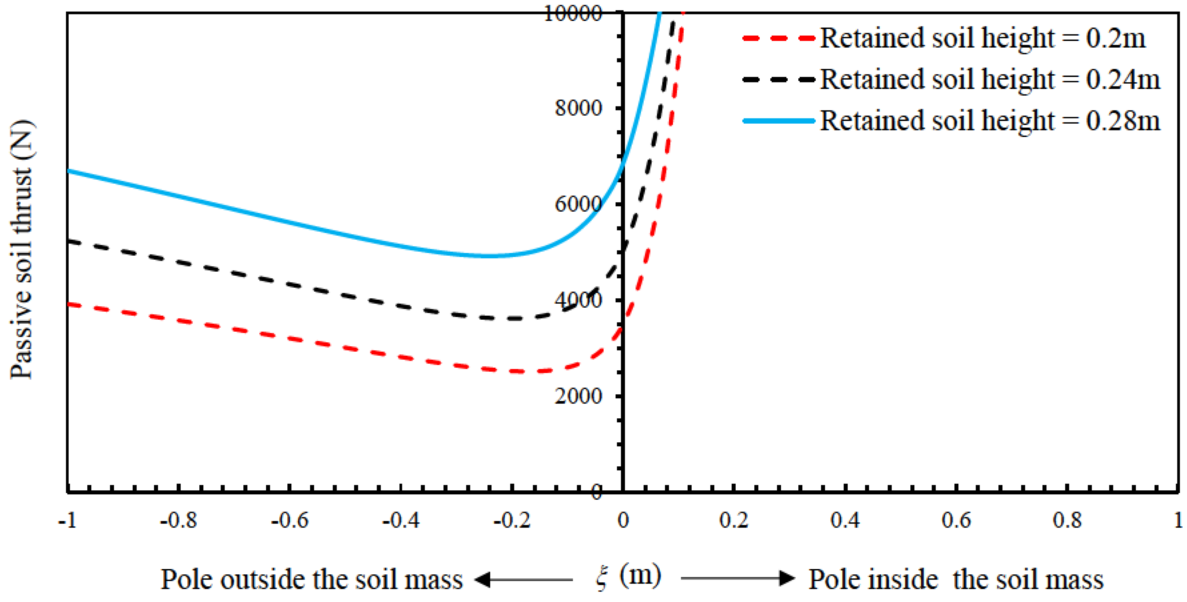

Figure 4.3 Passive force vs the radial distance (ξ)

The log-spiral results are then compared with the corresponding experimental results as well as those calculated using Coulomb and Rankine methods. In this case, the magnitudes of the angles β, ω and the surcharge q are equal to zero.

Table 4.2 illustrates a comparison between the measured and calculated data. It is apparent that the passive forces calculated using the developed log-spiral solution correlate well with the measured data. The passive forces determined using the Coulomb method overestimates the measured forces, while the Rankine method significantly underestimates the passive forces.

Table 4.2 Comparison between the calculated and measured passive forces

Test	Retained height (m)	Passive soil force (N)				
		Measured	Log-spiral solution (Chapter 3)		Coulomb	Rankine
			Force	ξ (m)		
1	0.2	3067.7	2511	-0.16	3286	1153.8
2	0.24	3593.6	3614.4	-0.2	4732.6	1661.4
3	0.28	4837	4919.1	-0.24	6441.6	2261.4

In an attempt to verify the assumption about the shape of the failure surface, which consists of a curved part (presumably spiral arc) and a tangent line, the actual failure surface was investigated using images captured during the experiments. The PIV technique developed by Stanier et al. (2015) was used to capture the actual failure surface developed in one of the experiments (retained height = 0.24 m). The failure surface can be clearly observed in Figures 4.4 and 4.5 (Sigdel et al. 2020).

Figure 4.4 shows the contour map for total displacements plotted across the soil mass. The failure surface can be seen along the dotted line, which consists of a curved part at the bottom and a tangent line rising towards the soil surface. Similarly, the shear band plot in Figure 4.5 clearly indicates the failure surface, which consists of a curved part and a straight line.

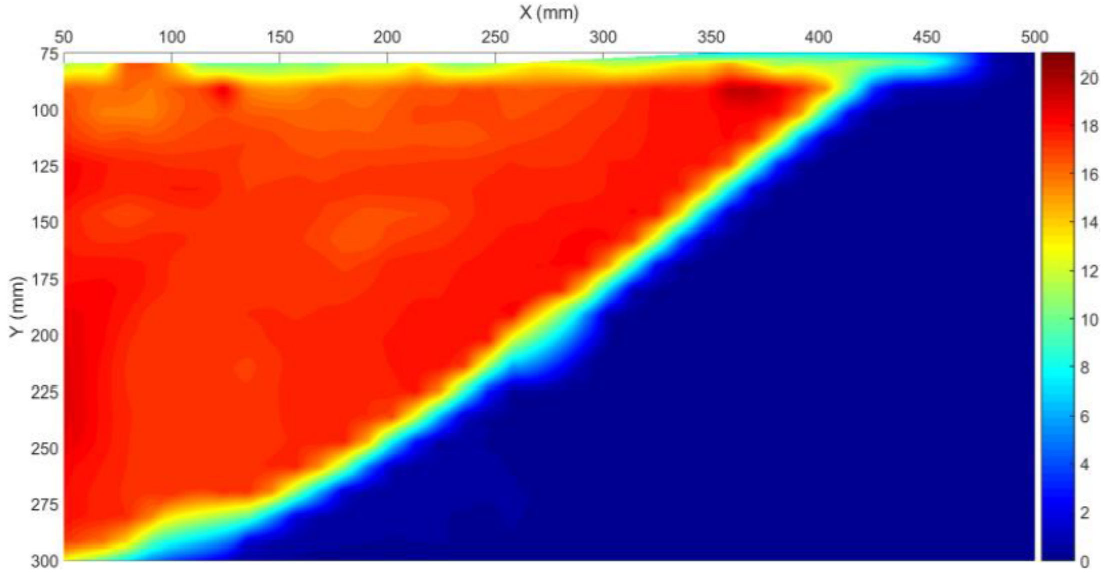

Figure 4.4 Total displacement contour map based on PIV analysis (Sigdel et al. 2020)

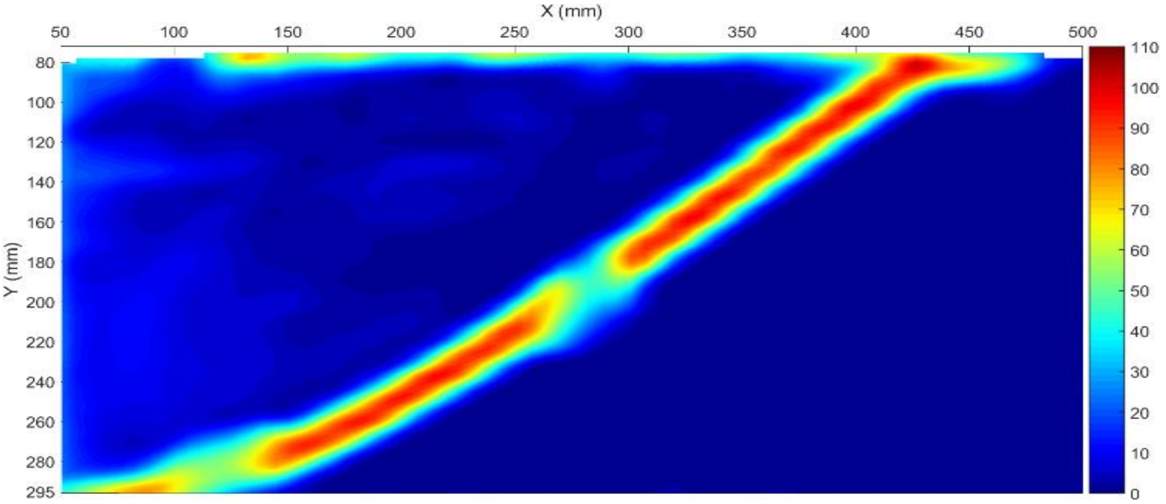

Figure 4.5 Shear band plot based on PIV analysis (Sigdel et al. 2020)

4.3 Investigation of the Soil-Structure Interaction in IABs

This section documents the investigation of the soil-structure interaction in IABs using data from the experimental laboratory tests as well as numerical modelling results. Initially, a series of tests are conducted, under cyclic wall movements, to replicate the abutment-soil interaction in IABs. Qualitative evaluations of the escalation in the lateral earth pressure and the soil settlement are conducted. The data obtained from these tests are then used to validate the finite element models developed using the ABAQUS/Standard (2017) software. Upon the validation a plane-strain model is then developed to simulate a prototype abutment wall of an IAB. A practical remedial measure, to alleviate the approach problems in IABs, utilising an EPS geofoam inclusion is investigated.

4.3.1 Temperature-Induced Abutment Movements

In IABs, the deck of the bridge often experiences transverse movements as a result of various causes including post-construction shrinkage, creep, long term settlement of bridge approaches in addition to the expansion and contraction due to the fluctuations in the ambient temperatures. However, the geotechnical issues experienced in the approaches of IABs, which are the principle scope of this study, are predominantly caused by the daily and seasonal temperature changes. Therefore, this chapter is aimed to investigate the soil-structure interaction behaviour of IABs due to the temperature-induced abutment movements.

In traditional bridges, the potential transverse movements are accommodated by the expansion joints. Hence, the deck of the bridge may expand and/or contract without transferring any effects into the bridge abutments or the adjoining backfill at the bridge approaches. However, unlike traditional bridges, IABs do not possess any joints to allow for unrestrained deck movements. Therefore, the movements, associated with the expansion and contraction of the bridge deck, are transferred to the abutments, which in turns, move against or away from the adjacent soil. This phenomenon leads to a complex interaction between the abutment wall and approach soil unique to this type of bridges.

The interaction between the approach soil and the abutments in IABs has a number of benefits. It augments the structural integrity of the bridge resulting in a better structural performance and seismic resistance (Arsoy et al., 1999). For instance, the soil-structural interaction in skewed semi-integral abutment bridges plays an important role in maintaining the stability of the bridge. However, the soil-structure interaction in IABs also involves some drawbacks which may undermine the perceived merits of this type of bridges.

4.3.1.1 Effects of the Cyclic Movement

Numerous research studies have shown that the abutments in IABs are continuously moving in a cyclic pattern following the ambient temperature fluctuations (Huntly and Valsangkar, 2016, Lafava et al., 2017). Each movement cycle involves two phases, passive phase (when the abutment moves toward the approach soil due to the expansion of bridge deck in hot weather) and active phase (when the abutment moves away from the soil following a contraction in the bridge deck in cold weather).

The repetitive abutment movements, against and away from the retained soil, result in two principle detrimental effects in the retained soil at the bridge approaches. These effects are: a long term build-up of the lateral earth pressure acting on the abutment and a significant settlement, and sometimes heaving, in the approach soil. In consequence to these effects,

- The IAB abutments will experience an escalated soil pressure that may well be underestimated based on established theories. The lateral earth pressure in this case is different, in both the magnitude and the distribution, from that developed in a static or monotonic passive movement,
- The developed settlement at the bridge approaches could lead to safety and riding quality issues for the bridge users. As such, these problems have somewhat curbed the benefits of IABs, resulting in regulatory authorities having to enforce significant restrictions on the overall design length of IABs.

To deal critically with these issues, researchers have extensively investigated thermally induced expansion/contraction effects on the abutment-soil interaction behaviour (as reviewed in Chapter 2). In a review of a significant number of relevant studies of various research methodologies, it is observed that the information reported in the literature regarding soil-structure interactions in IABs are dependent on the conditions under which they were obtained. Moreover, majority of these studies were mainly focused on analysing the problems rather than developing practical and effective remedial measures to alleviate these problems (Ng Et al., 1997; England et al.; 2000; Khodair and Hassiotis, 2013; Huntly and Valsangkar, 2016). Very limited studies were conducted to provide sufficient and specific insights into the methods available to overcome the approach settlement and lateral pressure issues in IABs. Hence, possible mitigation procedures for such problems are scant. The current design methodologies involve the following scenarios for soil-abutment interaction:

- No separation, where the backfill is pressed against and supported by the abutment wall
- Partial separation, where an intervening compressible inclusion layer separates the abutment wall and backfill. The backfill is not self-stable and is still being supported by the abutment wall with the compressible inclusion
- The backfill is self-stable with its own support mechanism (e.g. mechanically stabilised or reinforced earth) and separated from the abutment wall. The gap separating the self-stable backfill and abutment wall is typically filled with a compressible inclusion.

There are number of studies tended to adopt the reinforced soil wall design to accommodate the thermal expansion and contraction of the IABs (Fartaria, 2012; Tatsuoka et al., 2014; Zadehmohamad and Bazzaz, 2017). This method has been reported to be effective in attenuating the wall movement effects. However, there is a great uncertainty about the consequences of eliminating the interaction between the approach soil and the abutment on the bridge superstructure. Moreover, in certain cases such as where the approach backfill is underlain by a weak or compressible soil, this method may not be the most suitable solution (Keller, 2008).

4.3.2 The Compressible Inclusion

The use of a compressible inclusion as a pressure-relief layer between the soil and the abutment has been reported by a few research studies (Horvath, 2000; Hoppe, 2005; Hoppe et al., 2016, Duda and Siwowski, 2020). However, very little research was published in the literature about the potential application of the expanded polystyrene geofoam, EPS in IABs. The EPS geofoam possesses an excellent track record in geotechnical applications especially in attenuating earth pressures on retaining structures (Horvath, 2000; Bathurst and Zarnani, 2007; Dang and Xiao, 2010; Padade and Mandal, 2014; Hoppe et al., 2016). Penpeng et al.

(2016) studied the effects of EPS inclusion thickness on the static earth pressure on rigid retaining walls. They concluded that using EPS inclusion with a t/H ratio of 5-6% reduces the earth pressure by approximately 30%, where t represents the inclusion thickness and H is the retained height of the soil. Sherif et al. (2016) conducted an experimental study on walls retaining granular fill. They reported that using an EPS inclusion with a t/H equal to 50% reduces the static earth pressure by 55%.

Therefore, in this chapter, the potential use of EPS geofoam as an inclusion behind the abutment in IABs will be investigated.

4.4 Laboratory Model Tests

The results from a number of tests conducted on the laboratory physical model are presented in this section. In these test, the wall is moved in a cyclic displacement replicating the conditions of a short abutment translating against and away from the approach soil. Each test consisted of an application of 30 cycles of normalised wall translations Δ/H equal to ± 0.8%, where Δ represents the wall translational displacement and H is the retained height of the soil. The retained height of the soil was maintained at 240 mm in this group of tests. The displacements were applied at a speed of approximately 1 mm/min. It is worthwhile to mention that a cycle here is defined by the phases of movements in the following order: neutral–active–passive–neutral.

This part of the experimental program involved two types of tests: T1 when the soil was tested without EPS geofoam inclusion, and T2a and T2b when an EPS geofoam inclusion was placed at the soil-wall interface. The inclusions used in the tests involved, 20 kg/m^3 EPS blocks, (248 mm x 50 mm x 80 mm), (248 mm x 100 mm x 80 mm) and (248 mm x 150 mm x 80 mm), cut using a hot wire, and then placed between the wall and the backfill to render two different arrangements of inclusion buffer as illustrated in Figure 4.6.

The purpose of testing the soil with EPS geofoam inclusion was to evaluate the effectiveness of the EPS geofoam in alleviating the approach problems in IABs and to obtain experimental data necessary for validating the numerical models.

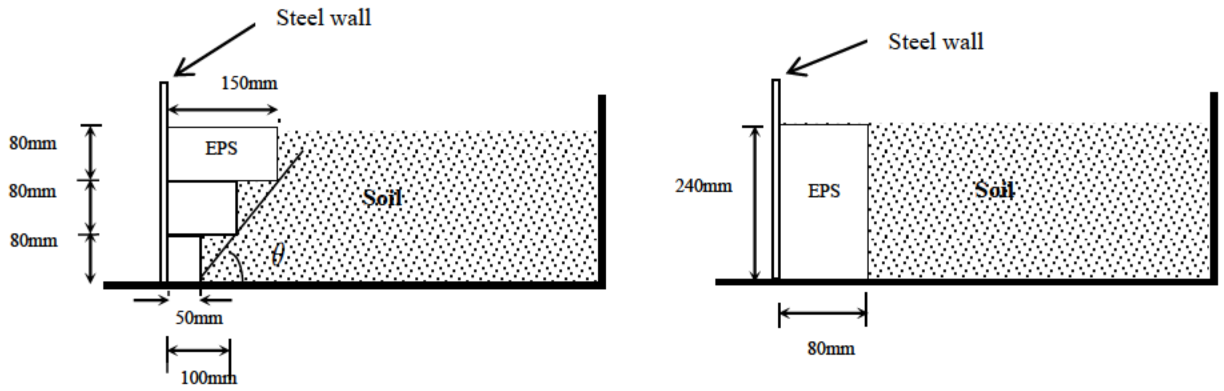

Figure 4.6 Schematic diagrams for the test setups with EPS inclusion

The properties of the EPS geofoam used in the tests are summarized in Table 4.3

Table 4.3 Properties of EPS Geofoam used in the small wall tests (Alqarawi, 2016)

Parameter	**Value**
Density	20 kg/m^3
Stiffness modulus (E)	4500 kPa
Yield stress (at 0.02% loading rate)	73 kPa

During these tests, wall movements due to temperature changes during summer and winter were simulated by moving the wall, in translation mode, from its neutral position away from (active movement) and toward (passive movement) the retained soil.

4.5 Discussion of Results

4.5.1 Test T1

The results from test T1 (Soil without EPS inclusion) showed that the magnitude of lateral earth pressure (σ_h) increased significantly during the wall movements. The maximum earth pressures increased rapidly when the wall moved towards the passive position while the minimum pressures were recorded during the active position. Figure 4.7 shows the lateral earth pressures (σ_h) when the wall is at the passive, neutral and active positions.

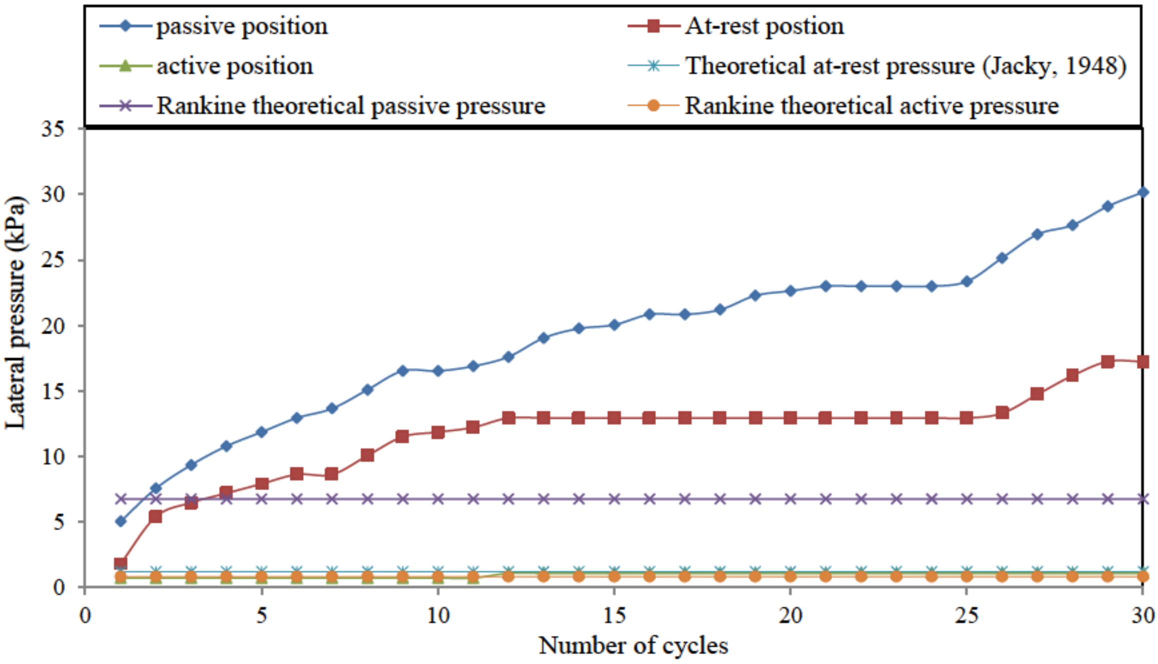

Figure 4.7 Measured lateral pressures at different wall positions -test T1

According to Figure 4.7, the lateral soil pressure at the passive position reached 30.2 kPa after 30 cycles which is 75% higher than that recorded at the neutral position. The magnitude of σ_h, in both passive and neutral positions, increased rapidly during the first ten cycles and notably exceeded Rankine passive pressure. After 30 cycles of wall movements, the pressure recorded at the passive and neutral positions were 4.5 and 2.5 times higher than Rankine passive pressure respectively.

The σ_h curve for the neutral position tended to asymptote and plateau after 10 cycles, while that of the passive position continued to increase but at a slower rate. The magnitude of σ_h at the active position remained almost constant at below 2 kPa and was insensitive to the number of loading cycles.

During test T1, the settlement at the interface between the soil and the wall was measured and recorded. The maximum soil settlement was located at the soil-wall interface. It was found that the maximum settlement increased significantly with the number of movement cycles. It reached 74.3 mm after 30 cycles, which exceeds 30% of the total retained height of the soil. The results also showed heaving at the soil surface between 150 mm and 200 mm from the wall. The backfill before and after the test are shown in Figures 4.8(a) and 4.8(b), respectively.

(a) (b)

Figure 4.8 The soil surface (a) before test T1 and (b) after the test T1

The settlement varied in a slightly nonlinear fashion with the number of cycles as presented in Figure 4.9 and the settlement rate decreased slightly as the number of cycles increased. However, settlement results did not asymptote or plateau during the test.

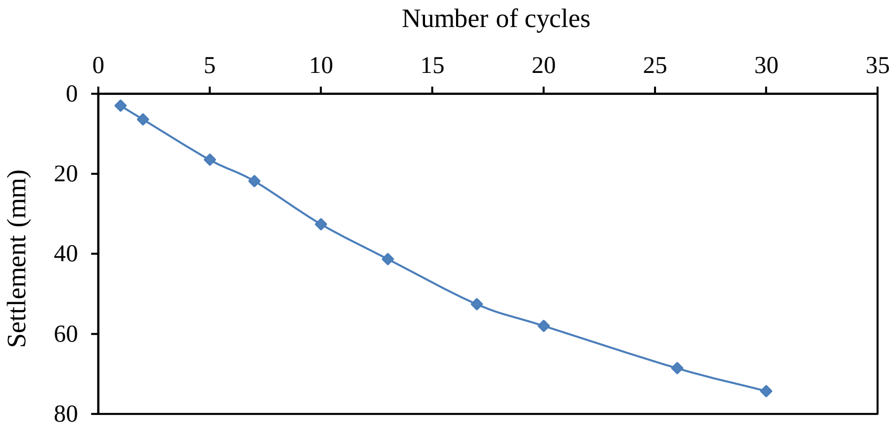

Figure 4.9 Maximum settlements measured in test T1

4.5.2 Tests T2a and T2b

Test T2a and T2b involved the same cyclic wall movements described earlier, but with an EPS geofoam inclusion positioned between the soil and the small steel wall. In the Test 2a, the inclusion was a uniform 80 mm thick, with 20 kg/m^3 density, EPS board as shown in Figure 4.10a ($t/H = 1/3$, where *t* is the thickness of the inclusion and *H* is the retained height of the soil). The wall movement would cause the elastic strain of the EPS material (0.1%) to be exceeded near the interface and accumulation of some plastic deformations during the test. This produced some effects of plastic deformations in the EPS on the soil settlements and lateral pressures.

At the end of the test, a small trough was noticeable in the soil surface adjacent to the EPS geofoam as shown in Figure 4.10b.

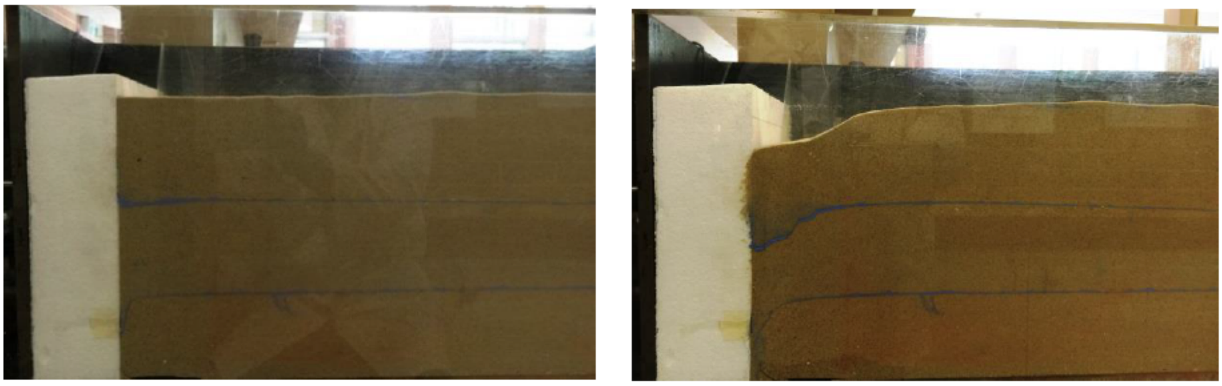

(a) (b)

Figure 4.10 Experimental setup of test T2a (a) before the test and (b) after the test

The lateral pressures measured during this test were considerably lower than those measured in test T1. A maximum lateral pressure of 9.7 kPa was recorded, which is approximately 32% of the corresponding value measured in test T1. Although the magnitude of pressure increased rapidly during the first few cycles, it showed a clear reduction in the rate of increment, and levelled off between 22 and 30 cycles. On the other hand, the measured values of lateral pressures σ_h at the neutral and active wall positions were very small and remained almost constant (about 2 kPa) throughout the test as shown in Figure 4.11.

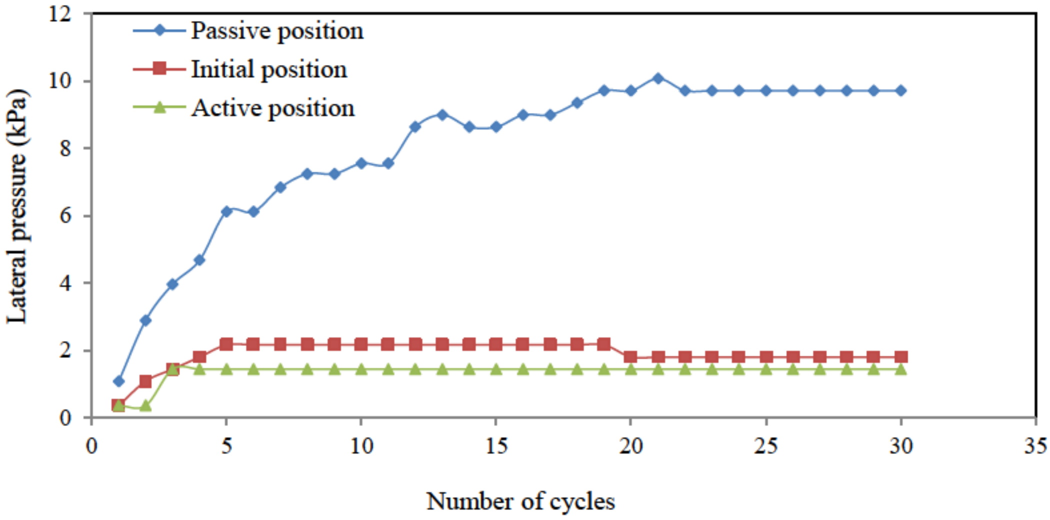

Figure 4.11 Lateral pressures results - Test T2a

The settlements measured in test T2a also show a significant reduction compared to those measured in test T1. According to Figure 4.12, the maximum settlement after 30 cycles was 31.3 mm, which is equivalent to 50% of the measured settlement in test T1.

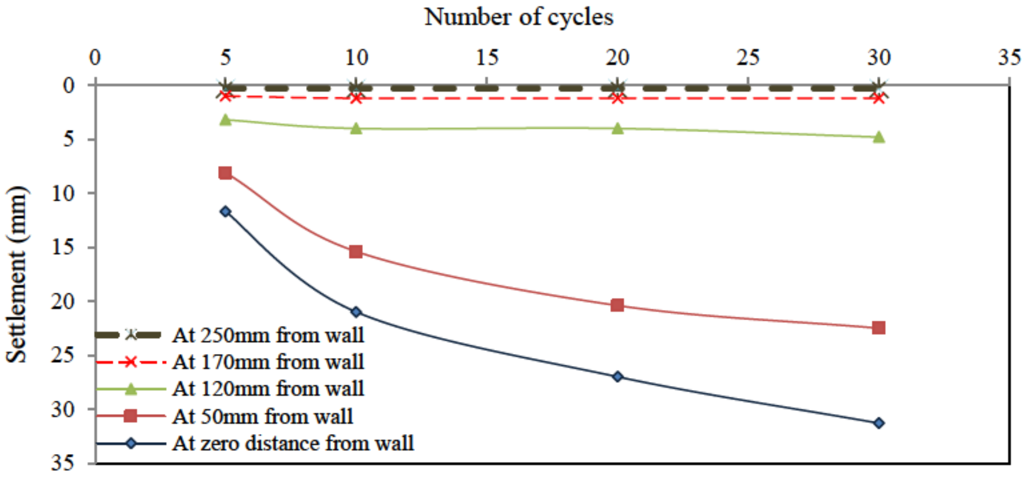

Figure 4.12 Soil surface settlements at different distances from the wall – Test T2a

In order to verify the potential effectiveness of EPS geofoam inclusion using different arrangements, test T2b was carried out using a wedge-shaped EPS inclusion between the soil and the wall. The settlement results of the test T2b were marginally but consistently less than that of test T2a, reaching a maximum settlement of 26.3 mm after 30 cycles as shown in Figure 4.13. However, the difference between measured lateral earth pressure (σ_h) for Tests T2a and T2b was negligible. Maximum lateral earth pressure recorded in test T2b was 8.9 kPa (8% less than that in test T2a). This can be attributed to the low stress levels in these tests. Therefore, different arrangements of the EPS inclusion result in relatively similar outcomes in terms of reducing lateral earth pressure.

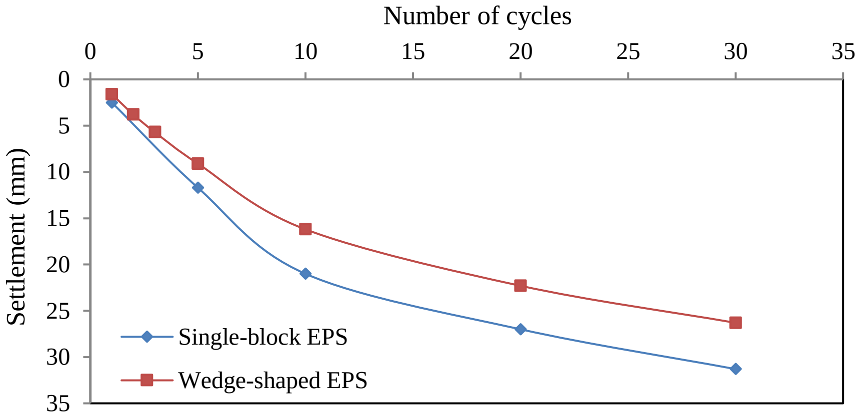

Figure 4.13 Maximum settlement in tests T2a and T2b using different arrangements for the EPS inclusion

4.6 Numerical Simulation of the Small Wall Tests

4.6.1 Constitutive Models and Materials Properties

Soil

The Mohr-Coulomb model was adopted for the backfill soil behind the wall. The Mohr-Coulomb elasto-plastic model in ABAQUS/Standard (2017) allows the material to harden and/or soften isotropically. ABAQUS/Standard (2017) uses a non-associated flow rule whereas the flow potential, G, for the Mohr-Coulomb yield surface is a hyperbolic function in the meridional stress plane and smooth elliptic function (Menetrey and Willams 1995) in the deviatoric stress plane;

$$G = \sqrt{\left(\varepsilon c|_o \tan\psi\right)^2 + \left(R_{mw} q\right)^2} - p\tan\psi \qquad (4.1)$$

Where, c is the initial cohesion yield stress

ψ is the dilation angle

ε is the meridional eccentricity

p, q are the equivalent pressure stress and Mises equivalent stress respectively

R_{mw} is a stress invariant and is a function of the friction angle ϕ, the deviatoric polar angle θ and the deviatoric eccentricity e.

By default, the ABAQUS/Standard (2017) assumes a small value, 0.1, for the meridional eccentricity ε and calculates the deviatoric eccentricity e, from

$$e = 3 - (\sin\phi)^3 + \sin\phi \tag{4.2}$$

In the Mohr-Coulomb formulation in ABAQUS/Standard (2017), the plastic strain increment is given by:

$$d\varepsilon^{pl} = \frac{d\bar{\varepsilon}^{pl}}{g}\frac{\partial G}{\partial \sigma} \tag{4.3}$$

where G is the flow potential.

g is given by:

$$g = \frac{1}{c}\sigma : \frac{\partial G}{\partial \sigma} \tag{4.4}$$

where c is the cohesion ($c \neq 0$). Therefore; a small value of 1.5 kPa was assumed for the cohesion of the soil in the numerical model to maintain numerical stability. Other studies, such as Zarnani and Bathurst (2009) & Crisfield, (1987), have also applied small cohesion values to model cohesionless soils to avoid convergence problems in Mohr-Coulomb (MC) model.

EPS Geofoam

In the present thesis, the EPS geofoam behaviour was simulated using the Hyperfoam model available in ABAQUS/Standard (2017), which is a non-linear isotropic material model suitable for cellular solids that permit large volumetric changes and allow for energy dissipation. The Hyperfoam model aligns well with the constitutive behaviour of the EPS. The model utilizes strain energy potential (*U*) in the form,

$$U(\overset{\wedge}{\lambda}_1, \overset{\wedge}{\lambda}_2, \overset{\wedge}{\lambda}_3) = \sum_{i=1}^{N} \frac{2\mu_i}{\alpha_i^2} \left[\overset{\wedge}{\lambda}_1^{\alpha_i} + \overset{\wedge}{\lambda}_2^{\alpha_i} + \overset{\wedge}{\lambda}_3^{\alpha_i} - 3 + \frac{1}{\beta_i} \left((J^{el})^{-\alpha_i \beta_i} - 1 \right) \right] \qquad (4.5)$$

where *N* represents the number of terms in the model

α_i, β_i and μ_i are the material parameters

$\overset{\wedge}{\lambda}_1, \overset{\wedge}{\lambda}_2, \overset{\wedge}{\lambda}_3$ are independent variables (principle stretches) and are related to the strain in a continuum, (Ogden, 1972), by;

$$\overset{\wedge}{\lambda}_i = 1 + \varepsilon_i \qquad (4.6)$$

J^{el} is the elastic volume ratio, and is a function of the principal stretches . $\overset{\wedge}{\lambda}_1, \overset{\wedge}{\lambda}_2, \overset{\wedge}{\lambda}_3$

There are two methods to define the material parameters, α_i, β_i and μ_i, in equation 4.5;

- Specify the Hyperfoam material parameters directly through the input file or the CAE-property module in ABAQUS/Standard (2017) or,
- Provide experimental data from different tests and allow the ABAQUS/Standard (2017) to calculate the material parameters.

In this study, the Hyperfoam model was experimentally calibrated using data from confined uniaxial compression test, simple shear test and three-dimensional drained hydrostatic test. Because the yield criterion of the EPS is rate dependent, samples were tested at a very low strain rate (0.02% /min) in an attempt to replicate a slow or a quasi-static loading condition induced by the wall movement. The results from these tests are shown Figure 4.14.

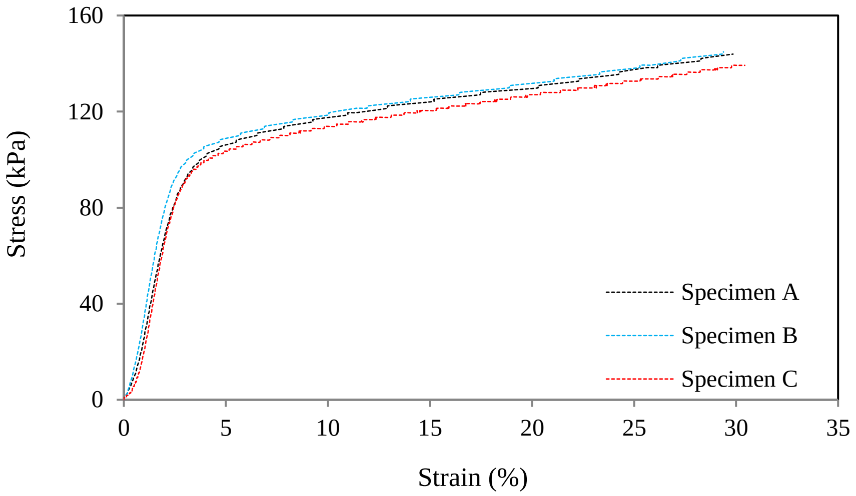

(a) Stress-Strain relationship of EPS samples in uniaxial compression test

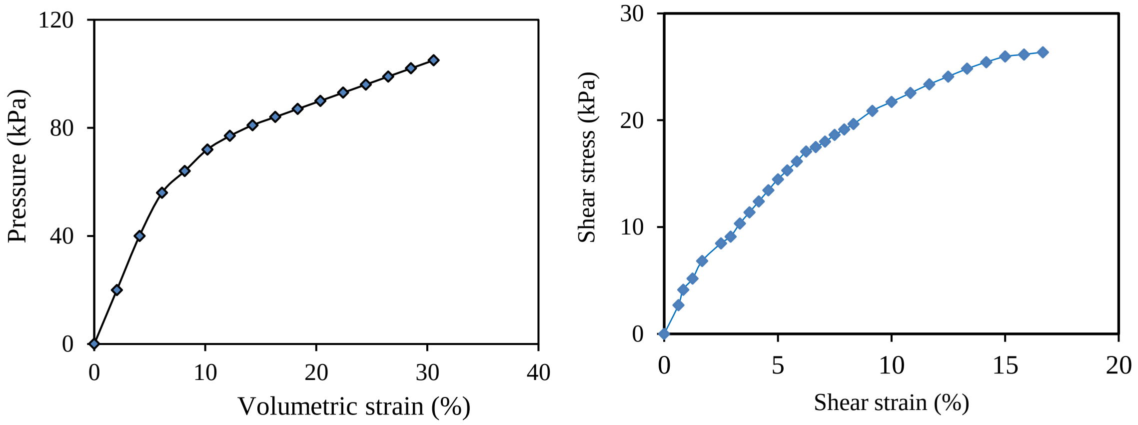

(b) Hydrostatic test results for EPS

(c) Simple shear test results for EPS

Figure 4.14 Results from different tests on EPS specimens used in Hyperfoam model

4.6.2 Plane-strain Model

A plane-strain finite element model of the small wall with EPS-sand backfill was developed using the ABAQUS/Standard (2017) for further numerical simulations. The interfaces (EPS-sand, EPS-wall and EPS-EPS) were modelled using the contact algorithm in ABAQUS/Standard (2017) for frictional surfaces based on the standard surface-to-surface contact with finite sliding. The normal behaviour at the interface was simulated as a hard contact, in which no separation is permitted between any two surfaces. The interaction was activated during the initial step of the analysis. The boundary conditions were introduced in the initial step to establish global equilibrium in the model.

It is worthwhile mentioning that the same material constitutive and interface interaction models were later applied for modelling of the prototype abutment wall, after they have been validated against experimental data from the small abutment wall tests.

4.6.3 Validation of the Numerical Simulation

Verification of the numerical modelling of soil-wall interaction behaviour without EPS inclusion was previously discussed by Alqarawi et al. (2016), using experimental data from centrifuge tests conducted by Ng et al (1999). It was concluded that the developed numerical model replicated the centrifuge results sufficiently well, when the cohesionless soil was modelled using the Mohr-Coulomb constitutive model and the soil-wall interface using the frictional contact algorithm in ABAQUS/Standard (2017). The FEM modelling of the small wall model also showed a relatively similar failure surface, with a notable non-planar shear band, to that observed in the PIV analysis (see Figure 4.15). This further supports the hypothesis of the log-spiral solution discussed in Chapter 3.

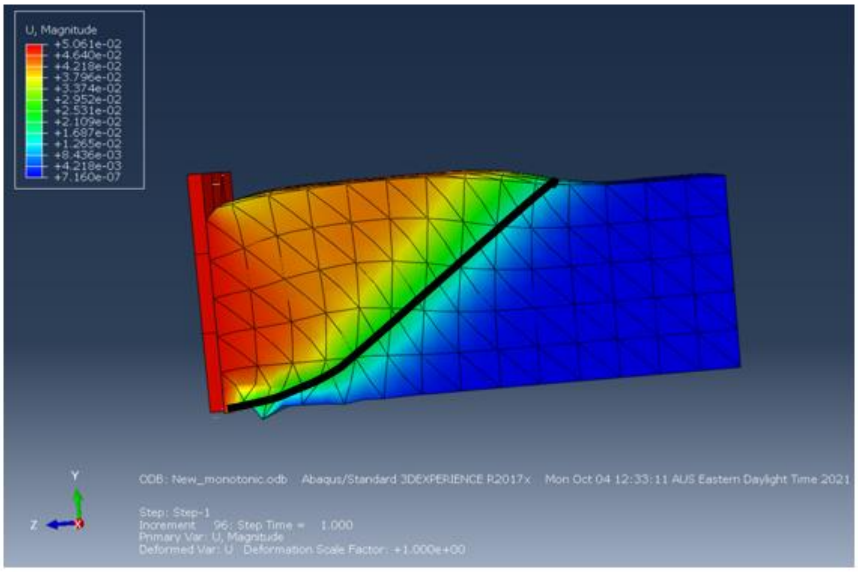

Figure 4.15 FEM results for the small wall model showing a notable non-planar shear band

In this section, experimental data from test T2b were used to validate the interaction behaviour at the wall-EPS, EPS-soil and EPS-EPS interfaces, and the application of the Hyperfoam model to simulate material behaviour of EPS geofoam. Test T2b used three EPS blocks which resulted in multiple EPS-EPS as well as EPS-soil interfaces. It thus provided a more challenging multi-interface scenario for numerical simulation than test T2a. The FE model with the mesh for test T2b is shown in Figure 4.16. The elasticity modulus of the soil was assumed as 30 MPa in reference to the value for uniform loose sand.

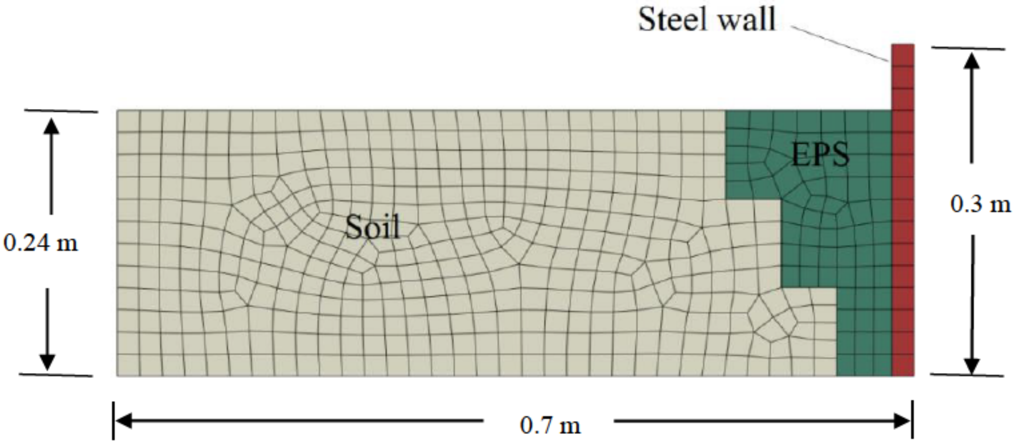

Figure 4.16 The meshed ABAQUS model for small wall test T2b

The FE modelling results for the maximum settlement of soil surface as well as the lateral earth pressures for test T2b have been plotted together with the corresponding experimental results for purpose of comparison as shown in Figures 4.17 and 4.18, respectively. The modelling and experimental results are notably in good agreement, and the discrepancies between them are very small. Therefore, the FE modelling using the aforementioned methodologies and material models especially for the EPS inclusions, are deemed to replicate the soil-EPS-abutment interaction behaviour in IABs reasonably well.

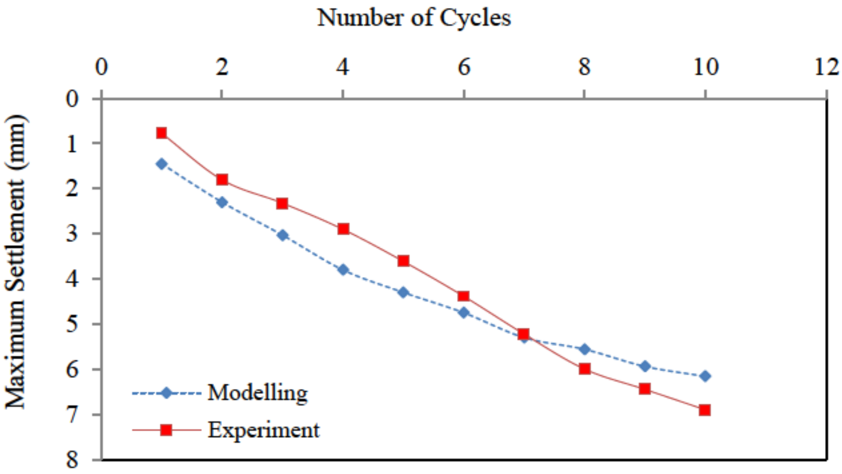

Figure 4.17 Finite element and experimental results for the soil settlement

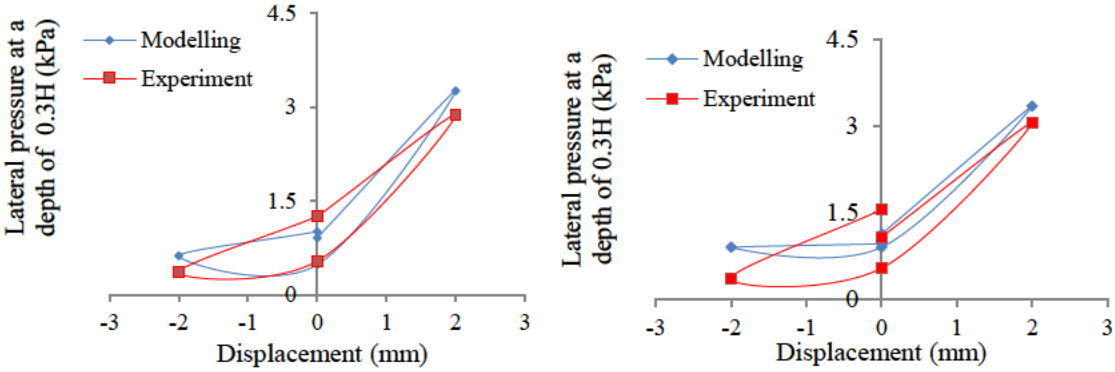

(a) (b)

Figure 4.18 (a) Lateral pressures acting on the wall during Cycle 5; and (b) lateral pressure acting on the wall during Cycle 10

4.7 Soil-Structure Interactions in Prototype Abutment Wall

Upon the validation of the numerical model and the constitutive materials models used therein, the soil-structure interactions in a prototype full integral abutment bridge, with and without the presence of EPS inclusion were investigated numerically and will be discussed in this section.

A plane-strain 2D model was developed, using the ABAQUS Standard (2017) finite-element software, to study the soil-structure interactions in a concrete abutment of an IAB (3 m height), supported on eight, HP [310 mm (section size) x110 kg/m (weight per unit length)] steel piles (bending about the weaker axis) and retaining a compacted backfill as illustrated in Figure 4.19. The backfill overlie two layers of medium-stiff and hard clay. The geometry presented in this model replicates a typical configuration of a prototype sub-structure of an integral abutment bridge. The load is applied in terms of a two-way cyclic horizontal displacement, of ± 20 mm ($\Delta/H = 0.33\%$), at the top of the abutment to simulate the expansion and contraction of the bridge superstructure. As a plane-strain model, the steel piles supporting the abutment have been idealized as an equivalent steel wall maintaining an equivalent axial and flexural stiffness (*AE*, *EI*).

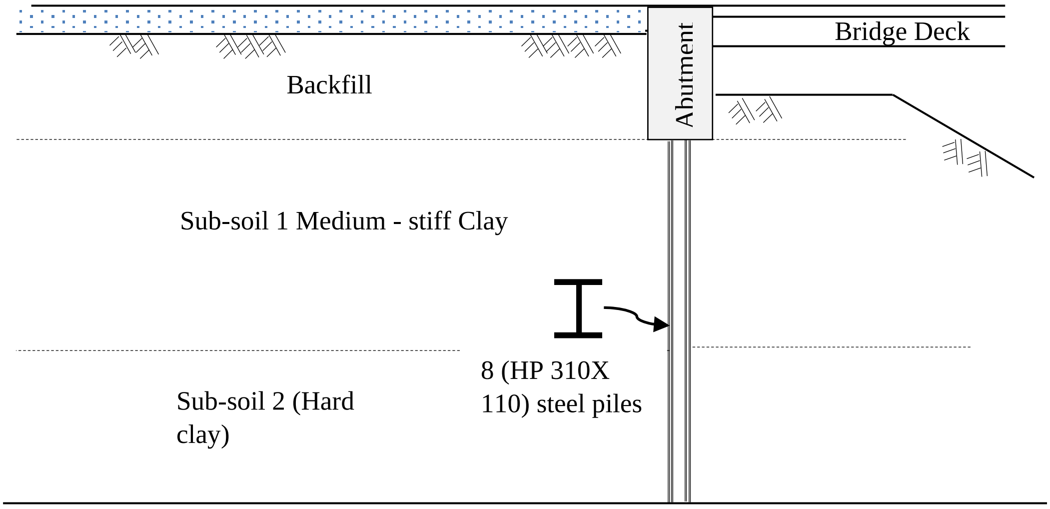

Figure 4.19 Sketch of the 2D full scale prototype abutment of IAB

The properties of the soil (backfill and the subsoils) and of the concrete abutment and the steel pile adopted in the analysis are given in the Tables 4.4 and 4.5 respectively. These properties were obtained from literature on embankments and bridge approaches.

Table 4.4 Properties of Soil layers used in the model. (Yapage et al., 2013; Jamswang et al., 2015)

Parameters	**Backfill soil**	**Sub-soil 1**	**Sub-soil 2**
Description	Dense sand	Soft clay	Medium clay
Unit weight (kN/m^3)	18	14.5	16.5
Elastic Modulus (kPa)	35,000	25,000	30,000
Friction angle (degrees)	38	15	20
Cohesion (kPa)	6	18	20
Dilation angle (degrees)	4	1	1
Poisson’s ratio	0.35	0.3	0.3

Table 4.5 properties of the concrete abutment and the steel pile

Parameter	**Concrete wall**	**Steel Pile**
E, (kPa)	30 x 10^6	200 x 10^6
Unit weight (kN/m^3)	23.4	78
Poisson’s ratio	0.25	0.3

The initial geostatic stresses were defined in the initial step to equilibrate the deformations posed by the gravity loads. This is important to exclude any settlements produced by the gravity loads and account only for those developed by the abutment movements. The gravity was applied in the geostatic step for the entire model. Plane-strain eight-node quadrilateral elements with reduced integration (CPE8R) were used for concrete, steel pile, soil and EPS geofoam, simulating a central section of a wide abutment wall as appears in Figure 4.20. The influence of mesh sensitivity on the numerical results has been evaluated carefully. The mesh size used in the numerical models has been selected such that refining the mesh has insignificant impact on the analysis results, rather it drastically increases the computational time.

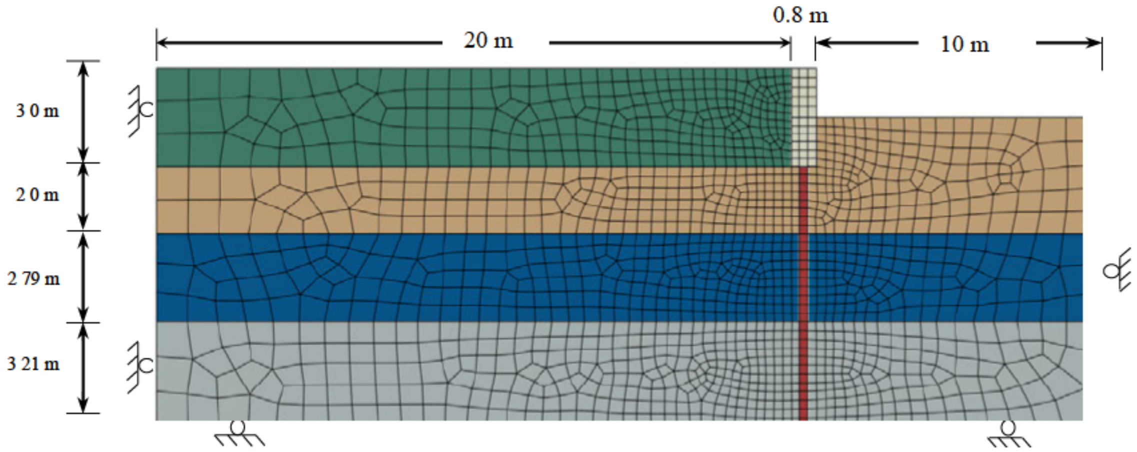

Figure 4.20 Two-dimensional plane-strain model of prototype abutment

4.8 Discussion of the FE Prototype Modelling Results

This section presents the results from the finite element simulation of the prototype abutment for two different scenarios: Case 1 - without EPS inclusion and Case 2a - with EPS block inclusion and Case 2b – with EPS wedge-shaped inclusion.

4.8.1 Modelling Results of Case 1

These results showed the pattern of the abutment movement in response to the applied displacement. Figure 4.21 illustrates the horizontal movements at the top and the bottom of the abutment. The amplitude of the horizontal displacement at the bottom was relatively small (around 5.5% of the amplitude at the top). The difference in the top and bottom displacements is a manifestation of the rotation and translation movements of the relatively rigid abutment. After 20 cycles of loading, the neutral position of the abutment toe was slightly shifted inward leaving the abutment inclined at 0.14% as shown in Figure 4.22.

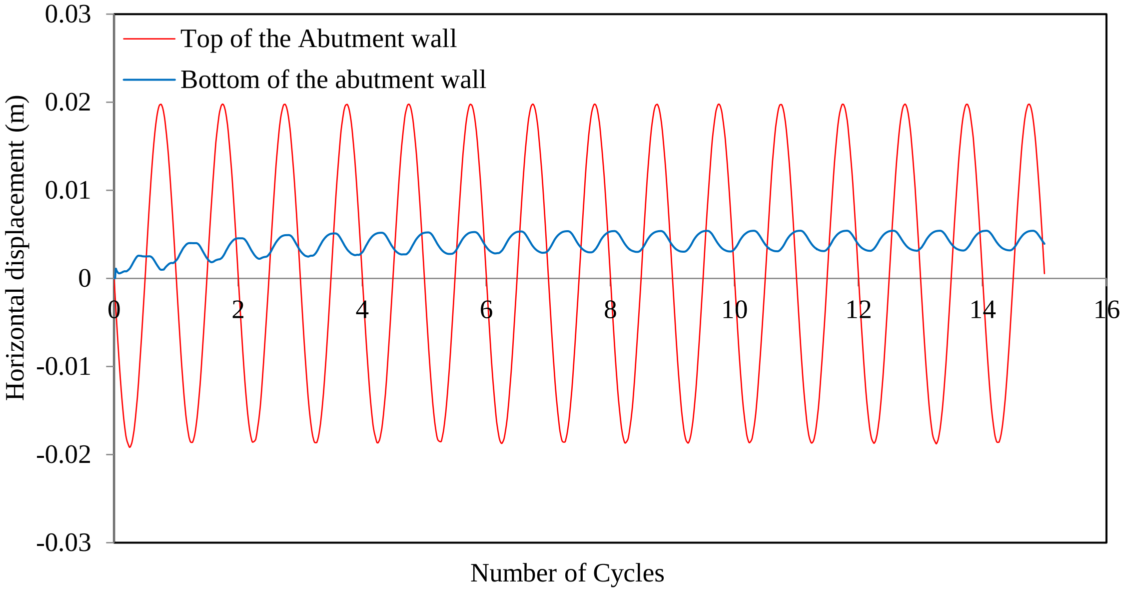

Figure 4.21 Horizontal displacements at the top and bottom of the abutment Case 1

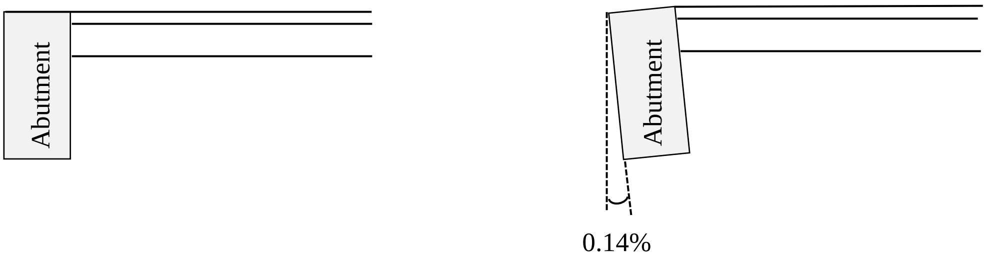

(a)

(b)

Figure 4.22 (a) Abutment neutral position before loading and (b) abutment position after 20 cycles of loading, Case 1

Figure 4.23 also shows the inward displacements of the abutment and the pile by comparing the active and passive movements in Cycle 1 and Cycle 20.

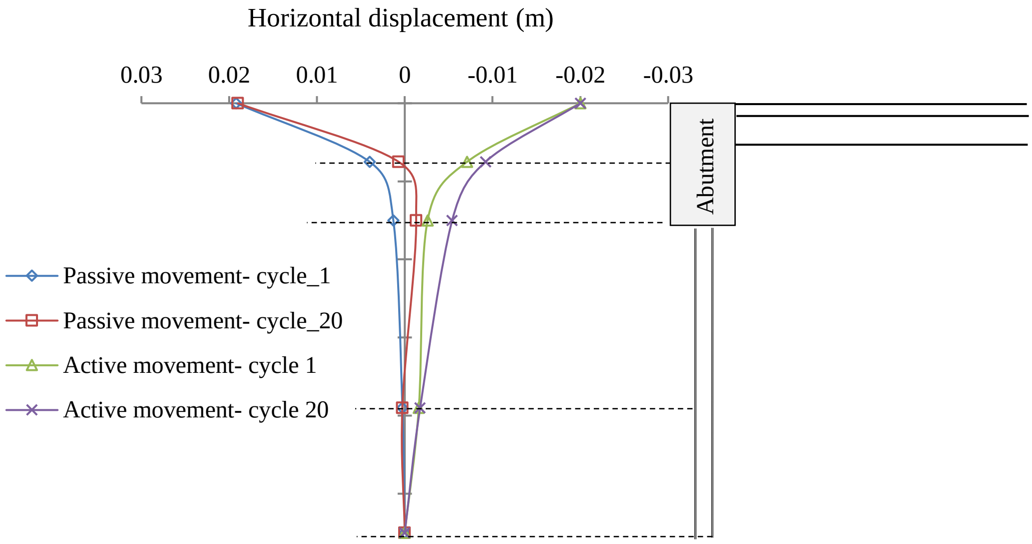

Figure 4.23 Abutment wall-pile assembly during passive and active movement, Case 1

4.8.1.1 Lateral Earth Pressure

The numerical results of Case 1 showed that the lateral earth pressure acting on the abutment is dynamic and continuously changing, during the wall movements, in terms of both the distribution and the magnitude. Figure 4.24 shows the maximum lateral earth pressure profiles recorded during different loading cycles. It can be observed that the maximum earth pressure is consistently occurring at the upper half of the wall then decreases toward the toe of the wall to a value close to the at-rest pressure. This pressure profile can be attributed to the mode of the abutment movement which is largely rotation (see Figure 4.21). In a rotational movement mode, the applied displacement Δ, is virtually greater at the top of the wall and minimum, or zero in pure rotational movement, at the bottom.

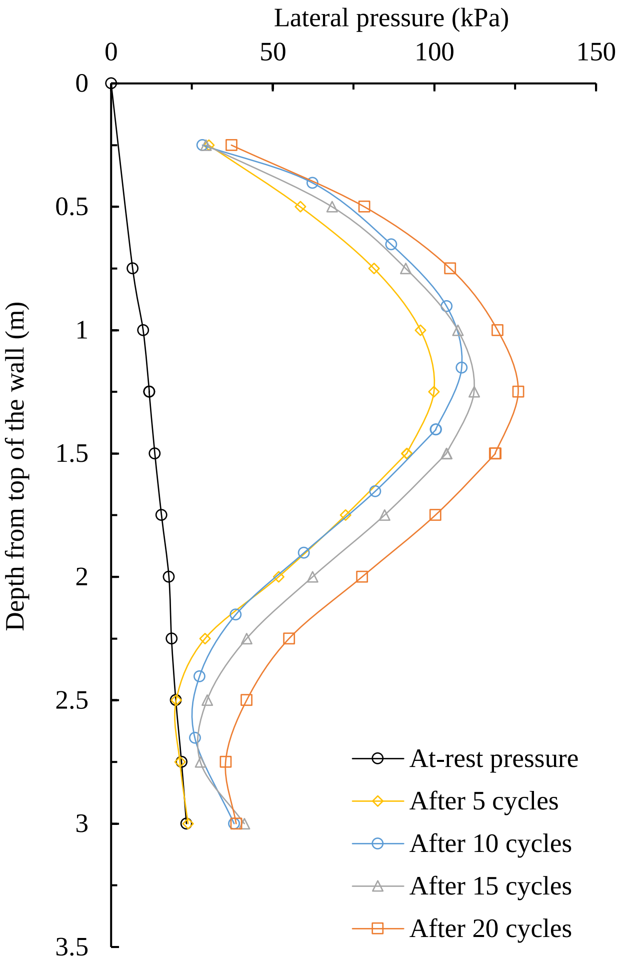

Figure 4.24 Maximum lateral earth pressure profile during different loading cycles

4.8.1.2 Soil Settlement

Figure 4.25 illustrates the maximum settlement versus number of cycles under ± 20 mm displacement amplitude at the top of the abutment. It is apparent that the settlement increased more rapidly within the first 10 cycles and subsequently the settlement rate was slightly reduced. This behaviour agrees with the small wall test results that showed a reduction in the settlement rate after 10 loading cycles (Figure 4.9) and conforms with the findings reported by England et al. (2000). The latter concluded that the settlement rate is relatively high at the initial cycles and then tends to asymptote to a lower rate under subsequent loading cycles.

Figure 4.26 shows the deformed soil surface, after 20 cycles of wall movements at the area adjacent to the wall. The soil profile shows a trough close to the abutment with maximum settlement, of 177 mm, recorded at the interface between the soil and the concrete abutment. It also shows a large soil heaving between 0.5 m and 2 m from the abutment wall face. The wall movement effects seem to be decreasing away from the wall and diminished at a distance of approximately 3m.

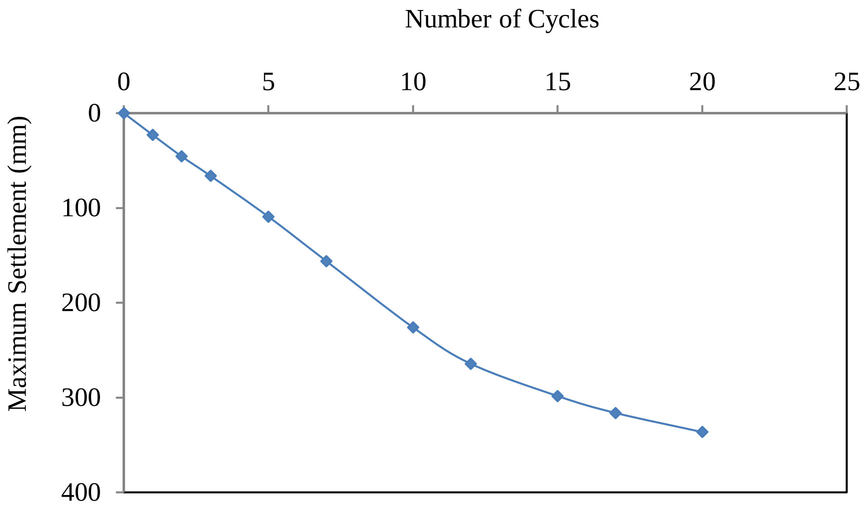

Figure 4.25 Maximum settlements vs. Number of cycles, Case 1

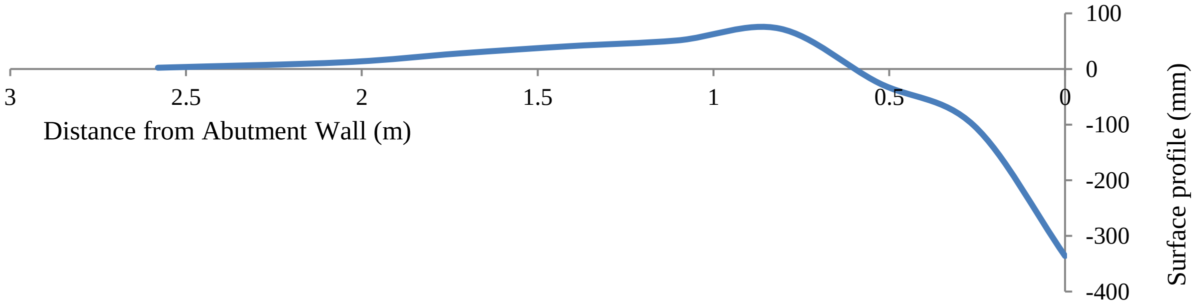

Figure 4.26 The deformed soil surface after 20 cycles, Case 1

4.8.1.3 Soil-Wall interaction

In order to develop effective and practical remedial measures for the approach problems in IABs, it is imperative to shed light on the complex interaction mechanism associated with the wall movements.

In a typical movement cycle, the top of the abutment wall travels from its initial neutral position (O) toward the extreme active position (A) then moves toward the passive position (P) (passing through, O) and eventually moves back to the neutral position (O) as illustrated in Figure 4.27.

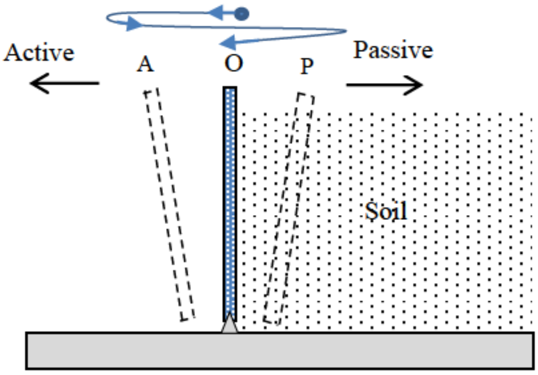

Figure 4.27 Abutment wall movements

During the active phase (O-A), a wedge of soil loosens and slips downward, under gravity effect, into the gap developed behind the abutment wall. The volume loss of that slipped soil wedge represents a negative volumetric strain and that is reflected as a slight settlement in the soil surface (Yang and Tang, 2017). In movement (A-O), principal stress reversal occurs when the wall compresses the adjacent soil, which now incorporates the previous soil slip. During that phase of movement, the slipped wedge is not substantially recovered to its former position. The reason is because the gravity load tries to steer the soil grains' movement downwards, while the wall is still predominantly moving horizontally, which results in inequivalent negative (contraction) and positive (dilation) volumetric strains during the O-A-O movement. Accordingly, an extent of residual settlement remains even when the wall reaches the neutral point O. Forced by the wall movement, the soil particles displaced during O-A phase are squeezed into the adjacent soil during the A-O phase. Soil loosening and re-densification will literally take place during the O-A-O movement. In the following movement (O-P) the wall continues to compress and displace the adjacent soil. This will result in both further soil densification and soil displacement. As a result, the densification effects will progress further to form a wider passive wedge. When the wall reaches to position (P), maximum compressive stresses will be developed and the soil suffers plastic strains. The following phase (P-O) represents an unloading state where the soil loosens again allowing the compressive stresses to relax. During this phase, voids between soil particles will open up. Consequently, soil particles will slump downwards under gravity causing an additional settlement.

In the following cycle, specifically during O-A phase, the adjacent soil will continue to loosen and further soil slumping occurs. The slipped soil wedge accumulates with the formerly slipped soil (from earlier cycle). The accumulated slippage of soil results in an incremental settlement rate. Travelling back from position A to O, the wall will have to overcome a higher soil resistance imposed by the enlarged slipped wedge. As in the past cycle, the soil particles in the slipped wedge will be squeezed into the adjacent soil resulting in further densification. This justifies the initial escalation in the lateral earth pressure.

The mechanism discussed above will be repeated with every loading cycle so that as the number of movement cycles increases, the soil adjacent to the wall becomes increasingly densified which leads to,

- Less soil slippage during the active phase because of the accumulated soil from previous cycles already filling the gap behind the wall. This will result in less settlement at that specific cycle, compared to the precedent one and eventually a decreasing settlement rate.

- A higher mobilized soil resistance to the passive wall movement and consequently escalation in the magnitude of the coefficient of lateral earth pressure *K*. In addition, the passive soil wedge will cause a heave beyond the settlement trough.
- The residual volumetric strain change becomes insignificant with increasing cycles resulting in closed hysteresis loops or the so-called *elastic shakedown* state (Ghadimi et al., 2016). At this stage the deformation in the soil is predominantly recoverable. The settlement will therefore, become less sensitive to the loading cycles and its curve will tend to asymptote and level off. Figure 4.28 shows the lateral earth pressure changes with the horizontal wall movements of Case 1. It is apparent that the stress loops became nearly closed during the last five cycles.

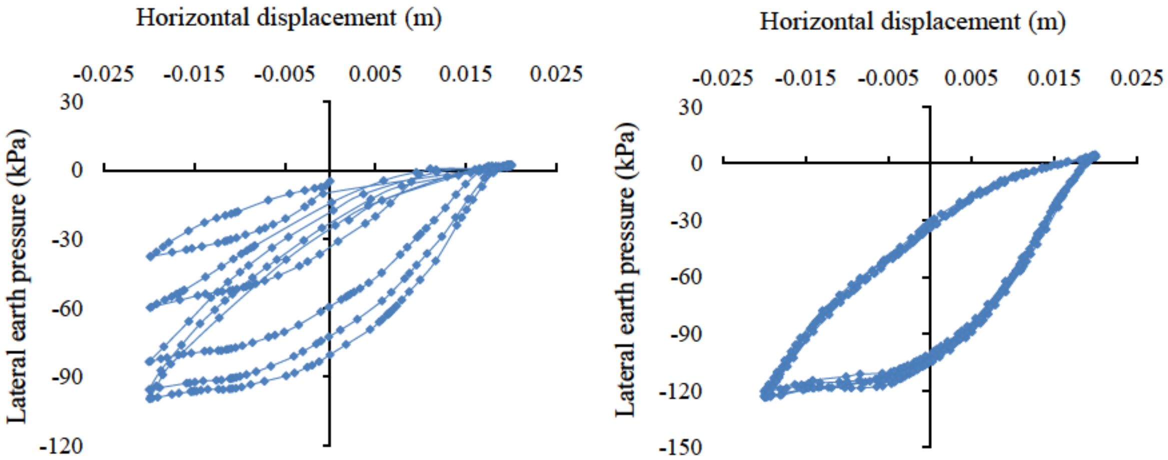

(a) (b)

Figure 4.28 (a) Stress loops at different loading during Cycles 1 – 5; and (b) stress loops at different loading during Cycles 15 - 20, Case 1.

Data from the small wall test have also supported the above interpretations. The settlement at the interface between the wall and the soil, of the small wall test, has been plotted against the horizontal movements as shown in Figure 4.29. Evidently, the deformations in the soil during cycles 25 to 30 becomes insignificant compared to those occurred during the first five cycles.

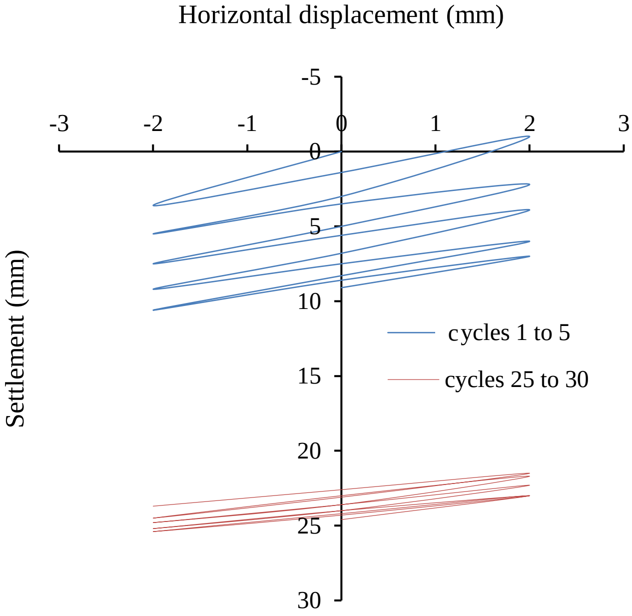

Figure 4.29 Settlement at soil-wall interface versus the horizontal displacement in the small wall Test T1

4.8.1.4 Settlement, Soil Displacement and Densification

The settlement trough observed in the numerical modelling of the backfill, (Figure 4.26) represents a displaced soil mass. Because the mass of soil initially occupying the trough must be conserved, it is in fact partly reabsorbed into the adjacent soil mass to densify it, and partly displaced to the surface. The latter is manifested as the soil heave above the initial soil level. Using the data given in Figure 4.26, the mass of soil displaced into the heaving part was estimated to be seven times larger than the mass of the trough. The large soil heaving is attributed to the dilatancy characteristics of the soil under the continuous shearing loads. The backfill material simulated in this model was a heavily compacted granular soil with an internal friction angle of 38° and a dilation angle of 4°. This reveals the fact that using well compacted backfill may alleviate the soil settlements behind the IAB abutments, however, it imposes another problem which is the excessive soil heaving eventually resulting in a hump on the road surface.

4.8.2 Modelling Results of Case 2a and Case 2b

The results of Case 1 revealed that relying on heavily compacted backfill as the only means to limit the approach settlement in IABs is not adequate. That said, using loose backfill would, however, worsen the approach settlement (Alqarawi et al. 2016). Therefore, this study investigates the use of EPS geofoam as a compressible material between the abutment and the approach backfill to alleviate the wall movement effects. This section discusses the results of two different arrangements of EPS inclusions, namely, a single block with uniform thickness (Case 2a) as well as a wedge-shaped block arrangement (Case 2b).

The modelling results show that the EPS inclusion was generally effective in alleviating the settlements and the lateral forces in the approach backfill. In a single-block arrangement (Case 2a), with 250mm EPS thickness, the maximum lateral pressure was minimized by 50%, compared to that in Case 1. Further reduction in the lateral pressure was achieved by using a thicker EPS block as shown Figure 4.30.

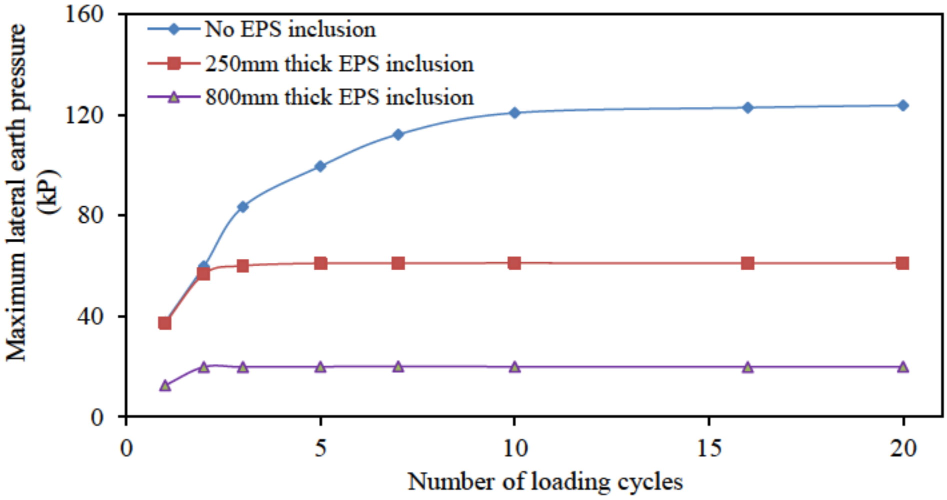

Figure 4.30 Lateral earth pressures at depth z equals to $H/3$ from the top of the abutment

Notably, the thickness of the EPS block is a critical parameter controlling the performance of the EPS inclusion. Using a thicker EPS board improves the efficiency of the inclusion. Figure 4.31 shows the relationship between the lateral soil pressure and the thickness of the EPS inclusion after 20 cycles of abutment movements.

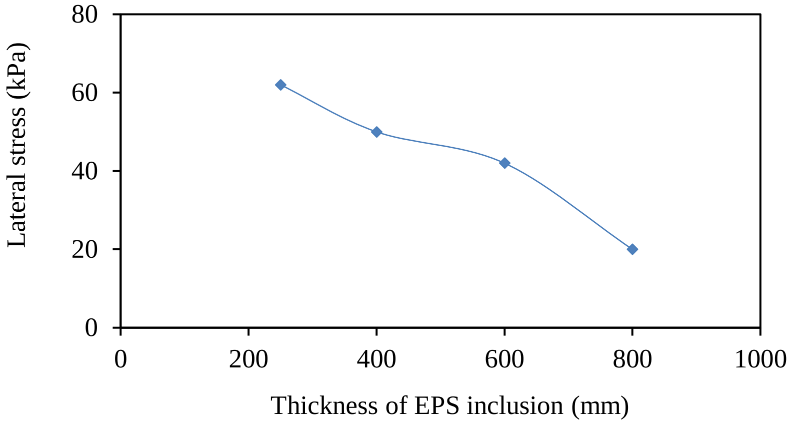

Figure 4.31 Earth pressures at $z = H/3$ versus thickness of the EPS inclusion, Case 2a

Likewise, the EPS inclusion significantly attenuated the maximum soil settlement with 50% reduction using 250 mm thick single block of EPS. Figure 4.32 shows the maximum settlements developed after 20 cycles of ± 20 mm ($\Delta/H = 0.66\,\%$) loading at different thicknesses. Evidently, using 600 mm thick board of EPS will help to keep the settlement below 20 mm.

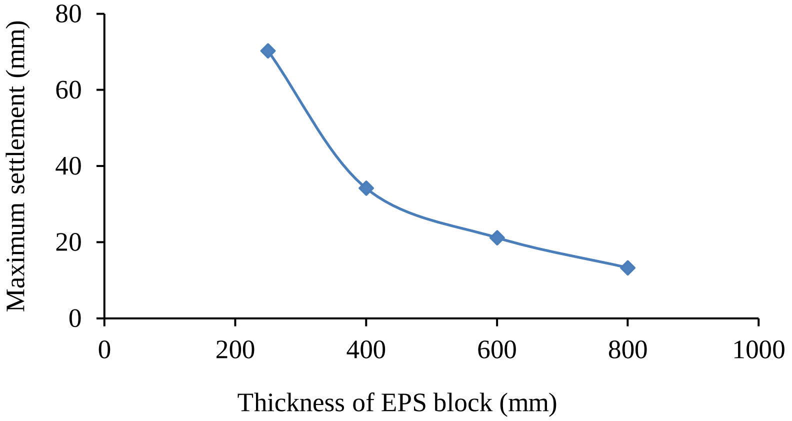

Figure 4.32 Maximum settlements versus thickness of the EPS inclusion, Case 2a

The results of Case 2b showed slight improvements, in having a further reduction of the lateral pressures by about 5% compared to that of Case 2a. The soil settlement results of Case 2a and Case 2b were virtually similar.

Figure 4.33 shows the maximum settlements against the number of cycles in both Case 1 and Case 2a with 600 mm thick EPS inclusion (they are almost the same for Case 2b). The magnitude of settlement was greatly attenuated in Case 2a compared with Case 1.

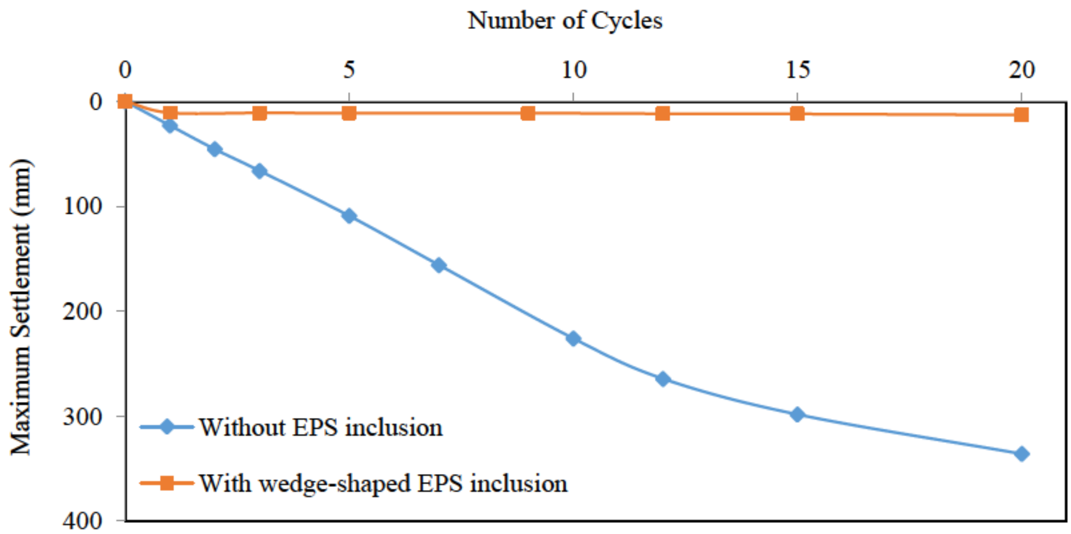

Figure 4.33 Maximum settlements versus number of cycles of Case 1 and Case 2a

The maximum settlement for Case 2a levels off to approximately 12 mm, after the first few loading cycles. As a highly compressible material, the EPS was absorbing most of the wall lateral displacement with only a small fraction of disturbance transferred to the adjacent soil. This is illustrated in Figure 4.34, which compares the horizontal displacements at the EPS-abutment and EPS-soil interfaces. Only 17% of the total applied amplitude (± 20 mm) was transferred to the backfill. Accordingly, the backfill at the EPS-soil interface was subjected to only ± 3.5 mm ($\Delta/_{H} = 0.11\%$) loading amplitude, which is a significant reduction of the abutment displacement.

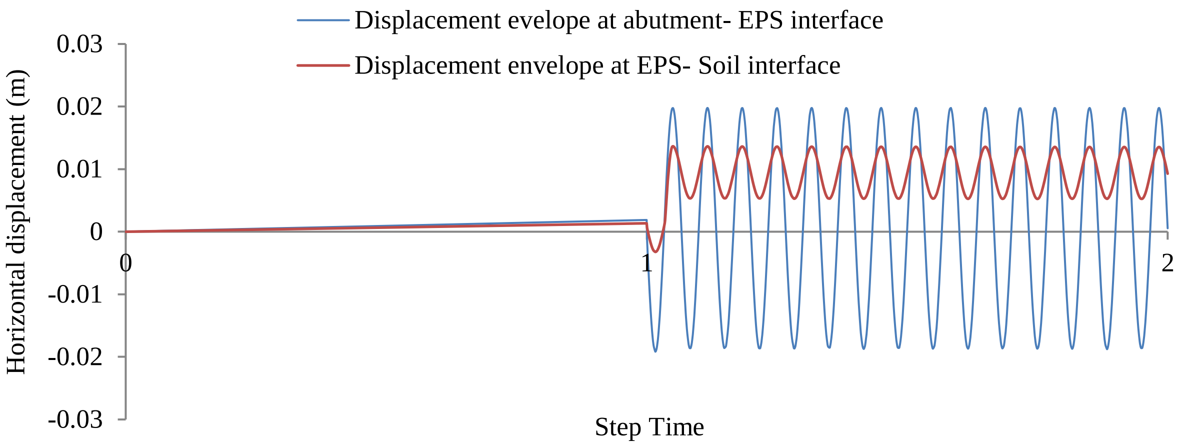

Figure 4.34 Displacement amplitudes at the soil-EPS and EPS-wall interfaces (negative displacement refers to passive wall movement)

This mechanism, in which the EPS inclusion reduces the displacement transferred from the wall to the adjoining soil, will be termed as the *transfer function* (Figure 2.24).

Based on the general equilibrium expression,

$$\sigma_{EPS} = \sigma_{soil} \tag{4.7}$$

$$\sigma_{EPS} = \varepsilon_{soil} \times E_{soil} \tag{4.8}$$

$$\varepsilon_{soil} = \frac{\Delta E_r}{t} \tag{4.9}$$

where Δ is the abutment movement (translation or rotation), t_{EPS} is the thickness of the EPS inclusion and E_r is the relative stiffness and is given by $\frac{E_{EPS}}{E_{soil}}$. According to equation 4.9, the “most important” strain in the retained soil is a function of the relative stiffness E_r and thickness of the EPS inclusion. To maximise the advantage of the EPS inclusion in rectifying the wall movement effects, an EPS with lower compressive strength and denser backfill need to be used. However, this criterion need to be employed with due attention to the other intended functions of the EPS inclusion such as bearing the vertical loads and the lateral soil pressure. It is also worthy noting that the placement of an EPS inclusion needs to be appropriately coordinated during the construction of the backfill. Compacting the backfill soil while the EPS inclusion is in place (between the soil and the concrete abutment) will impose lateral pressures on the EPS and may stress it beyond its elastic behaviour. Therefore, it is advised to provide temporary support for the backfill during the compaction. This can be achieved by installing temporary supporting formwork between the EPS and the soil for each layer of backfill.

4.9 Conclusions

This chapter discusses experimental and numerical analyses of the soil passive earth pressure as well as the abutment-soil interaction in IABs. A series of experiments were first carried out to validate the log-spiral solution developed earlier in Chapter 3. Then, a series of experiments were conducted on a physical laboratory model of a small wall retaining loose sand to examine the lateral pressures and soil settlements with and without the presence of EPS geofoam inclusion. A plane-strain numerical model was then developed using ABAQUS Standard (2017) finite element modelling software to study the soil-structure interactions in an integral abutment supported by steel piles in prototype dimensions. The results of the experimental and numerical investigations have been analysed to draw the following conclusions,

- The failure plane derived using the images captured during the experiments confirms that it is not a straight linear failure surface but a curved surface closer to the toe of the wall and a straight line towards the retained soil surface, which resembles the failure surface assumed for the log-spiral solution.

- The cyclic movement of the bridge abutment, in response to the superstructure movement of the bridge, results in escalation in the lateral soil pressures and settlements in the soil surface adjacent to the abutment.
- The deformation in the approach soil consisted of both a settlement trough and surface heaving. The negative volumetric strain, or the settlement, in the backfill soil adjacent to the abutment is caused by soil densification and soil displacement. The positive volumetric strain, or the plastic dilatancy, is generally greater when the soil is initially dense which results in a large surface heave beyond the settlement trough. On contrary, initially loose soil experiences large soil settlement and insignificant heaving when subjected to cycles of abutment wall movements.
- The settlement and the lateral pressure escalation rates are higher during the first few loading cycles. These rates decrease considerably or tend to asymptote as the loading cycles increase.
- Using heavily compacted backfill at the bridge approaches is not sufficient to limit the approach problems in IABs.
- The experimental as well as the numerical results showed that the EPS geofoam inclusion is effective in alleviating the abutment movement transferred to the approach soil. It has the effect of significantly reducing the lateral pressure acting on the abutment and attenuating the magnitude of the approach settlement.

Compacting the backfill soil will adversely affect the function of EPS inclusion, if proper measures are not adopted during the construction of the approach backfill. Such process may involve compacting the retained soil in multiple fills and build a self-stable soil mass with temporary shoring layer by layer before the EPS blocks are installed in place. The temporary shoring is removed once the EPS blocks are in place for that layer.

Chapter Five

Development of Physical Model - Materials and Methods

5.1 Introduction

This chapter describes the development of a physical model and the materials utilised to perform the experimental program in this research. The physical model is meant to replicate an abutment of an integral bridge retaining a cohesionless backfill and subjected to different patterns of displacements. The primary objective of the physical model is to investigate the interactions between the abutment and the approach backfill due to the temperature-induced abutment movements under similar in situ stresses as the full-scale prototype. Since soil behaviour is stress dependent, this helps to ensure that the soil-structure interaction established in the model is similar to that in the field. All the equipment, materials and methods involved in the experimental program are carefully designed and/or selected to model the same conditions as in the field for the studied case.

It is worthwhile mentioning that the physical model is uniquely developed to perform the present study and is not yet a generic testing chamber. The development of the physical model, including the design, fabrication and installation of the equipment, selection and acquiring of materials and developing the method statements are entirely conducted during the present candidature. The physical model is funded by Western Sydney University through the Australian Government Research Training Scheme Program.

5.1.1 Similarity of the Experimental Model with the Studied Case

Experimental studies in the engineering fields play a fundamental role in developing realistic databases and in validating the efficacy of numerical computation methods. In performing experimental tests on physical models to replicate an engineering problem, it requires the physical model to be ideally identical to the real world case. Sometimes, however, building an experimental model with the same dimensions as in the full-scale prototype is difficult, particularly when the actual dimensions are considerably large. Therefore, physical models are often scaled down and built with smaller dimensions than those in the prototype. Such physical models can help to perform qualitative studies or to investigate the general behaviour of members or materials in certain engineering problems. However, the results obtained from those scaled models are often compromised and are inapplicable to accurately quantify the response of the full-scale prototype unless appropriate measures are implemented to maintain the similarity with the prototype.

In the geotechnical engineering field, materials such as the soil possess nonlinear mechanical behaviour that depends on the stress level and the stress history. Therefore, the similarity between a scaled experimental model and the prototype, in a geotechnical experiment, is essential to achieve equivalent stress levels in both settings.

Pokrovsky (1936) introduced a principle to achieve the similarity between a geotechnical model and the prototype by increasing the gravitational force in the model using the centrifuge force (Schofield, 1980). This technique has since become one of the profound methods for testing scaled models of geotechnical systems such as soil slopes, retaining structures, tunnels, bridge foundations, etc. However, geotechnical centrifuge modelling is yet expensive and available only in advanced laboratories. Therefore, it does not provide an affordable and easily accessible option for researchers.

In order to build a physical model to study the soil-abutment, and soil-EPS-abutment interactions in IABs, a different approach than the centrifuge modelling was adopted in this study. The concept of the physical model was formulated upon the basis of maintaining similarity between the model and the prototype. Therefore, a rigorous similarity study was first carried out before building the model. The study involved the following principle stages:

- Dimensional analysis to determine the scaling factors
- Materials selection
- Determination of model dimensions (model design)

These stages are discussed in the following sections.

5.2 The Dimensional Analysis

The dimensional analysis is an effective tool for designing engineering experiments. It involves the determination of the relationships between different physical quantities to reduce the large number of variables involved in a certain problem (Butterfiled, 1999). This could be achieved by identifying the dimensionless groups in terms of primary quantities such as the physical length L, the mass M and the time t (Butterfield, 1999).

In relation to the case studied in this thesis, a reasonable set of variables that outlines the response of an integral abutment system, see Figure 5.1, to temperature-induced displacements is given by the matrix V (equation 5.1).

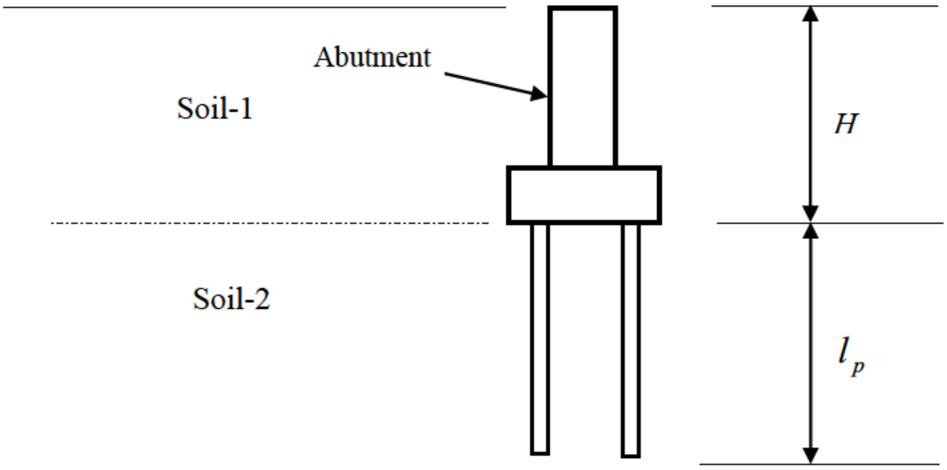

Figure 5.1 Schematic diagram of a typical integral abutment together with the supporting substructure

$$V = \{\sigma, \rho_1, g, H, c_1, \phi_1, \rho_2, c_2, \phi_2, E_1, E_2, \delta_w, S_i, n, E_p, d_p, l_p, I_p, \delta_p\} \tag{5.1}$$

The matrix V contains sixteen variables defined as shown below,

σ : stress

ρ_1, ρ_2 **:** densities of soil-1 and soil-2 respectively

H: retained height of the soil (in this case equal to the wall height)

g: gravity

$c_1, \phi_1,\ c_2, \phi_2$: shear strength parameters of soil-1 and soil-2 respectively

E_1, E_2 : elastic moduli of soil-1 and soil-2 respectively

δ_w, δ_p : friction angles at the soil-wall and soil-pile interfaces respectively

S : wall displacement

n: number of movement cycles

E_p, d_p, l_p, I_p : elastic modulus, diameter, length and moment of inertia of the cross section of the pile (if used), respectively

The matrix D involves three fundamental independent dimensions, *mass, length* and *time,*

$$D = \{M, L, t\} \tag{5.2}$$

Accordingly, the number of the dimensionless groups, N, is calculated as 16 – 3 = 13.

The matrix Q includes the repeated variables ρ, g and H. These variables were selected so that the matrix Q satisfies the following conditions,

- $Q \geq D_{\min}$ (i.e. = 3)
- Doesn’t contain:
  - Variables with no dimensions
  - Variables with identical dimensions
  - Variables that have dimensions which are power of one another

The matrix Q is written in the form,

$$Q = \{\rho_1, g, H\} \tag{5.3}$$

Accordingly, the dimensionless groups (*DG*) can be derived as,

$\{\sigma, \rho_1, g, H\}$, $\{c_1, \rho_1, g, H\}$, $\{\phi_1, \rho_1, g, H\}$, $\{\rho_2, \rho_1, g, H\}$, $\{c_2, \rho_1, g, H\}$, $\{\phi_2, \rho_1, g, H\}$, $\{E_1, \rho_1, g, H\}$, $\{E_2, \rho_1, g, H\}$, $\{\delta_w, \rho_1, g, H\}$, $\{S, \rho_1, g, H\}$, $\{n, \rho_1, g, H\}$, $\{K_p, \rho_1, g, H\}$, $\{\delta_p, \rho_1, g, H\}$.

where, $K_p = \frac{E_p . I_p}{E_s . l_p^4}$, $I_p = \frac{\pi . d_p^4}{64}$

The matrix *DG* can be written as,

$$DG = \{\frac{\sigma}{\rho_1 g H}, \frac{c_1}{\rho_1 g H}, \phi_1, \frac{\rho_2}{\rho_1}, \frac{c_2}{\rho_1 g H}, \phi_2, \frac{E_1}{\rho_1 g H}, \frac{E_2}{\rho_1 g H}, \delta_2, \frac{S}{H}, n, K_p, \delta_p\} \tag{5.4}$$

Or $$DG = \{\pi_1, \pi_2, \pi_3, \pi_4, \pi_5, \pi_6, \pi_7, \pi_8, \pi_9, \pi_{10}, \pi_{11}, \pi_{12}, \pi_{13}\} \tag{5.5}$$

A similarity between the prototype and the model settings required the dimensionless groups to be equated, i.e.

$$\pi_i^{\,m} = \pi_i^{\,p} \tag{5.6}$$

where, π^m is a dimensionless group at the model setting and π^p represents the same dimensionless group in the prototype.

In order to determine the scaling factors between the prototype and the model settings, equation (5.6) was solved for the thirteen dimensionless groups listed in equation (5.4) provided that;

- The model tests are conducted under a normal gravity, i.e., $g^m = g^p = g$ and,
- The height of the wall in the model is half of that in the prototype $H^m = \frac{H^p}{2}$. This will help to build an abutment with a reasonable height (half of the height of an actual abutment).

According to the conditions described above, the scaling factors were concluded and summarised in Table 5.1

Table 5.1 The scaling factors for the physical model

Parameter	Full-scale Prototype	Model
ρ	1	2
σ	1	1
ϕ	1	1
c	1	1
H	1	½
g	1	1
E_s (E_1, E_2)	1	1
S	1	½
δ_w	1	1
n	1	1

The conclusions emerged from the dimensional analysis outline the characteristics of the experimental model and the material (particularly the soil) to be used in the experiment. It is clear now, when the experimental model is built with a scale of 1:2 to the prototype

($H^m = \frac{H^p}{2}$) and exists in a normal gravity ($g^m = g$) the following measures must be implemented to maintain similar stress levels as in the full-scale prototype,

- The shear strength parameters of the soil in both, the model and the prototype, are equal ($\phi^m = \phi^p, c^m = c^p$),
- The modulus (stiffness) of the soil in both the model and the prototype are identical $E_s^m = E_s^p$
- The unit weight of the soil in the model must be equal to two times that in the prototype ($\rho^m = 2\rho^p$),
- The displacement applied at the abutment-soil interface in the model is half of that in the prototype $\left(S^m = \frac{S^p}{2} \right)$

The above concluded measures represent the outcomes of the first stage of the similarity study (the dimensional analysis). These outcomes are carried out forward and carefully implemented in the next two stages (Material Selection & Model Design). The large-scale physical model designed and built for this thesis is a version that does not include Soil-2 and the pile system. The physical modelling will instead only focus on the soil structure interaction in Soil-1 adjacent to the integral abutment.

5.2.1 Limitations of the Dimensional Analysis

The dimensional analysis discussed above addresses the parameter related to the prospective physical model (see Table 5.1). It must be noted that particle size can be a limitation of this dimensional analysis. However, the average particle size of soil used in the testing program is relatively small, as will be discussed in Section 5.3 (between 75 and 150 μm). Considering the potential dimensions of the model, the model to particle size ratio is well above 1000. According to Ng et al. (1996), particle size effects become insignificant for tests with such high model to particle size ratio. Therefore, this limitation is unlikely to have an impact on the similarity of the physical model and the stress levels therein.

5.3 Materials Selection

The prospective model is intended to replicate the soil-abutment and soil-EPS-abutment interactions in a typical integral abutment bridge. The materials involved in these interactions involve the backfill soil, EPS geofoam and the concrete abutment. The characteristics of these materials will be evaluated with close consideration of the dimensional analysis outcomes.

5.3.1 The Soil

According to the outcomes of the dimensional analysis, the potential backfill soil used in the experiment must be naturally heavier than the typical approach backfill soil by two times and possesses similar shear strength parameters (c and ϕ) and stiffness (E_s).

The traditional backfill used in the IABs approaches often consists of well-graded granular soil (Wolde-Tinsae et al. 1983; Hassiotis and Roman, 2005). The average unit weight of such backfill, in a loose state, ranges between 14 kN/m^3 and 15 kN/m^3. In view of this fact, the unit weight of the potential backfill soil, in its loose state, must be between 28 kN/m^3 and 30 kN/m^3. This requirement is quite challenging, as the options of finding such extremely heavy soil with regular granular properties are too limited.

An extensive search led to a special type of soil called *black sand* (sometimes termed as Iron Sand). The black sand is a natural granular sand that forms by the deposition of volcanic debris from the offshore volcanos. Black sand is rich in Iron and Basalt which makes it too heavy, compared to other types of sand, with a unit weight ranging between 27 kN/m^3 and 30 kN/m^3. This sand is an excellent choice for the model soil.

The black sand, however, is rare and exists in a few sites around the world. Among these sites is the Black Beaches in the north-west of New Zealand where the sand used in this study was obtained from. The black sand was supplied by Industrial Sand Ltd., a local supplier in Auckland, New Zealand and shipped to Sydney-Australia in large soil bags each with a weight of 1000 kg.

The black sand is a virgin material in terms of its engineering applications. Currently it has limited uses in the glass industry, particularly in the sand-blasting during the glass manufacturing process. The mechanical and physical properties of the black sand have never been investigated for the purpose of the geotechnical research. Therefore, a comprehensive material study is conducted to establish the primary characteristics of the black sand. The material study is discussed later in Section 5.4

5.3.2 The Bridge Abutment

The present study focuses primarily on the geotechnical behaviour of the approach soil in the IABs in response to the periodical movements of the bridge abutment. However, the behaviour of the bridge superstructure and/or the interaction between the abutment and the supporting substructure are beyond the scope of the present study.

The function of the abutment in the current model is first, to retain the backfill soil and second, to apply a uniform and controlled displacements on the retained backfill. Therefore, the bridge abutment can be simulated with any rigid object that exhibits minimal deformation under the lateral soil pressure.

In the experimental model, a rigid steel wall is used to simulate the bridge abutment. The steel wall has been heavily reinforced with a steel frame to assure near-zero deformation during the experiments. Dimensions and more details about the steel wall are discussed in Section 5.5 (Design of the Physical Model).

5.3.3 The EPS Geofoam

The potential use of the EPS Geofoam in the experiments is to serve as a lightweight inclusion between the backfill and the abutment wall. As a highly compressible material, the EPS is an effective inclusion material in reducing the adverse effects of abutment movements in IABs (Hope, 2016; Alqarawi et al. 2020). This is achieved by the so-called *transfer function* of the EPS inclusion which refers to minimizing the displacement transferred from the abutment wall to the approach soil. The transfer function of the EPS inclusion is highly dependent on its stiffness modulus. It was reported that the inclusion efficacy decreases when a stiffer EPS geofoam is used. Therefore, the medium-stiffness EPS geofoam with a density of 20 kg/m^3 is recommended, as a compressible inclusion in IABs, because it has balanced features in terms of its transfer function as well as its capacity to support vertical loads (Alqarawi, 2016)

In accordance with the similarity study outcomes, heavier EPS need to be used in the model. However, as an extremely lightweight material (unit weight less than one hundredth of the black sand), using a high-density EPS, has a negligible impact on the stress levels. For instance, using EPS Geofoam with 40 kg/m^3 density (two times heavier than the medium-stiffness EPS) will only increase the vertical stresses, by 0.2 kPa. On the other side, high-density EPS possesses a higher stiffness which consequently curbs its transfer function. Therefore, it was decided to use medium-stiffness EPS with (density equals to 20 kg/m^3) as a compressible inclusion in the model.

5.4 Investigating the Properties of the Black Sand

5.4.1 Physical Properties of Black Sand

Particles size distribution

The black sand particles are relatively fine with most of the particles sizes ranges between 75 and 150 microns. The sieve analysis results of 200 g specimen of the black sand are illustrated in Table 5.2 and Figure 5.2.

Table 5.2 Sieve analysis data for black sand

Sieve size (mm)	Mass Retained (g)	% Retained	Cumulative % Ret.	% Passing
0.425	0.00	0.00%	0.00%	100.00%
0.250	0.65	0.33%	0.33%	99.68%
0.150	43.10	21.55%	21.88%	78.13%
0.105	67.88	33.94%	55.82%	22.31%
0.075	89.22	44.61%	98.43%	1.58%
PAN	3.10	1.58%	100%	
TOTAL			**199.95**	
D_{10}			0.048mm	
D_{30}			0.104mm	
D_{60}			0.135mm	
C_u			2.81	
C_c			1.67	
Class according to USCS			SP	

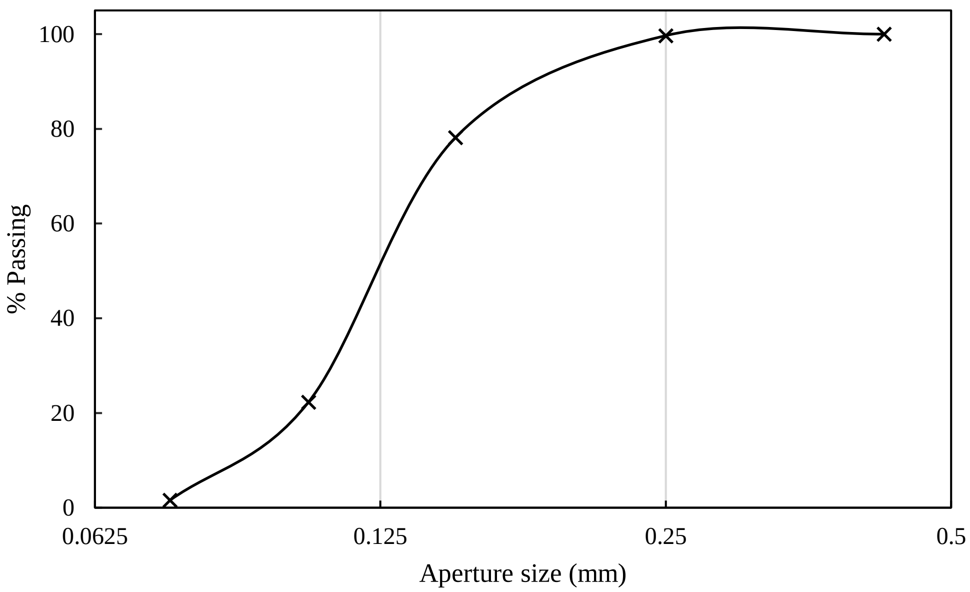

Figure 5.2 Particle Size Distribution of Black Sand

The microscopic images of the black sand, given in Figure 5.3 show that the particles are generally irregular in shape with angular edges.

Figure 5.3 Microscopic images for the Black Sand

Unit Weight

The unit weight of the black sand, in a loose state, has been measured, in the lab, using a digital micro-scale. The measurement was repeated multiple times to achieve an accurate value. The average unit weight of the specimens was 27.2 kN/m^3. This magnitude is sufficiently close to the required unit weight which is 28 kN/m^3.

The maximum unit weight of the black sand is also determined by compacting the sand in a steel mould using a shaking table and a surcharge load. The maximum unit weight is determined as 30.01 kN/m^3.

Specific Unit Weight

The specific unit weight of the grains of the black sand has been determined, in accordance with the Australian Standard AS 1289.3.5.1 (2006), using 500 ml water pycnometer with glass stoppered flask. The de-airing process was conducted using a hot plate to maintain the mixture at the boiling temperature. Weight measurements were taken using a digital micro-scale. A thermostatic soil oven was used to dry the sand specimens during the calculation of the natural moisture content of the sand. Following the directions of the AS 1289.3.5.1 (2006), the specific unit weight of the sand was calculated as 5.16.

Chemical Composition of Black Sand

Unlike the common types of sand, like the silica-sand or the calcium sand, the black sand contains very low silica and calcium carbonate contents. Instead, it contains high levels of Ferric Oxide which gives it a black colour and a heavy unit weight. It also contains small amounts of Aluminium Oxide and Magnesium Oxide. The chemical composition of the Black Sand is summarized in table 5.3.

Table 5.3. The chemical composition of the black sand (Industrial Sand, 2018)

Silica	3.1%
Aluminium Oxide	3.9%
Ferric Oxide	79.5%
Calcium Oxide	1.1%
Magnesium Oxide	3.3%
Loss on ignition	6.3%

As a natural material, the black sand is environmentally friendly and does not pose any hazard to humans during handling. However, standard protection gear, such as dust mask and gloves, has been used during the experiments.

5.4.2 Mechanical Properties of Black Sand

The black sand, in the current study, is used as a backfill to replicate the approach soil in an integral abutment bridge. The mechanical properties of the black sand, hence, must comply with those prescribed earlier by the dimensional analysis study. In accordance with the latter, the backfill soil used in the experiment must be two times heavier than that in the prototype but has similar shear strength parameters, c, ϕ and soil stiffness, E.

As a dry granular cohesionless soil, the shear strength of the black sand depends primarily on its internal friction angle (presumably has a very small or near zero cohesion). Hence, a series of direct shear and triaxial tests are carried out on specimens of black sand to determine its shear strength characteristics.

Triaxial Tests

Four monotonic triaxial tests were conducted on dry black sand specimens using a triaxial test apparatus. The testing system includes a 100 mm diameter triaxial cell with 1.7 MPa pressure capacity, a 50 kN Wykham loading frame and a GDS controller to control the cell pressure. As the tests were conducted on dry samples, the back pressure and the pore pressure were not measured during the tests.

In an attempt to determine the peak and the residual characteristics of the black sand, all the samples were compacted in four equal lifts using a small steel rod to obtain dense samples. Details of the test specimens are given in Table 5.4 below.

Table 5.4 Properties of the triaxial tests

Sample	Height (mm)	Diameter (mm)	Sample weight (gr.)	Unit weight (kN/m^3)	Relative density (%)	Cell pressure (kPa)
1	100	50	578	28.87	70.4	30
2	100	50	581	29.02	74.4	60
3	100	50	579	28.92	71.7	90
4	100	50	583	29.12	77.1	150

In each test, the sample is docked, by having the vertical load cell in contact with the top loading cap, before the cell pressure is ramped up to the required magnitude. When the cell pressure stabilizes, the axial load is applied.

It is understood that the potential confining stresses in the physical model are going to be low (150 kPa or less). Therefore, the tests were all conducted in relatively low cell pressures in order to investigate the shear strength of the black sand at a relatively low confining pressure. The selected magnitudes of the cell pressures (as shown in Table 5.4) are believed to give a very close estimation of the shear strength of the black sand to that in the physical model.

Triaxial Test Results

Shear Strength

The data obtained from the triaxial tests were used to determine the primary characteristics of the black sand. Figure 5.4 shows the deviatoric stress versus the axial strain curves plotted for the four specimens. It is apparent that the behaviour manifested by the specimens is typically known for intially dense cohesionless soil. The peak and the residual strengths of the samples are showed to increased proportionately with the cell pressure as summarized in Table 5.5.

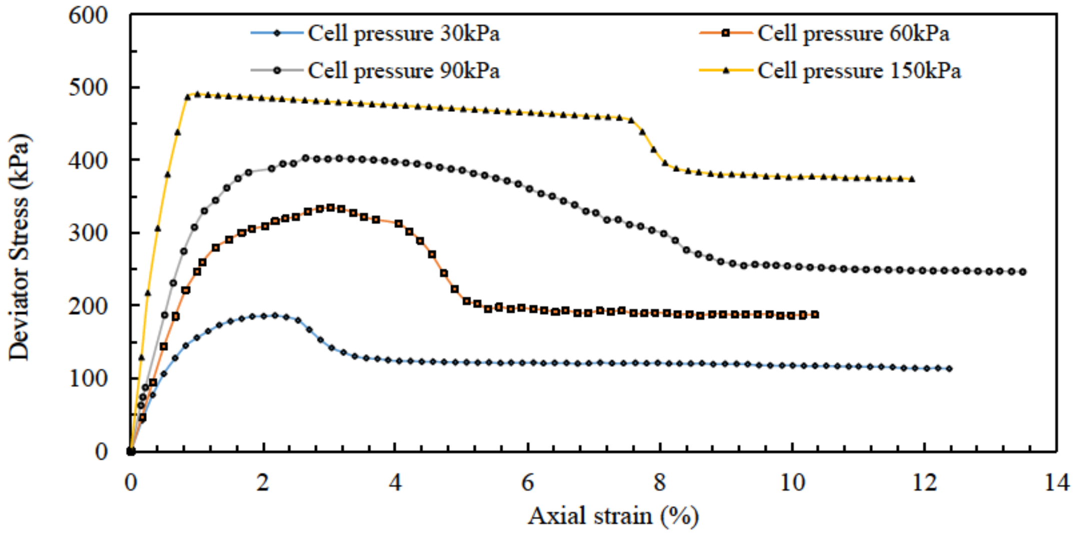

Figure 5.4 Deviator stress vs axial strain

Figure 5.5 shows the Mohr-Coulomb circles constructed based on the critical state strengths of the samples. The Mohr-Coulomb failure surface can be graphically plotted as the tangent to the circles.

Table 5.5 Peak and Residual strength of the samples

Sample	Deviator stress (kPa)	
	Peak	Residual
1	185.3	120.2
2	334.03	189.2
3	402.6	248.05
4	486.3	376.6

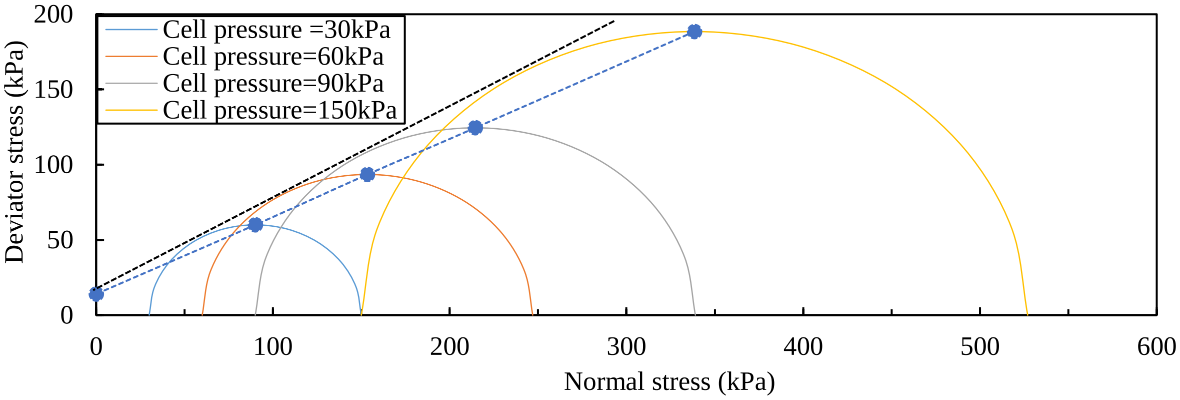

Figure 5.5 Mohr-Coulomb circles

The angle of friction of the black sand associated with, both the peak and residual strengths ($\phi_{critical}, \phi_{peak}$) were determined from the *p*-*q* diagram (where $p = \frac{\sigma_1 + \sigma_3}{2}, q = \frac{\sigma_1 - \sigma_3}{2}$) as illustrated in Figure 5.6

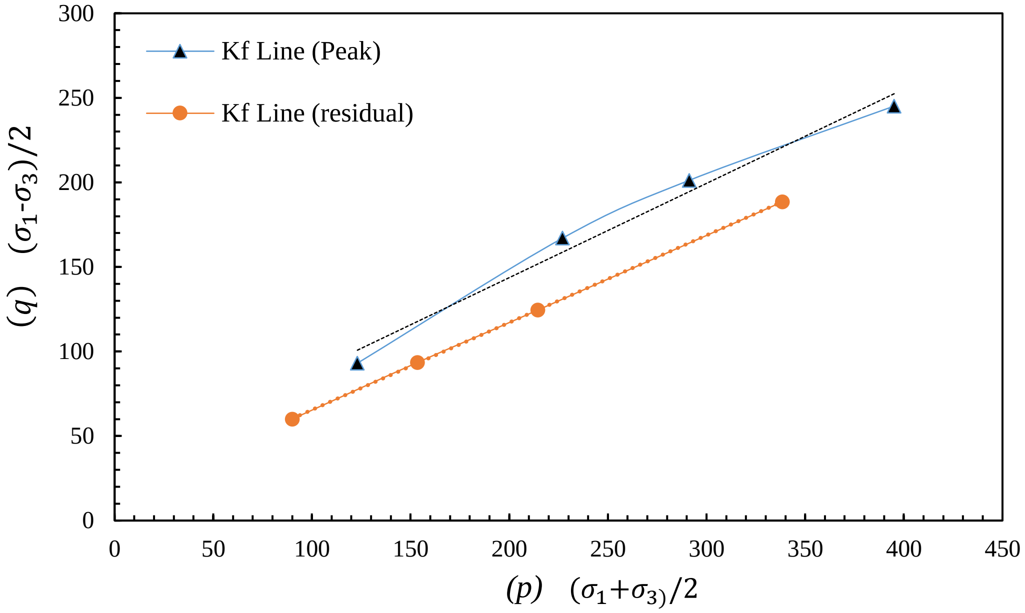

Figure 5.6 The *p*-*q* diagram of the black sand samples

The gradients of the of the k_f lines ($\frac{\partial q}{\partial p}$) are used to compute the friction angles of the black sand as follows,

$$\phi_{peak} = \sin^{-1}\left(\frac{\partial q}{\partial p}\right)_{peak} = \sin^{-1}(0.5575) \approx 34^\circ$$

$$\phi_{critical} = \sin^{-1}\left(\frac{\partial q}{\partial p}\right)_{critical} = \sin^{-1}(0.5163) \approx 31$$

Results also show that the black sand possesses a small magnitude of cohesion estimated as 13 kPa at the residual state which is believed to be attributed to the small percentage of fine particles or silt present in the specimens.

Direct shear tests have also been conducted on black sand specimens. The results indicated an internal friction angle of approximately 31.6° and a cohesion of 5 kPa for loose sand specimens.

Stiffness Modulus

The large-strain modulus of the black sand was estimated from the initial elastic stage in the deviator stress-axial strain curve. The large-strain, E_{50}, is evaluated as the slope of the secant at a 50% of the peak shear strength (50% of q_{peak}). Figure 5.7 illustrates the estimation of the large-strain modulus based on the data of Test-1 (cell pressure = 30 kPa). The values used to determine the E_{50} in this particular case were $q_{50\%}$ which is estimated as 92.65 kPa and the corresponding axial strain $\varepsilon_{50\%}$, estimated as 0.44%. Accordingly,

$$E_{50} = \frac{92.65}{0.0044} = 21 \text{ MPa}$$

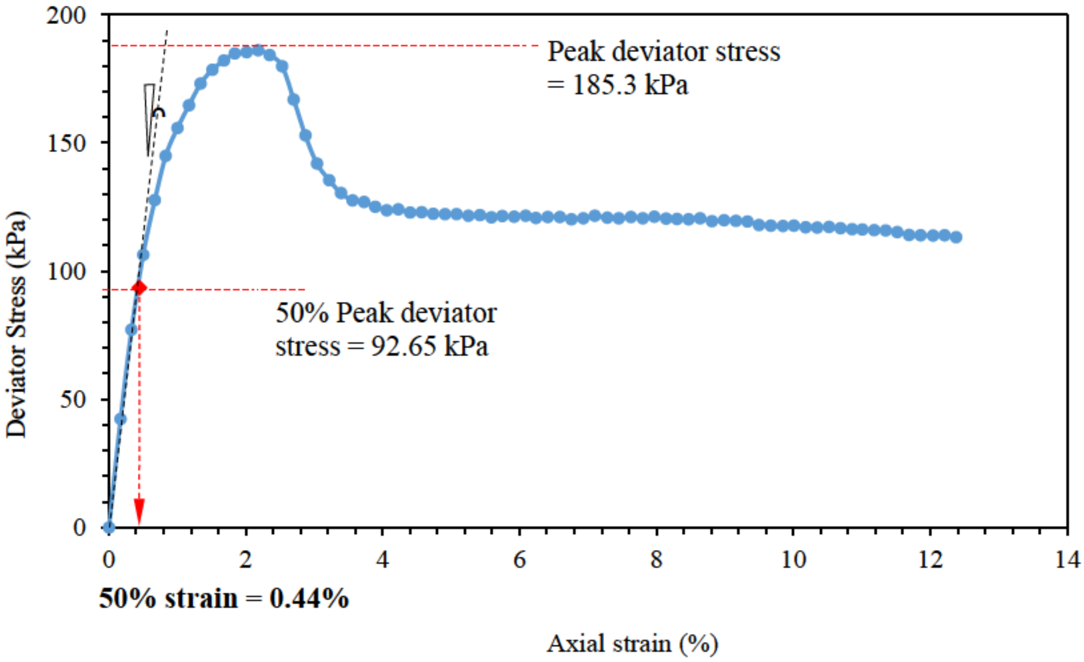

Figure 5.7 Determination of the stiffness modulus of the black sand (E_{50})

However, it is observed that the large-strain stiffness is effectively increasing as the confining pressure increases. This behaviour is predictable in granular soils and is attributed to the increase in the particle interlocking and the frictional resistance which result in an increase in the specimen's skeletal stiffness (Yun et al., 2007). Figure 5.8 shows a plot of the stiffness (E_{50}) of the four specimens against the cell pressure of each test

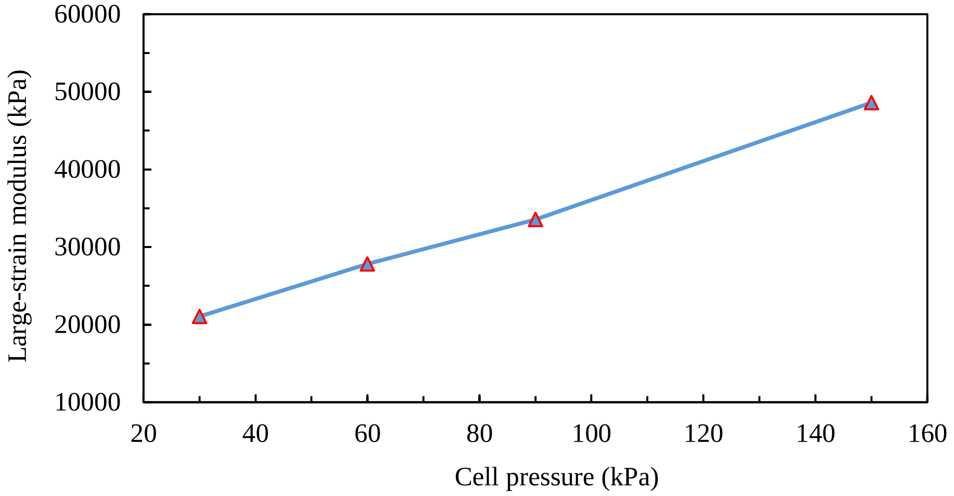

Figure 5.8 Large strain modulus of black sand

Stiffness moduli of the four specimens are given in Table 4.6 Below

Table 5.6 Stiffness moduli for the black sand specimens

Cell pressure (kPa)	Stiffness modulus (MPa)
30	21
60	28
90	33.5
150	49

In view of the calculations of the elastic modulus, it can be observed that the black sand has an elastic modulus ranging between 21 MPa and 49 MPa. These values are close to the stiffness modulus of loose to medium dense sand (Yun et a., 2007).

Poisson Ratio

Similarly, the Poisson ratio ν of the black sand was determined based on the data obtained from the triaxial tests. Knowing that the nominal slenderness ratio, S, of the specimen equals to 2, the radial deformation is suggested to be uniform across the height of the specimen (Farzin et al., 1975). Accordingly, the Poisson ratio is calculated; see equation 5.7, as the ratio between the average change in the radius to the axial displacement (Das, 2007).

$$\nu = -\frac{\Delta_r}{\Delta_a} \tag{5.7}$$

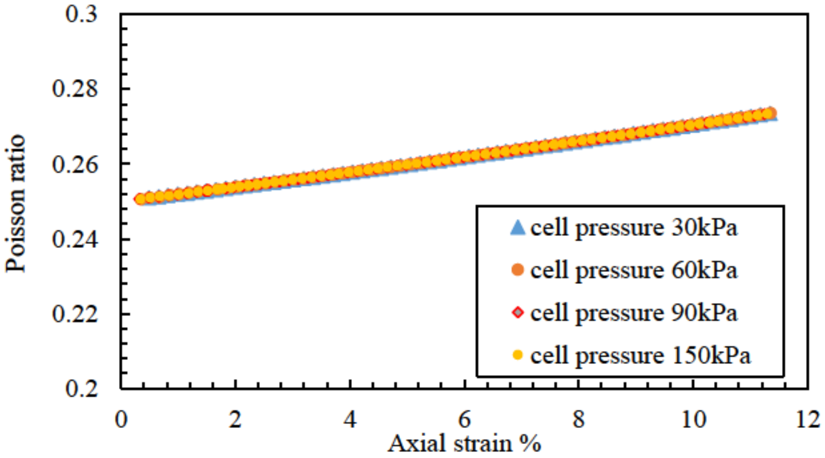

Figure 5.9 Poisson ratio of the black sand

Unlike the stiffness modulus, the Poisson ratio of the black sand is independent of the confining pressure but showed to slightly increase with the axial strain, as illustrated in Figure 5.9. The values calculated from four triaxial tests indicated that it is ranging between 0.25 and 0.27. Hence, an average value of 0.26 is suggested as the Poisson ratio of the black sand.

Dilatancy Properties

According to the triaxial test results, specimens exhibited a dilative plastic volumetric strain for the dense black sand. Figure 5.10 Illustrates the relationship between the total (cumulative) volumetric strain and the axial strain. It is apparent that the behaviour of the specimens is qualitatively identical. They showed a limited or small positive (compression) volumetric strain at the early elastic stage, at an axial strain between 0.5% and 1%. A clear transition in the curve then observed when a negative (dilative) volumetric strain surges at different rates. It is worthwhile mentioning that the soil mechanics sign convention is adopted in describing the volumetric strain, in which the compression is given as positive.

According to Marhana (2009) the dilation angle can be concluded from the dilatancy rate of the specimen during a monotonic compression triaxial test. Marhana (2009) suggested the following equation (equation 5.8) to calculate the angle of dilation ψ ,

$$\psi = \sin^{-1}\left(\frac{\frac{\partial\varepsilon_v}{\partial\varepsilon_a}}{\frac{\partial\varepsilon_v}{\partial\varepsilon_a}-2}\right) \qquad 5.8$$

where $\frac{\partial\varepsilon_v}{\partial\varepsilon_a}$ represents the dilatancy rate and is given by the ratio between the volumetric strain and the axial strain increments.

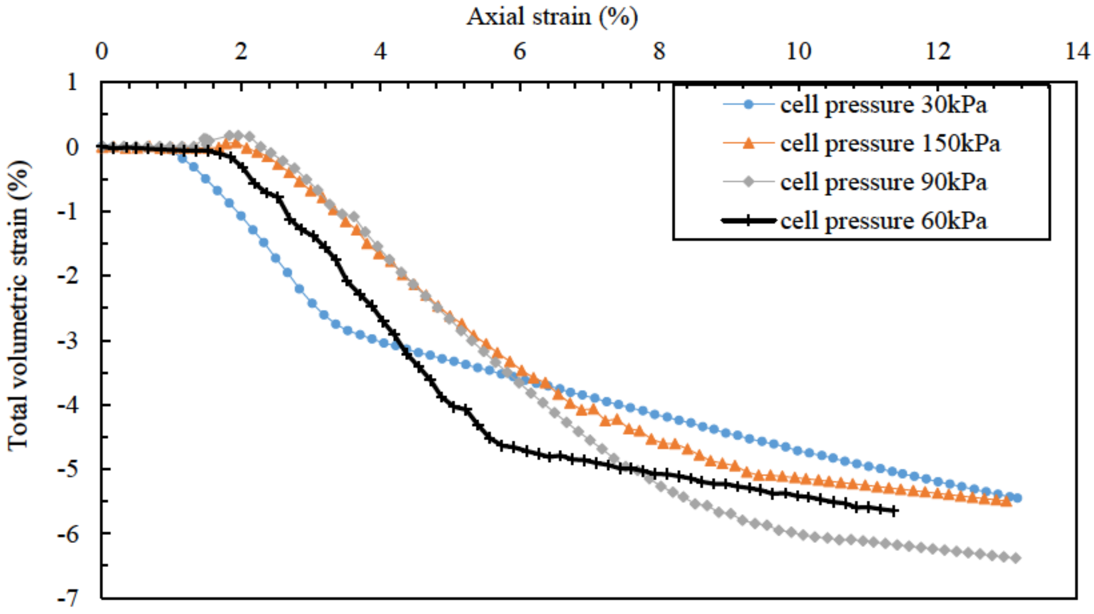

Figure 5.10 Total volumetric strain vs axial strain

To calculate the dilation angle of the black sand, the dilatancy rate is plotted against the axial strain for three different tests (30 kPa, 90 kPa and 150 kPa) as shown in Figure 5.11. It has been noticed that the dilatancy curves involve sharp spikes between some consecutive increments. Therefore, the moving average line is plotted to display a clear trend of the dilatancy rate (depicted by the thick lines). According to Figure 5.11, the maximum rates of dilatancy are attained at axial strains between 2% and 3% for sample 1 (with 30 kPa cell pressure) and between 4% and 5% for samples 3 and 4 (cell pressures 90 kPa and 150 kPa respectively). The aforementioned values of the axial strains coincide with the peak deviator stresses of these tests. This behaviour was also reported by Marhana (2009) when he conducted monotonic triaxial tests on dry cohesionless sand. Using the data given in Figure 5.11, the dilation angle is computed for each specimen using equation 5.8. The maximum dilatancy rates and the computed dilation angles of the samples are summarized in Table 5.7

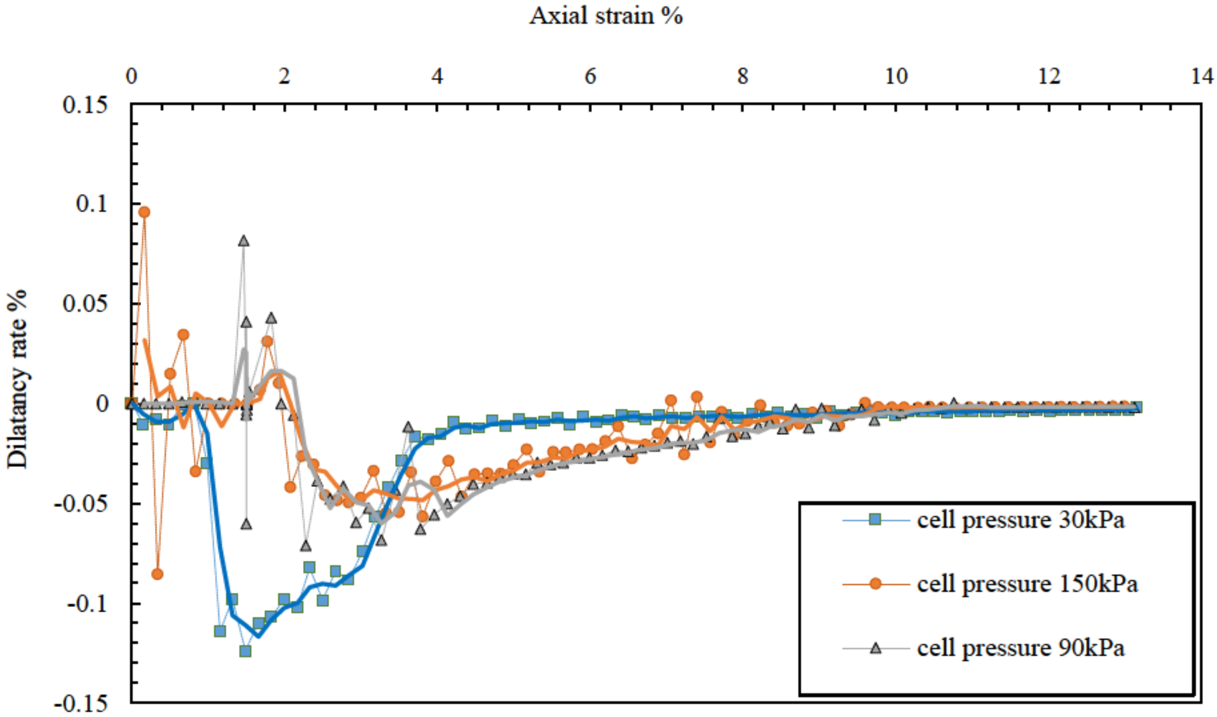

Figure 5.11 Dilatancy rate vs axial strain

Table 5.7 The computed dilation angles of the black sand specimens

Test	Cell pressure (kPa)	Maximum dilatancy rate (%)	Dilation angle ψ°
1	30	-0.12	4
2	90	-0.06	1.8
3	150	-0.05	1.5

Summary of Black Sand Properties

In view of the study of material properties discussed above, a valuable set of data is available for the physical and mechanical properties of the black sand as summarized in Table 5.8. The internal friction and stiffness of the black sand are within the range of the fill materials employed in the field. This ensures that the scale factor of 1 for soil friction and stiffness (Table 5.1) is maintained to achieve similarity. These properties will be implemented later in the computational modelling to study the interaction between the black sand and the abutment wall.

Table 5.8 Properties of black sand

Unit weight (dense)	30.01 kN/m^3
Unit weight (loose)	27.2 kN/m^3
Specific unit weight	5.16
Stiffness modulus, E_{50} (low confining pressure)	21 MPa
Average Poisson's ratio	0.26
Friction angle (peak)	34°
Friction angle (critical state)	31°
Dilation angle	4°
Cohesion	14 kPa

5.5 Design of the Physical Model

This section describes the last stage in the similarity study. The stage of physical Model Design focuses on the process of developing the physical model including all the methods and processes implemented to determine the geometry as well as the dimensions of the model.

5.5.1 Model Description

The model, as illustrated in Figure 5.12, involves a large chamber to accommodate the soil. One of the four sides of the chamber is movable and is depicting the bridge abutment (will be referred to as the “wall”) and hence can be moved in rotational and translational modes. The wall is made of a heavy steel frame covered by 5 mm thick steel sheet forming one rigid unit. The wall is connected to two hydraulic cylinder each with 25 tons load capacity to move the wall during the test. Behind the wall, a supporting steel frame is installed and fixed to the floor to provide a rigid support for the hydraulic cylinders. The wall is fitted through the chamber with only 5 mm gap around it. Teflon strips are fixed on the edges of the wall to close the gap around the wall and to minimize the friction between the wall and the sides of the chamber during the test.

The left side of the tank is made of 25 mm thick clear acrylic perspex, full-size, sheet braced by horizontal and vertical steel sections. This side was made clear to allow for visual observations during the test. The right side of the tank is made of 5 mm thick steel sheet braced by a steel frame. In order to maintain a similar surface friction over the left and the right sides, the latter was covered with 5mm thick acrylic perspex sheet similar to the one used in the left side. The model development has been given careful attention to the supporting frame as well as the soil chamber to achieve sufficient rigidity to avoid any deflections or distortions that might occur due to the potential lateral confining stress.

The design of the model, including the determination of its dimensions, has been conducted as a part of the present research, however, the mechanical drawings and fabrication of the model was carried out in Sydney-Australia, by PROGRAMMED Industrial Services. The latter is a leading Australian company specialised in the industrial equipment fabrication and maintenance. The test chamber parts were delivered to Western Sydney University and assembled by professional staff from PROGRAMMED.

5.5.2 Dimensions of the Model

The dimensions of the model (*Length, Height & Width*) as they appear in Figure 5.12 are determined, in accordance with the outcomes of the similarity study as well as the test requirements. The design criteria of the model are discussed in detail in the following sections.

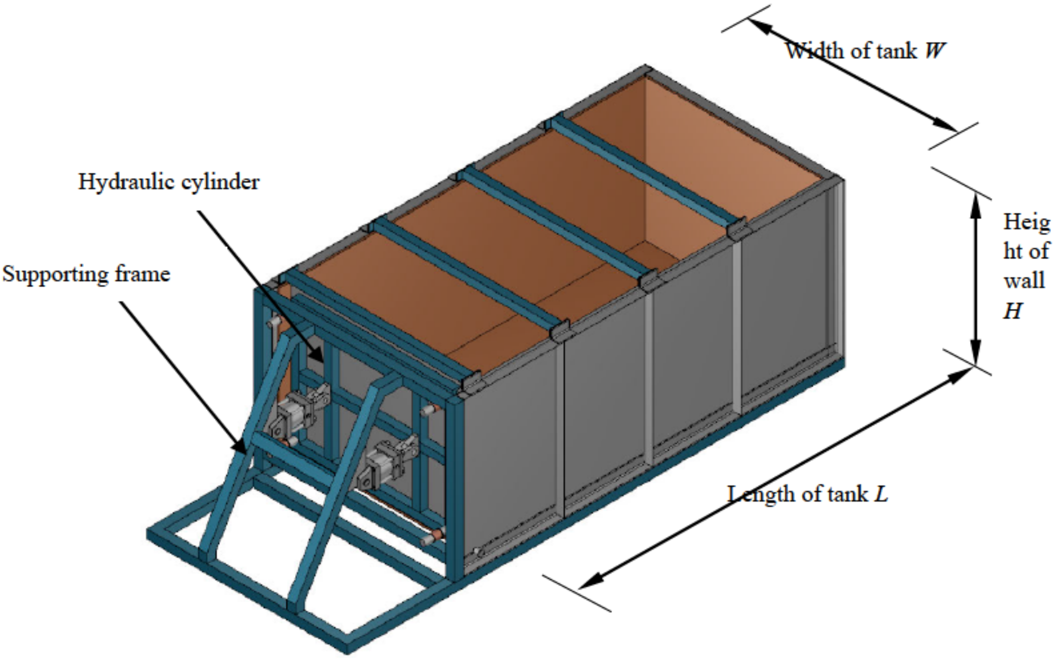

Figure 5.12 The experimental model

Height of the Wall (H)

The front side of the model, as mentioned earlier, is replicating the bridge abutment wall in the full-scale prototype. Therefore, its height must correlate well with the height of an abutment in a typical integral bridge according to the dimensional analysis discussed earlier, which in this case the scale model height: prototype height is one-half. In the present study, based on a review of published literature and data from in-service IABs, height of the wall (*H*) in the model was determined.

Kunnin and Alampali (1999) reported a survey conducted on in-service IABs in 38 states in the United States and Canada. Among the data collected during the survey are the guidelines adopted by each state concerning the height of the abutment. The survey showed that most of the participating states (about 70% of the responses) have no guidelines that set a specific value or boundary limits for the abutment height. The rest of the states indicated different limitations on the abutment height and that varied between 0.9 m and 4.6 m.

The British Standards BA42/96 (1996) and PD66/94 (2011) did not stipulate specific recommendations about the abutment height in IABs. However, it was stated, in the BA42/96 (1996), that the height of the Bank Pad or the End Screen abutments, which are generally short to medium height abutments, should not exceed 3 m.

The data reported in previous studies about in-service IABs also show a similar uncertainty regarding the height of the abutment. Table 5.9 summarizes the details of the abutments used in selected in-service IABs.

Table 5.9 Abutment height in number of in-service IABs

Location	**Abutment height (m)**	**Abutment type**	**Reported by**
New Brunswick - Canada	4	Full-integral	Huntley & Valsangkar, 2013
Alleghany County, VA -USA	1.83	Semi-integral	Hoppe, 2005
Orange-Wendell, MA - USA	2.94	Full-integral	Civjan et al., 2007
Rockingham, VA-USA	1.35	Semi-integral	Hoppe & Gomez, 1996
Gyungsangnamdo – South Korea	4	Full-integral	Nam & Park, 2014
Central, PA- USA	3.5	Full-integral	Kim & Laman, 2012
Rochester MN - USA	1.5	Full-integral	Lawver et al., 2000

In view of the information reviewed above, it is understood that the height of the abutment in IABs is a design issue and it varies according to the type of the abutment (full integral abutment or semi-integral abutment), the design requirements of the bridge as well as the nature of the supporting substructure. Considering this fact, the height of the front wall of the model is selected as 1.1 m, which corresponds to a 2.2 m high abutment in a prototype (according to the dimensional analysis). This value falls perfectly within the range of the realistic abutment heights, as appears in Figure 5.13, and forms a manageable wall size.

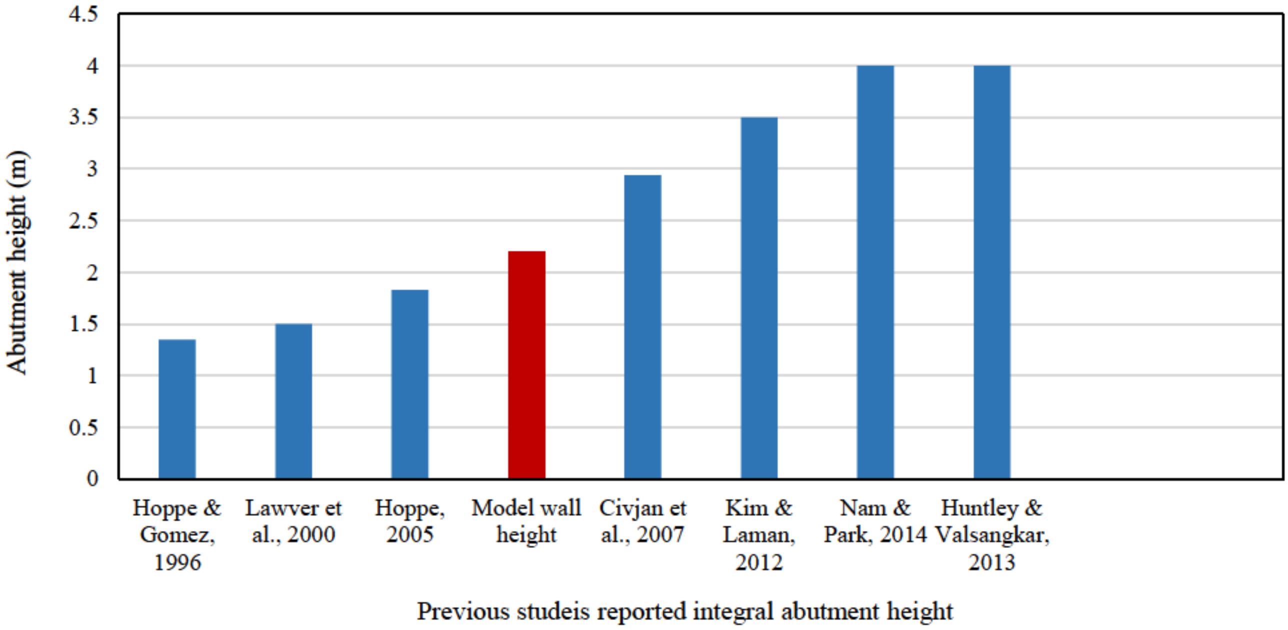

Figure 5.13 The selected height of the wall compared to abutment heights reported in previous literature

The length of the Tank (L)

The length of the tank, as illustrated in Figure 5.12, refers to the distance at which the backfill extends behind the abutment. This dimension in the model is critical to eliminate the boundary effects emerged from the rear wall of the tank. During the test, the soil may reach to a full active or passive state in response to the wall movements. As a plane-strain case, the failure plane (active or passive) occurs in the longitudinal direction of the chamber. This, however, requires the chamber to be long enough to include the entire failure surface without the latter cutting through the rear side of the chamber. Therefore, the minimum length L to satisfy this criterion must be determined.

According to Rankine (1857), the passive failure plane is planar and inclined by $(45-\phi/2)$ to the horizontal, as appears in Figure 5.14.

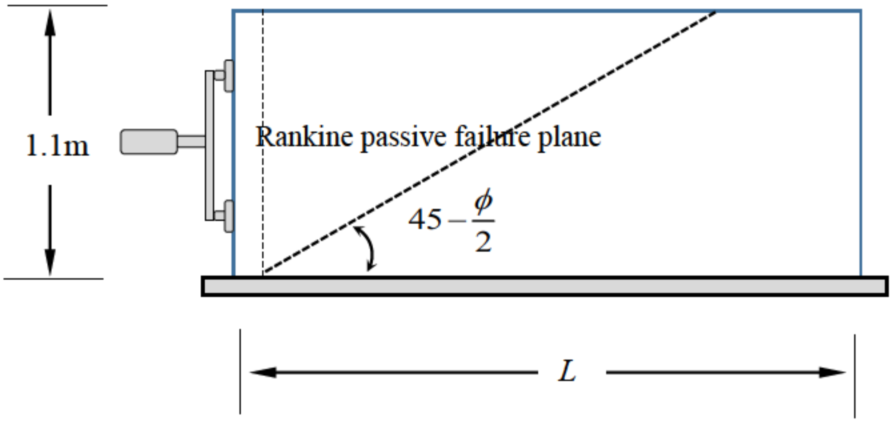

Figure 5.14 Rankine passive failure plane

Taking into account the height of the wall is 1.1m, and the friction angle of the black sand is 34° (determined earlier), the minimum length of the tank is calculated as,

$$L=\frac{1.1}{\tan\left(45-\frac{\phi}{2}\right)}=\frac{1.1}{\tan\left(45-\frac{34^\circ}{2}\right)}=2.7\text{ m}$$

In order to further examine the boundary effects during the wall movements, a three-dimensional numerical model was developed using the ABAQUS Standard (2017) finite element software (more details about the FE model are discussed in Chapter 7). The initial length of the model was first set to 1 m and then increased by 0.5 m in each trial. Thirty cycles of ± 30 mm wall translational displacements were applied to observe the effects the boundary effects.

The modelling results showed that the reaction forces at the rear side of the chamber become insignificant when the length *L* reaches 2.5 m. In view of the criteria above, the length of the tank (*L*) is decided to be 3 m to safely contain the potential failure surface during the tests.

The width of the Tank (W)

The experimental model replicates a plane-strain interaction between the soil and the abutment. Theoretically, the width of the model should not present as a design variable, in a plane-strain case. However, due to the potential interface friction between the soil and the sides of the chamber, it is important to consider a sufficiently wide chamber so that the total frictional force is insignificant compared to the lateral soil thrust.

It has been suggested to maintain the ratio between the frictional force (*F*) (acting on the soil-perspex interface) and the total horizontal soil thrust (*P*) less than 10%. The numerical model, developed earlier, was used to check the ratio F/P considering an initial value for the chamber width equals to 1.5 m. The parameters utilized in the model are given in Table 5.10

Table 5.10 Parameters used in the ABAQUS model

Sand				Sand-Perspex friction angle $(\delta_1)^\circ$	Sand – Steel friction angle $(\delta_2)^\circ$
Unit weight (kN/m^3)	Internal friction angle (ϕ)	Poisson ratio (ν)	Dilation angle (ψ°)		
28.27	34	0.26	4	12	20

The results of the ABAQUS Standard (2017) modelling indicated a ratio F/P of 8.2% is achieved at the given conditions. Accordingly, the suggested chamber width, (*W*=1.5 m) is sufficient to keep the frictional effects within insignificant margins.

Finally, the selected dimensions of the experimental model chamber are as follows:

- The Wall is 1.1 m high.

- The tank is 3 m long, 1.5 m wide and 1.2 m high. The sides of the tank were made slightly higher than the wall to prevent the sand from spilling over during the passive wall movement.

5.5.3 Handling of Sand

The process of handling the sand during the experiment involve the conveyance and deposition of sand into the tank and the removal of sand from the tank after completing the experiment. This process requires the planning of the following activities,

- Deposition of sand in the tank
- Design a mechanism to convey the sand into and out of the tank

Deposition of Sand

The sand is deposited in the test chamber via air pluviation using a mobile sand-raining system that is customized for this purpose. The advantage of air pluviation is to achieve a uniform soil configuration, in the test chamber, similar to a homogenous natural deposit. It also helps to deposit the sand in a controlled manner to produce consistent backfill density.

Previous research studies observed that the unit weight of the soil deposited by free air pluviation is a function of the falling height, which is the vertical distance from which the soil is disposed (Khari et al. 2014; Tabaroi et al. 2017). Therefore, it is necessary to evaluate the disposal height to be used in the experiment. Several sand-raining tests were carried out to identify the relationship between the unit weight of the black sand and the disposal height. The tests were conducted by raining the sand through a pair of sieves, with 1 mm aperture, into a collecting pan from different heights. At the end of each test, the unit weight of the deposited sand is calculated. Figure 5.15 shows the relationship between the disposal height and the unit weight of the black sand.

The optimum disposal height in this case, is that corresponding to the maximum unit weight. According to Figure 5.15, the maximum unit weight achieved during the test was 28.276 kN/m^3 and was obtained at a disposal height of 400 mm.

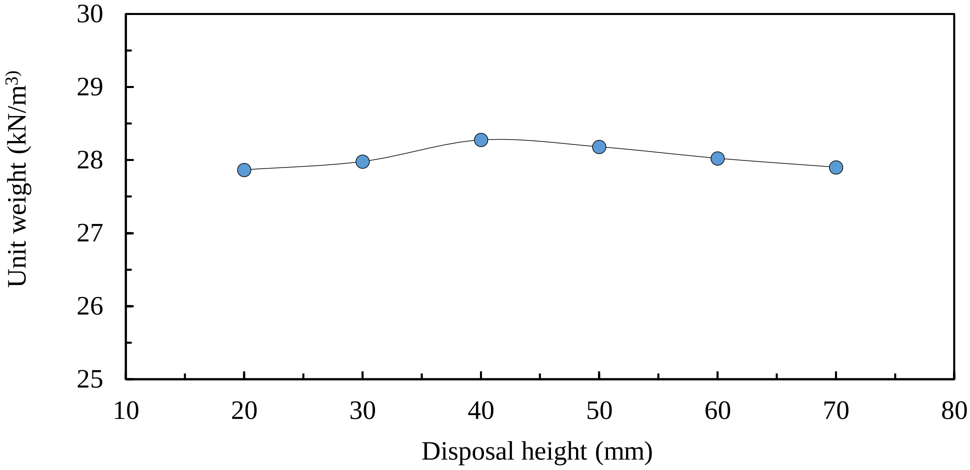

Figure 5.15 Unit weight of black sand vs. disposal height

It is understood that the water content in the backfill soil affects its density. However, this thesis discusses the effects of backfill density without necessarily linking it to the moisture content. Therefore, in the physical model, dry backfill soil will be used in all tests.

The Sand Conveyance System

During each test, the tank is filled by raining the sand using the mobile pluviator. After completing the test, the sand is moved back to the storage bags before conducting a new test. This handling process is carried out by a conveyance system that was developed for this purpose. The conveyance system consists of;

- Flexible screw conveyor
- Mobile lifting crane
- Sand raining box

The screw conveyor transfers the sand from the storage bags into the raining box. The conveyor intake is buried inside the sand while the outlet is positioned on a 2.6 m high steel frame to allow for a continuous flow into a sand raining box. The latter is attached to a mobile overhead crane using a wheeled trolley. The mobile crane moves, forth and back, in the longitudinal direction of the chamber while the trolley is moving horizontally along the crane transverse beam. The height of the raining box is adjustable and is controlled by an electrical motor. The system components work collectively to allow for the movements of the raining box in three orthogonal directions. Figures 5.16 and 5.17 show photos of the test chamber and the conveyance system.

Figure 5.16 The test chamber

Figure 5.17 The conveyance system

5.5.4 Instrumentation

Three pressure transducers have been attached to the wall at different positions, $\frac{H}{3}$, $2\frac{H}{3}$ and 10 cm from the bottom of the wall (*H* represents the height of the wall) as appears in Figure 5.18. Another pressure transducer is positioned at the centre of the rear wall of the tank. The readings of this pressure cell are used to evaluate the potential boundary effects emerged from the rear wall of the tank.

Two LVDTs are positioned at the top and bottom ends of the wall to measure the displacement during the test. The readings from the pressure transducers and the LVDTs are simultaneously communicated to a computer using a GDS data logger. High definition camera was used to take images to the side of the tank to track the changes developed during each test.

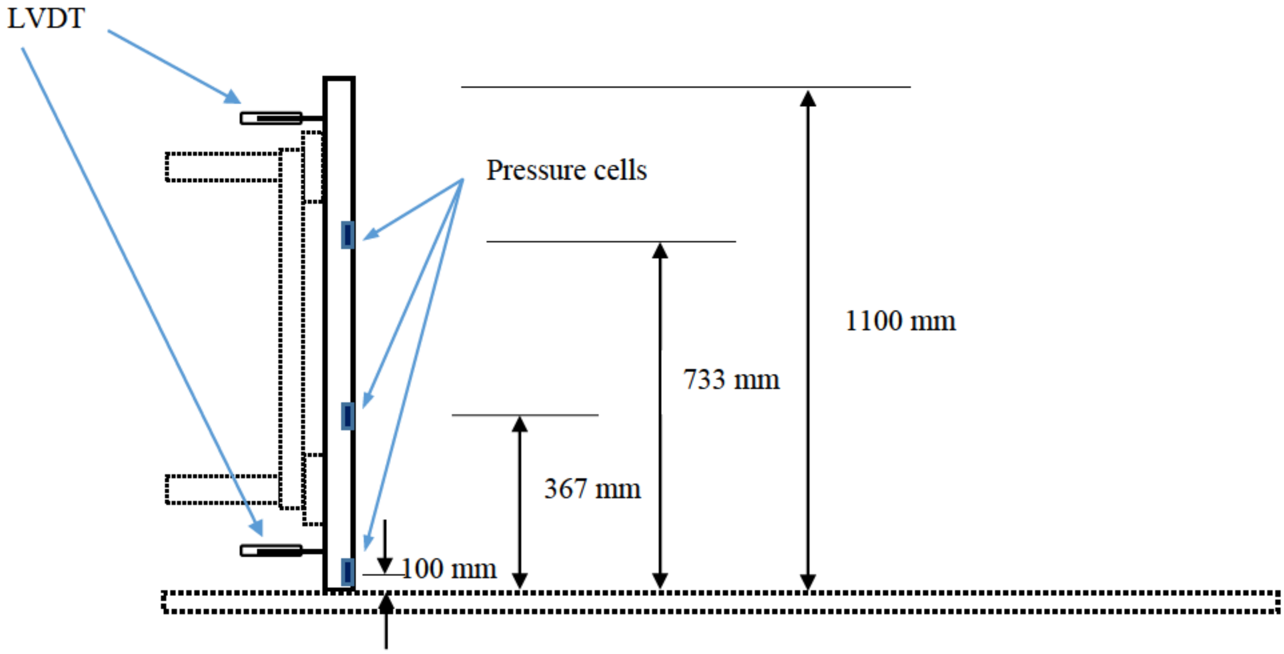

Figure 5.18 Schematic diagram of the wall

5.6 Conclusions

This chapter discusses the development of the physical model used in the experimental study in this thesis. Investigating the physical and mechanical properties of the black sand have also been discussed in this chapter. In view of these discussions, the following conclusions have been drawn:

- The outcomes of the dimensional analysis revealed that, at a normal gravity (g), certain measures must be considered to maintain the similarity of a half-scale physical model with the real prototype dimensions. Among these measures is to use a soil that is two times heavier than the normal soil as a backfill material.
- The black sand is a naturally heavy soil with a unit weight equals to, approximately, two times of a typical backfill soil. In spite of being extremely heavy, the black sand possesses regular granular behaviour and mechanical properties that are identical to a typical cohesionless backfill soil. This makes the black sand an excellent choice for the backfill soil to be used in a half-scale physical model.
- The test chamber together with the materials discussed in the chapter will be used to conduct experimental tests that, qualitatively and quantitatively, replicate the interaction behaviour, in IABs, in real world prototype dimensions.

Chapter 6

Large Scale Physical Model Tests

6.1 Introduction

Physical models have been utilised by a number of research studies to model the soil-structure interactions in IABs. These physical models are classified into scaled model tests at normal gravity (England et al., 2000; Cosgrove and Lehane, 2003; Tatsuoka et al., 2009, Khasawneh, 2014), scaled model tests at high gravity (Springman et al., 1996; Ng et al., 1998; England et al., 2000, Lehane, 2003) and full-scale prototype model tests (Thomas and Lutenegger, 1998; Tatsouka et. al, 2014; Huang et al., 2020). The principle variation among these methodologies is in the degree of similarity with the relevant aspects of actual or real world case in terms of the stress levels, soil constitutive behaviour and the consequent deformations.

In this chapter, a scaled physical model tests are used to conduct an experimental study on the soil-structure interaction in IABs. The similarity of the present half-scale model to the full-scale prototype has been discussed earlier in Chapter 5. The primary objectives of this experimental program are to:

- Evaluate the passive soil resistance to a controlled monotonic wall displacement.
- Provide an insight into the soil-structure interaction behaviour under different modes of abutment movements (rotation and translation) with emphasis on the lateral earth pressure and the deformations in the retained soil.
- Investigate the effectiveness of using a medium-stiffness expanded polystyrene geofoam (EPS) block, as a compressible inclusion to alleviate the effects of the wall movements.

6.2 The Test Program

The experimental program discussed in this chapter involves four tests by varying two principle parameters as described below:

6.2.1 The Mode of Abutment Movement

In IABs, the abutment moves in response to the expansion and contraction of the bridge deck. The research studies show that, the abutment movement is often a combination of two different modes, rotation and translation (Springman et al., 1996). This means the abutment will translate and rotate at the same time as a result of deck expansion and/or contraction. The reported field data showed that the rotation and translation movements are usually unequal and the domination of either mode is dependent on various factors including the type and height of the abutment, the type of the substructure and the properties of backfill (Huntly and Valsangkar, 2009). Generally, short abutments, such as semi-integral abutments, tend to translate more compared to full integral abutments, where the dominant movement mode is rotation. Accordingly, pure translation and pure rotation are defined as the limiting modes of movement for the abutments in IABs.

The mode of the movement, translation or rotation, has a significant impact on the magnitude and the distribution of the lateral earth pressure acting on the abutment (Huntly and Valsangkar, 2013; Alqarawi et al., 2017). It also affects the size and depth of the potential settlement trough in the approach soil. The latter forms an important criterion in the design of the approach slab and acceptability of the serviceability of the design. Therefore, investigating the variations imposed by the mode of abutment movement will broaden the existing knowledge about the approach issues in IABs and their possible remedies.

However, a rigorous analysis that quantifies such effects in IABs is currently unavailable; therefore, the present experimental program will examine two modes of wall movements,

- Translation: in this test, the wall will be moved in an absolute translation toward and away from the soil as shown in Figure 6.1.a. The actuating forces are applied at the top and the bottom of the wall.
- Rotation: in this test, the wall movement is restrained at its bottom end so that it can only rotate without any translation. The actuating force in this case is applied at the top end of the wall as shown in Figure 6.1.b.

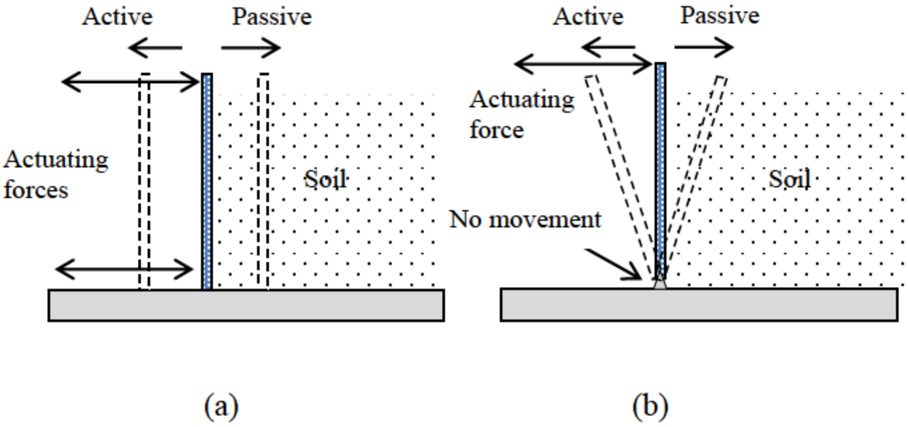

Figure 6.1 Modes of wall movement investigated in the test program (a) pure translation and (b) pure rotation

6.2.2 The Compressible Inclusion

The compressible inclusions reported in the IABs literature are generally classified into collapsible and non-collapsible inclusions. The term collapsible refers to a material that may collapse if no retaining element is provided, such as the rubber chips or tyre shreds. However, an experimental study in South Dakota, USA showed that the tyre shreds, in the inclusion layer, continuously rearranged, as a results of abutment movements, and eventually settled leaving a small trough at the top of the inclusion layer (Reid et al., 1999). This showed that the collapsible inclusion behaves as a granular fill but with significantly larger grains. Therefore, grain rearrangement will occur and will result in a settlement at the surface but to a smaller extent. This study utilises a non-collapsible inclusion.

It is believed that the stiffness of the inclusion and its intended function are both equally important and need to be carefully considered. The inclusion is supposed to minimise the lateral earth pressure but not to substantially eliminate it. As discussed earlier, the lateral backfill pressure in IABs is yet beneficial in maintaining bridge stability such as the case of skewed semi-integral bridges. Moreover, the inclusion must possess sufficient stiffness to carry the vertical loads without excessive deformations. Accordingly, using an extremely low-stiffness inclusion may involve some negative impact on the integrity of the abutment-backfill system.

In this study, a medium-stiffness EPS geofoam has been used as the compressible inclusion. The performance of medium-stiffness EPS geofoam has not been experimentally evaluated in prototype experimental settings. Therefore, the outcomes of the current experimental program will provide valuable insights into the potential application of medium-stiffness EPS as inclusions in IABs.

6.2.3 Types of Tests

The present experimental program involves four tests, as shown in Table 6.1. One test will be conducted for each loading case, monotonic, cyclic-translation, cyclic-rotation and cyclic-translation-with EPS inclusion. As large-scale tests, each test consumed significant resources and time. Hence each test has been managed carefully and unless errors are observed, repeat tests were not undertaken.

It is worth noting that this study aims to obtain an insight of the fundamental soil-structure interaction by separately studying purely translational and rotational abutment movements. Composite, rotational-translational, movements are considered outside the scope of this thesis.

Table 6.1 Descriptions of the large scale experiments

Test type	Test number	Type of movement	Amplitude
Monotonic	T1	Monotonic - translational movement	Monotonic displacement
Cyclic	T2	Cyclic - rotational movement	$\pm \Delta / H = 2\,\%$
Cyclic	T3	Cyclic - translational movement	$\pm \Delta / H = 1\,\%$
Cyclic	T4	Cyclic - translational movement with EPS inclusion	$\pm \Delta / H = 1\,\%$

Note: the ratio Δ / H *represents the normalised wall movement*

It is worthwhile mentioning that the use of EPS inclusion will be evaluated only for the cyclic-translational movement, because this mode of movement depicts the most severe condition in terms of the consequent settlement and earth pressure escalation.

6.2.4 Test Preparations

Each experiment described in this chapter involved set of preparation activities, beginning with the preparation of equipment, deposition of soil inside the tank and ending with removing the sand from the tank at the end of the test. Among the activities that required careful control is the deposition of soil inside the tank. Due attention was given to perform this activity in a consistent manner to achieve a similar soil density among the different tests. As a control measure, samples of the deposited soil were taken, from different levels, to measure the density of the soil in each test. ten cups, of predetermined volume, were distributed on the surface of the soil to collect the soil samples (see Figure 6.2). The collected samples were then used to calculate the relative density of the soil. Figure 6.3 shows the average unit weight of samples measured during the tests. It is worthwhile noting that, the reading form one of the cups was eliminated due to a damage that affected its standard volume. Therefore, only nine readings for the density were taken.

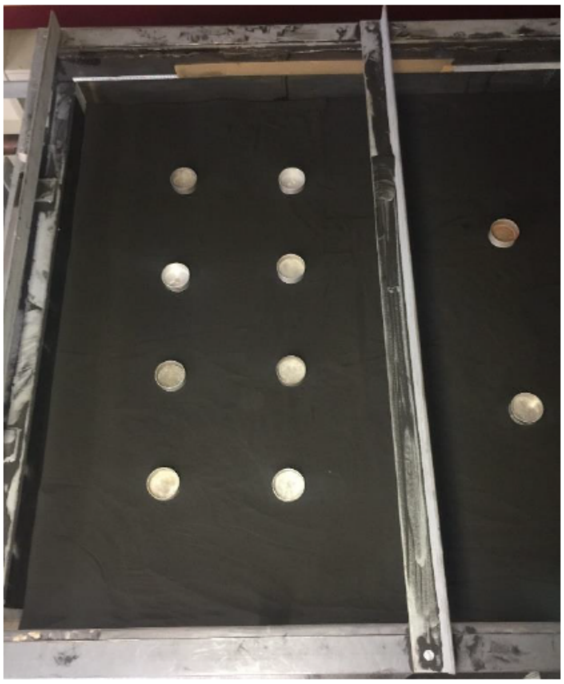

Figure 6.2 Soil samples collected during the soil deposition (top view)

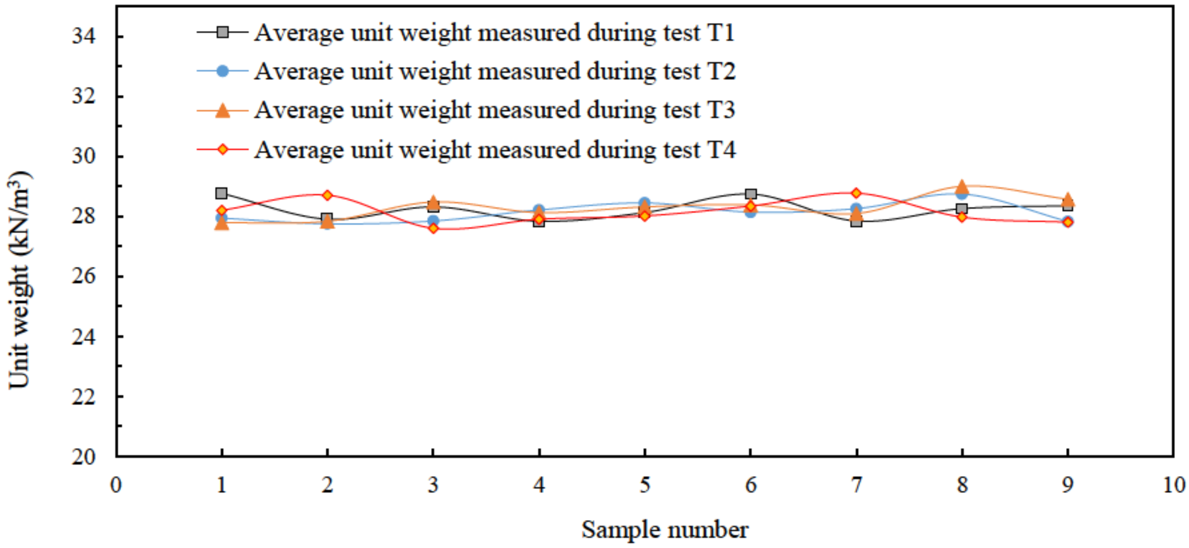

Figure 6.3 Density of deposited soil

According to Figure 6.3 the average unit weight of soil in the model tank was 28.2 kN/m^3. Considering the maximum and minimum unit weights and the specific unit weight of the black sand (as discussed in Chapter 5), the relative density and the void ratio of the soil in the test chamber were determined as I_d = 51.8% and e = 0.79 respectively.

6.3 Discussion of Test Results

6.3.1 Test T1

6.3.1.1 Recorded Lateral Pressures

The purpose of this test was to quantify the response of the black sand to a monotonic translational passive wall movement. The outcomes of this test will provide realistic data to;

- Further validate the log-spiral solution (developed in Chapter 3)
- Provide a benchmark for the magnitude and distribution of the lateral earth pressure to compare with those obtained from other tests conducted under cyclic movement.

During this test, the wall was displaced monotonically into the passive side (toward the soil) at a rate of 1 mm/min. The test was ended at a total displacement equals to 170 mm, where an excessive passive slippage became visible and the pressure readings were decreasing or relatively stable.

The lateral earth pressure recorded in the pressure cells increased immediately after the wall was moved and continued to increase, then asymptote at different displacements. Figure 6.4 shows the lateral earth pressures recorded during the test T1.

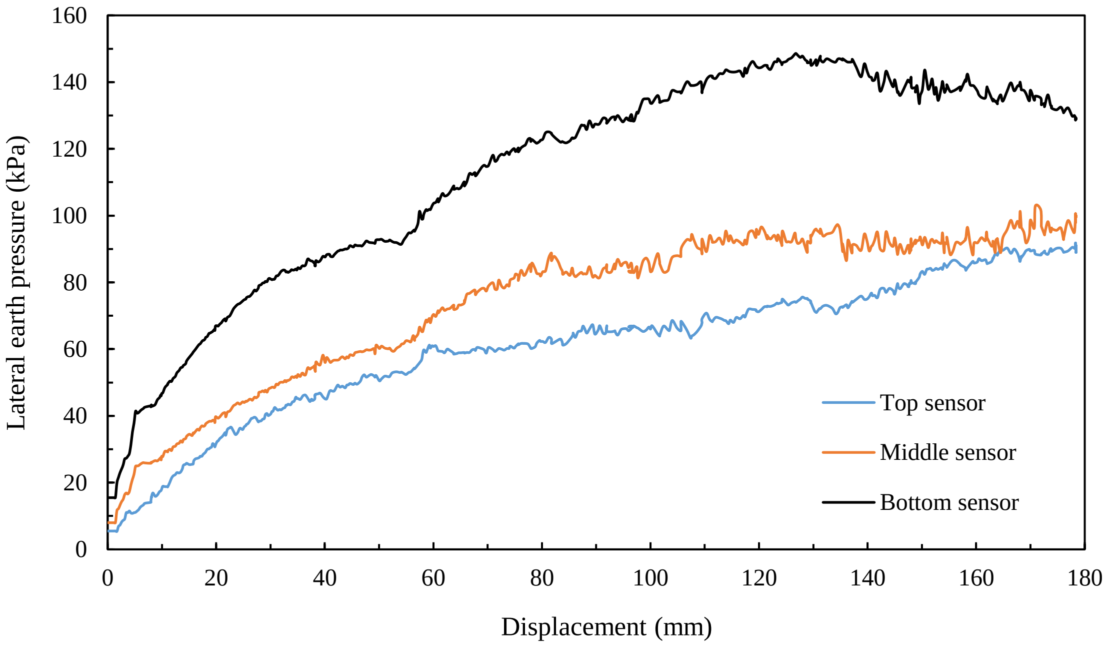

Figure 6.4 Lateral pressure vs wall displacement, test T1

It is apparent that, the pressure-displacement relationships at the three sensors are qualitatively different. This is attributed to the different confining pressures at different depths. Evidently, the soil at the bottom sensor is subjected to a higher confining pressure than other sensors. Therefore; the pressure-displacement curve, based on the readings from the bottom sensor, showed notable peak followed by a decrease in the lateral earth pressure. This behaviour was not observed in the middle and top sensors, where the pressure-displacement curves were relatively flat.

Prior to the test, the soil developed a right triangular lateral pressure (at-rest pressure) varying from 5.5 kPa, at the top sensor, to 15.3 kPa at the bottom sensor. During the test, the pressure increased, and its distribution changed progressively, from right triangular, to a trilinear as shown in Figure 6.5. The maximum lateral pressure recorded in this test was 148.7 kPa and was recorded by the bottom sensor at a relative displacement, Δ/H, equals to 12.7%.

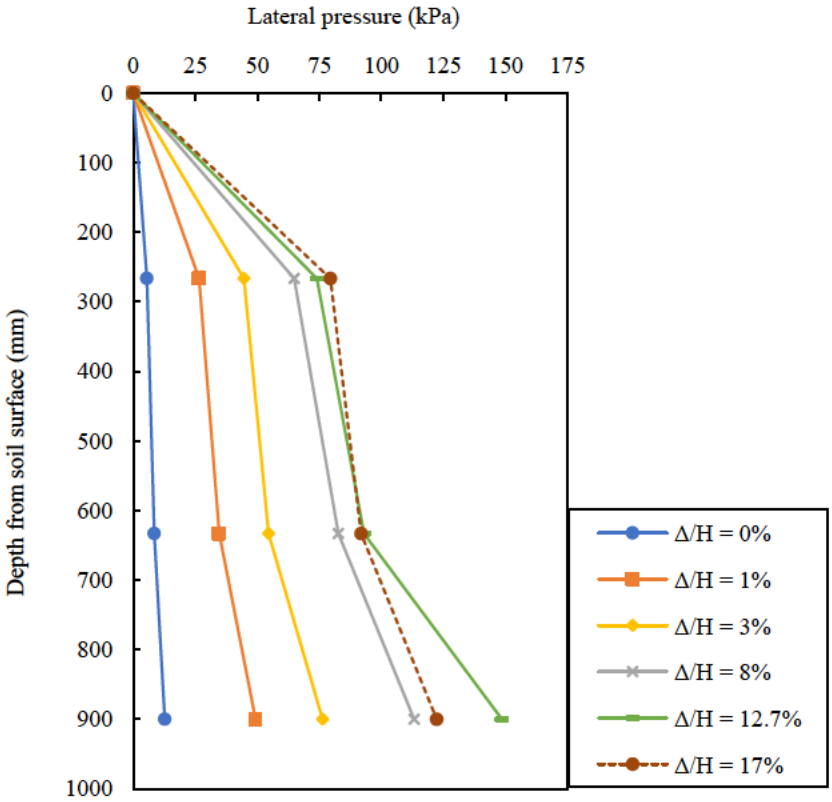

Figure 6.5 Vertical distribution of lateral earth pressure, test T1

6.3.1.2 Coefficient of Passive Earth Pressure

Among the primary objectives of this test, is to quantify the passive earth pressure coefficient of the soil, K_p. The magnitude of the mobilised earth pressure coefficients, during the wall movement, were calculated assuming a triangular area equivalent to the area delineated by the lateral pressure profile. The magnitude of the pressure at the bottom of the wall is extrapolated from those in the middle and bottom sensors.

The magnitude of the mobilised earth pressure coefficient, then computed using equation 6.1

$$K = \frac{2A}{\gamma H^2} \tag{6.1}$$

where A is the area outlined by the pressure profile, γ is the unit weight of the soil and H is the total retained height of the soil (in test T1, H = 1 m). The values of the earth pressure coefficient, K, are plotted against the normalized displacement Δ/H as shown in Figure 6.6.

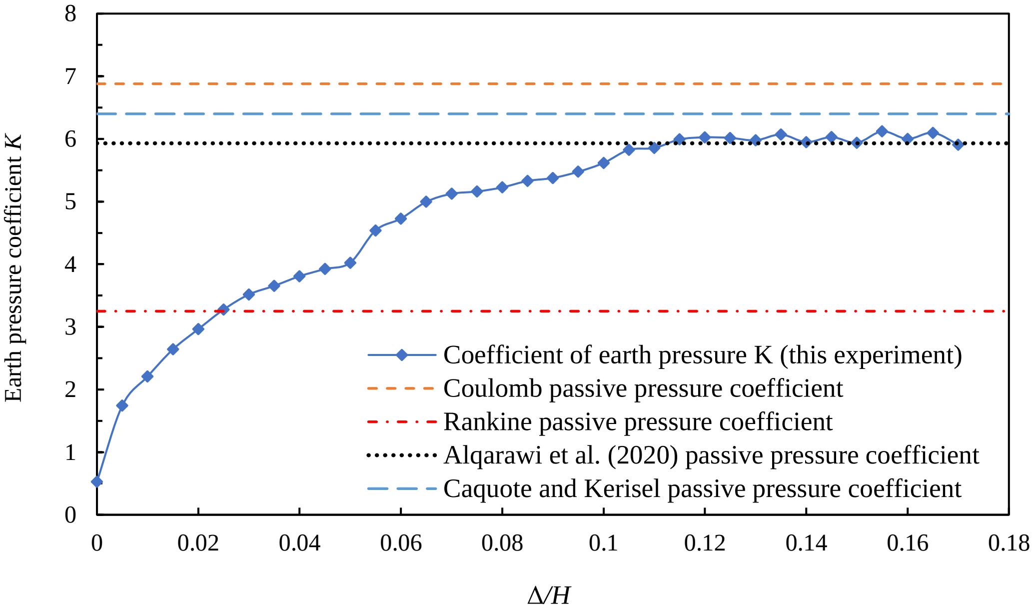

Figure 6.6 Earth pressure coefficient K vs the normalized wall movement (Δ/H), test T1 (H=1 m)

It can be observed that, the magnitude of lateral earth pressure coefficient K, increased steadily with the wall movement, then asymptote at a relative displacement, Δ/H, between 11% and 12%. The value of the passive earth pressure coefficient, K_p, is concluded as 6.07 which corresponds to the maximum value recorded in the test.

The magnitude of K_p measured in this test, was compared with theoretical values determined using different methodologies such as; Coulomb, Rankine, Caquote and Kerisel and the log-spiral solution discussed in Chapter 3 (Alqarawi et al., 2021). The parameters used in the calculation of these theoretical values are summarized in Table 6.2.

The lateral earth pressure measured during the test T1 has shown that coefficient of at-rest earth pressure K_o is about 0.52. This value is very close to the theoretical value of at-rest pressure coefficient estimated by the following Jaky's equation (Jaky, 1948), according to which $K_o = 0.47$

Table 6.2 Parameters used in the calculation of K_p

Soil friction angle (ϕ°)	Wall – soil friction angle (δ°)	Backfill inclination (β°)	Wall inclination (ω°)
32	20	0	0

The values of K_p computed using the aforementioned theories are shown in Table 6.3.

Table 6.3 Calculated and measured values of K_p

Coulomb	Rankine	Caquote and Kerisel	The log-spiral solution (Alqarawi et al., 2020)	The measured value
6.9	3.52	6.4	5.93	6.07

According to the data in Table 6.3, Rankine theory underestimated the value of K_p by approximately 45% while the value computed using Coulomb theory was greater than the measured K_p by approximately 14%. The log-spiral solution developed in Chapter 3, showed to be the closest estimation of the measured value of K_p with a difference of only 2.3%.

6.3.1.3 Soil Deformation

The side of the tank is made of clear acrylic, which allowed to visually observe the deformation in the soil mass during the test. In test T1, images were taken for the side of the tank, every 2 mm of the wall displacement, to monitor the development of the passive failure surface. An evaluation of the collected images showed that the traces of the passive failure surface become clearly visible at a displacement of 170 mm. The reading from the pressure sensors, at this displacement, showed either a decline in the lateral earth pressure (bottom sensor) or became relatively flat (middle and top sensors), which indicates the critical strength has been reached.

The slip surface was represented by a virtual line connecting the broken marker lines (see Figure 6.7 b). It can be observed that the slip surface comprising a curvature at the bottom part while the rest is close to a straight line. This finding agrees well with the hypothesis of a composite slip surface, (Terzaghi, 1984), which was adopted in Chapter 3 to develop the log-spiral solution (Alqarawi et al., 2021).

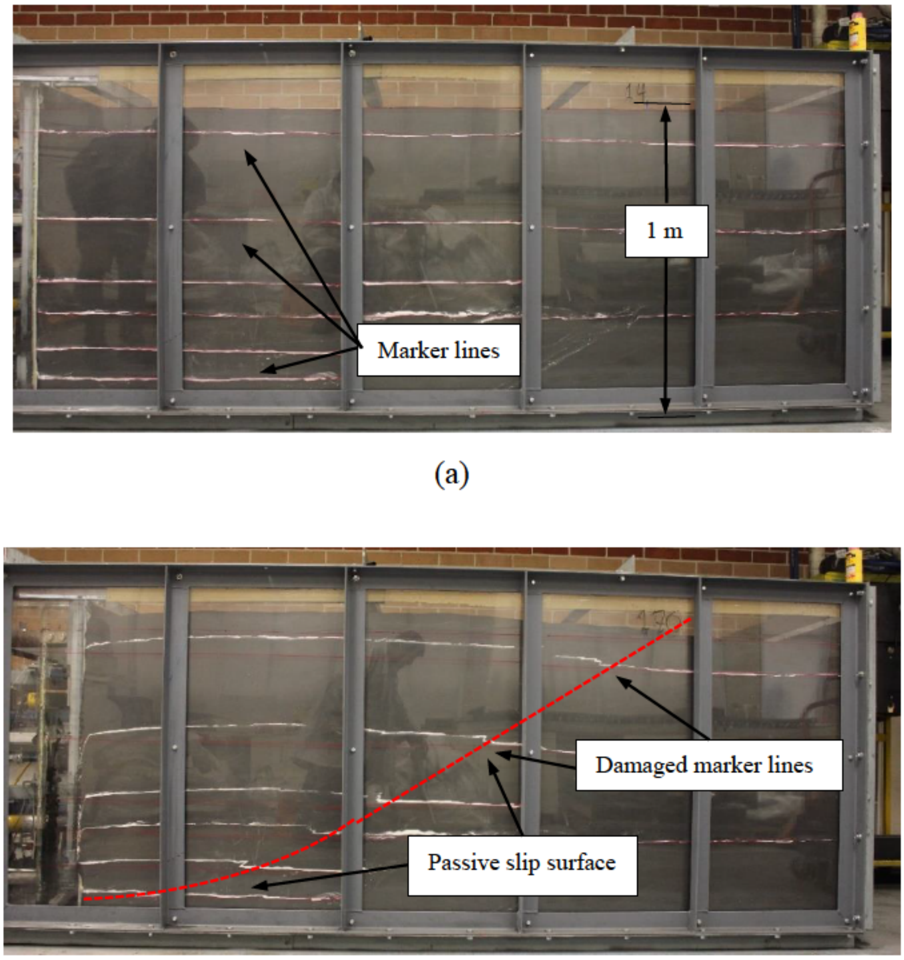

(a)

(b)

Figure 6.7 Images of the soil in the test chamber (a) before test T1 and (b) after test T1

6.3.2 Test T2

In this test the wall was moved in a cyclic rotational movement. The displacement amplitude involves the application of 20 cycles of ± 20 mm. The test was conducted at a rate of 1 cycle per 30 minutes.

6.3.2.1 Measured Lateral Pressure

The readings taken from the top pressure sensor increased sharply during the first few cycles recording a maximum stress of 68.8 kPa in Cycle 6. This value is approximately two times greater than the maximum stress recorded in the first cycle and 16 times greater than the at-rest pressure (at the same location of the top sensor). Following this spike, the stress, recorded at the top sensor, dropped to 50 kPa in cycle 10 and remained fluctuating at 40 kPa - 50 kPa until the end of the test.

The lateral pressure recorded in the middle sensor varied in a different pattern. It increased steadily over the first 10 cycles reaching a value of 64 kPa, then tend to level off at approximately 65 kPa.

The pressure recorded at the bottom sensor was less sensitive to the movement cycles, and increased only by 50% (from 17 kPa to 26 kPa) over the first 5 cycles and asymptote around this value. The lateral earth pressure recorded in the three sensors are shown in Figure 6.8. It must be noted that the initial values of earth pressure (at zero cycles) represent the at-rest pressures.

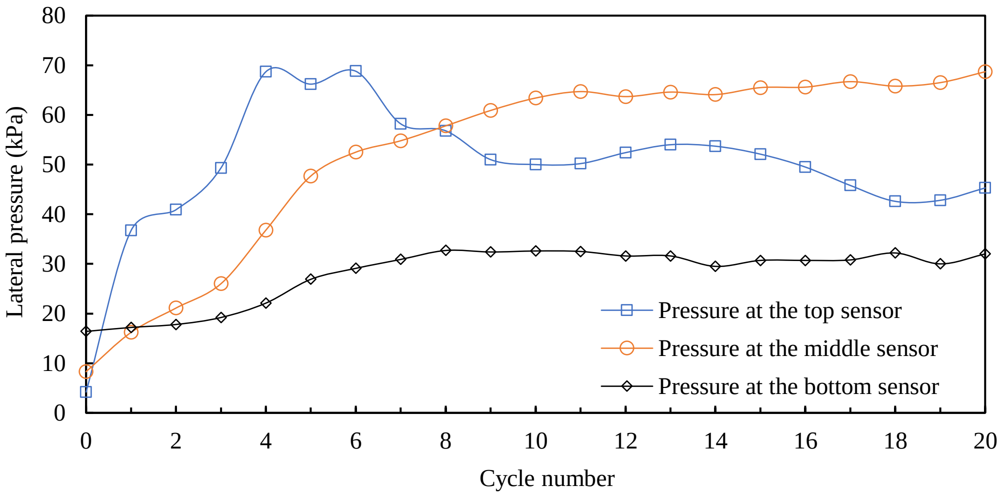

Figure 6.8 Lateral stresses recorded in Test T2

6.3.2.2 Lateral Pressure Distribution

The distribution of the lateral earth pressure across the height of the wall was plotted for selected cycles as shown in Figure 6.9. Theoretical pressure envelopes based on Rankine, Coulomb, Caquote and Kerisel and the log-spiral solution (discussed in Chapter 3) have been computed for comparison purposes. The pressure envelope of the log-spiral solution is determined by multiplying the vertical stress (vertical stress is the product of the unit weight multiplied by the depth from the soil surface) by the magnitude of lateral earth pressure coefficient *K* calculated using the log-spiral solution.

It can be observed that the maximum earth pressure, during the first few cycles, is occurring in the top part of the wall (at depth equals to $H/3$). This result agrees with the findings of other researchers about the location of the maximum earth pressure due to abutment rotations (Springmans et al., 1996; Lehane, 2003). However, the profile changed progressively, with the movement cycles, and the maximum pressure developed within the middle third of the wall (at depth between $H/3$ and $2H/3$) as shown in Figure 6.9d. This can be attributed to the propagation of the densified soil wedge deeper along the wall surface, which results in a stiffer soil and consequently a higher lateral earth pressure. However, this behaviour was not observed at the bottom sensor, where the pressure was insensitive to the movement cycles, because the soil arching effects largely reduced the vertical stresses at the bottom of the wall.

According to Figure 6.9, a right triangular earth pressure envelope does not address the actual profile, because the stress at the bottom part of the wall is largely overestimated, while that in the upper part is sometimes underestimated. Therefore, using a non-triangular pressure distribution profile is more appropriate in this case. Figure 6.10 shows a comparison between the maximum pressure in Cycle 20 with that calculated using the BS PD6694/1 (2011) (equation 2.15, Chapter 2). The latter assumes a bilinear earth pressure profile that varies from zero at the soil surface to $\gamma K^* H / 2$ at the mid height of the wall then decreases to $\gamma K_o H$ at the bottom of the wall. In this equation, the magnitude of the passive earth pressure coefficient K_p was determined as 6 according to the Eurocode 7 (2005) and the magnitude of the constant *C* was taken as 66 (free-end wall with $d'_d = 0.5 d_d$). According to equation 2.15, the magnitude of K^* was determined as 7.5. It is notable that the BS PD6694/1 (2011) pressure envelope addresses the measured lateral stresses very well.

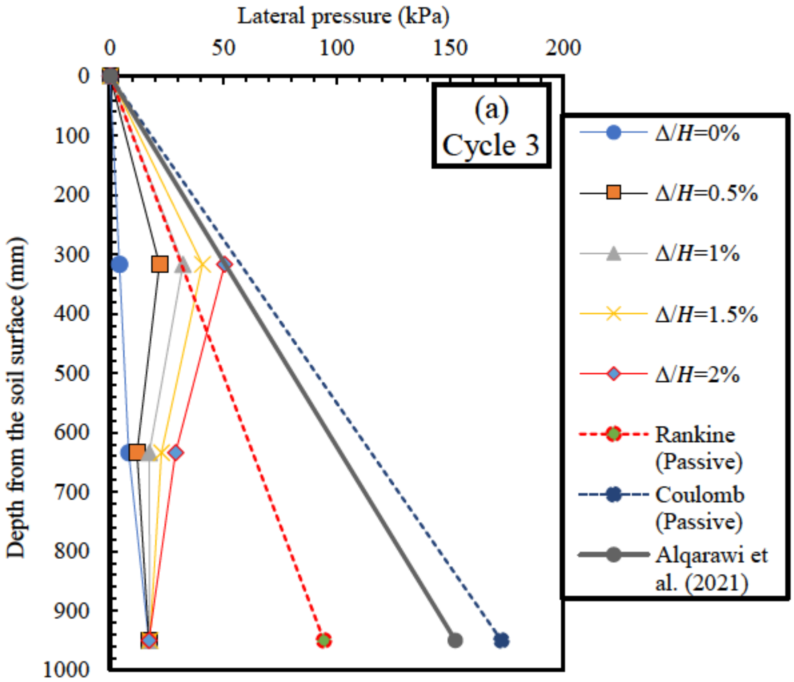
Lateral pressure (kPa)
0
50
100
150
200
Depth from the soil surface (mm)
0
100
200
300
400
500
600
700
800
900
1000
(a)
Cycle 3
Δ/H=0%
Δ/H=0.5%
Δ/H=1%
Δ/H=1.5%
Δ/H=2%
Rankine (Passive)
Coulomb (Passive)
Alqarawi et al. (2021)

(a)

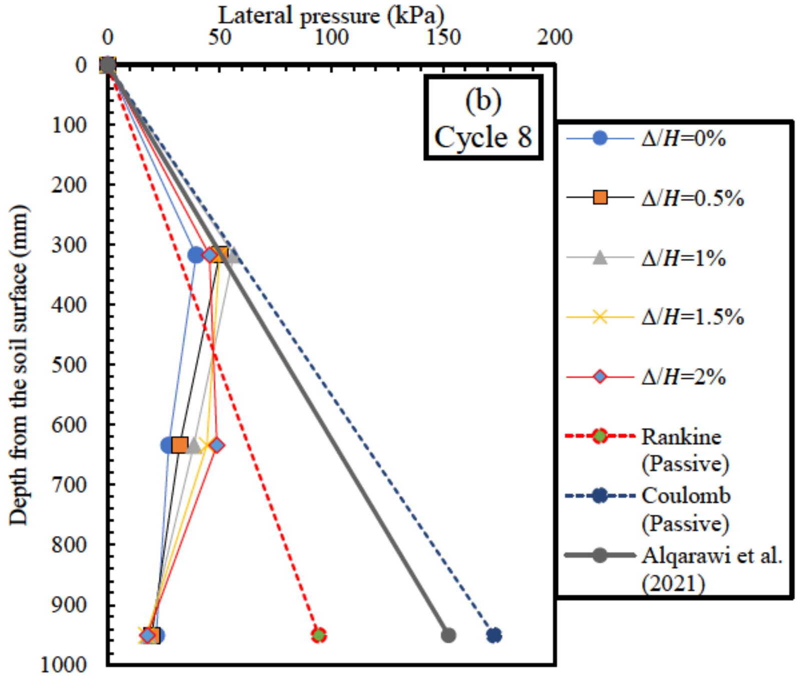
Lateral pressure (kPa)
0
50
100
150
200
Depth from the soil surface (mm)
0
100
200
300
400
500
600
700
800
900
1000
(b)
Cycle 8
Δ/H=0%
Δ/H=0.5%
Δ/H=1%
Δ/H=1.5%
Δ/H=2%
Rankine (Passive)
Coulomb (Passive)
Alqarawi et al. (2021)

(b)

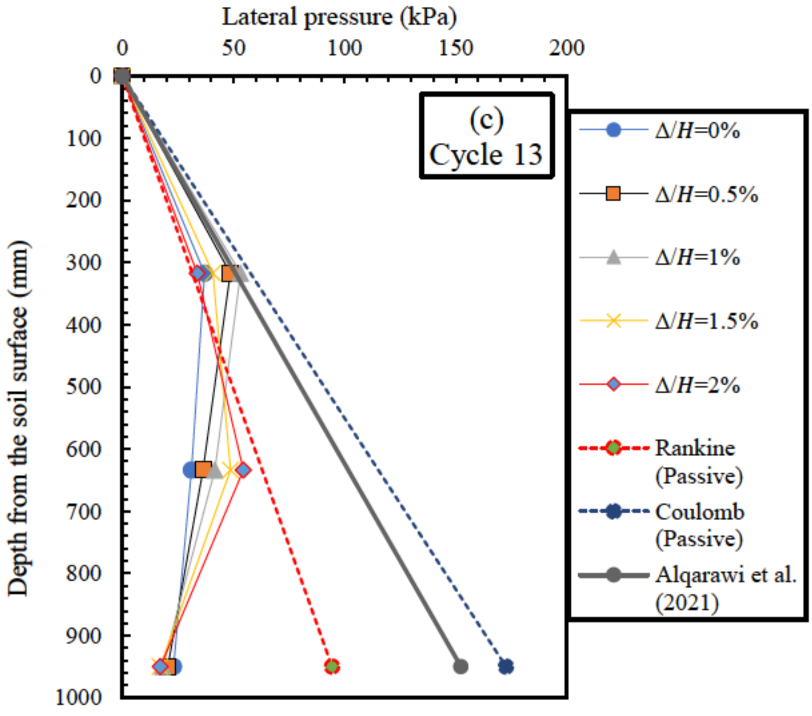

(c)

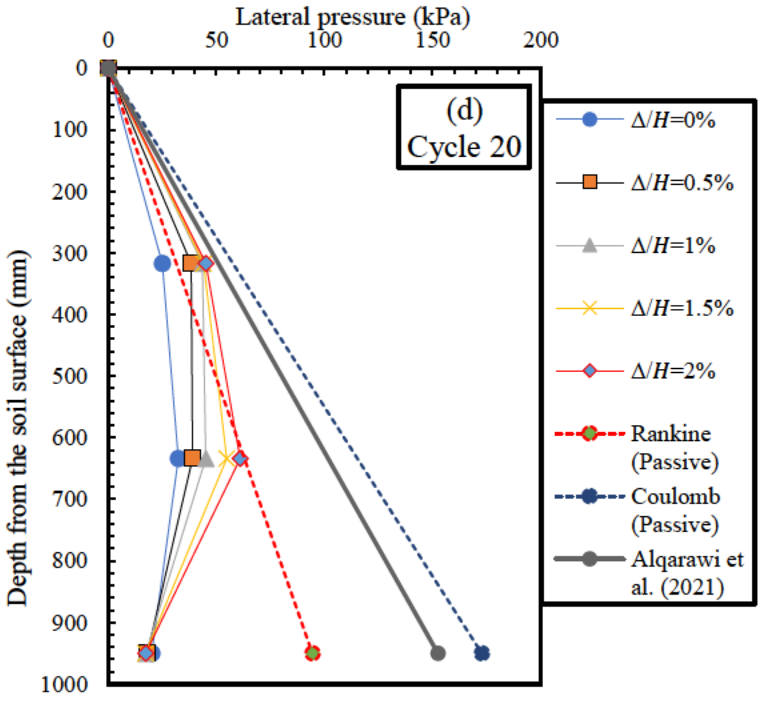

(d)

Figure 6.9 Lateral pressure profiles, Test T2 during (a) Cycle 3, (b) Cycle 8, (c) Cycle 13 and (d) Cycle 20

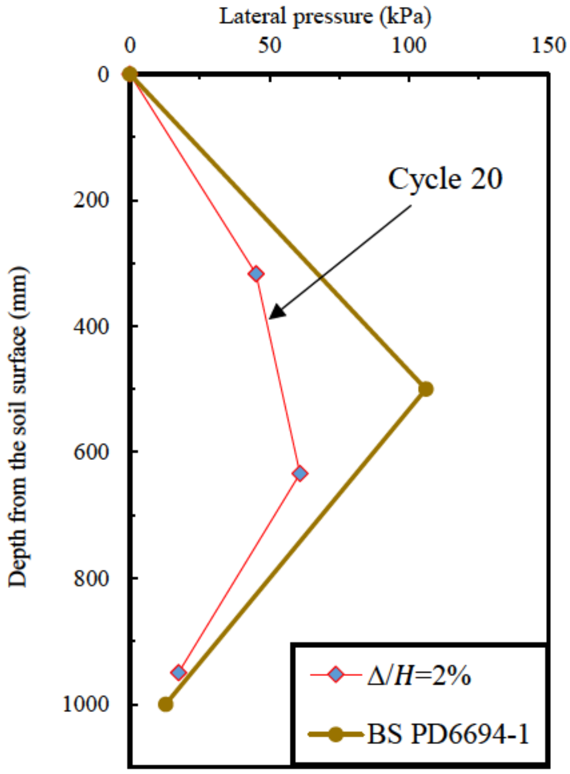

Figure 6.10 Comparison of measured earth pressure with the BS PD6694/1 (equation 2.15)

6.3.2.3 Hysteresis Loops

The variation of the lateral pressure with the wall displacement was plotted to view the pressure hysteresis loops. Figure 6.11 shows the hysteresis loops based on the data recorded in the top sensor. It is apparent that the pattern in which the lateral pressure changed with the displacement was inconsistent throughout the test. Cycles are getting closer to each other with the movement cycles, which indicates a reduction in the incremental hardening rate. Moreover, in the last 10 cycles a peak of lateral pressure became notably visible at a displacement equals to approximately + 10 mm. This behaviour is attributed to the soil in the upper part of the wall became increasingly dense and subsequently, the soil, exhibited peak and residual strengths.

Different behaviour was observed at the bottom part of the wall where the shape of the pressure cycles, recorded in the middle sensor, remained relatively similar throughout the test (see Figure 6.12). This indicates that the soil adjacent to the lower part of the wall experienced less dilation, compared to the soil adjoining the upper part of the wall, because of the higher confining pressure. Nevertheless, densification of soil, in the lower part, took place and hence, a considerable increase in the lateral pressure has occurred.

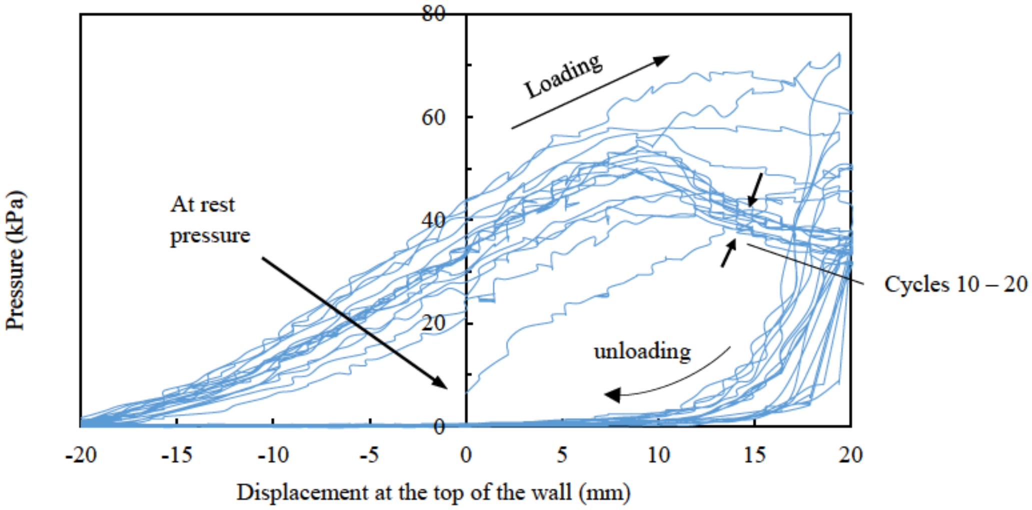

Figure 6.11 Pressure cycles at the top sensor, Test T2

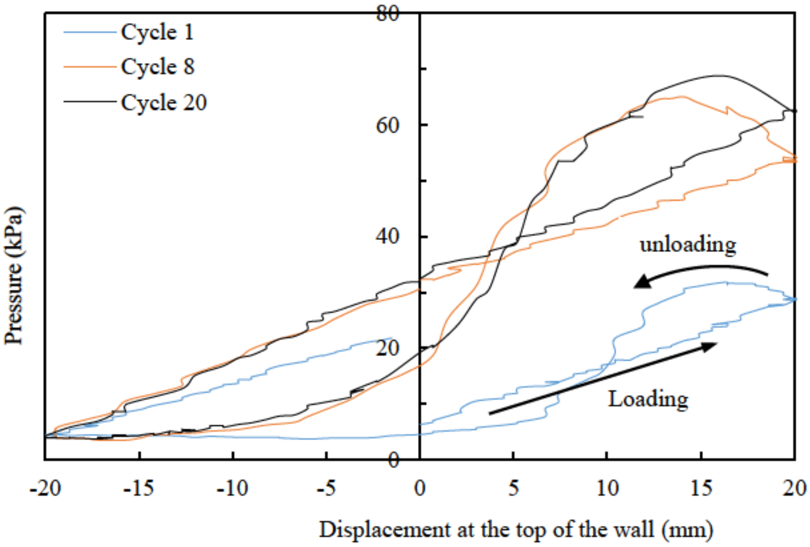

Figure 6.12 Selected pressure cycles at the middle sensor, Test T2

6.3.2.4 Soil Deformation

During the test T2, the maximum settlement has been measured at the active, passive and neutral positions of each cycle. A trough in the soil surface became visible as early as the first movement cycle was completed. The maximum settlements increased rapidly during the first 10 cycles then continued to increase but at a decreasing rate as shown in Figure 6.13.

The maximum settlement was consistently observed at the soil-wall interface and when the wall is at the active position. The depth of the settlement trough at the end of the test was 242 mm which corresponds to 484 mm in the prototype dimensions.

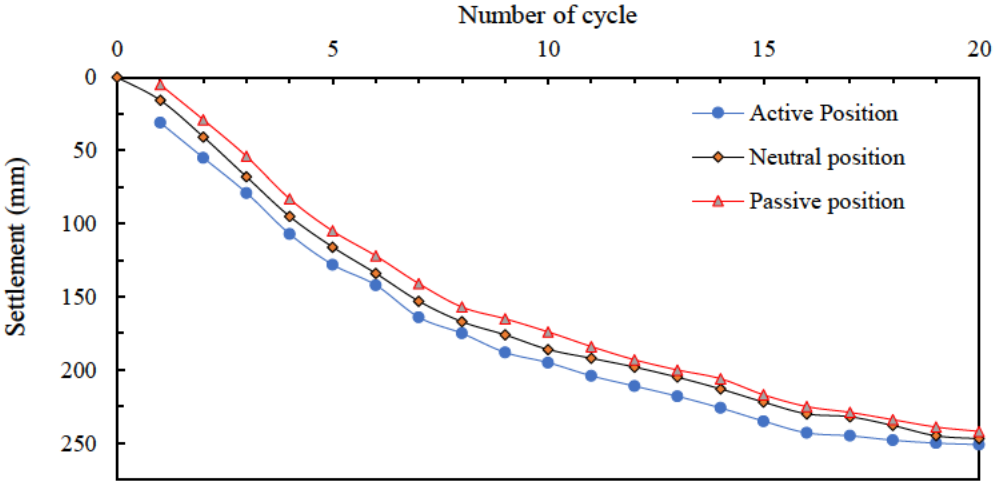

Figure 6.13 Maximum settlement vs number of cycle, Test T2

The deformed soil profile showed traces of several small active slippage lines in the soil near the wall, which confirms the soil slumping during the active phase of each movement cycle. However, a large active slippage line, that delineate the virtual active soil wedge is also observed as a straight line inclined at approximately 70° with the horizontal, as shown in Figure 6.14 b. A slight heaving of 10 mm to 15 mm was observed at the soil surface at a distance between 0.5 m and 1.1 m from the wall. However, no visible signs of passive failure surface were observed. The volume of the trough was determined by calculating the cross sectional area of the trough, using the Gauss's area formula, and then compared with the volume of the heave. It was found the latter represents approximately 10% of the total volume of the trough. This behaviour suggests that, most of the soil that initially occupied the trough is conserved through densifying the soil mass adjoining the wall.

(a) (b)

6.14 (a) Soil profile before test T2 and (b) Deformed soil profile after test T2

6.3.3 Test T3

In this test, the wall was displaced in translational mode against and away from the soil. The volume of the soil displaced, and the consequent average shear strain, due to a translational movement is theoretically two times greater than that in the rotational movement. Therefore, the displacement amplitude used in this test was chosen to be equivalent to 50% of that used in test T2 to maintain a consistent loading effects over the two tests. Accordingly, 20 cycles of ± 10 mm ($\Delta/H = 1\%$) were applied in test T3.

The results collected from this test showed quantitative and qualitative variations to those observed in test T2. The lateral earth pressures recorded during this test were considerably higher than those recorded in test T2. Figure 6.15 shows the maximum stresses recorded during test T3. It can be observed that, the maximum pressure, during the first 10 cycles, was consistently recorded in the bottom sensor. The highest stress therein was 123 kPa which is 80% greater than the highest stress recorded in test T2. The maximum stresses in the middle sensor increased steadily from 33.7 kPa in the first cycle to record a maximum value of 114 kPa in cycle 16, then declined slightly to 100.3 kPa in the last cycle.

The pressures in the top sensor were generally low, as they increased slightly over the first 10 cycles, then interrupted by the excessive settlement in the soil surface. The readings from the sensor at the rear wall of the tank, showed an insignificant increase during the first five cycles, then asymptote at 11.5 kPa until the end of the test.

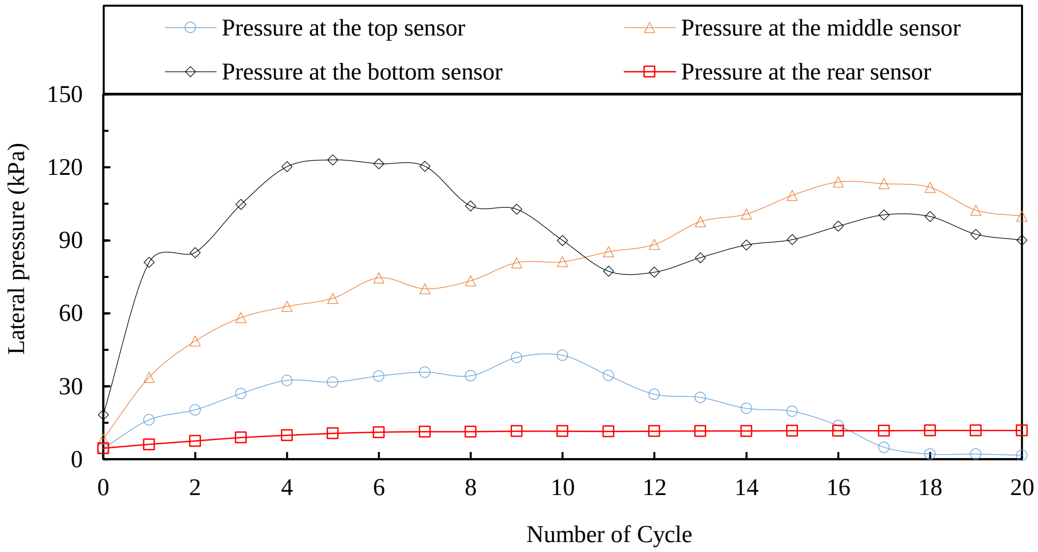

Figure 6.15 Lateral pressure vs number of cycle, Test T3

6.3.3.1 Lateral Pressure Distribution

The vertical distribution of the maximum lateral pressure in test T3 was largely different from that in test T2. According to Figure 6.16, the maximum pressure preserved a right triangular profile over the first few cycles (up to cycle 5). During the following cycles, the pressure profile transformed progressively from right triangular with a peak at the bottom into triangular with a peak in the middle third of the wall, between cycles 10 and 15, and maintained this profile until the end of the test.

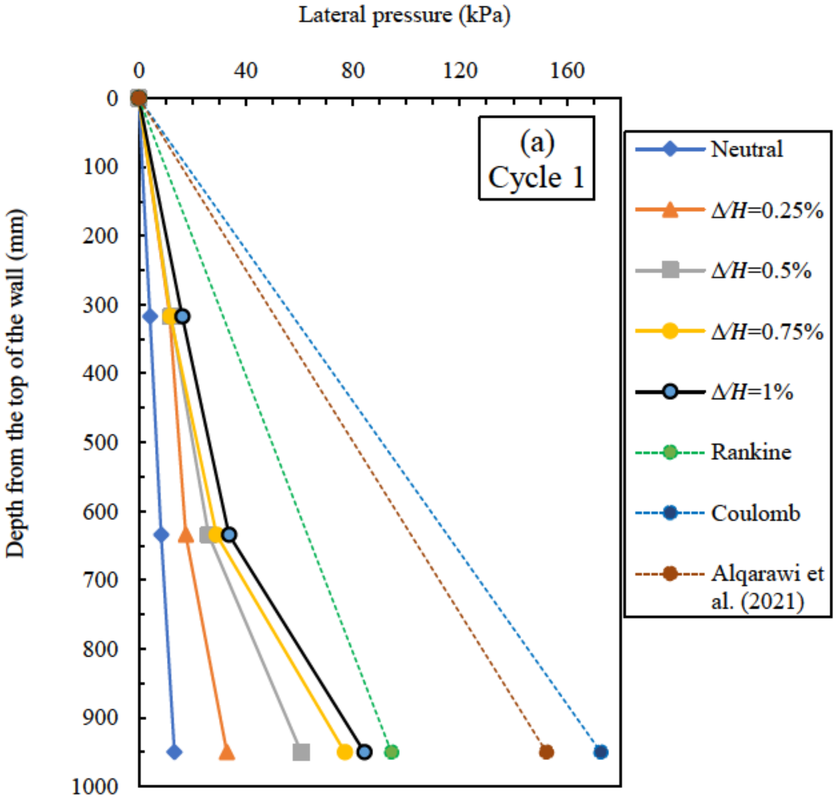
Lateral pressure (kPa)
0
40
80
120
160
Depth from the top of the wall (mm)
0
100
200
300
400
500
600
700
800
900
1000
(a)
Cycle 1
Neutral
Δ/H=0.25%
Δ/H=0.5%
Δ/H=0.75%
Δ/H=1%
Rankine
Coulomb
Alqarawi et al. (2021)

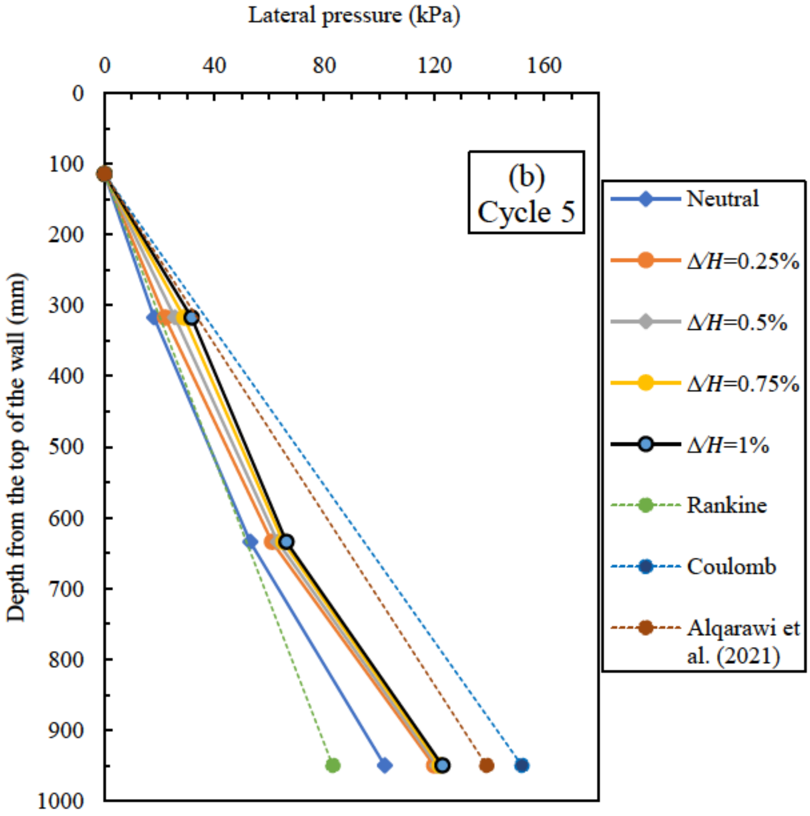
Lateral pressure (kPa)
0
40
80
120
160
Depth from the top of the wall (mm)
0
100
200
300
400
500
600
700
800
900
1000
(b)
Cycle 5
Neutral
Δ/H=0.25%
Δ/H=0.5%
Δ/H=0.75%
Δ/H=1%
Rankine
Coulomb
Alqarawi et al. (2021)

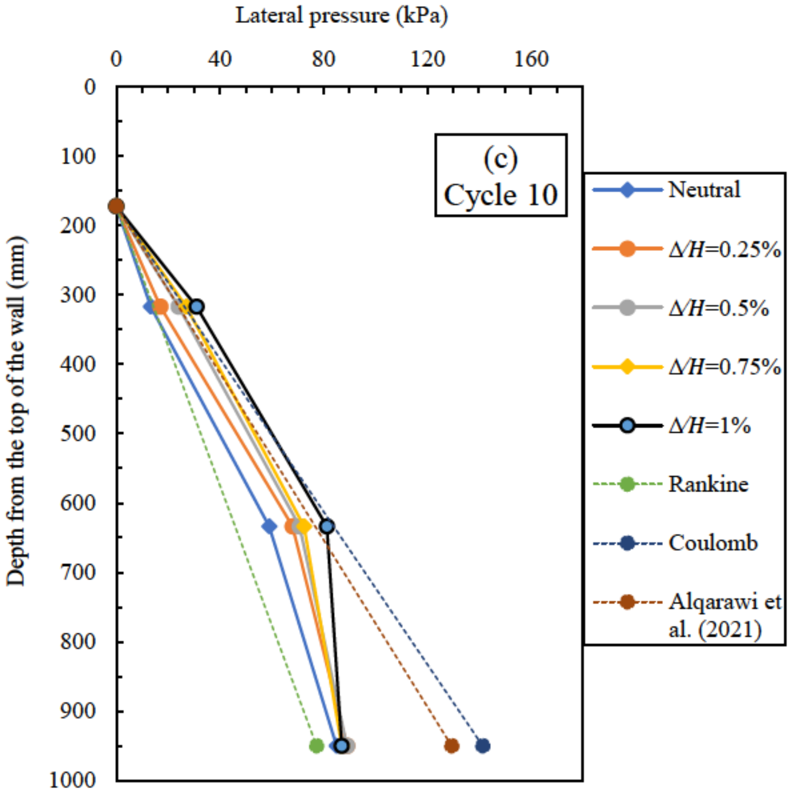
Lateral pressure (kPa)
0
40
80
120
160
Depth from the top of the wall (mm)
0
100
200
300
400
500
600
700
800
900
1000
(c)
Cycle 10
Neutral
Δ/H=0.25%
Δ/H=0.5%
Δ/H=0.75%
Δ/H=1%
Rankine
Coulomb
Alqarawi et al. (2021)

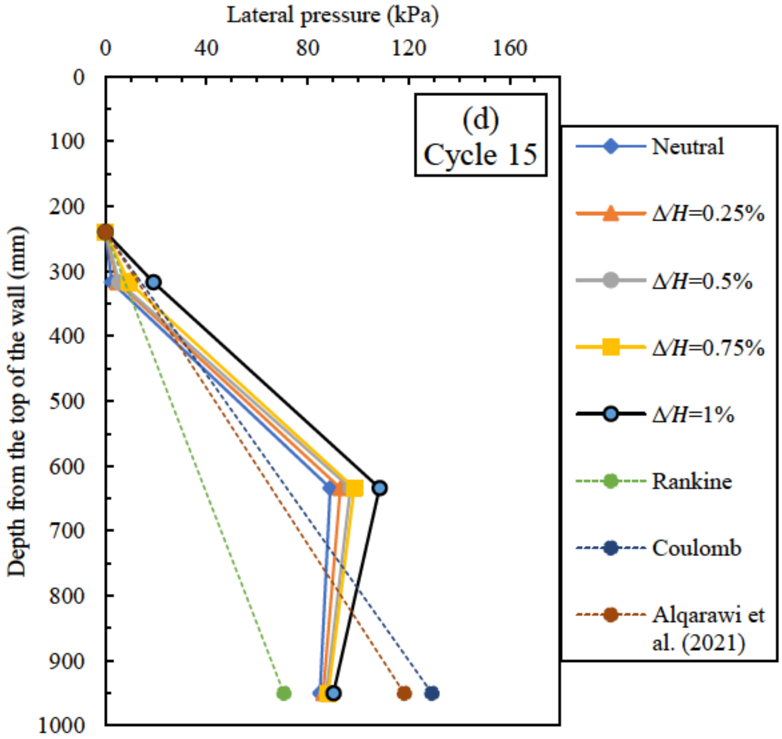
Lateral pressure (kPa)
0
40
80
120
160
Depth from the top of the wall (mm)
0
100
200
300
400
500
600
700
800
900
1000
(d)
Cycle 15
Neutral
Δ/H=0.25%
Δ/H=0.5%
Δ/H=0.75%
Δ/H=1%
Rankine
Coulomb
Alqarawi et al. (2021)

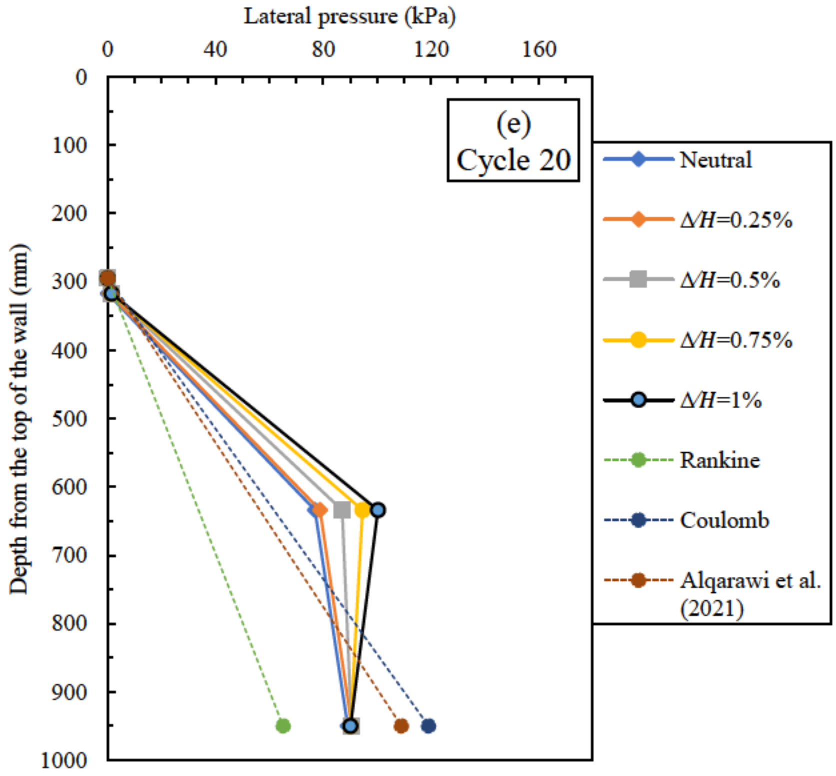

Figure 6.16 Pressure profiles during (a) Cycle 1, (b) Cycle 2, (c) Cycle 10, (d) Cycle 15 and (e) Cycle 20, test T3

It can be observed that, starting from cycle 5, the maximum pressure was consistently exceeding Rankine passive pressure. This finding raises a serious concern about those design guidelines which adopt Rankine passive triangular pressure in the design of abutments in IABs. This applies especially for SIAB and IAB with foundations that slide with the cyclical displacements of the superstructure. Moreover, Coulomb passive pressure envelope underestimated the maximum pressure through cycles 15 to 20, by more than 50%, given the fact Coulomb passive pressure depicts the upper estimate among classical earth pressure theories. This emphasized the fact that, using a right triangular passive pressure, based on any of the current theoretical methodologies, does not replicate the lateral earth pressure in IAB abutments that experience translational movements. In fact, such assumptions may largely underestimate the actual earth pressure and may result in structural distress consequences.

In order to compare the results from test T3 with the British Standard PD6694/1 (2011), equation 2.12 has been used to calculate the magnitude of earth pressure coefficient K^*. It is worthwhile mentioning that, equation 2.12 applies to short abutments where the movement is dominantly translation. Equation 2.12 is preserved from BA42/96 (2003) and has not been superseded by the changes imposed by PD 6694/1 (2011). The magnitude of the at-rest earth pressure coefficient K_o is determined using Jacky's (1948) equation and K_p is determined in accordance with the Eurocode 7 (2005). The magnitude of K^*, then is determined as 5.9.

It is understood that PD6694/1 (2011) provided guidelines about the distribution of earth pressure in IABs, but did not differentiate between the distribution of earth pressure behind short abutments and other abutment types. BA42/96 (2003) provided two different earth pressure distributions for frame abutments and full height embedded walls (see Figure 2.4). However, both are relatively deep abutments, and hence the movement is different from that observed in short abutments.

Nevertheless, in Figure 6.17, a pressure profile is plotted based on the British Standard PD 6694/1 (2011). It can be observed that, the latter underestimates the lateral pressure at the lower half of the wall. The assumption, made by PD6694/1 (2011), about the lateral earth pressure being reduced from a maximum, at the mid height of the wall, to an at-rest pressure at the bottom is non-conservative when the movement mode is translation. While the measured lateral pressure at the bottom, in test T3, decreases slightly with the number of cycles, it remains significantly higher than the at-rest pressure.

In accordance with the results of test T3, the lateral pressure ratcheting effects are more significant in the lower half of the wall. Therefore, a modified lateral pressures envelop, for an abutment wall that experiences translational movement, can be proposed considering the following,

- An appropriately conservative value of earth pressure coefficient K^* need to be considered. This can be achieved by increasing the value calculated from equation 2.12 by 25%.
- The lateral pressure varies from zero, a the top of the wall, to $\frac{3}{4}\gamma HK^*$ at a depth equals to $\frac{3}{4}H$ and remains constant, at this value, over the lower part of the wall.

The proposed lateral pressure envelope captures the earth pressures in test T3 very well compared to that proposed by PD6694/1 92011) as shown in 6.17.

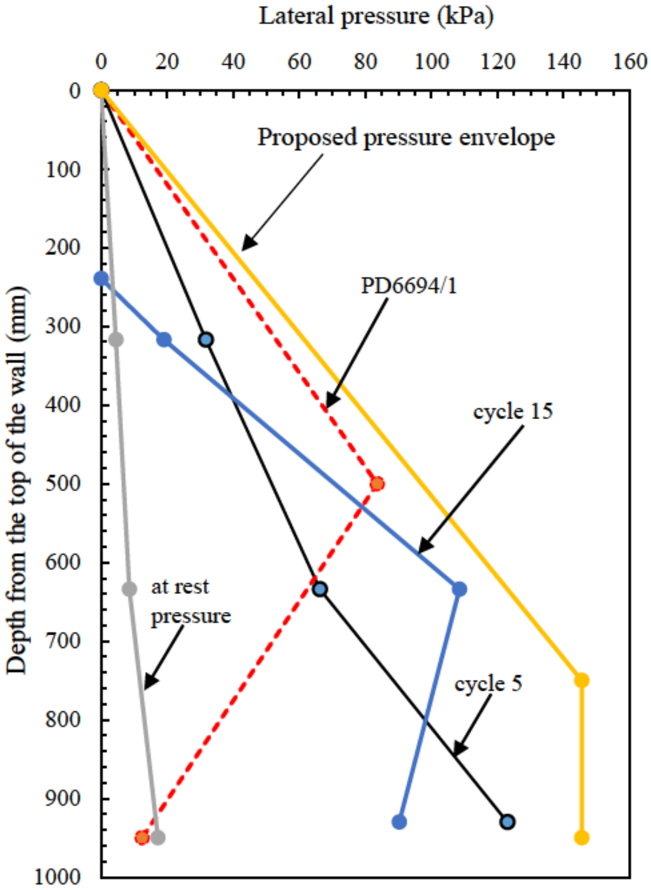

Figure 6.17 Comparison of measured earth pressure with the BS PD6694/1 (equation 2.12)

6.3.3.3 Soil Deformation

The measurements of the soil surface settlements have been taken during the test when the wall is at the neutral and at the active positions. The settlements increased rapidly during the first 5 cycles, then continued to increase but at a lower rate (see Figure 6.18). At the end of the test (after 20 cycles), a significant settlement trough is observed with a maximum settlement of 313 mm (approximately 30% of the total retained height of the soil).

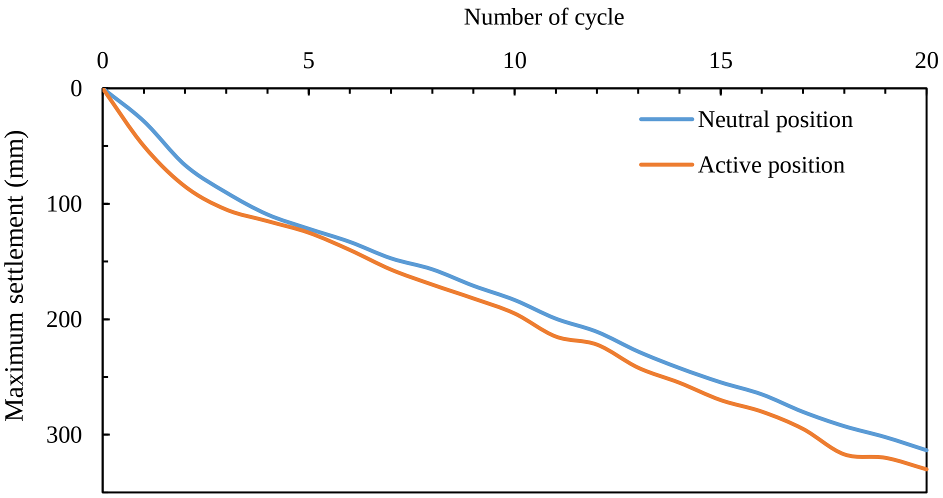

Figure 6.18 Maximum settlements recorded in test T3

It is evident that the settlement observed in test T3 is different from that in test T2 in terms of the depth and size of the trough. The settlement rates also vary among tests T2 and T3. According to Figure 6.19, the settlement increment rate in test T2 was constantly decreasing throughout the test. However, in test T3, the settlement increment rate decreased over the first 5 cycles, but remained fluctuating about an average value of 4% until the end of the test.

This behaviour indicates the plastic strains continued to accumulate as the wall movements effects progressed to a larger extent.

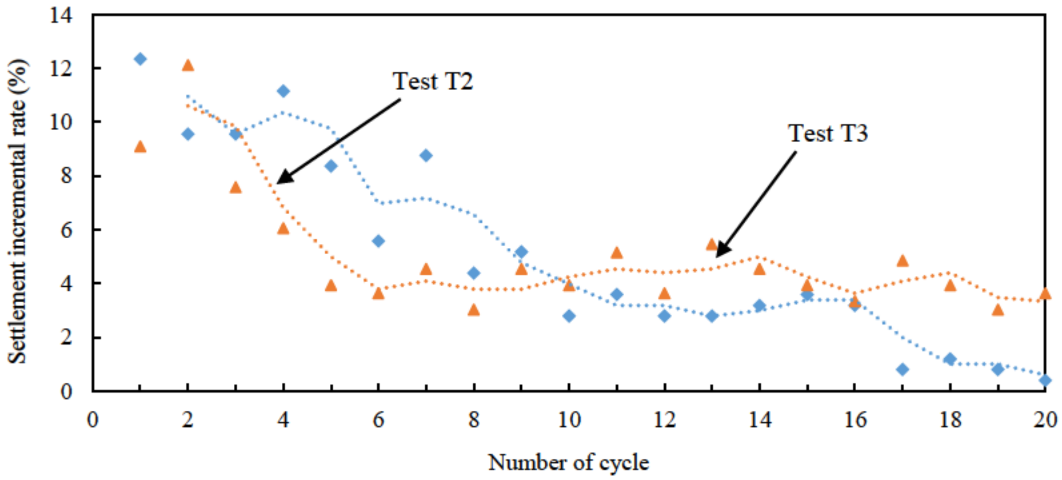

Figure 6.19 Settlement incremental rate in test T2 and T3

(* the settlement incremental rate is defined by the ratio between the settlement increment, at any two consecutive cycles, and the total settlement)

The deformed profile of the soil surface, showed a considerable heave over the distance between 0.63 m and 1.7 m from the wall. Maximum height of the heave was 75 mm. This behaviour was not observed in test T2 where the heave was insignificant (see Figure 6.20). The total volume of the heave is estimated as 57% of the total volume of the trough which suggests a notable dilative behaviour in the densified soil mass. This dilative behaviour is attributed to the greater densification effects taken place in the soil next to the wall which led to a larger densified soil wedge than that developed in test T2.

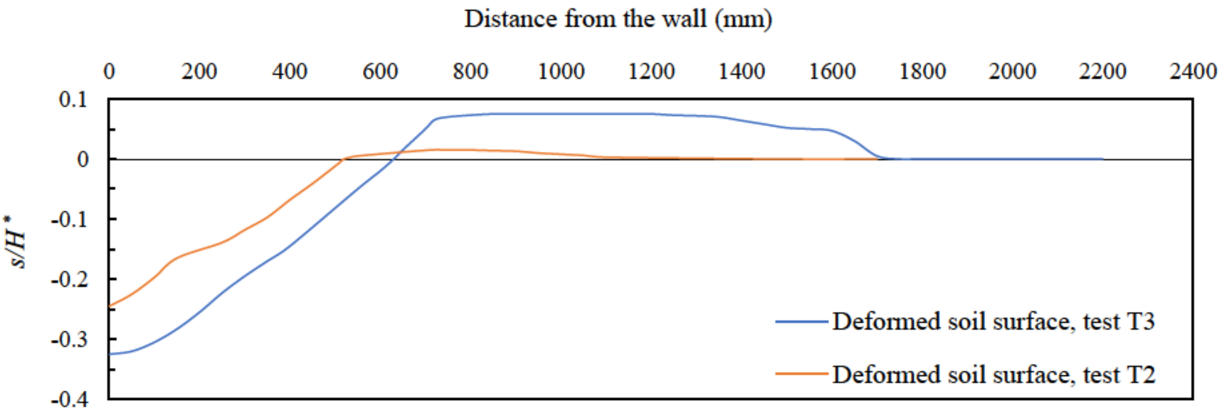

Figure 6.20 Deformed soil surface in test T2 and T3

(* s/H represents the ratio between the settlement and the total height of the soil)

In addition to an active failure, a passive failure surface has clearly developed during test T3. The images taken from the side of the tank showed the path of the passive failure surface following the broken marker lines as shown in Figure 6.21 b. Similar to test T1, the line plotted to follow the path of the passive failure surface resembled a curve at the bottom part closer to the toe of the wall, which again confirms the assumption of a composite failure surface (as discussed in Chapter 3).

(a)

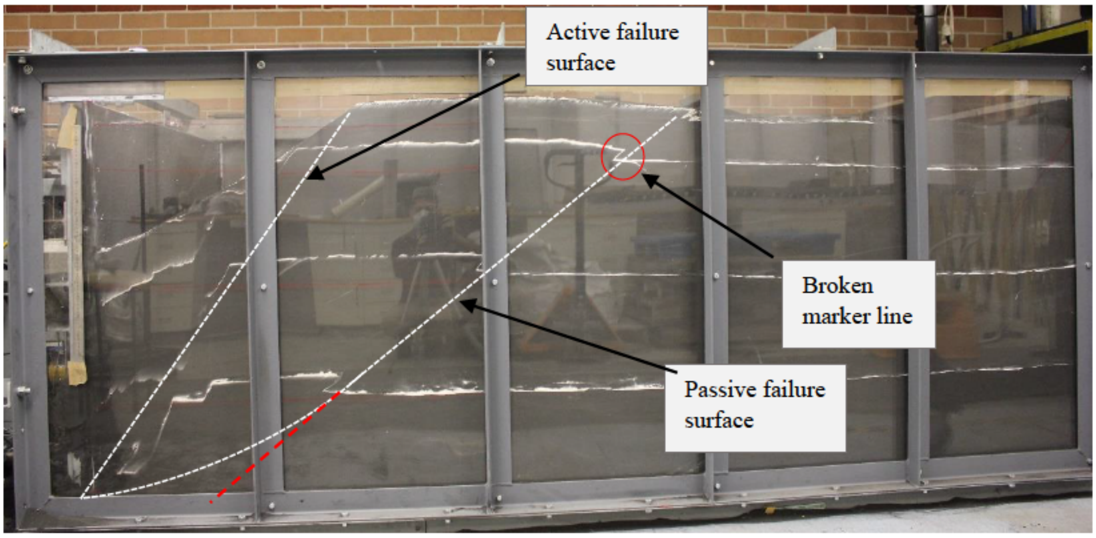

(b)

Figure 6.21 The test chamber (a) before the test T3 and (b) after the test T3

The marker lines close to the wall (within the active soil wedge) were severely distorted and displaced, but they show a clear traces of settlements occurring across the height of the retained soil in this zone. In accordance with the deformed soil profile shown in Figure 6.21 b, the retained soil mass can be divided into three zones,

- Zone 1 (active soil wedge); this zone is located between the wall and the active failure surface. The soil in this zone experienced continuous densification and loosening as a results of the passive and active wall movements. The deformation of the soil, in this zone, is primarily settlement at angle corresponding to the slope of the active failure surface.
- Zone 2 (passive soil wedge); This zone is subtended by the active and passive failure surfaces. The soil in this zone experienced incremental densification as a results of the active wedge continuously pushing into it. Therefore, the soil in zone 2 suffers an accumulation of shear strains that are not fully recovered during the active phase. This is because the soil in this zone is beyond the active wedge and hence does not loosen during the active wall movement. As the elastic strains of the soil are exhausted, the plastic strain will accumulate in the soil in Zone 2. The passive failure eventually occurs and the soil slips upward along the passive failure surface as illustrated in the magnified deformation zones in Figure 6.22.
- Zone 3; this zone is located beyond the passive failure surface. The soil in this zone is intact as the effects of the wall movements do not progress beyond the passive failure surface

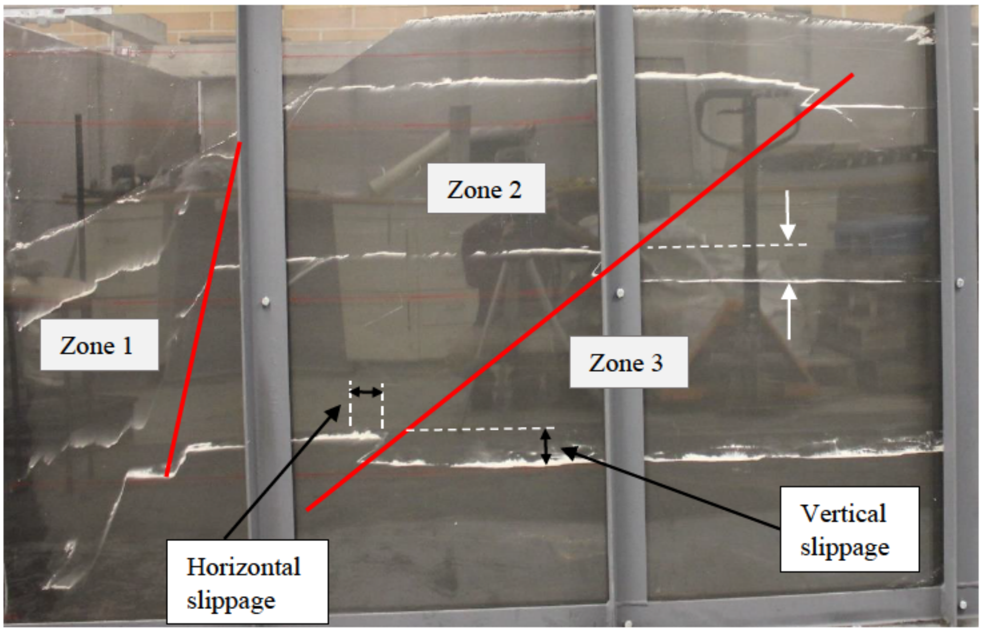

Figure 6.22 Zones of deformed soil in test T3 (zoom - in image from Figure 6.21b)

6.3.4 Test T4

In this test, 600 mm thick, block of medium-stiffness EPS geofoam was used as a compressible inclusion between the soil and the wall. Translational movement mode was adopted in this experiment with 50 cycles of ± 10 mm amplitude to test the efficacy of the EPS inclusion in the most sever condition.

The EPS block was cut to size before it was fitted inside the tank. The sides of the EPS inclusion were properly sealed to prevent the sand from leaking into the sides and beneath the EPS inclusion. This was done by applying a paper tape along the corner joints between the EPS and the sides and the base of the tank. The initial position of the front face of the EPS inclusion was marked prior to the placement of sand in the tank to use it as a reference in measuring the deformation in the EPS.

6.3.4.1 Lateral Pressure

The lateral pressure recorded in this test showed entirely different behaviour from those recorded in tests T2 and T3. The pressure recorded in each of the pressure sensors increased sharply in the first two cycles then asymptote at a value close to 80 kPa for the rest of the movement cycles. It is interesting to see the lateral pressure becomes independent to the number of cycles and remain constant without any signs of ratcheting (see Figure 6.23).

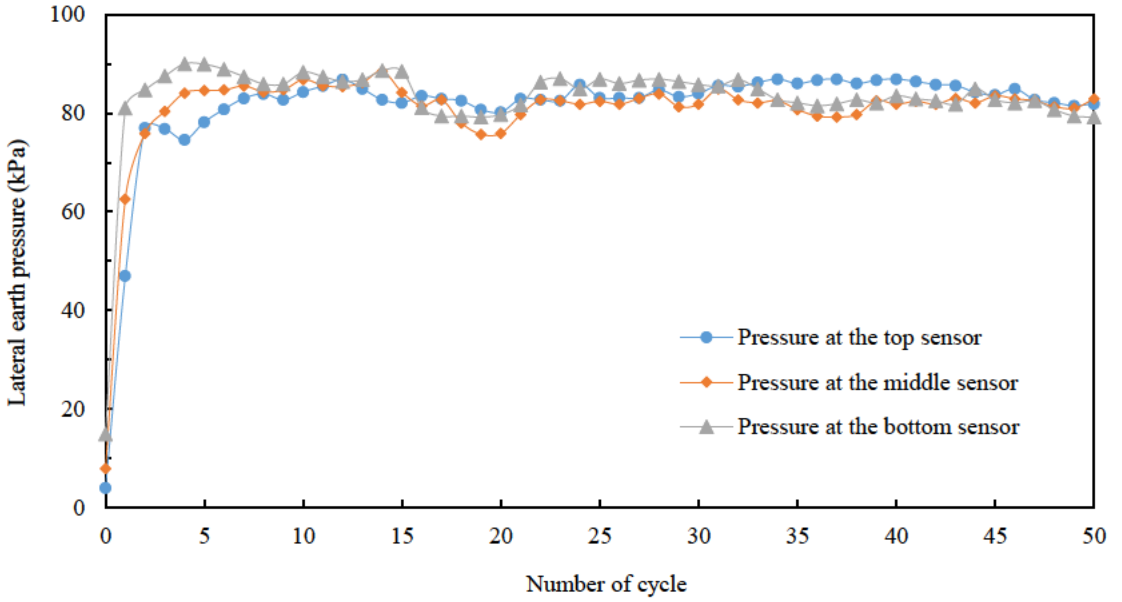

Figure 6.23 Lateral pressures recorded in test T4

The magnitude of the pressure at which the readings were levelling off, coincides with the yield stress of the EPS at a similar loading rate. The yield stress of a medium-stiffness EPS, at a loading rate between 0.1% and 0.2%, is estimated as 80 kPa.

The distribution of the lateral pressure is also different from those observed in other tests. The pressure profile in most of the cycles is bilinear and tends to become a vertical line as the wall reaches the passive position as shown in Figure 6.24.

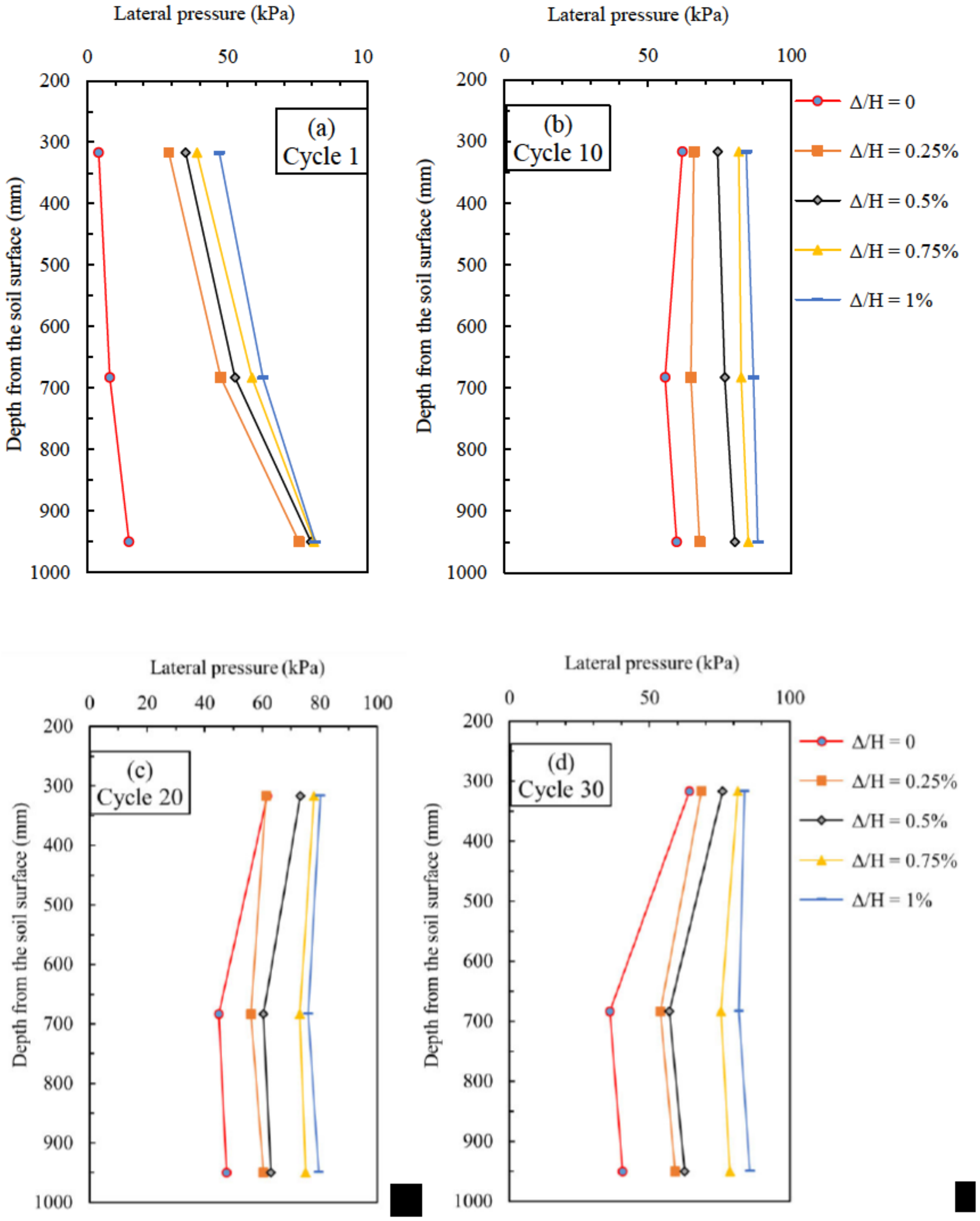

Figure 6.24 Lateral pressure distribution, test T4 during (a) Cycle 1, (b) Cycle 10, (c) Cycle 20 and (d) Cycle 30

6.3.4.2 Soil Deformation

The settlement measurements were taken throughout the test in addition to the displacements at the face of the EPS inclusion. After 50 cycles of wall movements, the maximum settlement was 175 mm (see Figure 2.25). However, the settlement recorded after 20 cycles was 124 mm, which represents only 37% of the maximum settlement observed in test T3. Moreover, the deformed soil surface in this test did not show any heave even after 50 cycles of wall movements. This highlights the role of the EPS inclusions in attenuating the wall movement effects on the adjoining soil.

The trend of the settlement curve in this test showed a qualitative agreement with those observed in test T2 and T3. The settlement increment rate was relatively high (4%) over the first 5 cycles then decreases considerably to approximately 1% in cycle 30 then levelled off, at this value, afterwards.

It was not possible to compare the final settlement recorded in this test with that in Test T3, because the latter involved the application of only 20 cycles. However, a theoretical estimation using the trajectory of the settlement curve of Test T3 shows excessive settlement that may well exceeds 900 mm at 50 cycles.

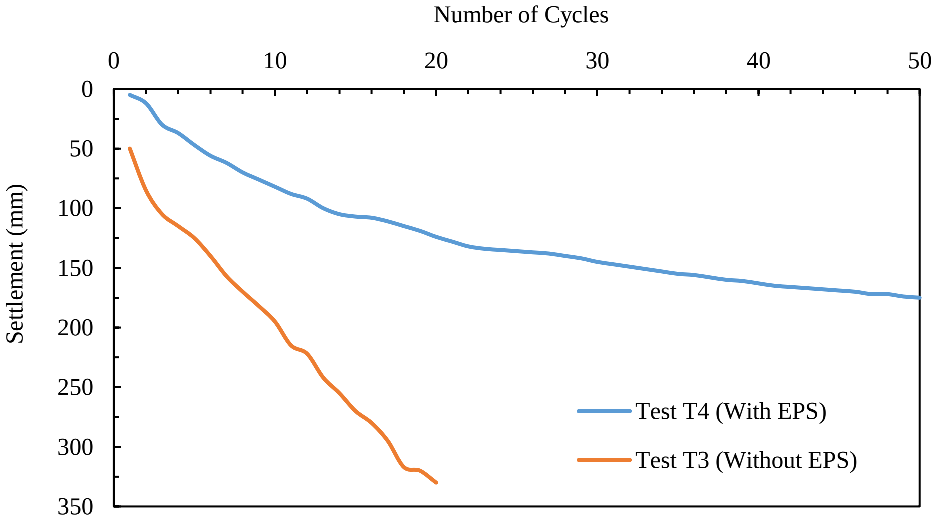

Figure 6.25 Soil Settlement vs number of cycles for test, T3 and T4

Figure 6.26 shows photos of the test chamber before and after test T4. The deformed soil profile shows a notable active slippage and a small trough in the soil adjoining the EPS inclusion. The size of the trough is calculated and is equivalent to approximately 50% of that developed in test T3. However, no heaving was observed in this test.

(a)

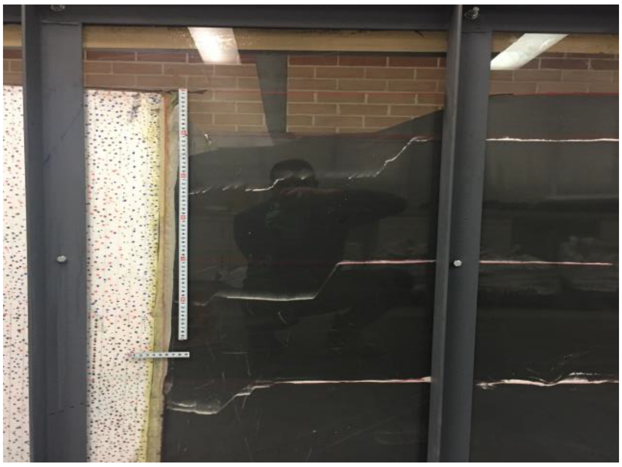

(b)

Figure 6.26 Soil profile, (a) before test T4 and (b) after test T4

6.3.4.3 Transfer Function of the EPS Inclusion

The deformations in the soil adjacent to the EPS inclusion observed in test T4 were considerably less than those developed in test T3. This is, indeed, attributed to the transfer function of the EPS inclusion. The latter was effective in reducing the displacement transferred to the soil during the movement cycles. In order to evaluate the transfer function of the EPS inclusion, the position of the EPS-soil interface was constantly monitored and compared with its initial position marked before the test started. For an easy reference, this EPS-soil interface will be referred to as the “EPS facing”.

The first loading cycle begun with the wall moving, from the neutral position, towards the passive position. During this phase, the top point of the EPS facing showed no movement, while the bottom of the EPS facing experienced a displacement of -3 mm. The negative sign means the EPS facing is displaced to the left of the initial position (in this case the displacement was in a direction opposite to the direction of wall movement). This clearly indicates that the EPS inclusion absorbed the entire passive displacement component without transferring any effects to the soil. Following to that, during the active phase of the same cycle, the EPS inclusion was displaced, under the active soil pressure. However, the movement of the EPS facing was not uniform, whereas the top and bottom movements were -2 mm and -22 mm respectively. Accordingly, a small gap at the top of the wall-EPS interface became visible. In the next cycle, and when the wall travelled to the passive position again, the EPS inclusion could not retrieve its previous position. The EPS facing’s top and bottom movements were 0 and -15 mm respectively (all these numbers are measured with respect to the initial EPS facing position). This behaviour suggests that, although the wall travelled 20 mm, from the active to the passive positions, the bottom of the EPS facing moved only 7 mm (-15 - (-22) = 7). In the active phase of the second cycle, the EPS facing top and bottom movements were -7 mm and -23 mm respectively.

This behaviour led to the displacement envelopes at the top and bottom ends of the EPS facing are constantly smaller than the envelope of the applied displacement (see Figure 6.27).

At the end of the test, the top and bottom ends of the EPS facing were displaced by -11 mm and -30 mm respectively.

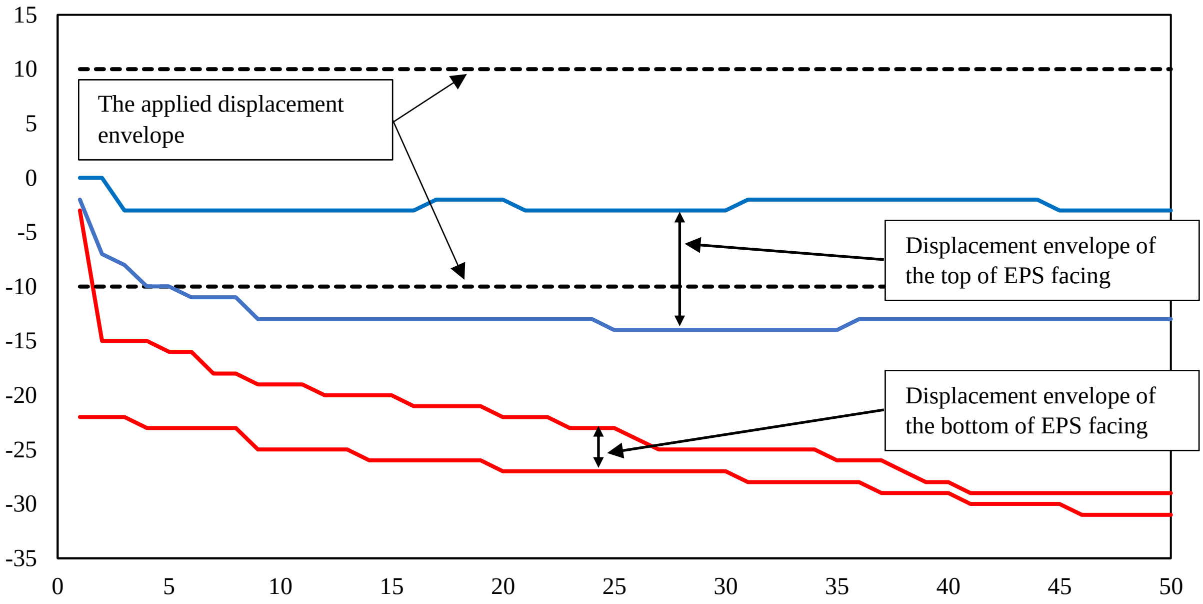

Figure 6.27 Displacement envelopes of the wall and the EPS–soil interface

According to Figure 6.27, the EPS facing did not cross the initial EPS-soil interface (toward the passive side) at any time during the test. The displacement envelopes at the top and bottom of the EPS facing remained less than the total applied amplitude (20 mm). Nevertheless, settlement was accumulated to a certain extent during the test. This behaviour suggests that, the EPS inclusion was very effective in eliminating the effects associated with the passive wall movements. In the passive phase, the EPS inclusion deformed and, hence, absorbed the wall passive displacement (10 mm) with no effects being transferred to the adjoining soil. However, during the active phase, the EPS inclusion did not withstand the active earth pressure, therefore; it moved along with the wall towards the active side. This movement was sufficient to develop a slippage in the active soil wedge. This case depicts a wall that moves with a small amplitude between the neutral and active positions only. Therefore, soil settlement will still develop under such loading pattern but with a smaller extent than that if the wall moves between the active and passive positions.

6.4 Conclusions

This chapter presented the results of 4 experiments conducted on medium-dense soil (black sand) using a physical model that simulate prototype dimensions. The analysis of the results revealed the following critical conclusions;

- The log-spiral solution developed in Chapter 3 gives the best estimation for the passive earth pressure coefficient K_p over other classical theories such as Rankine, Coulomb and Caqout and Kerisel (1948).
- The mode of the wall movement has a significant impact on the magnitude and vertical distribution of the pressure and the deformation in the soil adjacent to the wall. The escalation in the lateral pressure and soil deformation are greater when the mode of movement is translation.
- The deformation of soil under translational mode involve a considerable soil heaving due to the slippage of the passive wedge. In the rotational movement mode, the heaving is insignificant.
- The existing design guidelines that adopt right triangular earth pressure distribution based on classical theories may well underestimate the lateral pressure, especially in semi-integral bridges where the movement mode is dominantly translation.
- The design guidelines that use a bilinear stress distribution such as BS PD 6694/1 (2011) provide a sufficiently conservative estimation for the lateral earth pressure when the movement mode is rotation. However, in the case of translational movement mode, these guidelines underestimate the lateral earth pressure at the bottom half of the wall.
- The passive failure surface developed under monotonic or cyclic loading involves composite surface comprising a straight line and a curve at the bottom near the toe of the wall.

- Using a 600 mm thick, medium-stiffness, EPS inclusion reduced the soil settlements by more than 60%. However, a small trough will develop in the soil but with considerably small extent compared to the case without EPS inclusion. This settlement is due to the EPS inclusion not standing the active soil pressure during the active phase of the movement.
- The lateral earth pressure developed at the wall-EPS interface correlates with the yield stress of the EPS inclusion. The pressure showed to be uniform, across the wall-EPS interface and is independent of the number of cycles. Using a low-stiffness EPS inclusion may reduce the lateral pressure but may lead to a greater settlement.
- A better EPS inclusion arrangement may involve a thin strip of low-stiffness EPS placed between the wall and a large wedge-shape EPS inclusion. The low-stiffness EPS strip will keep the lateral earth pressure at lower levels while the wedge-shaped inclusion provides a self–stable soil mass to avoid soil slippage during the active phase of the wall movement.

Chapter 7

Finite Element Modelling of Soil-Structure Interaction in Integral Abutment Bridges

7.1 Introduction

Computer simulations utilising reliable numerical models have been applied extensively in many engineering applications of practical interest. The numerical modelling provides an effective tool to produce results at minimal time, cost and effort. In its application to IABs, computer modelling based on the finite element method has been used to investigate the soil-structure interaction behaviour under the temperature induced loads (Springman et al., 1996; Dicleli, 2000; Horvath, 2000; Kim and Laman, 2010; Bloodworth et al., 2012; David et al., 2014). However, to develop an efficient and reliable computer model, sufficient calibration and validation with physical data need to be undertaken.

In this chapter, three-dimensional finite element models are developed using the ABAQUS/Standard (2017) finite element modelling software and validated against the experimental data reported earlier in Chapter 6. The validation process involves the evaluation of the modelling results against the results of tests T3 and T4 (Translational movement without EPS inclusion and Translational movement with EPS inclusion)

7.2 The GSK Soil Model

In the present chapter, the soil is modelled using a nonlinear Mohr Coulomb criterion following the principle of the GSK soil model proposed by Krabbenhoft et al. (2012). The main objective of using this modelling approach is to account for the changes in the soil properties resulting from the cyclic wall movements which are addressed in terms of the changes in the confining pressure.

The GSK model offers the possibility of either using an associated or non–associated flow rule to simulate cohesive and non-cohesive frictional soils. Unlike Mohr Coulomb, the GSK model takes into account the stress dependency of the strength by varying the internal friction angle and the cohesion of the soil with the minor principle stress. According to Krabbenhoft and Christensen (2019), the GSK model assumes a curved failure envelope, in the $\sigma - \tau$ plane, rather than a straight line.

In the GSK model, the yield function is given by:

$$F = -[\sigma_1 - a_2(\sigma_3 - \sigma_t)] - (k - a_2\sigma_t)\left\{1 - \exp\left[\frac{a_1 - a_2}{k - a_2\sigma_t}(\sigma_3 - \sigma_t)\right]\right\} \tag{7.1}$$

where a_1, a_2 and k are the parameters characterising the yield envelope in the $\sigma_3 - \sigma_1$ space (see Figure 7.1) and are given by the following formulas:

$$a_1 = \frac{1 + \sin\phi_1}{1 - \sin\phi_1} \tag{7.2}$$

$$a_2 = \frac{1 + \sin\phi_2}{1 - \sin\phi_2} \tag{7.3}$$

$$k = \frac{2c\cos\phi_2}{1 - \sin\phi_2} \tag{7.4}$$

where σ_1 and σ_3 are the major and minor principle stresses, ϕ_1 and ϕ_2 are the angles of internal friction at low and high stress levels respectively (see Figure 7.1), c is the apparent cohesion at high stress level and, σ_t is a finite tensile strength.

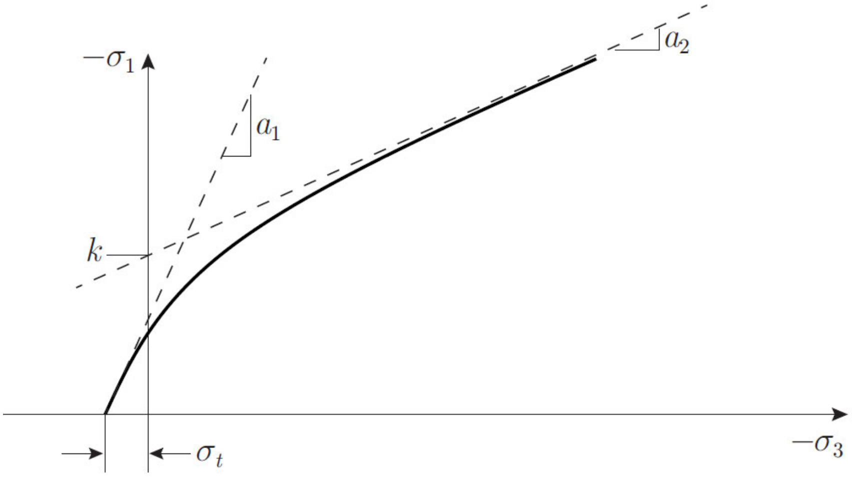

Figure 7.1 GSK yield envelope in the $\sigma_3 - \sigma_1$ plane

In view of equations (7.2) - (7.4), the GSK model is characterised by parameters ϕ_1, ϕ_2 and c which delineate the yield function in the $\sigma - \tau$ space. According to Figure 7.2, the yield function of the GSK model involves a curve with an initial slope equals to $\tan\phi_1$ and an asymptote follows the equation, $c + \tan\phi_2$.

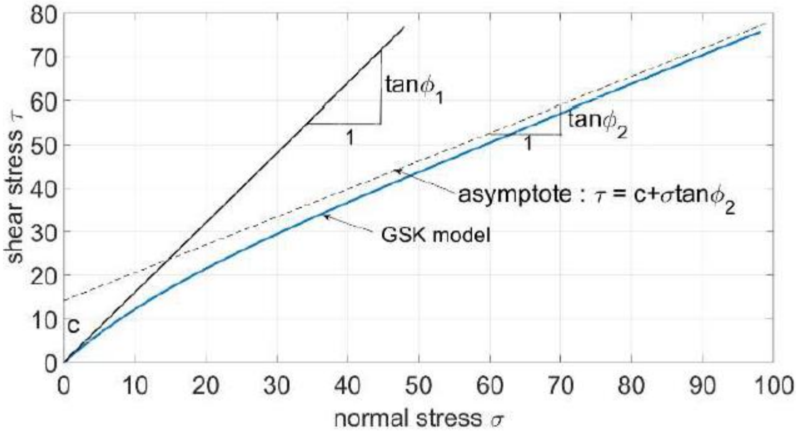

Figure 7.2 The GSK model yield function (Krabbenhoft and Christensen, 2019)

The attractive feature of the GSK model is that the parameters involved in the model can be interpreted in terms of Mohr Coulomb criterion. Therefore, it provides a nonlinear Mohr

Coulomb envelope with confining pressure-dependent shear strength parameters; friction angle ϕ_{MC} and cohesion c_{MC} given by:

$$\phi_{MC} = \arcsin\left(\frac{B-1}{B+1}\right) \tag{7.5}$$

$$c_{MC} = \frac{1-\sin\phi_{MC}}{2\cos\phi_{MC}}\left(A + B\sigma_3\right) \tag{7.6}$$

where;

$$A = a_2(\sigma_t - \sigma_3) + (k - a_2\sigma_t)\left\{1 - \exp\left[\frac{(a_2 - a_1)(\sigma_t - \sigma_3)}{k - a_2\sigma_t}\right]\right\} \tag{7.7}$$

and,

$$B = a_2 - (a_2 - a_1)\exp\left[\frac{(a_2 - a_1)(\sigma_t - \sigma_3)}{k - a_2\sigma_t}\right] \tag{7.8}$$

7.2.1 Soil Stiffness

It is understood that, under a cyclic loading condition, the stiffness of the soil, *E*, changes considerably with the loading/unloading cycles. The stiffness of the soil during the initial (virgin) loading is typically less than the loading/unloading stiffness in the subsequent cycles (see Figure 7.3). In the default Mohr-Coulomb model in ABAQUS Standard (2017), the soil stiffness is considered to be constant and only one value can be specified for the stiffness of the soil in the material property module. As a matter of fact, even GSK model does not consider an increase in the soil stiffness in response to the loading and unloading of the soil.

However, the interaction between the abutment and the approach soil, in an integral abutment bridge, involves cycles of loading and unloading due to the potential active and passive abutment movements. Therefore, it is pivotal to address the increase and decrease in stiffness in different parts of the soil when simulating the abutment-soil interaction in IABs.

In order to address this deficiency in the original GSK model, the stiffness of the soil will be introduced as a pressure-dependent variable (similar to c and ϕ). This modification establishes an extension to the GSK model where the change in the soil stiffness as a result of the cyclic loading will be taken into account. Therefore, the model proposed in this Chapter will be referred as the “Extended GSK” model or the EGSK model for an easy reference.

The pressure-dependent soil stiffness can be calculated using equation 7.9 (Chanaton et at., 2012; OPTUM CE, 2016)

$$E = E_{ur,ref}\Pi\left(\sigma_3'\right) \tag{7.9}$$

where, $E_{ur,ref}$ is the stiffness at the unloading/reloading and is estimated based on the large strain stiffness modulus $\left(E_{50}\right)$, as given in equation 7.10

$$\left(\frac{E_{ur,ref}}{E_{50}}\right) \approx 2-5 \tag{7.10}$$

$$\Pi\left(\sigma_3'\right) = \left(\frac{-\sigma_3' + c/\tan\phi}{p_{ref} + c/\tan\phi}\right)^m \tag{7.11}$$

with σ_3' as the minor principal stress (confining pressure),

p_{ref} is the confining pressure in the triaxial compression test which was used to calculate E_{50} and, *m*, is a fitting parameter and its value depends on the soil type. It is suggested that for sands and other coarse grained soils, a value of 0.5 is appropriate while for clay, the value of *m* can be assumed between 0.9 and 1 (Chanaton et al., 2012).

It is worthwhile noting that, in modelling the black sand, the value of the exponent parameter *m* is taken as 0.7 taking into account the fact that the black sand particles are generally of small size (between 0.075 - 0.150 mm), which suggests that its behaviour, in this context, is between coarse-grained soil and clay (or fine-grained soil). Furthermore, this value showed that the computed moduli for confining pressures, 30 kPa, 60 kPa, 90 kPa and 150 kPa, fits well to the values measured in the triaxial tests (as reported in Chapter 5).

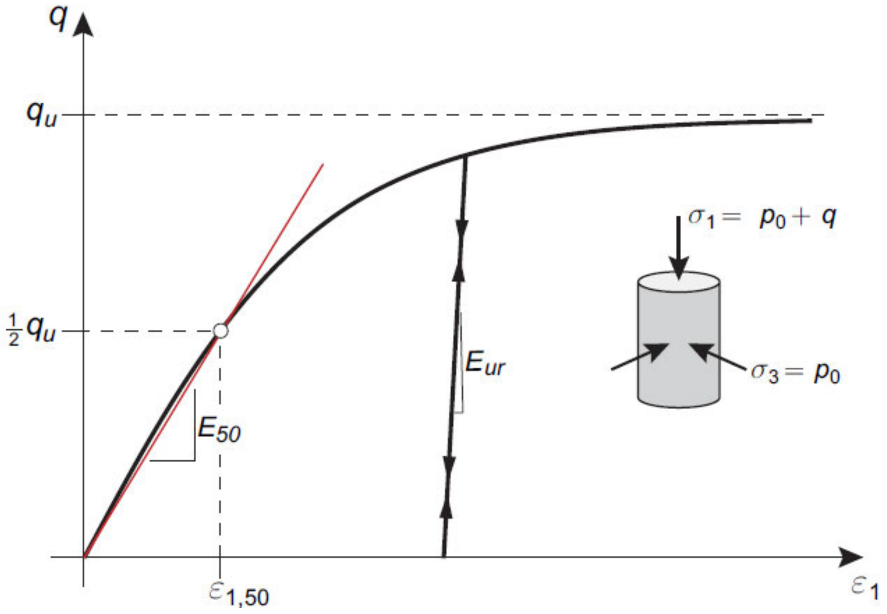

Figure 7.3 The soil behaviour in the virgin loading and subsequent unloading/reloading compared to Mohr Coulomb model

7.3 Formulation of Extended GSK Model for the Black Sand

In order to use the Extended GSK model (EGSK model), as a material model for the black sand, the model parameters must first be determined. The data from four triaxial tests, conducted on black sand specimens (as discussed in Chapter 4), were used to calibrate the

$\sigma_3 - \sigma_1$ curve. This curve is then used to calibrate the parameters a_1, a_2 and k as shown in Figure 7.4.

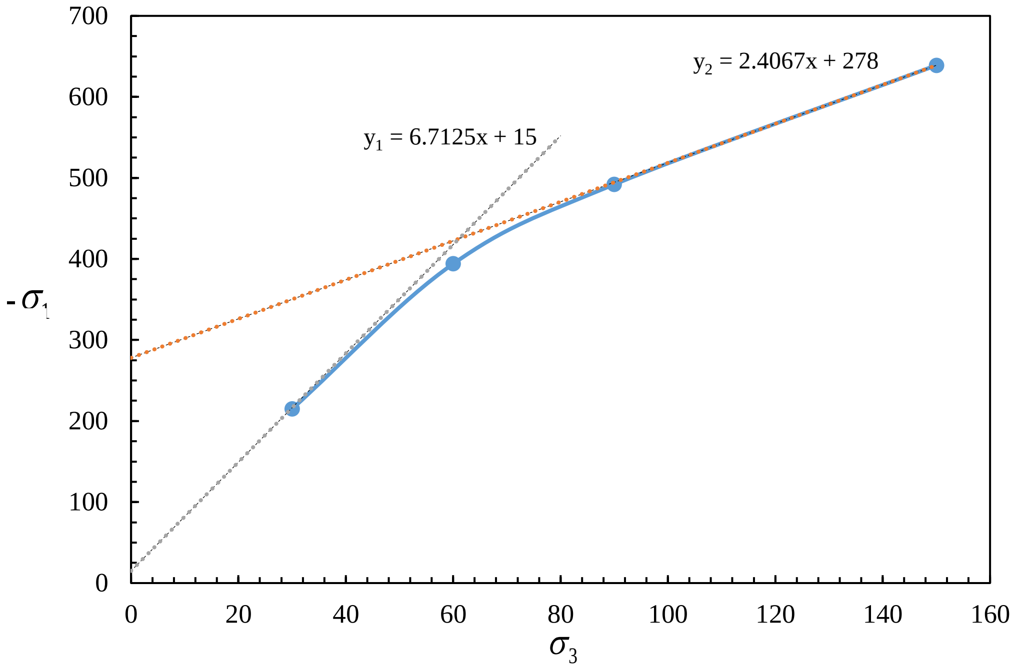

Figure 7.4 The $\sigma_3 - \sigma_1$ plot for the black sand based on triaxial test results

In accordance with Figure 7.4 the EGSK model parameters are determined as:

$a_1 =$ 6.7, $a_2 =$ 2.4, $k =$ 278 kPa and $\sigma_t =$2.45 kPa

These parameters have been used to calculate the modified Mohr Coulomb parameters, ϕ_{MC} and c_{MC} for a range of confining pressure σ_3 between -1 kPa and -300 kPa (the negative sign indicates a compressive stress). According to the experimental data (as discussed in Chapter 6), this range of stresses covers the potential confining pressures developed during the modelling and expected to develop in a full-scale prototype. The magnitudes of soil stiffness have also been calculated for this range of confining pressures using equations 7.9 to 7.11. In these equations the values of E_{50} and P_{ref} were taken as 48000 kPa and 150 kPa respectively based on data from the triaxial tests.

The dilation angle, ψ, at different confining pressures, is determined as a function of the peak and critical state friction angles, using the equation proposed by Bolton (1986) (equation 7.12).

$$\psi = \phi_{peak} - \phi_{critical} \tag{7.12}$$

where, $\phi_{peak} = \phi_{MC}$ while the friction angle at the critical state is deemed equal to the slope angle of the asymptote (ϕ_2).

A summary of the pressure-dependent parameters used in the EGSK model are shown in Table 7.1.

Table 7.1 Values of ϕ_{MC} and c_{MC} for various values of confining pressure

σ_3 (kPa)	A	B	ϕ°_{MC}	c_{MC} (kPa)	ψ°	E (MPa)
-1	6.67	6.63	47.56	0.01	23.2	14.4
-30	175.28	5.11	42.26	4.88	17.9	17
-60	312.30	4.10	37.46	16.29	13.1	28.5
-90	425.25	3.47	33.57	30.22	9.22	37.1
-150	611.26	2.83	28.50	55.75	4.16	48
-180	625.31	2.79	28.22	57.51	2.71	51.5
-210	771.2	2.57	26.06	72.44	1.74	54.5
-240	847	2.51	25.43	77.7	1.11	57.3
-270	921.7	2.47	25.02	81.4	0.71	60
-300	995.3	2.44	24.7	84.1	0.45	62.3

7.4 Validation of the EGSK Model

This section presents the verification of the modelling results obtained, using the GSK model, against experimental data from the physical model tests discussed in Chapter 6. It involves comparisons between the results of two modelling approaches, first, using the elasto-plastic

Mohr Coulomb model; and second, using the EGSK model (which is essentially a non-linear Mohr Coulomb model).

In the default Mohr Coulomb model, in ABAQUS Standard (2017), the properties of soil, including ϕ, ψ, c and the stiffness of soil *E*, are introduced by entering their values in the property module. Such values are preserved during the analysis without any change. Unlike Mohr Coulomb material model, in the EGSK model, the values of the aforementioned parameters vary according to the changes in the confining pressure (σ_3).

A user defined field subroutine is written in ABAQUS Standard (2017) to vary the soil stiffness and strength with σ_3.

Strictly, the non-associated flow rule of the Mohr Coulomb model in ABAQUS Standard (2017) is used with the GSK failure surface with σ_3 dependency (Table 7.1) in the modelling in this chapter.

7.4.1 The Finite Element Model

Three-dimensional finite element models are developed, using the ABAQUS Standard (2017), to simulate the two physical tests, T3 and T4. The model is created using 10-node quadratic tetrahedron elements (C3D10) with quadratic geometric order.

The interactions between the wall and the soil and between the soil and the sides/bottom of the tank have been modelled using a frictional interface using a penalty friction formulation with finite sliding for the tangential behaviour and hard contact for the normal behaviour.

The loading is applied as a periodic uniform wall displacement following the equation,

$$a = A_0 + \sum_{n=1}^{N} B_n \sin n\omega \qquad (2.13)$$

were,

A_0 is the initial amplitude

N represents the total number of the movement cycles

n is the cycle number

B_n is the coefficient of the Sine term (in this model, $B_n = 1$) and,

ω is the circular frequency and is given by $2\pi N$

The geostatic stresses are applied in the initial step using the predefined field feature in ABAQUS Standard (2017), and in the Geostatic step, a gravity load is applied to balance the predefined initial stresses to eliminate any deformations due to initial stress state.

7.4.2 Modelling Results – Test T3

The test T3 involves the movement of the wall in translational mode against and away from the retained soil with an amplitude of ± 10 mm. The loading conditions in test T3 depict the most severe case in terms of the deformations and the stresses developed as a result of the wall movements. Therefore, this test presents a relatively challenging case to validate the efficacy of the EGSK model. As mentioned earlier, the conditions in test T3 were modelled considering both, the Mohr Coulomb model and the EGSK model proposed here.

Figure 7.5 shows the deformed three-dimensional model of test T3 after the analysis using the EGSK model.

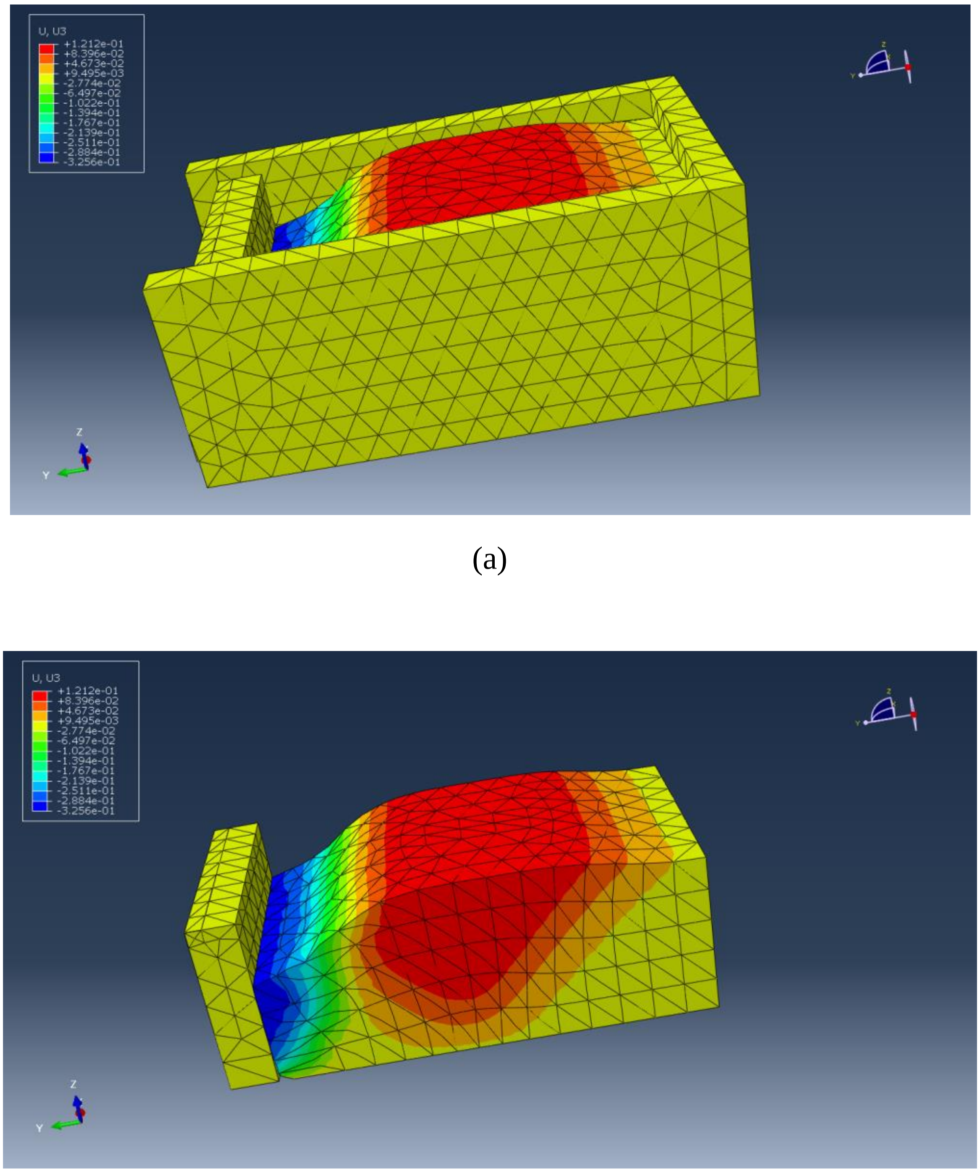

(a)

(b)

Figure 7.5 The deformed 3D model of test T3 showing (a) The complete model and (b) The soil and the wall only

The maximum settlements recorded at the soil-wall interface are plotted against the number of cycles, as shown in Figure 7.6.

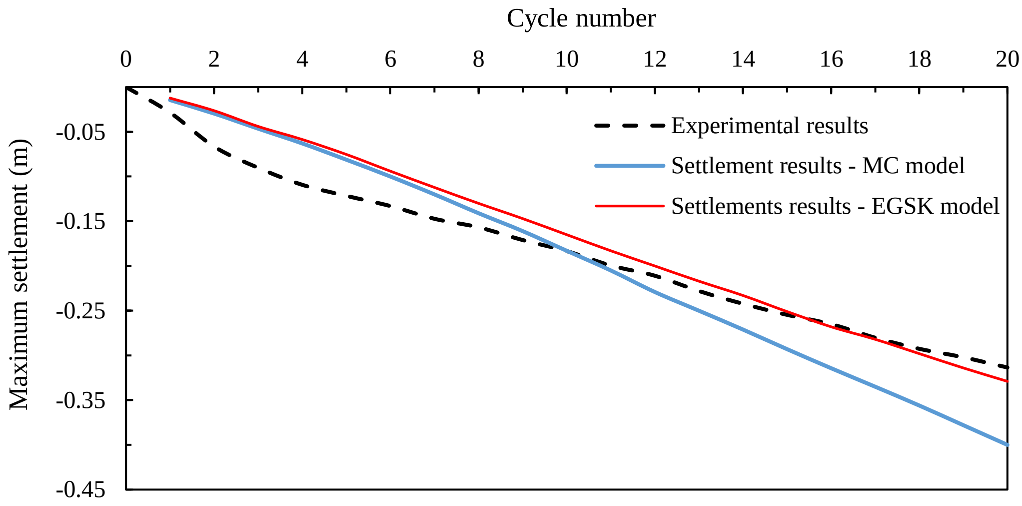

Figure 7.6 Experimental and modelling results of the maximum settlements of test T3

The settlement results computed using the EGSK model are notably closer in the final cycles to the actual measured data than those computed using Mohr Coulomb model. The latter produces settlement results that increase quite linearly with the number of cycles which results in overestimating the total settlement after 20 loading cycle. The results of the EGSK model show a slight nonlinearity with the settlement rate decreasing with the number of cycles. A comparison of the cumulative settlement results between the two modelling approaches together with the measured data is shown in Table 7.2. It can be observed that the EGSK model overestimates the actual measured data after 20 cycles by less than 5% while that of Mohr Coulomb model overestimates the measured data by approximately 27%.

Table 7.2 Comparison of the modelling results with the measured data of test T3

Results type	Total settlements (after 20 cycles) (mm)	Error margin
Mohr Coulomb	401	+ 27%
GSK model	329	+ 4.7%
Measured data	314	-

The modelling results for the lateral pressures at the soil-wall interface have also been determined using both modelling approaches (Mohr Coulomb and EGSK models) and compared with those recorded during test T3. Figure 7.7 shows the computed lateral pressure at a depth $H/3$ from the soil surface which depicts the location of the top sensor. It can be observed that the lateral pressures computed using the EGSK model are also replicating the measured data better compared to those computed using the Mohr Coulomb model.

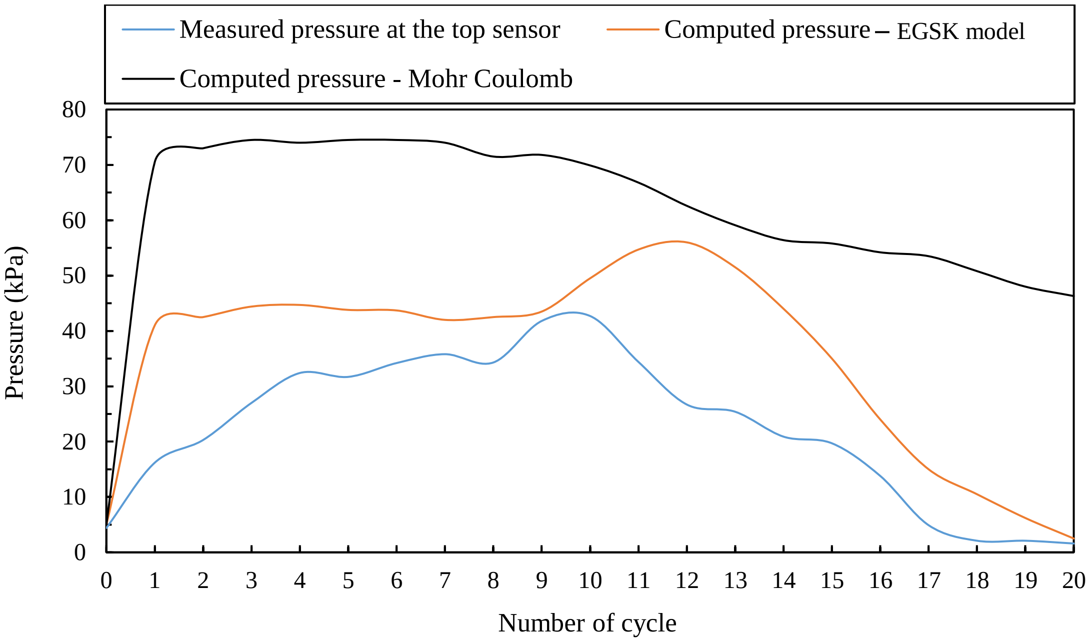

Figure 7.7 The computed and measured lateral pressures at the top sensor, test T3

Similarly, the lateral pressures computed using the EGSK model at the middle sensor (at depth of $2H/3$ from the soil surface) showed to be in a good agreement with the measured data as shown in Figure 7.8. The results computed using Mohr Coulomb model, at the location of the middle sensor, are overestimating the measured data by more than 50%.

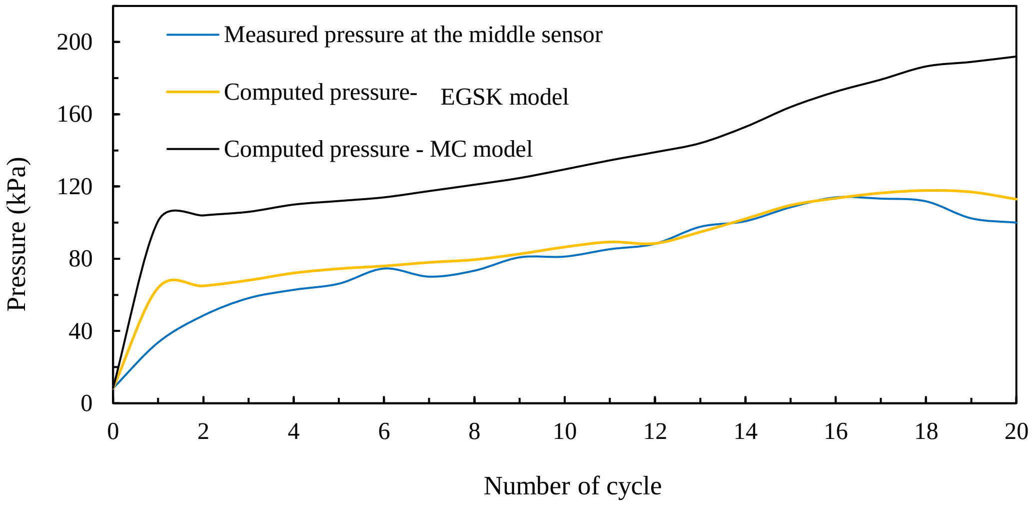

Figure 7.8 The computed and measured lateral pressures at the middle sensor, test T3

7.4.3 Modelling Results – Test T4

In order to explore the validity of the proposed modelling approach under more complex soil-EPS-wall interactions, the test T4 has been carried out. A three-dimensional finite element model is therefore developed to replicate the conditions in test T4, including the EPS-wall and soil-EPS interactions.

The EPS inclusion has been modelled as a solid deformable material using the hyperfoam material model, available in ABAQUS Standard (2017). The hyperfoam model is calibrated using experimental data from a number of laboratory tests carried out on EPS specimens (as discussed earlier in Chapter 4). Tangential and normal behaviours have been defined, using the Interaction Property module in ABAQUS Standard (2017), to model the interactions at the wall-EPS and EPS-soil interfaces.

Comparison between the measured and modelling results of the maximum settlement in test T4 is shown in Figure 7.9. Similar to the modelling results of test T3, the settlements computed using the EGSK model are in a closer agreement with the measured data than those obtained from the modelling using the Mohr Coulomb model. Similar to the modelling of test T3, the settlements from the EGSK model show signs of curvature and is approaching an asymptote in the last few cycles with a final increment rate of 0.8%. This rate is relatively close to that in the measured data which is 0.57%. However, the settlement results computed using the Mohr Coulomb model replicate almost a linear relationship between the settlement and the number of cycles which results in overestimating the final settlement by more than 20%.

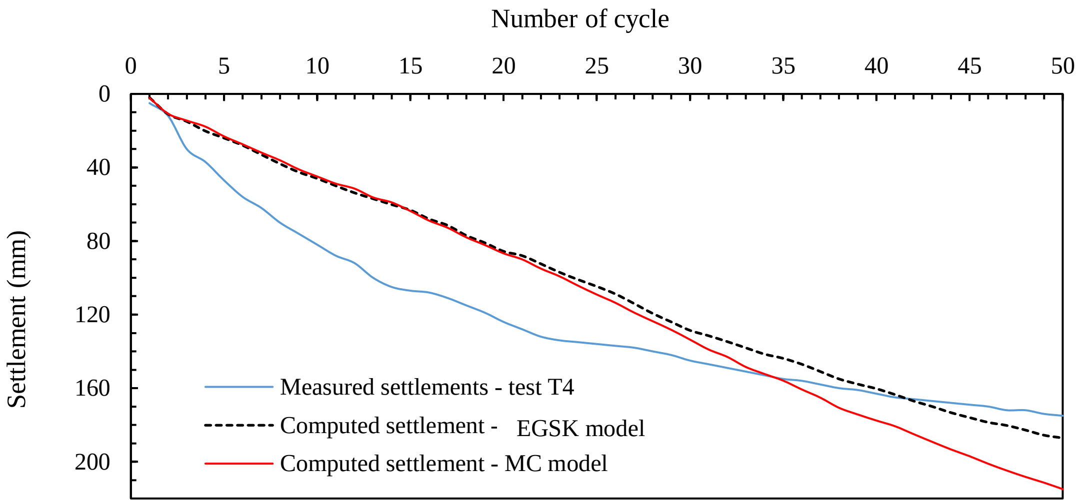

Figure 7.9 Experimental and modelling results of the maximum settlements of test T4

The proposed modelling approach has also been tested in calculating the lateral pressure at the EPS-wall interface in test T4. The lateral pressures at the locations of the top, middle and bottom sensors have been computed using the EGSK and the Mohr Coulomb models and then compared with the measured data of test T4. It is worthwhile noting that, the values of the lateral pressures measured in the three sensors, in test T4 were very close and cannot be separately delineated in the plot (see Figure 6.23). Therefore, the average value of 80 kPa is taken as the measured pressure for all three sensors.

According to Figures 7.10, the curves of lateral pressures, computed using the EGSK model, tend to level off with the number of cycles at values between 80 kPa and 90 kPa for middle and bottom sensors. This behaviour agrees well with the measured data from test T4.

However, the pressures computed at the location of the top sensor showed to be slightly below the average value of the measured data.

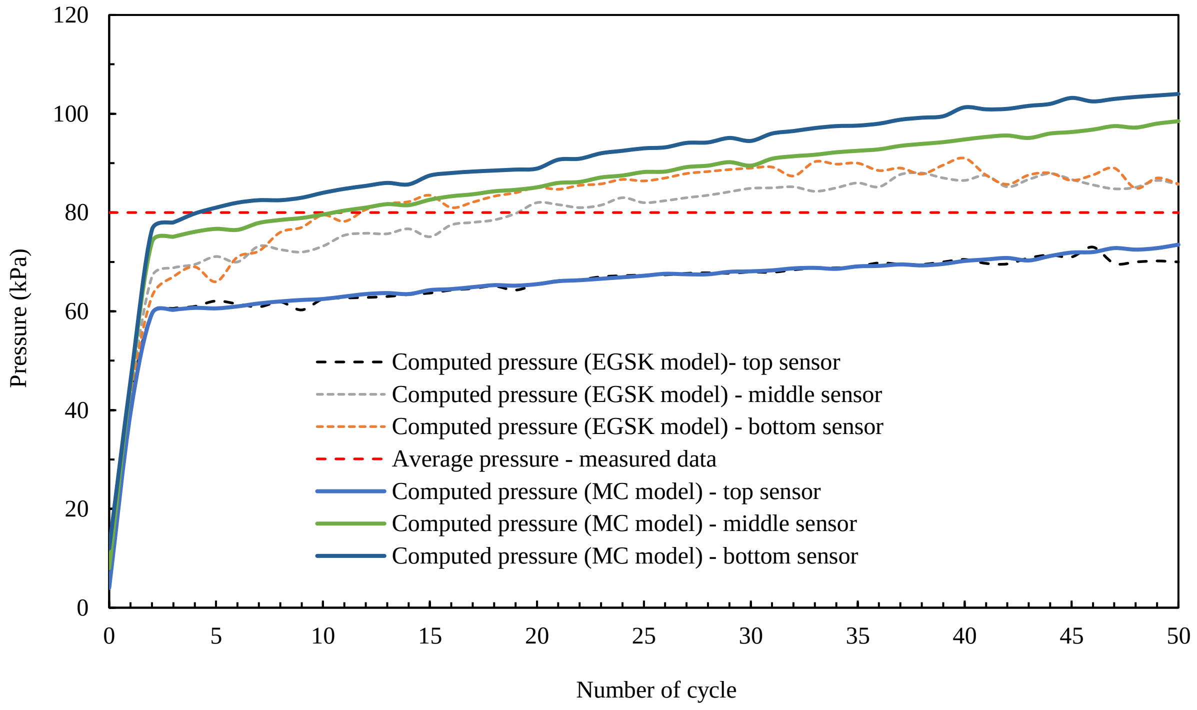

Figure 7.10 Computed lateral pressure using EGSK model, test T4

The pressures computed using the Mohr Coulomb model showed noticeable qualitative and quantitative variations from those computed using the EGSK model as well as the measured data. It can be observed, from Figure 7.10, that the relationship between the pressure and movement cycles depicts an elasto-plastic behaviour with the pressure increasing steadily with no sign to asymptote even after 50 loading cycles. This behaviour does not follow the data observed in test T4.

Quantitatively, the pressures computed, using the MC model, at the locations of the middle and bottom sensors are higher than those in the measured data. After 50 cycles, the pressure computed at the location of the bottom sensor is 104 kPa which overestimates the average measured data by approximately 30%

The aforementioned results suggest that the EGSK model is better in modelling the soil settlement and stress ratcheting at the soil-wall interface than the default MC model. This may indeed underpin the advantage of using the EGSK model in modelling deep abutments in IABs where the soil-structure interaction requires rigorous numerical analyses as recommended by the British Standard PD6694-1 (2011) specifically for such cases.

7.5 Application of EGSK Model in a Deep Embedded Integral Abutment

The validation process discussed in the previous section shows that the EGSK modelling results are closer to the measured data than those produced by the MC model. It has also been concluded that the EGSK can be better applied in modelling cases over a higher range of confining pressure, such as those in IABs with deep abutments.

In order to explore the efficacy of the EGSK in modelling such cases, a three-dimensional model of a prototype IAB with a deep abutment is developed using the ABAQUS Standard (2017) finite element software. The modelled case involves 5 m high concrete abutment, with 45° inclined wing walls, supported by 9 (8 m long) steel H piles. The model replicates the approach of 16 m wide fully integral abutment bridge (FIAB) as shown in Figure 7.11.

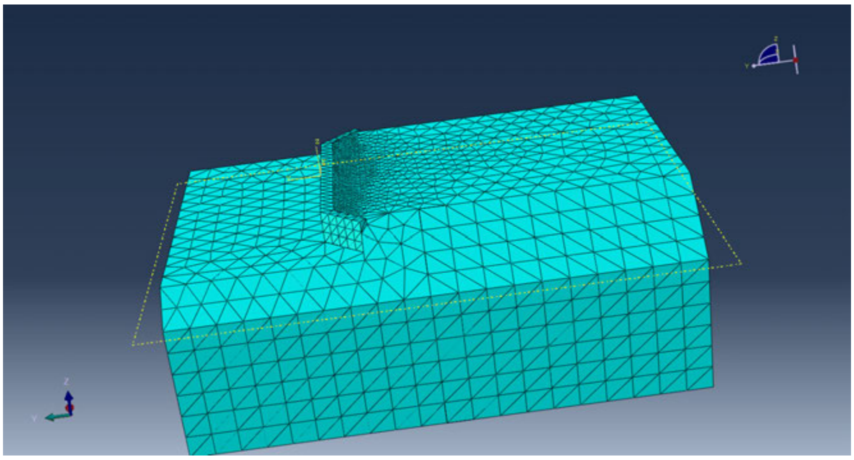

(a)

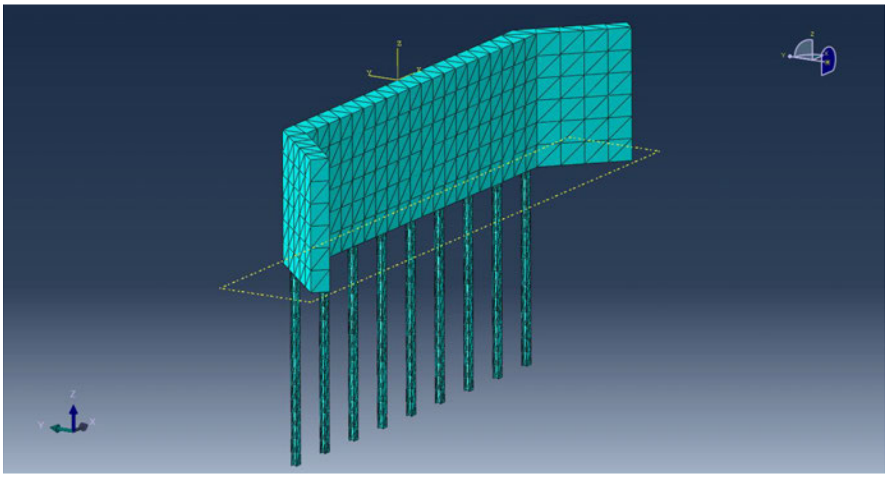

(b)

Figure 7.11 Three-dimensional model of deep abutment IAB showing (a) The complete 3D model and (b) The abutment and piles

For the sake of comparison, the properties of soil, in both the MC and the EGSK models, have been taken similar to those used in the modelling of the physical tests with an exception to the unit weight which is taken as 18 kN/m^3.

The boundary conditions are defined in terms of displacement controls in x, y and z directions. Vertical boundaries were restrained in the direction orthogonal to the plane at which the boundary exists. Bottom boundary has been restrained in x, y and z directions. Mesh setup was selected so that larger mesh utilised near the boundaries to avoid the boundary effects and finer mesh near the abutment wall.

The properties of the concrete abutment and the steel piles are shown in in Table 7.3

Table 7.3 properties of the concrete abutment and the steel piles

Parameter	**Concrete wall**	**Steel Pile**
E, (kPa)	30 x 10^6	200 x 10^6
Unit weight (kN/m^3)	23.4	78
Poisson's ratio	0.25	0.3
Type/specification	-	HP 310 x 110

The loading is applied in terms of active and passive horizontal displacements of 0.4% at the top of the abutment (equivalent to ± 20 mm). Thirty loading cycles have been applied in each of the modelling cases (MC and EGSK models).

7.5.1 Modelling Results

The maximum settlement results observed in the two modelling methodologies are illustrated in Figure 7.12. The total settlements recorded, after 30 cycles, were 193 mm and 147 mm for the MC and EGSK models respectively. This reflects a difference of more than 30% which is greater than those observed in modelling tests T3 and T4 (about 20% in both). Furthermore, the settlement curve of the EGSK modelling results is highly nonlinear with a considerable reduction in the settlement rate. The latter decreased from an average of 7.9%, over the first five cycles, to an average of 1.4% over the last five cycles. The settlement results computed using the MC, on the other hand, showed a similar behaviour to that observed before, with the settlement increasing linearly with the number of cycles.

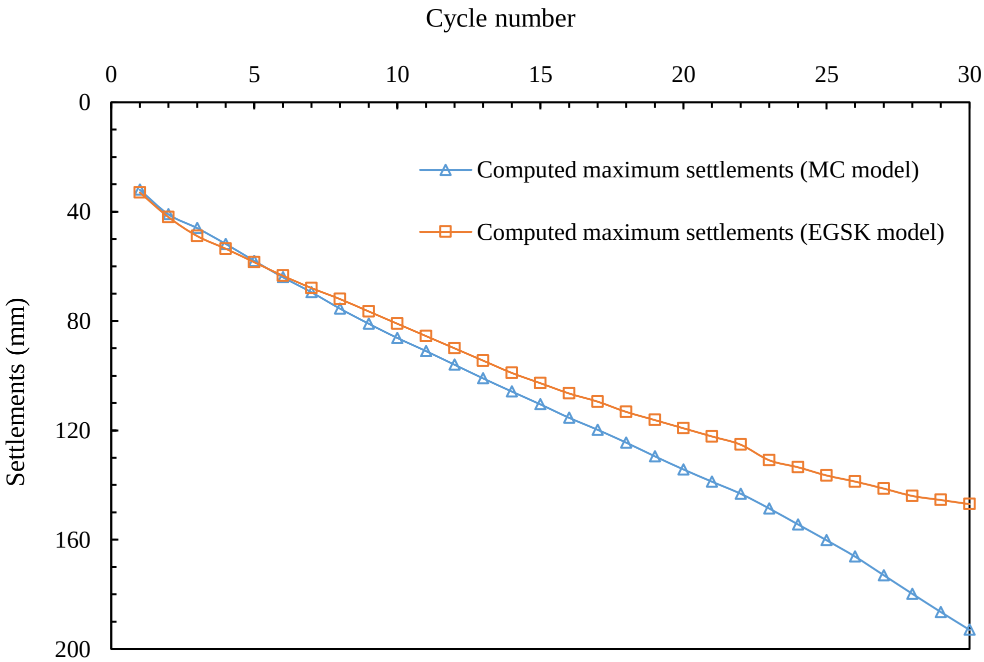

Figure 7.12 Settlements computed using the MC and the Extended GSK models, 3D prototype model

The computed lateral pressures at depths ${}^{H}\!/_{3}$, ${}^{2H}\!/_{3}$ and H, from the initial soil surface, have also been observed. According to Figure 7.13, notable variations between the results of the two modelling approaches can be seen. The pressures computed, in the three locations, using the MC model are generally greater than those calculated using the EGSK and demonstrated linear lateral pressure increase in the first few loading cycles and asymptote after that. No peak is observed regardless of the depth from the soil surface. On the contrary, the plots of the pressures from the EGSK model show a non-linear behaviour over the initial 5 loading cycles. The pressure at depth equals to ${}^{H}\!/_{3}$ records a peak of 171 kPa followed by a slight decrease in the post-peak region ending with 151 kPa in the last cycle. The pressure at a depth $2H/3$ shows a noticeable peak after 15 cycles with the lateral pressure increasing from 91.5 kPa, in cycle 15, to 101 kPa in the last cycle.

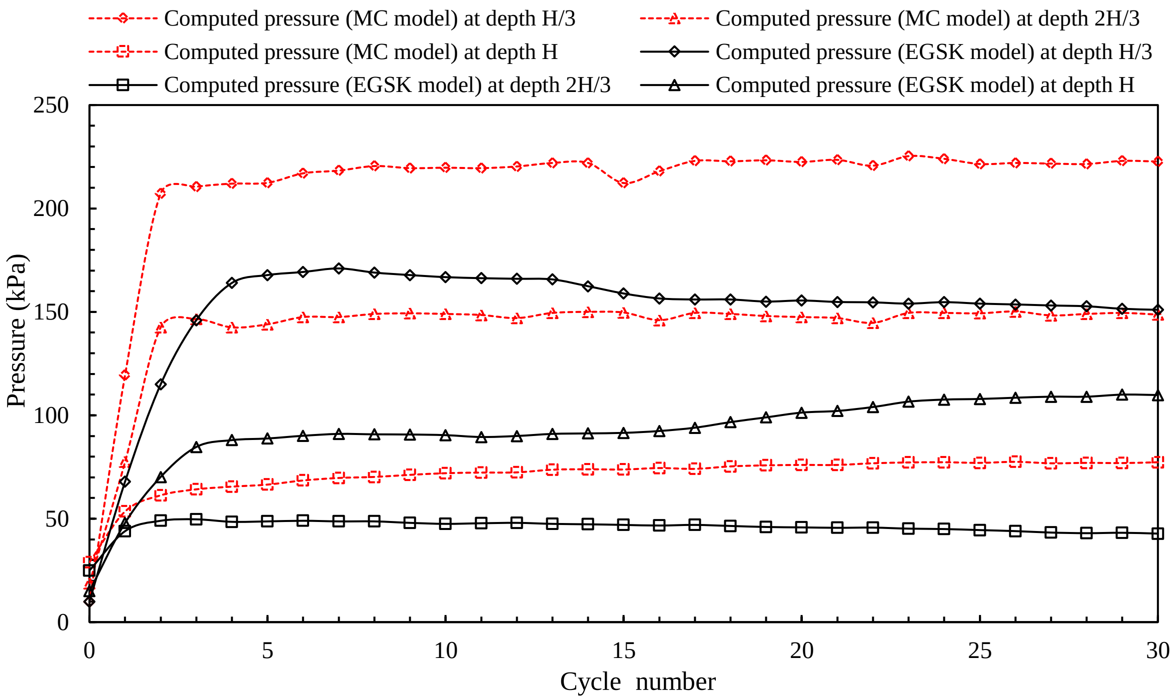

Figure 7.13 The lateral pressures computed using the MC and the Extended GSK, 3D model of deep embedded integral abutment

7.6 Conclusion

This chapter presented a finite element modelling approach that utilises a non-linear Mohr Coulomb failure criterion, for the soil, similar to that in the GSK constitutive model proposed by Krabbenhoft et al. (2012). Three-dimensional finite element models were developed using ABAQUS Standard (2017) to validate the efficacy of the proposed modelling approach against experimental data from tests T3 and T4 (discussed in Chapter 6). After validating the proposed model, a three-dimensional model of a full integral abutment bridge was developed to evaluate the application of the EGSK model in replicating the abutment-soil interaction under a higher range of confining pressure as would occur in a deep embedded integral abutment. Based on the modelling results, the following conclusions have been drawn,

- The GSK constitutive model provides an efficient soil model with a relatively simple calibration process. The GSK model parameters can be determined based on data from triaxial tests with different confining pressures.
- The GSK model can be extended by incorporating the changes in the soil stiffness during soil-structure interactions by relating the soil stiffness to the confining pressure similar.
- The validation outcomes showed that the results of the EGSK model are generally in closer agreement with the measured data in terms of the settlement and the lateral pressure ratcheting at the soil-wall interface than those given by the Mohr Coulomb model.
- The modelling results using the EGSK model showed a non-linear relationship between the maximum settlement and the loading cycles. This behaviour deviates from that observed in Mohr Coulomb modelling results where the relationship is quite linear.

- The settlements and the lateral earth pressures computed using the Mohr Coulomb model are generally overestimating the actual measured data.
- In the EGSK model, the stiffness and the strength parameters are dependent on the confining pressure. Therefore, the Extended GSK model is more effective in modelling real-world cases where a wide range of confining pressures resulting from soil-structure interactions is expected. However, since even the EGSK model tends to underestimate initial settlement, future improvements to the model can be made to better capture the initial stiffness of the soil.

Chapter 8

Summary, Conclusions and Recommendations for Future Work

8.1 Summary

Integral abutment bridges are receiving growing interest as a favourable construction practice in many countries around the world. This is due to the merits perceived in IABs compared to the traditional (jointed) bridges. Among these merits, is the elimination of the expansion joints, and bearings in some case, which are the primary causes of most of the recurring, costly and traffic retarding maintenance works. In addition, IABs are easier and faster to construct and they possess an improved structural performance in various aspects of design, such as the resistance to seismic loading. However, the absence of expansion joints in the IABs results in temperature induced cyclic movements in the bridge abutments due to expansion and contraction of the bridge deck, which consequently lead to a settlement in the approach soil and an escalation in the lateral earth pressure acting on the abutment. These issues attracted research studies, where interaction problems in IABs were investigated. However, only a few of those studies investigated the possible mitigation measures for the settlements and the lateral pressure escalation in the approaches of IABs. Therefore, a standard design practice that account for the mitigation of the approach problems in IABs is currently not available. The present design practices of the soil-abutment interaction in IABs are classified into:

- No separation: In this case, the approach soil is built in contact with the abutment, so that any abutment movement is equally transferred to the adjacent approach soil.
- Partial separation: In this case, an inclusion is provided between the soil and the abutment so that only partial abutment movement is transferred to the soil through the

inclusion layer. The inclusions used for this purpose include collapsible inclusions (such as loose granular soil, tyre shreds or rubber chips) or non-collapsible inclusions such as EPS geofoam or cardboard.

- Full separation: in this case, the approach soil is built as a self-stable mass (such as MSE walls) with a gap separating the soil and the abutment.

None of the above measures can be said to have completely solved the approach issues. There is a room for development of other effective solutions for the broad spectrum of IAB cases.

Developing a practical remedial measure for the approach problems in IABs requires an in-depth knowledge about the soil-structure interaction at the bridge approaches, mobilised by the movements of the bridge abutments. Such knowledge, if adequately established, will form the cornerstone for any potential practical and efficient remedial measures.

This overall objective of the research presented in this thesis is to conduct a fundamental study of the soil-structure interaction in IABs and the mitigating effects of geofoam inclusions. This is performed through a series of experimental tests coupled with numerical simulations for the soil-abutment wall interaction.

8.2 Summary of Conducted Work

The work conducted in this thesis includes analytical, experimental, and numerical analyses of the soil-abutment wall interaction. The analytical work involves the development and validation of a new generalised solution to estimate the passive earth pressure on rigid retaining walls based on the log spiral method. The experimental work was conducted using a small-scale and a large-scale physical model. The experimental program investigated the soil-wall interaction behaviour under cyclic wall movements. The numerical analyses included proposing an extension to the GSK soil model developed by Krabbenhoft et al. (2012), which adopts a nonlinear Mohr Coulomb criterion, by incorporating the non-linear stiffness dependency of the soil on the stress level. The proposed EGSK model has the ability to capture the stiffness and strength variations in soil due to changes to confining as a result of wall movements realistically.

8.2.1 The Log-Spiral Solution

This part of the thesis includes the development of an analytical solution to estimate the passive earth pressure. The objectives of this work address the need for an efficient, and easy-to apply, method to estimate the passive earth pressure considering different parameters including the slope of the backfill, the soil friction angle, the soil-wall interface friction and the inclination of the face of the wall. Such a general yet simple solution developed in a spreadsheet was previously not available. The solution is formulated based on the hypotheses of Terzaghi (1948) considering a composite failure surface comprising a log-spiral arc and a tangent line. The solution is validated against experimental data from physical model tests performed in this study and experimental and numerical data found in the literature. It showed to replicate the validation data better than other classical theories of earth pressure.

The log-spiral solution developed in this study provides a simple and accurate method to estimate the passive earth pressure and it can also be easily formulated in Matlab as an alternative to an Excel spreadsheet.

8.2.2 Experimental Work (Small Wall Model)

This work is conducted using a physical model simulating a small wall retaining sandy soil. The objectives of this physical model are to evaluate the soil-wall interaction behaviour under different modes of cyclic wall movements, replicating rotation and translation. Small displacements of ± 2 mm were applied to replicate the abutment movements in an IAB due to expansion and contraction of the bridge deck due to temperature rise and fall. The results obtained from this experimental program provide a qualitative insight into:

- The stress ratchetting effects
- The vertical distribution of lateral earth pressure on the wall and,
- The complex mechanisms (soil densification, confinement and displacement) that leads to the settlement and/or heaving in the soil surface

Small wall experiments also investigated the potential application of the Expanded Polystrene (EPS) Geofoam as a compressible inclusion, between the abutment and the soil, to mitigate the adverse effects of wall movements. The EPS Geofoam is an excellent choice for such applications being a highly compressible material, has an extremely light weight and a relatively low stiffness. In addition to its potential use as a compressible inclusion, EPS Geofoam can largely reduce the loads applied on the subsoil and at the same time EPS Geofoam can support vertical loads adequately.

The function of the EPS Geofoam inclusion in attenuating the effects of wall movements on the adjacent soil is investigated through experimental and numerical modelling. New insights into the effects of the thickness, stiffness and the configuration of EPS Geofoam inclusion on its transfer function have been obtained from these investigations.

8.2.3 Experimental Work (Large Scale Model)

In this part of the thesis, a large experimental model is developed to replicate a 2 m high abutment retaining soil and subjected to different modes of movements. The model aims to investigate the abutment-soil interaction behaviour under similar stress, strain and loading conditions as in a real-world prototype case. The development of the model involved the following stages:

- Dimensional analysis to identify the measures required to achieve similarity between the model and real-world prototype conditions.

- Determination of model geometry and dimensions following the outcomes of the dimensional analysis study.
- Identifying and acquiring the materials to be used in the model, particularly the soil. In accordance with the outcomes of the dimensional analysis, a naturally heavy soil (two times heavier than the traditional backfill) need to be used to maintain the similarity of the model with the prototype. The soil used in this experimental model (the black sand) has never been utilised in a similar purpose of geotechnical research. Therefore, a comprehensive study of the back sand was conducted to determine its physical and mechanical properties.

Following the completion of the large-scale physical model, four experimental tests were carried out with the emphasis on observing the effects of the mode of wall movement and the presence of the EPS inclusion on the soil-wall interaction behaviour. These tests involved:

- Monotonic wall movement: in this test, the wall was moved in a monotonic movement until a full passive failure was observed. The objectives of these tests were to validate the log-spiral solution developed earlier in this thesis and to capture the shape of the passive failure surface of the soil.
- Cyclic wall movement: two tests were conducted under cyclic wall movements including pure rotation and pure translation. The primary purpose of these tests is to provide qualitative and quantitative evaluation of the deformations in the soil surface as well as the ratcheting effects in the lateral earth pressures. These two tests were conducted without including an EPS Geofoam inclusion.
- Cyclic, translational, wall movement with EPS Geofoam inclusion: in this test a 600 mm thick, medium stiffness, EPS inclusion was inserted between the wall and the soil. The test was conducted under a translational cyclic movement to evaluate the efficacy of the EPS Geofoam inclusion under the most sever scenario. This test was aimed to

establish new knowledge about the double interaction (Soil-EPS-wall) mechanism and to evaluate the function of the EPS inclusion in alleviating the wall movement effects on the backfill soil.

8.2.4 Numerical Analysis

In this part of the thesis, two-dimensional and three-dimensional models were developed using the ABAQUS/Standard (2017) finite element software. This was completed in two parts:

- Two-dimensional modelling (Chapter 4): in this part, two-dimensional models were developed and validated using data from the small wall tests. The soil was modelled as an elasto-plastic material using the Mohr Coulomb failure criterion. Upon the validation of this modelling approach, two-dimensional model of a 3 m high full integral abutment was developed to investigate the soil-structure interaction in prototype dimensions.
- Three-dimensional modelling (Chapter 7): in this part, three-dimensional models were developed to replicate the large-scale physical model tests. In these models, a new finite element modelling approach was proposed utilising a non-linear Mohr Coulomb failure criterion for the soil, similar to that in the GSK constitutive model proposed by Krabbenhoft et al. (2012). The proposed soil model incorporated the changes in the soil stiffness, extending the original GSK model, to study soil-structure interactions. This is achieved by relating the soil stiffness to the confining pressure which changes during unloading/loading. This Extended GSK model was validated using data from the large-scale experiments. The purpose of this modelling approach is to address the dependency of the soil stiffness and strength on the confining pressure where such effects are more prominent in modelling the interaction in three-dimensional settings and at relatively high range of confining pressures.

8.3 Conclusions

The outcomes of the analytical, numerical and experimental studies conducted in this research are summarized below:

- The observations of the failure surface in the large-scale experiments together with the analysis of the PIV images captured during the small wall experiments both confirm that the passive failure surface of the soil comprises of an arc at the bottom part and a straight line. This conclusion supports the assumptions made during the development of the log-spiral solution developed in this thesis.
- The classical theories for lateral earth pressures such as Coulomb and Rankine do not capture well the lateral soil pressures in IABs due to the ratcheting effects developed under cyclic abutment movements. Moreover, the assumption of a linear earth pressure distribution, by these classical theories, misrepresents the vertical profile of earth pressure in IABs. This thesis proposes a profile that addresses the lateral earth pressure behind an abutment experiencing translational movement. In this profile, the pressure varies linearly from zero at the soil surface to a maximum value of $\frac{3}{4}\gamma H K^*$ at a depth equals to $\frac{3}{4}H$ and remains constant, at this value, over the lower part of the wall. An appropriately conservative value of earth pressure coefficient K^* need to be considered. The value of K^* recommended by the British Standards PD 6694/1 (2011) underestimates the lateral earth pressure when the movement is dominantly translation. Therefore, this thesis recommends increasing the value of K^*, calculated based on PD 6694/1 (2011), by 25%.
- The mode of abutment movement (rotation or translation) is not appropriately addressed in the major international design guidelines as a dominant factor that governs both the magnitude and the distribution of the lateral earth pressure acting on

the abutment. The experimental study conducted in this thesis revealed that abutments with mainly translational movement experience more severe effects compared to that with principally rotational movement. In practice it will be necessary and important to distinguish between dominantly translational (short walls) or dominantly rotational wall (tall walls). Guidelines for what constitutes a short or a long wall, however, are lacking.

- The experimental and numerical analyses conducted in this thesis showed that the location of maximum earth pressure, in response to a translational abutment movement, occurs at a depth equals to approximately $2H/3$ from the soil surface instead of $H/2$ as proposed by the British Standard PD 6694-1 (2011).
- The experimental and numerical results showed that the deformation in the approach soil consists of both a settlement trough and surface heaving. The negative volumetric strain, or the settlement, in the backfill soil adjacent to the abutment is caused by soil densification and soil displacement. The positive volumetric strain, or the plastic dilatancy, is generally greater when the soil is initially dense which results in a large surface heave beyond the settlement trough. On contrary, initially loose soil experiences large soil settlement and insignificant heaving when subjected to cycles of abutment wall movements.
- The black sand, which was used for the first time in this thesis, provides a potential for geotechnical physical conditions similar to a 2*g* environment because the unit weight of back sand is nearly twice as high as that of normal sand. Despite of its unusual high unit weight, the black sand possesses regular granular characteristics, strength and stiffness similar to those of a traditional backfill soil.

- The EGSK can provide a better model of soil-structure interactions by considering the changes in the strength and stiffness of soil. However, further development is required to capture densification effects and address the under-prediction of soil displacement in the first few cycles
- The EPS geofoam in current configuration shows a promise in mitigating both lateral pressure ratcheting and settlement trough. However, a more self-stable configuration may be needed to further improve the results. A better EPS Geofoam inclusion arrangement may involve a thin strip of low-stiffness EPS placed between the wall and a large wedge-shaped EPS inclusion. The low-stiffness EPS Geofoam strip will keep the lateral earth pressure at lower levels while the wedge-shaped inclusion provides a self-stable soil mass to avoid soil slippage during the active phase of the wall movement.
- The Log-spiral solution developed in this study provides an accurate estimation of the limiting passive earth pressures. The results obtained from the log-spiral solution showed to be in closer agreement with the measured data than those computed using classical Rankine and Coulomb theories. Therefore, it provides an excellent tool for practicing engineers specially it can easily be programmed using MATLAB or even Excel spreadsheet.
- The transfer function of the EPS geofoam inclusion depends largely on the soil-EPS relative stiffness E_r ($E_r = \frac{E_{EPS}}{E_{soil}}$), which is the ratio between the stiffness of EPS to that of the backfill soi. The transfer function of the inclusion improves when the value of E_r decreases.
- The results of large-scale experiments showed multiple active failure planes develop due to the wall movement. This was observed in all tests conducted with cyclic

movement, including that with the EPS inclusion. This indicates that cumulative active slippage occurs with the movement cycles.

- The experimental results showed that the passive failure under a cyclic translational movement occurs at a significantly smaller displacement than that at a monotonic movement. The results of test T3 revealed that the passive failure became clearly visible after 20 cycles of displacement of $\Delta/_{H}$ = 1 %. However, the results of test T4 (where the wall moved monotonically), showed that signs of the passive failure became visible after a displacement of $\Delta/_{H}$ = 17%.

8.4 Recommendation for Future Studies

- This research shows that unified and explicit standards about the consideration of lateral earth pressure in IAB approaches are currently unavailable. Therefore, further research is necessary to quantify the magnitude and the distribution of the lateral earth pressure in IABs. Such research needs to employ an experimental program to investigate the lateral earth pressure under similar in situ stress conditions as in the field for various loading scenarios including different displacement amplitudes, modes of wall movements, wall skew angles, number of cycles and different backfill densities.
- The EPS geofoam showed to perform effectively in reducing the approach problems in IABs, namely in terms of preventing the lateral pressure ratcheting and alleviation of the approach settlement. The EPS utilised in the experimental and numerical analyses involved a single block of medium stiffness EPS with a density of 20 kg/m^3. Further studies are advised to consider EPS geofoam in different self-stable arrangements, such as providing a thin board of resilient EPS between the wall and the full EPS wedge, to further reduce the temperature effects on IAB approaches.

- The EGSK model utilised in this study, presents an effective model to capture the nonlinear soil behaviour. However, the soil densification effects have not been taken into account in the EGSK model. Therefore, further development of this model is advised, to more accurately consider the densification effects in response to the abutment cyclic movement.
- Although the EGSK model addresses the non-linear response of soil, the numerical results of the soil settlement showed that the settlement curve does not capture the realistic response at the first few loading cycles. Further studies are advised to further develop the EGSK model to better replicate the soil settlement at the early loading stages.
- The hyper-foam model provided by the ABAQUS Standard (2017) is able to replicate the EPS behaviour reasonably well. However, in order to simulate the EPS behaviour when plastic deformations and hardening effects are expected, a constitutive model with hardening plasticity such as the one developed by Wong and Leo (2006) need to be employed in the FE modelling.
- The temperature induced movements of the abutment take place in a slow pattern corresponding to the annual temperature fluctuations. Therefore, time dependent creep deformation is likely to occur in the EPS geofoam due to its rheological behaviour. Further studies are recommended to involve the creep strain component in the analysis of EPS when used in IAB approaches.
- Guidelines for what constitute a translational-dominant, a rotational-dominant wall or mixed wall movements need to be investigated and established.
- While solutions may be found to significantly reduce settlement trough (such as the EPS inclusion solution investigated in this thesis), finding the final step solution to bring it to within acceptable settlement performance criteria during its design life is

also the most difficult step. By understanding the fundamental mechanics of soil-structure interactions, it is hoped that the work in this thesis will lead to finding the final step solution.

References

American Association of State Highway and Transportation Officials, 2020. AASHTO LRFD Bridge Design Specifications,

ABAQUS Inc. (2013). ABAQUS Version 6.13 user's manual, Providence, Rohde Island, USA.

AbdelSalam, S. S., Azzam, S. A., & Fakhry, B. M. (2016). Reliability and 3D modeling of flexible walls with EPS inclusion. *International Journal of Geomechanics*, *17*(7), 04016153.

Alampalli, S., & Yannotti, A. (1998). In-service performance of integral bridges and jointless decks. Transportation Research Record: Journal of the Transportation Research Board, (1624), 1-7.

Alaska Department of Transportation and Public Facilities. (2017). Alaska Bridges and Structures Manual, September 2017.

Alqarawi, A. S., Leo, C. J., Liyanapathirana, D. S., & Ekanayake, S. D. (2016). A study on the effects of abutment cyclic movements on the approach of integral abutment bridges. *Australian Geomechanics Journal*, *51*(2). https://doi.org/10.4992/jjpsy.32.381

Alqarawi, A. S., Leo, C. J., Liyanapathirana, D. S., Sigdel, L., Lu, M., & Hu, P. (2021). A spreadsheet-based technique to calculate the passive soil pressure based on the log-spiral method. *Computers and Geotechnics, 130*, 103926.

Al-Qarawi, A., Leo, C. J., & Liyanapathirana, S. (2017). A study on the effects of mode of abutment wall movements in integral abutment bridges. In *Proceedings of the 1st International Conference on Geomechanics and Geoenvironmental Engineering (ICGMGE2017), 20-22 November 2017, Sydney, Australia* (pp. 180-185).

Arellano, D. and T. D. Stark (2009). Load bearing analysis of EPS-block geofoam embankments. 8th International Conference on the Bearing Capacity of Roads, Railways and Airfields.

Arsoy, S., Barker, R. M., & Duncan, J. M. (1999). The behaviour of integral abutment bridges (Vol. 3, p. 13). Charlottesville, VA: Virginia Transportation Research Council.

BA42/96 (2003). Design manual for roads and bridges, Vol. 1, Section 3, Part 12: The design of integral bridges: Amendment 1. UK Highways Agency

Barr, P. J., Halling, M. W., Huffaker, C., & Boyle, H. (2013). Behaviour and analysis of an integral abutment bridge. Bridges Transportation Research Board.

Bartlett, S. F., & Neupane, R. (2017). *Seismic Evaluation of Expanded Polystyrene (EPS) Geofoam Bridge Support System for Overpass Structures* (No. MPC 17-328).

BASF Aktlengesellschaft (2006). Rigid styropor foam as a lightweight construction material for highway foundations: GEOFOAM. Technical Information. Ludwigshafen- Germany 510/1 - 510/10

Bathurst, R. J., Zarnani, S., & Gaskin, A. (2007). Shaking table testing of geofoam seismic buffers. *Soil Dynamics and Earthquake Engineering*, *27*(4), 324-332.

Bathurst, R. J., & Zarnani, S. (2013). Earthquake load attenuation using EPS geofoam buffers in rigid wall applications. *Indian Geotechnical Journal*, *43*(4), 283-291.

Bayoglu F., (2004). Soil – structure interaction for integral bridges and culverts. Licentiate Thesis, KTH.

Bloodworth, A. G., Xu, M., Banks, J. R., & Clayton, C. R. (2011). Predicting the earth pressure on integral bridge abutments. Journal of Bridge Engineering, 17(2), 371-381.

Bolton, M. D. (1986). The strength and dilatancy of sands. *Geotechnique*, *36*(1), 65-78.

Broms, B. B., & Ingelson, I. (1971). Earth pressure against the abutments of a rigid frame bridge. Geotechnique, 21(1), 15-28.

Burke Jr, M. P. (2009). Integral and semi-integral bridges. John Wiley & Sons.

Butterfield, R. (1999). Dimensional analysis for geotechnical engineers. *Geotechnique*, *49*(3), 357-366.

Caquot, A., Kerisel, J., 1948. Tables for the Calculation of Passive Pressure, Active Pressure and Bearing Capacity of Foundations. Gauthier, Villars, Paris.

Civjan, S. A., Bonczar, C., Brena, S. F., DeJong, J., & Crovo, D. (2007). Integral abutment bridge behaviour: Parametric analysis of a Massachusetts bridge. Journal of Bridge Engineering, 12(1), 64-71.

Chun, B. S., H.-S. Lim, M. Sagong and K. Kim (2004). "Development of a hyperbolic constitutive model for expanded polystyrene (EPS) geofoam under triaxial compression tests. Geotextiles and Geomembranes 22(4): 223-237.

Colorado Department of Transportation. (2020). Bridge Design Manual.

Cosgrove, E., & Lehane, B. M. (2003). Cyclic loading of loose backfill placed adjacent to integral bridge abutments. International Journal of Physical Modelling in Geotechnics, 3(3), 9-16.

Coulomb, C. A. (1973). Essai sur une application des regles de maximis et minimis a quelques problemes de statique relatifs a l'architecture (essay on maximums and minimums of rules to some static problems relating to architecture).

Deng, A., & Xiao, Y. (2010). Measuring and modelling proportion-dependent stress-strain behaviour of EPS-sand mixture 1. *International Journal of Geomechanics*, *10*(6), 214-222.

Denton, S., Christie, T., Shave, J., & Kidd, A. (2011). PD 6694-1: Recommendations for the design of structures subject to traffic loading to EN 1997-1. In *Bridge Design to Eurocodes: UK Implementation* (pp. 434-450). ICE Publishing.

Dicleli, M. (2000). Simplified model for computer-aided analysis of integral bridges. Journal of Bridge engineering, 5(3), 240-248.

Duncan, J. M., & Mokwa, R. L. (2001). Passive earth pressures: theories and tests. *Journal of Geotechnical and Geoenvironmental Engineering*, *127*(3), 248-257.

Elragi, A. F. (2000). Selected engineering properties and applications of EPS geofoam.

England, G. L., Bush, D. I., & Tsang, N. C. (2000). Integral bridges: a fundamental approach to the time-temperature loading problem. Thomas Telford.

Fang, Y. S., Chen, J. M., & Chen, C. Y. (1997). Earth pressures with sloping backfill. *Journal of Geotechnical and Geoenvironmental Engineering*, *123*(3), 250-259.

Fang, Y. S., Ho, Y. C., & Chen, T. J. (2002). Passive earth pressure with critical state concept. *Journal of Geotechnical and Geoenvironmental Engineering*, *128*(8), 651-659.

Faraji, S., Ting, J. M., Crovo, D. S., & Ernst, H. (2001). Nonlinear analysis of integral bridges: finite-element model. Journal of Geotechnical and Geo-Environmental Engineering, 127(5), 454-461.

Fartaria, C. (2012). Soil-structure interaction in integral abutment bridges.

Frosch, R. J., & Lovell, M. D. (2011). Long-Term Behaviour of Integral Abutment Bridges (No. FHWA/IN/JTRP-2011/16).

Ghadimi, B., Nikraz, H., & Rosano, M. (2016). Dynamic simulation of a flexible pavement layers considering shakedown effects and soil-asphalt interaction. Transportation Geotechnics, 7, 40-58.

Gibbens, B., & McManus, A. (2011, October). Design of Peninsula Link Integral Bridges. *Austroads Bridge Conference, 8th, 2011, Sydney*, New South Wales, Australia (No. AP-G90/11).

Greimann, L. F., Yang, P. S., & Wolde-Tinsae, A. M. (1986). Nonlinear analysis of integral abutment bridges. Journal of Structural Engineering, 112(10), 2263-2280.

Hassiotis, S., & Roman, E. K. (2005). A survey of current issues on the use of integral abutment bridges. *Bridge Structures*, *1*(2), 81-101.

Hoppe, E. J., & Gomez, J. P. (1996). Field study of an integral back wall bridge (No. FHWA/VA-97-R7).

Hoppe, E., Weakley, K., & Thompson, P. (2016). Jointless bridge design at the Virginia Department of Transportation. *Transportation Research Procedia*, *14*, 3943-3952.

Horvath, J. S. (2000). Integral-abutment bridges: problems and innovative solutions using EPS geofoam and other geosynthetics. Res. Rpt. No. CE/GE-00, 2.

Huang, F., Shan, Y., Chen, G., Lin, Y., Tabatabai, H., & Briseghella, B. (2020). Experiment on Interaction of Abutment, Steel H-Pile and Soil in Integral Abutment Jonitless Bridges (IAJBs) under Low-Cycle Pseudo-Static Displacement Loads. *Applied Sciences*, *10*(4), 1358.

Huntley, S. A., & Valsangkar, A. J. (2013). Field monitoring of earth pressures on integral bridge abutments. Canadian Geotechnical Journal, 50(8), 841-857.

Huntley, S. A., & Valsangkar, A. J. (2016). STR-997: INSTRUMENTATION AND LONG-TERM MONITORING OF AN INTEGRAL-ABUTMENT BRIDGE SUPERSTRUCTURE.

Illinois State Toll Highway Authority. (2019). Structures Design Manual.

Jacky, J. (1948). “The coefficient of earth pressure at rest. Journal for Society of Hungarian Architects and Engineers, 355–358.

Keller, G. R. (2008). Use of geosynthetic reinforced soil (GRS) for bridge abutments. In ARRB Conference, 23rd, 2008, Adelaide, South Australia, Australia.

Kérisel, J., & Absi, E. (1990). Tables for the calculation of passive pressure, active pressure and bearing capacity of foundations. *Gauthier-Villard, Paris*.

Khasawneh, Y. A. (2014). *Soil structure interaction of integral abutment bridges* (Doctoral dissertation, Purdue University).

Khodair, Y. A., & Hassiotis, S. (2013). Rigidity of abutments in integral abutment bridges. Structure and Infrastructure Engineering, 9(2), 151-160.

Krabbenhoft, S., Clausen, J., & Damkilde, L. (2012). The bearing capacity of circular footings in sand: comparison between model tests and numerical simulations based on a nonlinear Mohr failure envelope. *Advances in Civil Engineering*, *2012*.

Krabbenhoft, S., & Christensen, R. Design of Railway embankment using the Mohr Coulomb Criterion and GSK Model for cohesionless soil.

Kunin, J., & Alampalli, S. (2000). Integral abutment bridges: Current practice in United States and Canada. *Journal of performance of constructed facilities*, *14*(3), 104-111.

LaFave, J., Fahnestock, L., Brambila, G., Riddle, J., Jarrett, M., Svatora, J., ... & An, H. (2017). *Integral abutment bridges under thermal loading: Field monitoring and analysis*. Illinois Center for Transportation/Illinois Department of Transportation.

Laman, J. A., & Kim, W. S. (2009). *Monitoring of integral abutment bridges and design criteria development* (No. FHWA-PA-2009-005-PSU 002). Pennsylvania. Dept. of Transportation.

Lawver, A., French, C., & Shield, C. (2000). Field performance of integral abutment bridge. Transportation Research Record: Journal of the Transportation Research Board, (1740), 108-117.

Lehane, B. M. (2011). Lateral soil stiffness adjacent to deep integral bridge abutments. Géotechnique, 61(7), 593-603.

Lima, J. M., & de Brito, J. (2009). Inspection survey of 150 expansion joints in road bridges. *Engineering structures*, *31*(5), 1077-1084.

Liu, S., Xia, Y., & Liang, L. (2018). A modified logarithmic spiral method for determining passive earth pressure. *Journal of Rock Mechanics and Geotechnical Engineering*, *10*(6), 1171-1182.

Lock, R. J. (2002). Integral bridge abutments. MEng Project Report. CUED/DSOILS/STR320, 2002 (Cambridge, UK: Schofield Centre).

Maine Department of Transportation. (2018). Bridges Design Guide.

Maranha, J. R., & das Neves, E. M. (2009). The experimental determination of the angle of dilatancy in soils. In *Proceedings of the 17th International Conference on Soil Mechanics and Geotechnical Engineering: The Academia and Practice of Geotechnical Engineering, Alexandria, Egypt, 5-9 October 2009, Volume 1* (pp. 147-150). IOS Press.

Mayne, P. W., & Kulhawy, F. H. (1982). Ko- OCR Relationships in Soil. *Journal of the Soil Mechanics and Foundations Division*, *108*(6), 851-872.

Minnesota Department of Transportation. (2016). LRFD Bridge Design.

Nam, M. S., & Park, Y. H. (2015). Relationship between earth pressure and thermally induced movement of integral abutments. *Journal of Performance of Constructed Facilities*, *29*(4), 04014093.

Nevada Department of Transportation. (2009). Bridges Design Manual.

New Hampshire Department of Transportation. (2016). Bridge Design Manual, Chapter 6. Substructures

New Jersey Department of Transportation. (2016). Design Manual for Bridges and Structures. Sixth Edition.

New York State Department of Transportation. (2019). Bridge Manual.

Ng, C. W., Springman, S. M., & Norrish, A. R. (1998). Centrifuge modelling of spread-base integral bridge abutments. Journal of geotechnical and geoenvironmental engineering, 124(5), 376-388.

Ni, P., Mei, G., & Zhao, Y. (2016). Displacement-dependent earth pressures on rigid retaining walls with compressible geofoam inclusions: physical modelling and analytical solutions. *International Journal of Geomechanics*, *17*(6), 04016132.

North Dakota Department of Transportation. (2013). Design Manual.

Oesterle, R. G., & Tabatabai, H. (2014). Design considerations for integral abutment/jointless bridges in the USA. *The 1st International Conference on Integral Abutment/Jointless Brides, Fuzhou, China, 2014.*

Ogden, R. W. (1972, February). Large deformation isotropic elasticity–on the correlation of theory and experiment for incompressible rubberlike solids. In *Proc. R. Soc. Lond. A* (Vol. 326, No. 1567, pp. 565-584). The Royal Society.

OPTUM CE. (2016). Optum G2, Materials, Optum Computational Engineering, Newcastle. *New South Wales, Australia*.

Oregon Department of Transportation. (2019). Bridge Design Manual.

Ossa, A. and M. P. Romo (2009). "Micro- and macro-mechanical study of compressive behaviour of expanded polystyrene geofoam. Geosynthetics International, 16(5): 327-338.

Padade, A. H., & Mandal, J. N. (2014). Expanded polystyrene-based geomaterial with fly ash. *International Journal of Geomechanics*, *14*(6), 06014013.

Paraschos, A., & Amde, A. M. (2011). A survey on the status of use, problems, and costs associated with Integral Abutment Bridges. *Better Roads*, 1-20.

Patki, M. A., Mandal, J. N., & Dewaikar, D. M. (2015). Determination of passive earth pressure coefficients using limit equilibrium approach coupled with the Kötter equation. *Canadian Geotechnical Journal*, *52*(9), 1241-1254.

Pennsylvania Department of Transportation. (2014). Publication 15M-Design Manual, Part 4. Appendix G, Integral bridges.

Perić, D., Miletić, M., Shah, B. R., Esmaeily, A., & Wang, H. (2016). Thermally induced soil structure interaction in the existing integral bridge. Engineering Structures, 106, 484-494.

Pétursson, H., Collin, P., Veljkovic, M., & Andersson, J. (2011). Monitoring of a Swedish integral abutment bridge. *Structural engineering international*, *21*(2), 175-180.

Pokrovsky, G. I. (1936). Studies of soil pressures and soil deformations by means of a centrifuge. *Proc. of 1^< st> ICSMFE*, *1*, 70-71.

Queensland Department of Transport and Main Roads. (2020). Design Criteria for Bridges and other Structures. Queensland. Australia.

Rankine, W. J. M. (1857). II. On the stability of loose earth. *Philosophical transactions of the Royal Society of London*, (147), 9-27.

Rollins, K. M., Scott, E., & Marsh, A. (2017). Geofoam Inclusions for Reducing Passive Force on Bridge Abutments Based on Large-Scale Tests. In *Geotechnical Frontiers 2017* (pp. 59-68).

Schofield, A. N. (1980). Cambridge geotechnical centrifuge operations. *Geotechnique, 30*(3), 227-268.

Sigdel, L. D., Leo, C., Liyanapathirana, S. & Hu, P. (2020). Integral Bridge Abutment-soil Interaction Analysis Using PIV Technique. *The 3rd International Conference on Geotechnical Engineering, Colombo, Sri Lanka. "In press".*

Stanier, S. A., Blaber, J., Take, W. A., & White, D. (2015). Improved image-based deformation measurement for geotechnical applications, Canadian Geotechnical Journal, Vol. 53, pp. 727-739.

Shiau, J. S., Augarde, C. E., Lyamin, A. V., & Sloan, S. W. (2008). Finite element limit analysis of passive earth resistance in cohesionless soils. *Soils and Foundations*, *48*(6), 843-850.

South Dakota Department of Transportation. (2020). Bridge Design Manual.

Springman, S. M., Norrish, A. R. M., & Ng, C. W. W. (1996). Cyclic loading of sand behind integral bridge abutments. *TRL REPORT 146*.

State of Ohio Department of Transportation. (2020). Bridge Design Manual.

Surarak, C., Likitlersuang, S., Wanatowski, D., Balasubramaniam, A., Oh, E., & Guan, H. (2012). Stiffness and strength parameters for hardening soil model of soft and stiff Bangkok clays. *Soils and foundations*, *52*(4), 682-697.

Tabaroei, A., Abrishami, S., & Hosseininia, E. S. (2017). Comparison between two different pluviation setups of sand specimens. *Journal of Materials in Civil Engineering*, *29*(10), 04017157.

Tabatabai, H., Magbool, H., Bahumdain, A., & Fu, C. (2017). Criteria and practices of various states for the design of jointless and integral abutment bridges.

Tan, D., Reid, C., Rajeev, P., Piratheepan, J., & Sivakugan, N. (2014). Earth pressure development in integral abutment bridge subjected to thermal loadings. 8th Australasian Congress on Applied Mechanics (ACAM), PP 408-415.

Tatsuoka, F., Hirakawa, D., Nojiri, M., Aizawa, H., Nishikiori, H., Soma, R., Tateyama, M. & Watanabe, K. (2009). A new type of integral bridge comprising geosynthetic-reinforced soil walls. Geosynthetics International, 16(4), 301-326.

Tatsuoka, F., Tateyama, M., Koseki, J., & Yonezawa, T. (2014). Geosynthetic-reinforced soil structures for railways in Japan. *Transportation Infrastructure Geotechnology*, *1*(1), 3-53.

Terzaghi, K. (1943). Theoretical Soil Mechanics. John Wiley & Sons, Inc. *New York*, 11-15.

Terzaghi, K., Peck, R. B., & Mesri, G. (1996). *Soil mechanics in engineering practice*. 3rd ed. New York. John Wiley & Sons, Inc.

Thomas Jr, T. A., & Lutenegger, A. J. (1998). Passive earth pressure tests on an integral bridge abutment.

Utah Department of Transportation. (2017). Structures Design and Detailing Manual.

Varmazyar, M., Wozniak, R., & Walsh, R. (2017, April). Utilizing compressible inclusions and cement stabilised sand for integral bridges. In *Austroads Bridge Conference, 10th, 2017, Melbourne, Victoria, Australia*.

VicRoads, 2018. Design of Integral and Semi-Integral Bridges. Bridge Technical Note BTN 010/2018. Victoria. Australia

Virginia Department of Transportation. (2020). Bridge Design Manual. Chapter 17, Abutments.

White, H., Pétursson, H., & Collin, P. (2010). Integral abutment bridges: the European way. *Practice periodical on structural design and construction*, *15*(3), 201-208.

Wilson, P., & Elgamal, A. (2010). Large-scale passive earth pressure load-displacement tests and numerical simulation. *Journal of Geotechnical and Geoenvironmental Engineering*, *136*(12), 1634-1643.

Wong, H., & Leo, C. J. (2006). A simple elastoplastic hardening constitutive model for EPS geofoam. Geotextiles and Geomembranes, 24(5), 299-310.

Yang, M., & Tang, X. (2017). Rigid Retaining Walls with Narrow Cohesionless Backfills under Various Wall Movement Modes. *International Journal of Geomechanics*, *17*(11), 04017098.

Zadehmohamad, M., & Bolouri Bazaz, J. (2017). Cyclic behaviour of geocell-reinforced backfill behind integral bridge abutment. International Journal of Geotechnical Engineering, 1-13.

Zarnani, S., & Bathurst, R. J. (2009). Numerical parametric study of expanded polystyrene (EPS) geofoam seismic buffers. Canadian Geotechnical Journal, 46(3), 318-338.